Precipitation Variability and Change over Morocco and the Mediterranean

by

Alexandre Tuel

B.S., École polytechnique (2015)
S.M., École polytechnique (2016)

Submitted to the Department of Civil and Environmental Engineering
in partial fulfillment of the requirements for the degree of

Doctor of Philosophy in Hydrology

at the

MASSACHUSETTS INSTITUTE OF TECHNOLOGY

September 2020

Author ..... DocuSigned by: Alexandre Tuel 44A94A6D1C3E415...
Department of Civil and Environmental Engineering
August 17, 2020

Certified by ..... DocuSigned by: Elfatih A.B. Eltahir CB08F7CA77C8422...
Elfatih. A. B. Eltahir
Professor of Civil and Environmental Engineering
Breene M. Kerr Professor of Hydrology and Climate
Thesis Supervisor

Accepted by ..... DocuSigned by: Colette Heald 6E1050957 18A45F...
Colette L. Heald
Professor of Civil and Environmental Engineering
and Earth, Atmospheric and Planetary Sciences
Chair, Graduate Program Committee

Precipitation Variability and Change over Morocco and the Mediterranean

by

Alexandre Tuel

Submitted to the Department of Civil and Environmental Engineering
on August 17, 2020, in partial fulfillment of the
requirements for the degree of
Doctor of Philosophy in Hydrology

Abstract

Water is a critical factor limiting economic and social development in Morocco and the Mediterranean Basin. In addition to strong seasonality and high inter-annual variability, annual precipitation remains low (<500mm) across much of the region. Furthermore, the situation is not expected to improve under climate change as models project a sustained decline in precipitation in the Mediterranean, most pronounced during the winter season. Despite the significance of such projections, a comprehensive theory for Mediterranean winter climate change is still lacking. Here, we adopt a multi-faceted approach to investigate precipitation variability and change over Morocco and the Mediterranean, with a focus on resulting water availability. First, we link inter-annual variability of seasonal precipitation in Morocco to global sea-surface temperatures, and develop empirical forecast models that can predict up to 35% of this variability with a one-month lead time. Turning our attention to regional climate change processes and impacts, we show how future winter precipitation trends in the Mediterranean directly result from projected circulation anomalies. The enhanced advection of dry air from the Sahara Desert caused by these anomalies is key in causing precipitation to decline over Morocco. In addition, a major contribution of this work is to propose a physical explanation for the circulation trends involving planetary-scale circulation shifts and reduced warming of the Mediterranean Sea compared to land. We develop high-resolution regional climate simulations over Morocco to assess future risks from drought and weather extremes relevant to agriculture. Our results point to robust declines of 25-45% in annual precipitation and confirm physical drivers identified at the regional scale. Because snow is such an important component of the water cycle in this semi-arid region, we also investigate snowpack dynamics in the High Atlas and we quantify components of the snow water balance for the first time. Future trends in snowpack and associated runoff are also investigated: at best, snowpack volume will decline by at least 60%, which, combined with increased air dryness, will likely reduce mountain runoff by 60%. Our findings have important implications for climate change adaptation and water management in Morocco, particularly in agriculture, which uses 90% of all available water.

Thesis Supervisor: Elfatih. A. B. Eltahir
Title: Professor of Civil and Environmental Engineering
Breene M. Kerr Professor of Hydrology and Climate

Acknowledgments

This doctoral thesis is the result of four years of fruitful work with my advisor, Elfatih Eltahir, to whom I am very much grateful for his guidance, suggestions, and many hours spent in fruitful discussions. If I had to remember one thing from him, it is that looking at a map often goes halfway towards solving the problem! I also warmly thank my thesis committee members, Earle Williams and Paul O'Gorman, for their useful advice and contributions that have greatly improved this work. Over the years, I have also had the pleasure to work alongside the numerous members of our research group. I particularly thank Catherine Nikiel for her advice and support, Suchul Kang for his life-saving help with Fortran and MRCM, and Yeon-Woo Choi for his help and our last few months of collaboration. This research emerged from the UMRP collaboration program between MIT and Université Mohamed VI Polytechnique (UM6P), Morocco, and has been generously supported by UM6P and its sponsor, the Office Chérifien des Phosphates. Money is not everything, however; this collaboration would have been nowhere as successful without the hard work and diligence of Nabil El Moçayd, who helped me find my way in Morocco.

Contents

List of Figures

List of Tables

Chapter 1

Introduction

"We don't govern water. Water governs us."[1] Few places in the world embody this statement more than Morocco, where water is the key limitation to economic and social development. Located along the Atlantic and Mediterranean coasts, at the northwestern border of the immense Sahara Desert, Morocco lives on the scarce winter rains brought by rare North Atlantic storms. Every single accessible drop is used for human activity, but the threat of drought is always present. The dry climate and large inter-annual variability in precipitation make efficient water management a real challenge, and the country is compelled to live at the rhythm of the rains. Overall, the water resource per inhabitant, at about 800m^3 (by comparison, this figure is 8500m^3 for the United States), puts the country under permanent water stress, though there are significant spatial disparities between the wetter north and the drier south. In parallel, climate change is expected to make the situation even harder for Morocco with a projected 40% decrease in precipitation under a business-as-usual greenhouse gas emission scenario. By 2040, Morocco may be among the world's top 10 most water-stressed countries [161]. While climate models generally fail to agree on the sign of future precipitation changes over land, the Mediterranean Basin, and Morocco in particular, is one of the few land regions where all models converge in predicting a robust drying over the upcoming decades. If realized, this would put severe constraints on the country's future development.

[1] *Heart of dryness: How the Last Bushmen Can help Us Endure the Coming Age of Permanent Drought*, James Workman, Walker & Company, 2009

Over the last decades, Morocco has gone through several major droughts which took their toll on agricultural production and the economy. Although the country has been developing and slowly shifting to industry and services, 40% of its workforce works in agriculture – mainly smallholder farmers – and its burgeoning industry requires large amounts of water as well. At the same time, large cities like Casablanca and Marrakech have been growing fast, and with them the number of tourists attracted by the Moroccan sunshine. This puts a severe strain on the water resource; desalination is not sufficient to compensate for demand growth and drier regions even resort to unsustainable groundwater pumping to satisfy local demand. This critical situation has led the Moroccan government to implement new large-scale water conservation practices in the context of the "Green Morocco Plan", an ambitious strategy to bring national agriculture into the 21^{st} century. Construction is also currently expected to begin on a costly water transfer project, designed to bring close to one billion cubic meters a year from the wetter northern regions down to the drought-stricken central plains. Still, the demand for water in Morocco already exceeds by far its renewable resources. To continue on its path of development into the 21^{st} century, Morocco will be compelled to make more profound changes to its water use, technology and management practices, from agricultural planning to the development of new infrastructure. Yet, despite, or rather because of, the numerous constraints that it has to abide by, water management in Morocco has not evolved in a long time. The water community is well aware of the problems and challenges it faces, and of the necessity to adapt for the coming century, but is in dire need of fresh ideas that science, among others, can bring to them.

To this day, robust knowledge of future water scenarios, whether at the seasonal or multi-decadal horizon, is still lacking. Short-term projections are difficult because of the large internal variability in the processes that govern seasonal precipitation. Additionally, long-term trends point towards a strong regional decline in precipitation, but the processes responsible for this drying are still largely unknown, and therefore it is hard to understand and trust model projections, and reduce their uncertainty. Finally, the regional impacts on the water cycle of the projected climate trends remain uncertain; the scarcity of data makes it difficult to assess how river runoff may respond to drying and warming, especially in the high mountains where snow is a major component of the water cycle.

This work tackles these challenging questions by developing a detailed understanding of Morocco's hydroclimate and of its predictability for present and future conditions. We begin with a broad overview of the water cycle in Morocco (Chapter 2), followed by the analysis of inter-annual variability in precipitation and its predictability at seasonal timescales using simple statistical models (Chapter 3). Long-term hydroclimatic trends are then investigated with a variety of global and regional climate simulations, and put in the context of Mediterranean climate change, for which we develop new physical insights that explain the robustness of model trends in this area (Chapters 4 and 5). Finally, we develop projections for river runoff and water availability at the catchment scale by modeling snowpack in the High Atlas under current and future climates (Chapter 6), before summarizing our main findings and discussing potential future work (Chapter 7). Existing literature and datasets used for our analyses are presented and discussed at the beginning of each chapter.

Chapter 2

Morocco, A Hotspot for Climate Variability and Change

2.1 Introduction

Niched at the junction of the Atlantic and Mediterranean coasts, on the north-western border of the Sahara Desert, the Kingdom of Morocco extends over an area of 710850 km^2 between latitudes of 21° and 36°N, and longitudes 17° and 1°W. Because of its topography and geographical location, Morocco is characterised by a wide range of climates, from the desert to the south to the relatively wet regions to the north. The country lies between the southern edge of the mid-latitude storm track and the northwestern fringe of the Hadley cell descent region, in the transition zone between the subtropical desert and wet mid-latitudes. Large parts of the country are mountainous, especially in its interior, home to one of Africa's major mountain chains, the Atlas Range (Fig. 2-1), peaking at 4167m (Jbel Toubkal). The Atlas stretches eastwards from the Atlantic coast near 30°N to Tunisia, roughly following northern Africa's Mediterranean coast. This very specific geographical setting is responsible for steep gradients of precipitation and temperatures, and substantial levels of intra- and inter-annual precipitation variability. Water is almost everywhere scarce and erratic, except in the very north of the country. Cropland is essentially limited to the northwestern plains, which either

receive sufficient rainfall or which can be irrigated from rivers draining mountain regions.

Morocco is home to 36 million people, a number that has been growing at 1-1.5% per year for the last three decades [272]. While its economy is largely focused on services (a sector that accounts for 55% of the national GDP), it remains very dependent on industry (31%) and agriculture (14%). Tourism, agriculture and phosphate minerals are Morocco's three major resources, responsible for most of the jobs and much of the income. Agriculture itself employs 40-45% of the country's workforce, mostly smallholder farmers [14]. Consequently, almost 40% of the population still lives outside cities [272]. Morocco is also the world's third largest producer of phosphate minerals and home to about 75% of proven global reserves. Exports are dominated by textile products (23% of exports), phosphate rock and its derivatives like phosphoric acid and fertilizers (16%), agricultural products (15%) and industrial equipment (14%) [183]. Consequently, the economy is highly sensitive to agricultural and phosphate prices, as well as to the amount of annual precipitation which impacts agricultural yields. It is also very dependent on water, for crop production obviously, but also phosphate transport and refining, as well as textile and industrial production, all large consumers of freshwater.

Therefore, water largely constrains life and socio-economic development in Morocco. Its scarcity and variability within the year and from year to year create enormous challenges that must be addressed to sustain viable agricultural and industrial systems. In addition, long-term prospects under climate change point to ever-increasing dryness from decreases in precipitation and rising temperatures. Consequently, Morocco can justifiably be considered a top hotspot of climate variability and change. This chapter gives a broad introduction to the water challenges faced by Morocco, which the rest of the thesis will address. We begin with an overview of Morocco's hydroclimate, followed by a presentation of its water resources and management strategies, to finish on the important challenges that the country faces now and will face in the future.

2.2 Hydroclimatology of Morocco

2.2.1 Geography and climate

Although warm and dry overall, Morocco exhibits a significant spatial variability in climate and water availability [147]. The country can be roughly divided into three main climate zones: the northwestern plains, home to 95% of the country's population, the mountainous interior, and the arid south [27, 147]. The coastal plains stretch from the Atlantic and Mediterranean coasts to the Rif, the Middle and the High Atlas ranges. There, the climate is of the Mediterranean type, characterized by mild and wet winters, and hot and dry summers. Minimum daily temperatures occur in January, at about 10-15°C in the plains, seldom going below freezing; maximum daily temperatures are reached in July, and range from 30-35°C to the north and along the Atlantic coastline, up to 45-50°C in the interior, near Marrakech for instance. The wet season in the northwest extends from about October to April around 35°N and November to March around 31°N (Fig. 2-2), and brings 80-85% of annual precipitation. Rainfall events during this season are few (10-15 at most), short (1-2 days) and irregular in time. Precipitation is brought by mid-latitude weather systems that formed along the North Atlantic storm track and subsequently drifted east under the influence of prevailing westerlies. Some storms also originate from the Mediterranean, particularly during fall and spring when the land-sea temperature contrast and topography favor condensation of sea moisture exports over land. The Rif and Atlas Range act as a barrier, lifting air masses, condensing water vapor, and generating precipitation.

Along the border of the plains, the northern slopes of the Atlas similarly receive much of their precipitation during winter, although they also experience non-negligible summer rainfall due to local-scale convection triggered by surface heating. Above 2000m altitude, sub-zero temperatures are common from November to March, and consequently a significant fraction of winter precipitation falls as snow. Persistent snowpack can regularly be seen near the highest peaks (3500-4000m) between December and February. Annual precipitation is highest in the Rif, the small (∼1500m) mountain chain located along Morocco's Mediterranean coast (Fig. 2-2), where it can reach 1000mm. It generally decreases as one goes south and inland, reaching

a low of about 200mm in the arid plains near Marrakech (Fig. 2-2).

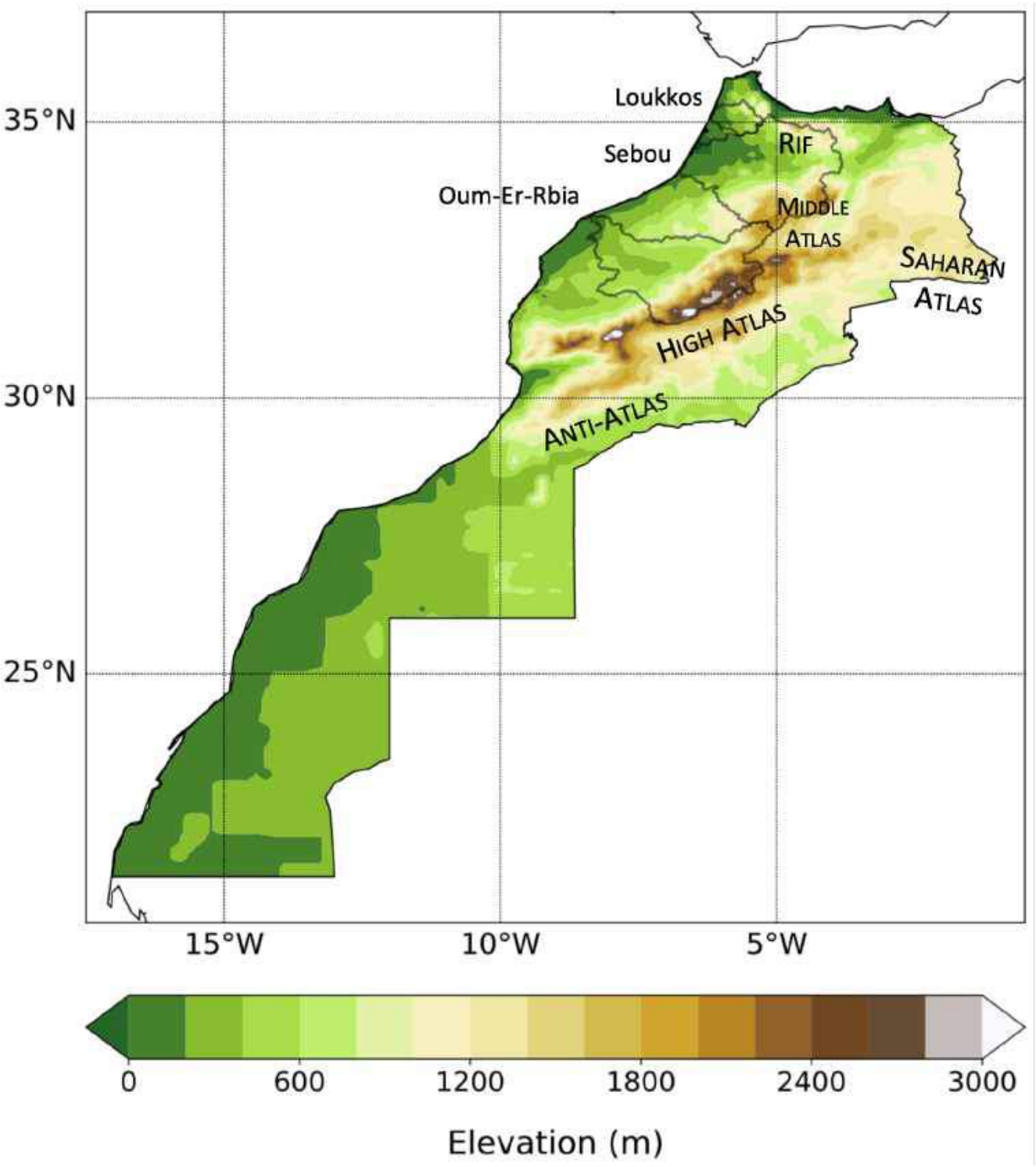

Figure 2-1: Topography of Morocco. The five major mountain ranges are indicated (capital letters), as well as the country's three largest watersheds: the Sebou, Loukkos and Oum-Er-Rbia. Data is from STRM90 [135], regridded at 0.5° resolution.

The mountainous interior (Anti-Atlas, southern High Atlas and Saharan Atlas, Fig. 2-1), above 1000m altitude, is characterized by a much more continental climate, of mainly cold desert and cold semi-arid types, with local patches of alpine climate at high elevations. Winter temperatures ordinarily range from 0-10°C, and summer temperatures from 25-35°C [32]. Annual precipitation is low, generally 150-300mm, and about equally distributed among all months outside the dry summer months (June-August) (Fig. 2-2). A slight peak around March-May can sometimes be seen, typically associated with springtime tropical moisture exports interacting with the topography [27]. Finally, all regions south of the Atlas Range are part of the Sahara Desert. Precipitation is almost non-existent; the rare rainfall events, though, tend to be intense, and regularly trigger flash floods, evidenced by the large and dry rivers beds that adorn the landscape. Overall, outside a few oases and the coastal strip, the region is inhospitable and very sparsely inhabited.

In addition to its strong spatial variability, precipitation is also highly variable in time, at the seasonal, annual, decadal and multi-decadal timescales [147]. The strong seasonal precipitation cycle owes its existence to Morocco's geographical position, between the subtropical pressure high to the south and the mid-latitude storm track to the north, whose positions evolve over the year. During winter, the North Atlantic storm track reaches its southermost position and westerlies are strongest, which allows mid-latitude storms to reach Morocco. During spring, it recedes polewards as the subtropical high moves northeastwards, bringing strong descent, and warm and dry conditions over Morocco that culminate in summer. Beginning in the fall, the cycle starts again. In a given season, several consecutive dry months are not uncommon outside the wettest regions to the north, and consequently short-term seasonal lack of moisture is also frequent. The combination of scarce vegetation, complex terrain and intense, short-term precipitation episodes make floods very common in Morocco, and in fact they rank as the second environmental disaster after droughts in terms of economic damage [171].

Precipitation varies also substantially from year to year and across decades. The coefficient of variation of annual precipitation ranges from 20-25% along the Atlantic coastline to more than 50% in the most arid regions (Fig. 2-3). In most areas, wet years typically receive twice as much precipitation as during an average dry year. Droughts are very common, with on

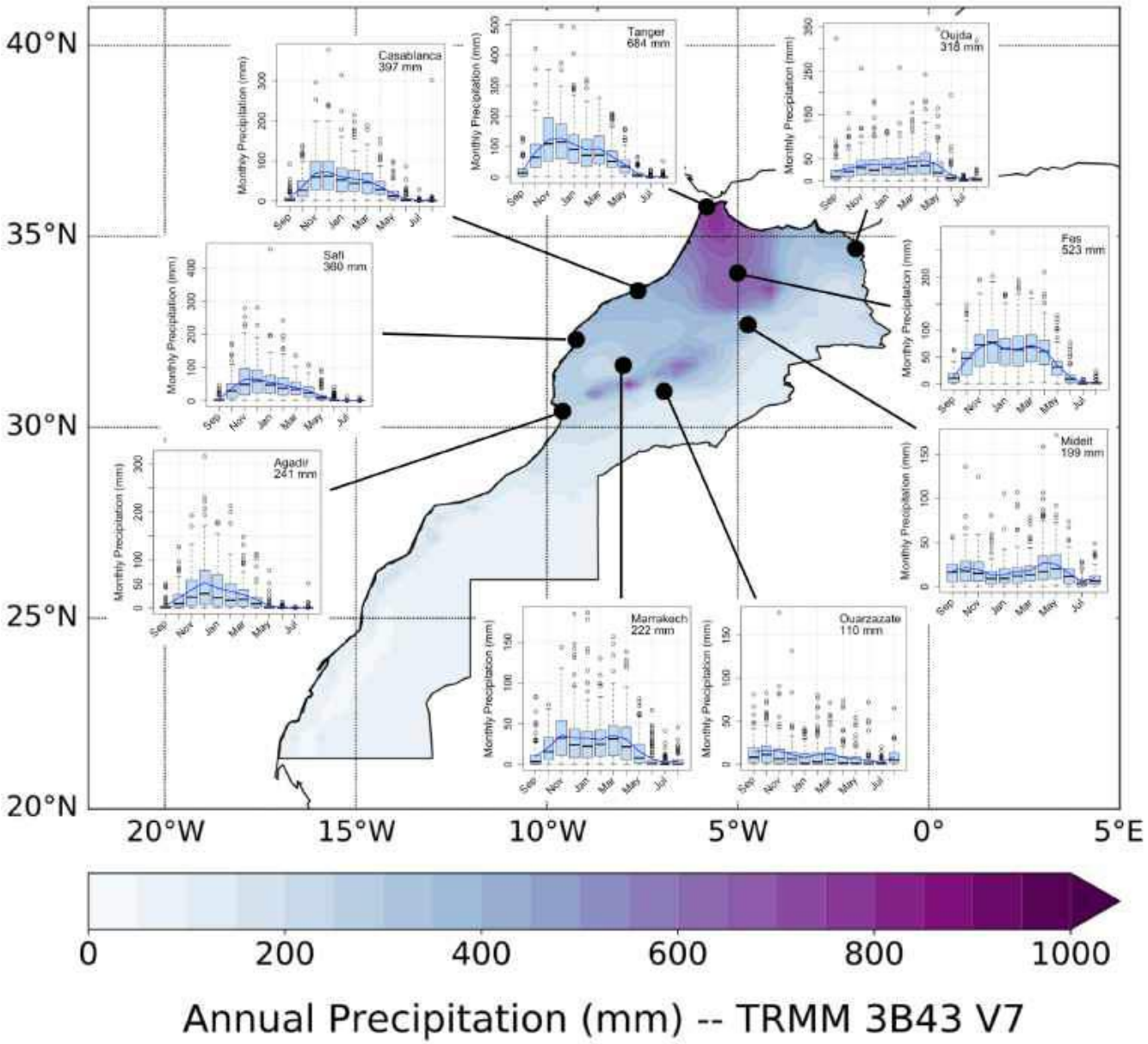

Figure 2-2: Annual precipitation (shaded contours, from TRMM 3B43 V7 [126], 1998-2018) and annual precipitation cycles in major Moroccan cities (from CRU TS4.04 [108]). Boxes in the annual cycles include 50% of values, and whiskers 95%. Monthly means are shown by the solid blue lines; horizontal black lines indicate monthly medians. Mean annual totals are shown in the top right-hand corners of station plots.

average one year per decade with less than 40% of mean rainfall. In fact, long periods of droughts, lasting several years and affecting wide areas, occur regularly. Wet and dry decades alternate in the observed record. The 1960s were a period of exceptionally wet conditions, while the beginning and the end of the 1980s, the mid-1990s and the 2000s have been dry.

The most severe drought occurred from 1980 to 1985, when rainfall deficits averaged from 20 to 50% depending on the years and areas (with extremes of 85% between 1982 and 1984). These droughts affected wide areas and lasted for several years, putting considerable stress over the country's water resources and taking their toll on agricultural production. For the last decade, precipitation has been somewhat on the low side, despite two wetter-than-average seasons (2011-2012 and 2017-2018).

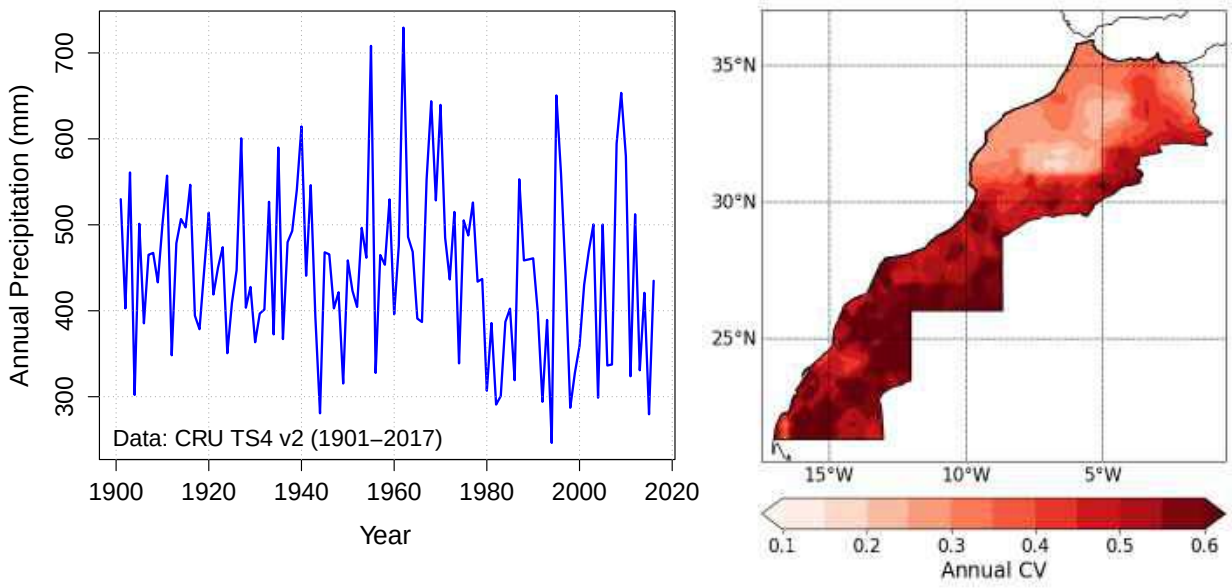

Figure 2-3: *Left*: Annual (Sep-Aug) precipitation over Morocco's northwestern plains, 1901-2015 (station-based data from CRU TS4 [108]). *Right*: Coefficient of variation (CV) of annual precipitation (satellite-based data from TRMM 3B43 V7 [126]).

2.2.2 Inter-annual variability of precipitation and the North Atlantic Oscillation

The large inter-annual variability in winter precipitation is associated with the North Atlantic Oscillation (NAO), the dominant mode of seasonal atmospheric variability over the North Atlantic [128, 129]. The NAO emerges from variations in the relative strength of the two sea-level pressure (SLP) poles characteristic of the North Atlantic circulation: the Azores High, a large region of relatively high pressure centered over the Azores islands, and the Icelandic Low, one of low pressure centered over Iceland (Fig. 2-4). Between the two, steep SLP gradients

correspond to the strong westerlies of the storm track, whose intensity increases with latitude to peak around 55-60°N. Winter storms originate from baroclinic instability in the northwestern Atlantic, and their subsequent strength and trajectory are therefore mainly driven by the large-scale pressure pattern. As the relative strength of the two pressure poles evolves, meaning that atmospheric mass is alternately redistributed between the Arctic and subtropical Atlantic areas, so does the intensity and position of the storm track. These dynamics are characterized by the NAO index, usually defined as either the difference in SLP between Reykjavík (Iceland) and Ponta Delgada (Azores), or as the projection of the North Atlantic SLP field onto its first Empirical Orthogonal Function (EOF) [129] (Fig. 2-4).

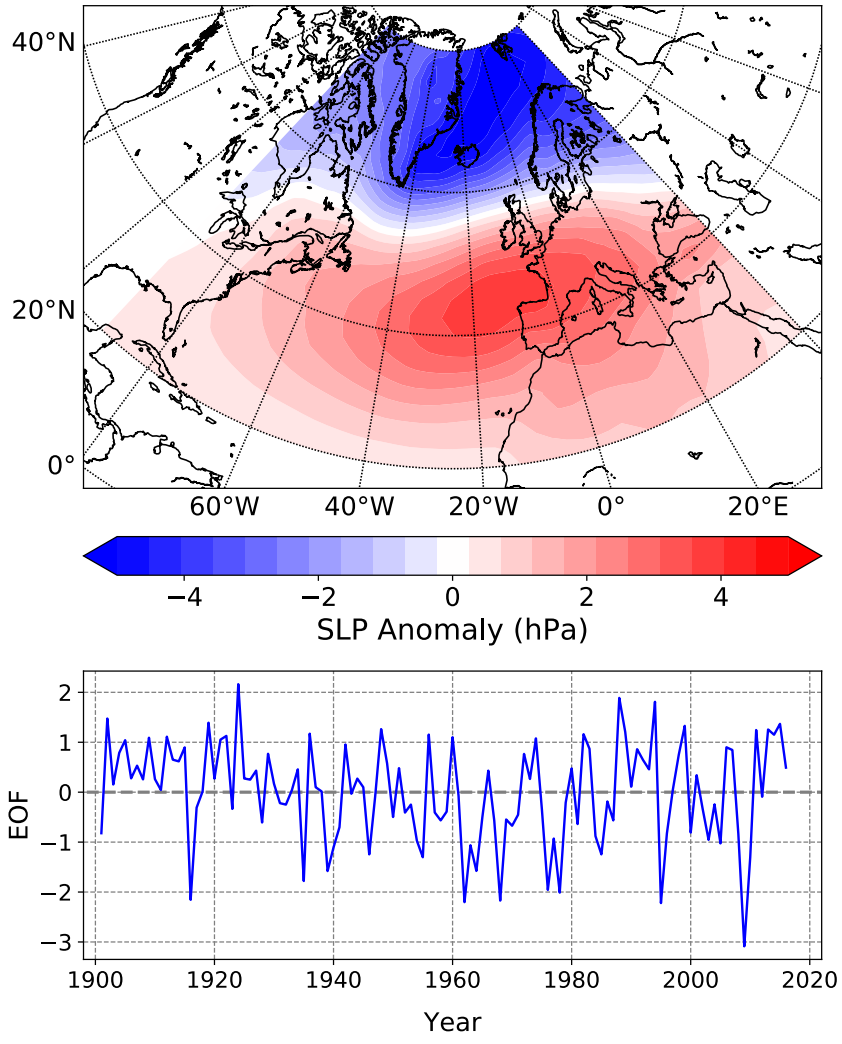

Figure 2-4: Regression slope of North Atlantic DJF SLP onto its first principal component (top) and time series of this first principal component from 1901 to 2016 (bottom). Data from ERA20C [197].

The NAO is strongly linked to patterns of winter temperature, precipitation and storminess over the whole North Atlantic sector [128], including northern Africa (Fig. 2-5) [147]. The amplitude and timescale of NAO variations are also large enough to impact weather over several years in a row [136]. In its positive phase, by convention when the equator-to-pole SLP gradient is larger than average, the storm track is strengthened and deflected polewards, leading to wet, mild and windy conditions north of the 45°N parallel, and dry and cool weather to its south [262]. In its negative phase, the subtropical high is considerably weaker, allowing for a more southward propagation of North Atlantic storms towards the Mediterranean Sea and northwestern Africa, which experience higher-than-average precipitation and milder temperatures due to enhanced advection of oceanic heat. At the same time, Northern Europe is drier and colder. The influence of the NAO over Morocco, along much of southern Europe, is limited to the extended winter (October-April), when the storm track reaches its southermost position (Fig. 2-6). By contrast, during summer, the impact of the NAO is essentially felt over Northern and Central Europe [22]. The regions at each limit of the storm track distribution are the most impacted by the NAO: Morocco and the Iberia Peninsula to the south, and Scotland and Norway to the north. In Morocco, NAO variability accounts for half of December-to-January precipitation variance, about the same as for the southern half of the Iberian Peninsula (Fig. 2-6). Although precipitation anomalies associated with unit change in the NAO are larger at the northern edge of the stormtrack (about 150-200mm, against 50-100mm to the south), high latitudes receive much more precipitation on average (700-800mm in winter against 150-200mm at 30-35°). Consequently, regions to the south, including Morocco, are much more sensitive to NAO variability relative to their average precipitation.

The NAO has been shown to be a natural mode of variability of the climate of the northern hemisphere and the most prominent atmospheric pattern over the middle and high latitudes, particularly from late fall to early spring (November to April) [17, 150]. The NAO is believed to owe its existence not to coupled ocean-atmosphere interactions, but to internal, nonlinear dynamics intrinsic to the atmosphere [244], as even atmospheric models with no orography nor land-sea contrasts run with constant ocean forcing have displayed the emergence of patterns of variability very similar to the NAO [24, 129]. Still, ocean forcing is thought to drive much of the variability in NAO dynamics at the seasonal, inter-annual and decadal scales ([129, 191,

219], and further discussion in section 2.2.3). The NAO indeed fluctuates on a wide range of timescales, from days to decades, and extended periods when one phase dominates are common. Large changes can occur from one winter to the next, and there is also a considerable amount of variability within a given winter season. The spectral analysis of winter NAO reveals a rather red spectrum: power increases with period, with most of the variability concentrated at timescales of two weeks and above [236]. Many winters are not dominated by one regime in particular. In a single season, the NAO index typically oscillates between positive and negative phases, generally on a timescale of 7-20 days [257]. Such anomalies last long enough to potentially impact precipitation, as their length roughly corresponds to the response time of the atmosphere. On longer timescales, strong inter-annual and -decadal variability is evident (Fig. 2-4). Positive winter NAO tended to prevail from the early 1900s until about 1930, when the series reverted to more negative values up to the 1960s. The winter of 1979 witnessed an abrupt transition back to a positive phase which persisted for most of the following 15 years. Since then, the NAO reverted to a regime of shorter oscillations, although fewer negative regime months have been observed recently [233].

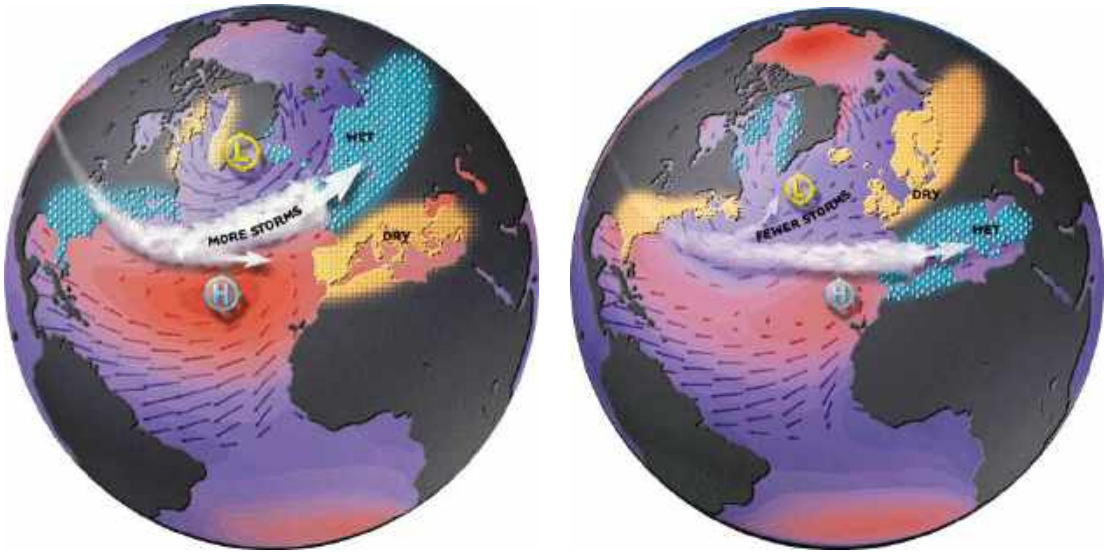

Figure 2-5: Idealized mean SLP, wind and storm track position during a positive (*left*) or negative (*right*) NAO phase. [Credits www.ldeo.columbia.edu/res/pi/NAO/, © Martin Visbeck]

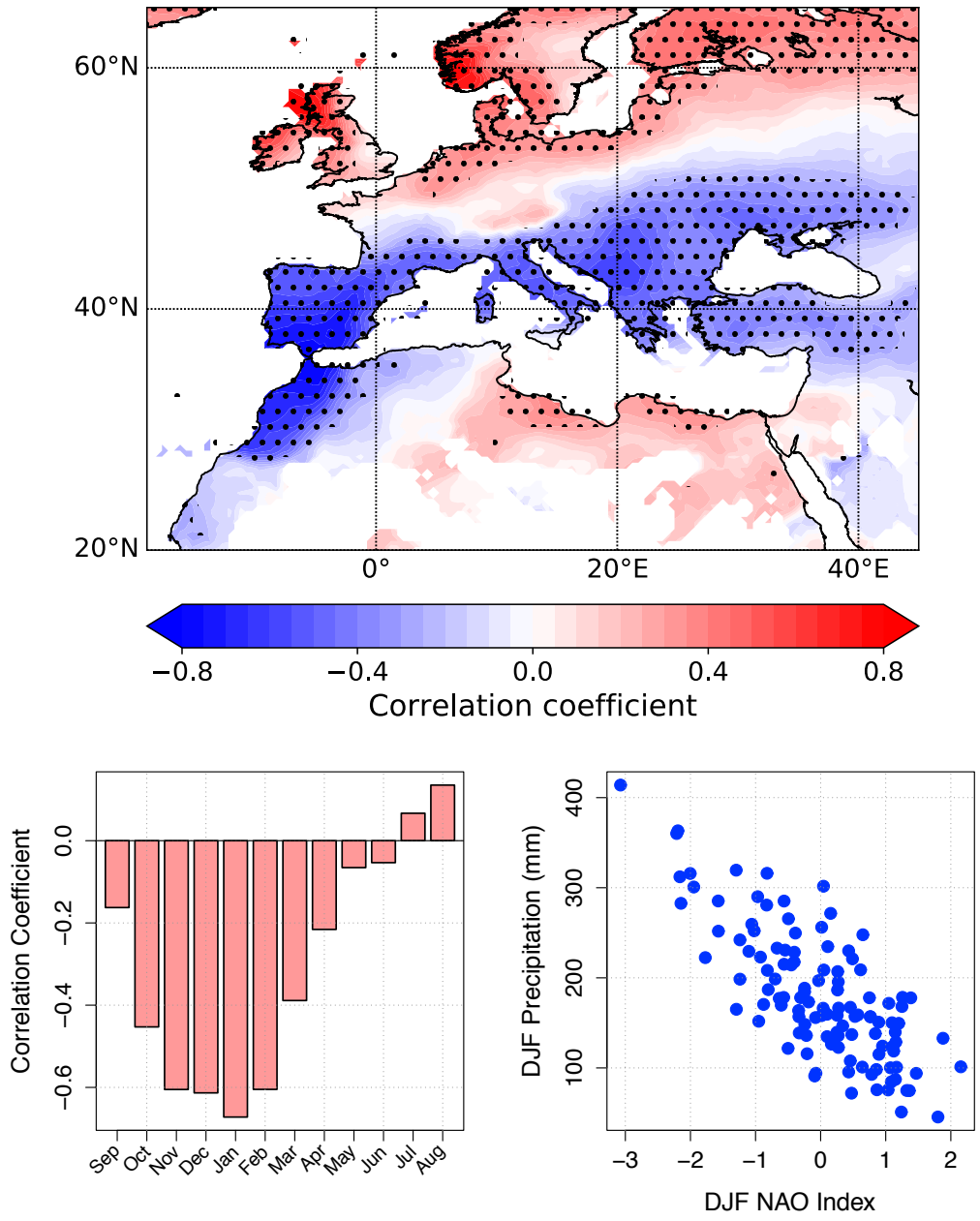

Figure 2-6: *Top*: Pearson's correlation coefficient of DJF NAO and concurrent European/Mediterranean precipitation (data from CRU TS4 [108]). Dots indicate significant correlation at 1%. *Bottom*: Monthly correlation of northwestern Moroccan precipitation and NAO index (left) and DJF northwestern Moroccan precipitation against concurrent NAO index, 1901-2015 (right).

2.2.3 Predictability of seasonal precipitation

In spite of the major impacts of precipitation variability on agriculture and the economy, the predictability of Moroccan precipitation at seasonal time scales has received extremely limited attention, and in practice, only short-term dynamical forecasts are available to water managers. A number of studies, however, have focused on the larger issue of European precipitation predictability, and in particular the predictability of the NAO given its substantial impact on European weather.

Traditionally, seasonal climate forecasting has either relied on numerical weather models (NWM) or on statistical models. The statistical (or empirical) approach relies on the identification of a predictand (or target) variable – in this case, seasonal precipitation or NAO – and of predictor variables, to which a statistical model is fitted; the model is then evaluated and used to make future predictions. In this approach, physics usually inform the choice of predictors, but the physical links between predictors and predictands are not made explicit, though they are often assessed a posteriori. NWMs, on the other hand, explicitly solve the equations governing atmospheric flow. Simulations initialized with observed fields at the time of the forecast are run until the end of the desired forecast horizon, and forecasts are directly derived from model output. In this approach, large ensembles of runs are typically required to address the uncertainty on initial conditions and its impacts on atmospheric predictability. Thanks to improvements in computational efficiency, NWMs have become dominant for short- to medium term forecasts, from one to about 10 days. Statistical forecasts, on the other hand, still find use in long-term forecasts, also known as season-to-season forecasts (S2S) or simply seasonal forecasts, with lead times considerably longer than the limit of deterministic atmospheric predictability [267].

A number of studies have attempted to identify large-scale climate drivers relevant for seasonal predictability of precipitation in Europe and the Mediterranean Basin. In particular, Sea-Surface Temperatures (SSTs) have attracted most of the attention since they are a significant driver of atmospheric motion at seasonal timescales. Empirical connections of winter and spring Western Mediterranean precipitation to North Atlantic and tropical Pacific SSTs several months ahead were identified early on and confirmed by many authors

[283, 63, 210, 211, 158, 159, 79]. Similarly, the El Niño Southern Oscillation (ENSO) phenomenon has also been found to impact European precipitation during winter and spring [156, 198], possibly through the excitation of planetary waves [228]. The link between SSTs and the NAO has also been explored. Much of the variability in inter-annual to inter-decadal winter NAO is indeed believed to be related to North Atlantic Sea-Surface Temperature (SST) patterns and Arctic sea-ice [20, 149, 214, 24]. Connections to other oceans basins have been proposed as well, such as to the tropical Atlantic [209, 50, 129] and tropical Indian and Pacific oceans [119, 240]. Recent modeling also suggests that the NAO responds to slow changes (decadal and longer) in global ocean temperatures, and more particularly to changes in tropical and equatorial regions. SSTs are indeed a major driver of atmospheric circulation at seasonal to multidecadal timescales, because of their effect on the atmospheric energy and moisture budget, thus paving the way for season-to-season weather forecasts [233]. The winter NAO has also been linked to variability of the stratospheric polar vortex via downward coupling of the circulation and planetary waves[193, 15, 184], sea-ice cover in the Barents Sea [214, 89, 245, 263] and anomalies in Eurasian snow cover extent (SCE) [45, 25, 220, 200]. Sea-ice and SCE both impact the surface radiative balance, with potential feedback on the hemispheric circulation. Numerical modeling experiments forced with varying Eurasian SCE indeed reproduced an atmospheric NAO response in winter similar to the observations [44, 82, 190]. Increased snow cover over Eurasia in the fall would result in surface cooling that favors the development of a cold and dense mass of air over Siberia which, when it spreads out (Arctic outbreaks), brings cold and dry air to Europe and North America. More than snow cover itself, however, the rate of its increase in autumn appears to correlate even more strongly with a westward expansion of the Siberian High over Europe and the North Atlantic, thereby influencing the evolution of the wintertime atmospheric circulation [46].

When fitted at the global scale with SSTs as predictors, empirical models have generally turned out to have mediocre skill over the Mediterranean region [18, 70]. Brands et al. (2012) attempted to predict European winter precipitation based on Eurasian snow cover data only. Significant skill was found for Norway to the north and the Iberian Peninsula and Morocco to the south; still, only 15% of the variance in northern Moroccan precipitation could be explained, and 20% at best for a few grid points [33]. More recently, Totz et al. (2017)

developed a clustering-based method in which recurring spatial patterns of European winter precipitation were identified, and associated with composite patterns in the predictor fields [245]. As predictors, they selected variables believed to influence either precipitation directly or through the NAO: North Atlantic and Mediterranean SSTs, Eurasian snow extent and Arctic sea ice. The methodology yielded reasonable skill over Europe, and even correlations up to 0.65 over Northern Morocco. Still, their results over Morocco are questionable, because both significant positive and negative correlations are found over the northwestern Moroccan plain, whereas a uniform correlation sign would be expected given the region's homogeneous weather during winter [147].

Similarly, empirical analyses suggest a limited though significant predictability of winter NAO based on SST anomalies as early as the preceding spring and up to November [63, 49, 212, 219, 81], especially west of the British Isles [137, 219] and off the coast of Newfoundland [204, 214, 212]. Models and regression analyses suggest however that the oceanic influence on North Atlantic climate is nonstationary and has varied, sometimes significantly, over the last two centuries [119, 240, 92]. Prediction skill of winter NAO regressed on North Atlantic SSTs is notably consistently lower for the first half of the 20th century, as well as during the 1960s and 1980s, but higher in the 1970s and 1990s [219]. Simple statistical forecast models based on lagged SST predictors have demonstrated significant skill in predicting winter NAO ($r^2 \approx 0.3 - 0.4$) at a lead time of 0-1 month [219]. Up to 58% of interannual winter NAO variability may be predictable when including all suspected predictors [263], although such analyses can only be limited to the recent decades (1980-present), mainly because of the availability of satellite data [81]. Stratospheric data are also of questionable validity before then. Models are consequently trained on short periods, with high risk of over-fitting.

Improvements in computational efficiency have fostered attention to dynamical NAO and precipitation forecasts in recent years. The poor skill of global circulation models in predicting seasonal European and Mediterranean precipitation, especially during winter and spring, has been documented in a number of studies [60, 266, 177]. We illustrate here with an example of hindcast skill in five models part of the North American Multimodel Ensemble (NMME: CMC1-CanCM3, CMC2-CanCM4, NCAR-CESM1, NCAR-CCSM4 and GFDL-FLORB-01)[1].

[1]Data is available at https://www.earthsystemgrid.org/search.html?Project=NMME

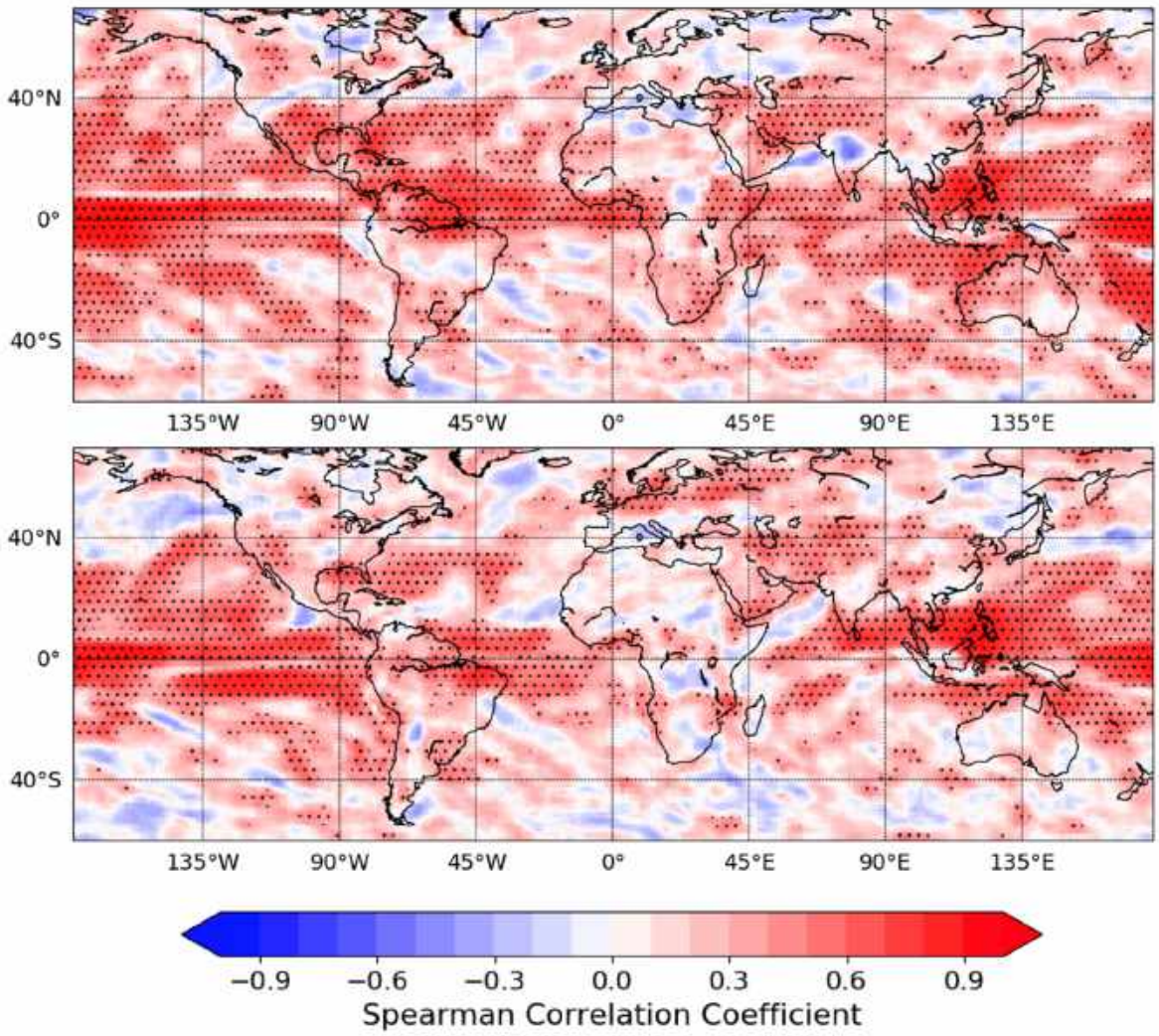

Figure 2-7: Spearman correlation coefficient between NMME multi-model mean seasonal precipitation forecasts and satellite-based (GPCP) observed precipitation, 1982-2010, for (top) December-January-February and (bottom) February-March-April.

NMME is a project of seasonal forecasting intercomparison of coupled ocean-atmosphere models. Retrospective forecasts are issued on the fifteenth day of each month. Figure 2-7 shows model forecast skill for two three-month periods, issued fifteen days into the period. Forecast skill for Morocco and, more generally, the Mediterranean region, is poor for both periods, with generally less than 10% of explained variance. By contrast, potential for predicting multi-decadal European precipitation tendencies has emerged in coupled dynamical models. Simpson et al. (2019) found that model skill in representing low-frequency SST influence on the atmosphere during March led to enhanced predictability of winter precipitation mulit-

decadal variability in western Europe [232], and predicted average March precipitation for the upcoming decade based on a 40-member ensemble of climate runs.

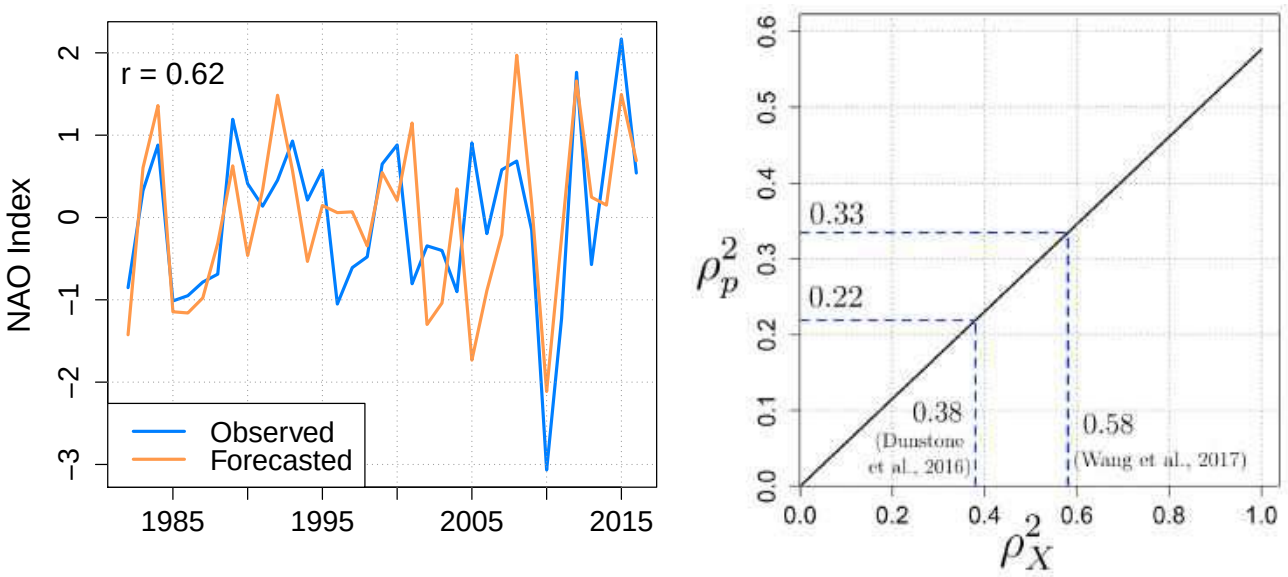

Figure 2-8: *Left*: Observed (blue) and predicted (red) DJF NAO, using the Met Office Decadal Climate Prediction System model, 1982-2016 (from *Dunstone et al.* [69]). *Right*: Potential predictability of DJF Moroccan precipitation against that of the concurrent NAO, with results from two different NAO forecasts (one dynamical [69] and one statistical [263]).

Dynamical models have generally showed better skill at forecasting large-scale North Atlantic atmospheric patterns, notably the NAO, with useful implications for seasonal precipitation. Large ensembles of winter coupled simulations have shown satisfying skill in predicting inter-annual NAO variability [221, 69], though at high computational cost (40-member ensemble in Dunstone et al. (2016) [69], for instance). Correlations of $r \approx 0.6$ have been found for DJF NAO forecasts at 1-month lead times (November 1st). To see how this could translate into precipitation forecats, let us assume a simple NAO-precipitation model:

$$\begin{cases} \text{NAO} &= X + \epsilon \\ p &= \alpha \text{NAO} + \eta \end{cases} \tag{2.1}$$

where the NAO is equal to the sum of its predictable part X and independent random noise $\epsilon \sim \mathcal{N}(0, \sigma_\epsilon^2)$, and precipitation p is a linear function of the NAO with a random residual $\eta \sim \mathcal{N}(0, \sigma_\eta^2)$. In this idealized case, the potential predictability of the NAO is given by

$\rho_X^2 = \frac{\sigma_X^2}{\sigma_{\mathrm{NAO}}^2}$, and that of precipitation is

$$\rho_p^2 = \frac{\alpha^2 \sigma_{\mathrm{NAO}}^2}{\sigma_p^2} = \rho_X^2 \frac{\alpha^2 \sigma_X^2}{\sigma_p^2} \tag{2.2}$$

A typical value for Morocco is $\alpha \approx -0.75$ (Fig. 2-6, bottom), which yields $\rho_p^2 \approx 0.56\rho_X^2$ assuming scaled variables. Therefore, the best that could be achieved from current NAO forecasts, assuming no uncertainty on α, is roughly 30% of explained variance in winter precipitation (Fig. 2-8). In practice, the value is lower when cross-validation is implemented (see Chapter 3). In any case, accurate dynamical NAO forecasts remain a challenge because many of the physical processes impacting the NAO remain unknown or are not well understood [221, 233].

2.3 Water resources and management

The scarcity, variability and unpredictability of precipitation therefore create great challenges for water management in Morocco. Because the resources are so limited and fickle, water management has always been a top priority for the country. The rejuvenation of Morocco after its independence in 1956 involved large infrastructure projects to develop agriculture and improve water management and water use efficiency. Since then, the country has withstood several severe droughts, but demand for water is now rapidly approaching the amount that is sustainably available (section 2.4).

2.3.1 Water cycle and available resources

A simplified water cycle for Morocco is shown on Figure 2-9. Of the 140km^3 of precipitation that fall on average on Morocco every year, the vast majority (118km^3, or 84%) return directly to the atmosphere through evapotranspiration before it can be captured and utilized. However, part of this total volume is still used productively in rainfed agriculture, particularly. This leaves only 22km^3 of potential resource, which translates into about 600m^3/capita, well below

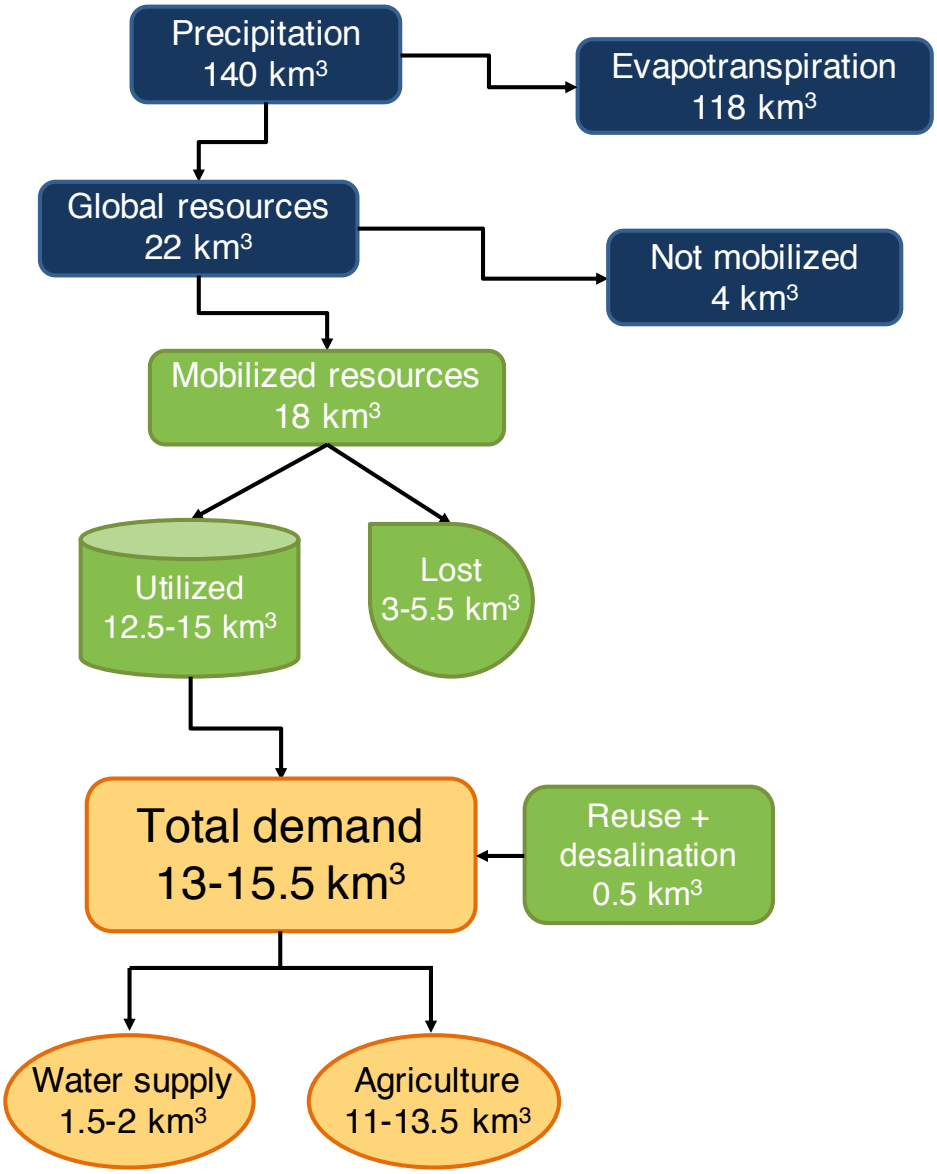

Figure 2-9: Simplified water cycle of Morocco; data averaged over the 2008-2018 period. Source: Direction de la Recherche et de la Planification de l'Eau, Rabat.

the generally accepted scarcity threshold of 1000m^3/capita/year. Accounting for productive evapotranspiration would naturally increase that amount, but to an extent that is yet to be quantified for Morocco. Roughly 80% of these 22km^3 are captured to be used. The rest is lost, typically in basins with no or little water infrastructure (like the Drâa catchment south of the Atlas). Surface water accounts for three-quarters ($\approx$ 13km^3) of the mobilized resource, with the rest being groundwater. Groundwater is particularly critical south of the Atlas, where surface resources are scarce, but is also heavily relied on in many irrigated agricultural

plains to the northwest. 3.5-5km^3 of mobilized resources are lost every year, through direct evaporation (from dams or irrigation canals), river discharge into the sea, as well as runoff that goes through existing infrastructure but that is not captured (dam overflow, etc.). A further 0.5km^3 from desalination and water reuse ("gray water") complement the renewable resource. In total, satisfied consumptive water demand amounts to 13-15.5km^3, *i.e.* 360-430m^3 per inhabitant.

Water availability varies across space, following the non-uniform distribution of precipitation. 15% of Morocco's land surface, essentially the northern tip of the country, receives about 50% of the precipitation and accounts for 60% of river discharge. All of Morocco's major rivers are located in its northwestern portion (Fig. 2-1). They begin their course in the comparatively wetter Atlas and Rif, and flow across the plains to the Atlantic Ocean and Mediterranean. The Sebou river is the country's longest, draining an area of around 35000km^2 between the Rif and Middle Atlas. Its renewable water resources are estimated at about 5.5km^3 (4.5km^3 of surface runoff and 1km^3 of groundwater), of which 3.5km^3 are effectively used (25% of the country's total use). The second longest, the Oum-Er-Rbia river, drains a similar area that includes much of the High Atlas. 2.9km^3, out of its 3.3km^3 annual runoff and 0.5km^3 groundwater infiltration, are captured (20% of national total). At the northern tip of the country, several smaller catchments, including the Loukkos and Mediterranean coastal basins, account in all for 2.5km^3 of discharge and 1km^3 of groundwater, of which 2.2km^3 are used (15% of national total). Also in keeping with precipitation, water resources vary in time as well, with wide fluctuations around the 20km^3 average (Fig. 2-10). The driest year of the last few decades was 1992, when only 3km^3 were utilized, when in 1962, that figure reached 48km^3. Seasons just one or two years apart can also see wide differences, for instance 8km^3 in 2007 and 42km^3 in 2009.

2.3.2 Water use and infrastructure

To mobilize such water volumes under this large variability, the country relies on an extensive network of 135 dams, with a combined withholding capacity of 17.5km^3, as well as numerous water transfer systems between dams, and from dams to irrigated areas. The largest dam

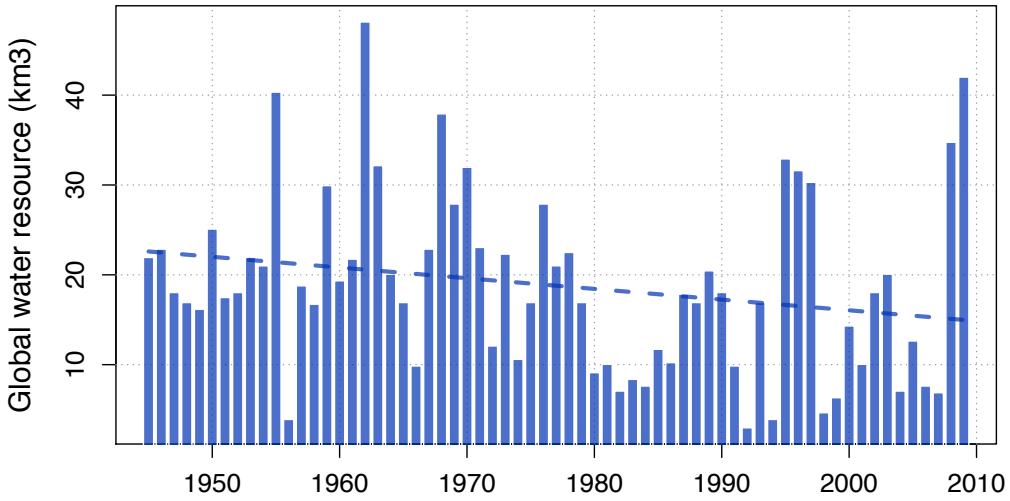

Figure 2-10: Annual water resources (km^3) in Morocco, 1945-2009. Source: Direction de la Recherche et de la Planification de l'Eau, Rabat. A linear regression fit is shown by the dashed line (p-value: 0.07).

is Al Wahda, in the Sebou watershed, with a capacity of $3km^3$, and the second largest is Al Massira, along the Oum-Er-Rbia, with its $2.7km^3$ capacity. Most of the water use (88%) is directed to agriculture, with the rest going to industry (4%) and cities (8%). Water is also put to non-consumptive uses: most large dams are equipped with hydroelectric turbines (1800MW of total installed capacity) that produce electricity each time water is discharged. Since the 1960s, Morocco has pushed for the development of irrigation, and today about 1.5 million hectares are irrigated in the country (16% of total arable land) [134], close to the official estimated potential of 1.65 million hectares. Two-thirds of this surface was developed and is managed by the government, in what are called "irrigated perimeters". There are 9 major irrigated perimeters in the country, accounting for almost 900000 hectares, and associated with extensive water collection and delivery infrastructure. The rest is fractioned into more than 100 small-scale irrigated areas, typically located farther away from dams and depending comparatively more on local groundwater pumping. With only 16% of the arable surface, irrigation accounts for 45% of added value in agriculture on average, a fraction that can reach 70% in dry years, and 75% of agricultural exports [5]. Revenue per hectare is four to eight times higher than for rainfed crops.

Yields in rainfed agriculture are indeed overall quite low and highly dependent on the timing and amount of seasonal rainfall [76, 134], particularly for cereals (Fig. 2-11). As an example, during the 1994-1995 cropping season, drought was so severe that the precipitation deficit reached -60% in the north and -80% in the south. On average, in the northwestern plains, cumulative rainfall was 198mm for the 1994-1995 season and 591mm for the following season. Cereal production in 1994-1995 totaled a mere 1.73 million tonnes (average yield: 479 kg/ha), compared to 9.8 million tonnes in 1995-1996 (1730 kg/ha) [14]. More recently, the exceptional 2017-2018 season saw a record 10.2 million tonnes of cereal production, which declined by 49% to 5.2 million tonnes in 2018-2019 following large rainfall deficits, and is projected to decline even further to 4 million tonnes for the dry 2019-2020 season.

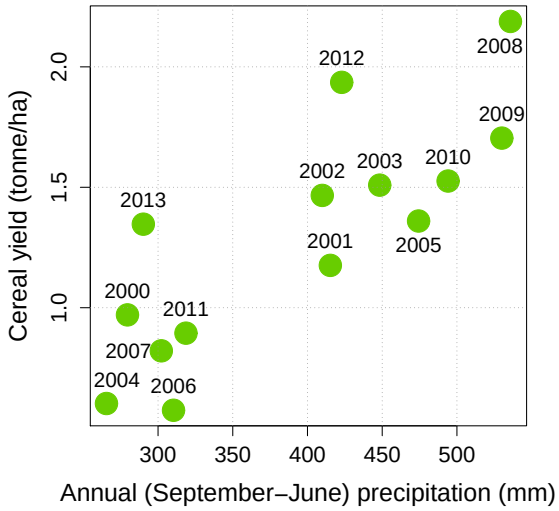

Figure 2-11: Average cereal yield (t/ha) as a function of total annual precipitation in the Oum-Er-Rbia watershed management area, 2000-2013 seasons [data from Dr. Mohamed El Gharous].

Still, even during good years, cereal yields are only 25-30% of what they are in Europe, notably because of low technology adoption and low fertilizer use. National wheat yields have slowly increased, from 0.7 tonnes in the 1940s to 1.6 tonnes per hectare in the 2000s [14], but discrepancies between regions remain high: 0.62 tonnes/ha in the Safi province, up to 2 tonnes/ha in the Kenitra province. Within provinces, year-to-year variations are also significant, with coefficients of variation between 0.34 (Beni Mellal province) and 0.67 (Settat province) [134]. Consequently, Morocco imports about a third of its cereal consumption, only down to a quarter in good years (25% in 2008-2009 when production reached a record of 10.2 million tonnes). By 2010, most irrigated fields (70%) were still watered by furrow irrigation, with the remainder evenly split between irrigation by aspersion and localized irrigation (like drip irrigation). The share of the latter has been growing fast over the last decade, under the impulsion of the

"Green Morocco Plan". Launched in 2007, this plan aims to transform Morocco's agriculture system to improve practices, yield and water use efficiency, lower overall water use and and make it more resilient to drought and climate change. Drip irrigation has been particularly encouraged, since its efficiency is vastly higher than that of furrow irrigation. Currently, the efficiency of the whole irrigation system (*i.e.*, including losses before the water reaches the field) is estimated at about 40-45%, mainly because of evaporation in the open-air canals and low efficiency of furrow irrigation. Water is illegally taken from many canals as well . Still, part of the "losses" definitely replenish aquifers from which groundwater is also extracted for irrigation, though the volume this represents is not precisely known.

2.3.3 Water management

When the development of water infrastructure accelerated in the 1960s, irrigation and overall water use were meant to be managed locally, at the level of each irrigation scheme. The government limited its action to enforcing controlled cropping patterns that were part of a national production strategy (notably the cultivation of sugar beets). The decade-long drought of the 1980s and early 1990s, however, caused widespread reductions in water availability, at a time of growing demand, compelling the Moroccan government to adopt a more integrated and regulatory framework. Passed in 1995, the Water Law defined rules for the sustainable use of water and established the institutions in charge of their enforcement. A network of nine watershed agencies, under the responsibility of the Ministry of Public Works, was created, one for each of Morocco's main river basins (Sebou, Oum-Er-Rbia, Moulouya, Tensift, Bouregreg, Souss-Massa, Loukkos, Guir and Sahara area). Their purpose is to monitor, develop and allocate water resources between competing users within each basin, based on a management plan (PDAIRE, *Plan Directeur d'Aménagement Intégrée des Ressources en Eau*, or Master Plan for the Integrated Management of Water Resources) that is revised every 5 years. They maintain observation networks to assess the state of water resources, in terms of both volume and quality.

Irrigated areas were also consolidated into official irrigated perimeters, centrally managed by Regional Offices for Agricultural Development (*Office Régionaux de Mise en Valeur Agricole*,

ORMVA), tasked with planning agricultural development and giving farmers the resources to achieve production goals and to manage water resources at the scheme scale. In practice, they provide credit, selected seeds, fertilizer and farm equipment to farmers, and manage irrigation water which they supply to farmers for a fee fixed by the government. That money pays for infrastructure maintenance, and a fraction goes to the corresponding watershed agency. The price of water, however, is very small, around 0.5 USD cents per cubic meter – by comparison, French farmers pay around 7 cents per cubic meter, while American farmers can pay anywhere from 0.5 to 10 cents.

Water is managed at the basin scale, on an annual (September-August) basis, by watershed agencies in coordination with the government and regional stakeholders. A delicate balance must be struck between all the users: agriculture – represented by the regional agricultural offices; industry; cities, represented by the *Office National de l'Eau Potable* (National Office for Potable Water, ONEP), and the *Office National de l'Électricité*, the national electricity producer. Water allocations between the different consumers are decided in late June-early July for the upcoming hydrological year. First, each user states their demand, within bounds defined by the management plan. These demands are expressed at the level of each dam, and not aggregated at the basin scale. Then, starting with what is available in dams at that time, a simple water balance is applied to each dam, assuming fixed losses by evaporation and infiltration and a river discharge level that is exceeded, on average, in 4 out of every 5 years, based on historical records. In other words, the risk of not meeting the demand is constrained to only 20%, following government regulations. The outcome is an estimated storage for each dam at the end of the upcoming year, from which user demands are then subtracted. If the levels thus calculated are below 25% of dam capacity, user allocations are then reduced to bring dam storage at the end of the year to that 25% level. After very dry years, agencies will occasionally accept to go below that level, but must seek special authorization to do so. Municipal water supply has priority (its demand is systematically met), followed by industry. Agriculture is therefore the main variable of adjustment if water supply is low. As a result from chronic droughts and growth in water demand from other users, agricultural water allocations are always substantially less than requested amounts, on average by about 35%, but as much as 70% in very dry years.

Water allocation decisions are revised every term (September, December and March), to take into account actual precipitation and dam inflows, primarily to avoid excessive crop losses. However, once a decision is made, the Agency will stick to it until the next revision and will deliver all promised water in time. If the year ends up being too dry, water restrictions will typically be postponed to the following year. Still, possibilities for interannual water management are quite limited, due to the overall scarcity of water. Interannual strategies rely mostly on the largest dams, built to help the country withstand large droughts by storing as much water as possible during wet years.

While seasonal water amounts are fixed, the schedule and volumes of delivery to the plots are generally more flexible. Water releases are determined by the Agency on a 3-day to weekly basis, based on the demand schedule devised by agricultural offices in accordance with annual water allocations. The short time horizon allows last-minute cancellations due to unexpected rain, for instance. Municipal water systems manage their own supply and inform the agency of their withdrawals every week. Apart from upstream dams intended for hydroelectricity production and not water storage, hydroelectric production is conditioned by the water release schedule, in which electricity demand plays no role. At the field level, each farmer is given an entitlement for a specific water volume, based on the size of their field and the crops they pledged to grow. Water deliveries are scheduled in advance, and farmers cannot transfer unconsumed water until a subsequent delivery, so most of them take all the water they can get at each turn. In case of unexpected water scarcity during the season, priority will be given to specific crops – usually trees to help them survive droughts – and specific locations – high-yield fields, for instance. Annual crops in marginally productive areas are consequently regularly abandonned in the course of the growing season.

Groundwater management is decoupled from surface water management. Until recently, few regulations existed to limit pumping from aquifers, but the severe overpumping of the last few decades (see Section 2.4) prompted watersheds agencies to devise and enforce restrictions on aquifer withdrawals. Today, most groundwater is pumped by individual farmers who, while they do not need to pay anything for that water, must still request permission for drilling from the watershed agencies, and respect the cap on withdrawals imposed on them if the permission is granted. In addition to direct measurement of piezometric levels, watershed agencies

increasingly rely on numerical simulations to monitor the health of groundwater resources and determine whether to hand out drilling permits. Yet, much remains unknown about aquifer recharge, either natural or from irrigation losses; in addition, unlawful wells are plenty and many farmers pump more than what they are supposed to, because regulations are still only partly enforced.

2.4 Trends in water availability: past, present and future

2.4.1 Recent trends

While it may seem from Fig. 2-9 that large water supplies are still untapped, in practice, water consumption in Morocco is very close to the amount that can be reasonably captured for human use. The remaining unmobilized water resources are generally difficult to access; they can be located in remote or undeveloped regions where demand is low and capture and transportation costs would be high (high mountain aquifers, for instance), or they are simply not captured, either due to the absence of infrastructure, or to the failure of existing infrastructure to capture them. Dam overflows during flash floods are not uncommon south of the Atlas, and even in the comparatively wetter plains to the north, mild flash floods leading to water losses are common. As a result, water resources are overexploited in much of Morocco outside the very north. In addition, water resources are inequitably distributed in space; demand in some places cannot be satisfied while other regions are in surplus, as is regularly the case of northern Morocco. Water is not easy to transport, and as a consequence the surpluses can be lost.

Recent trends highlight how critical Morocco's water situation has become. Due to economic development and population growth, demand for water has grown significantly over the last few decades, from 10.9km^3 in 1990 [4] to 14.3km^3 today (Fig. 2-9). The development of irrigation in particular has strongly contributed to this trend: from 215000 hectares in 1960, the area equipped for irrigation in Morocco has increased to 750000 hectares around 1990 and to close to 1.5 million hectares today [4]. Advancements in irrigation efficiency, in particular the push to develop drip irrigation, have failed to fully compensate for the increase in irrigated

surfaces. In parallel, runoff has generally been on the decline since the middle of the 20th century (Fig. 2-10), by about 6% per decade between 1945 and 2009. One should keep in mind however that the magnitude of inter-annual variability makes the significance of such trends always challenging. If we start the trend analysis in 1980 for instance, at the beginning of a decadal drought, a significant upward trend in runoff is detected.

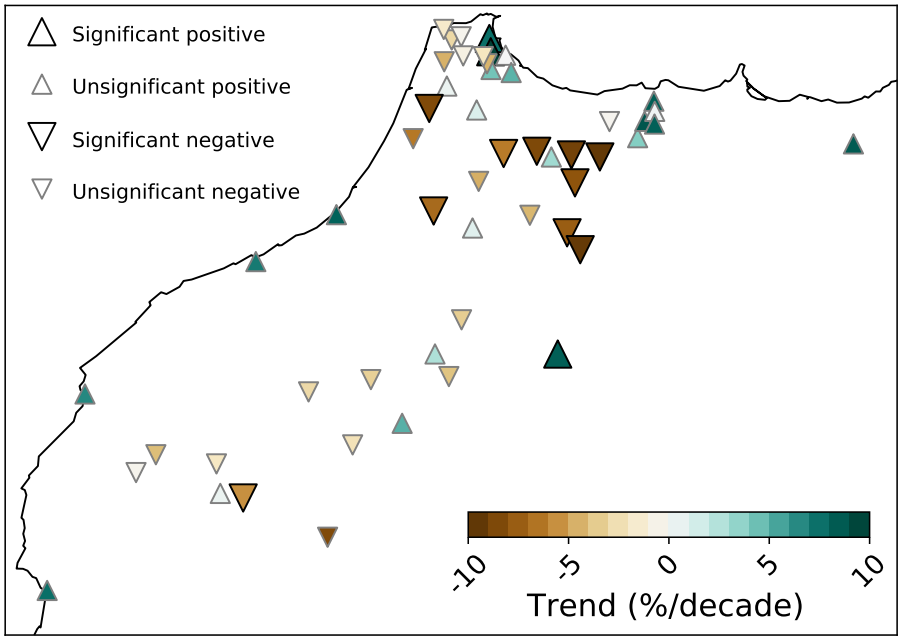

Figure 2-12: Trends in wet season (November-April) precipitation across available stations in Morocco (see Chapter 5 for details on station data.

Overall, water availability per capita has dropped from 1900m^3 in 1970 to about 600m^3 today [123]. By some estimates, Morocco's water demand could even be as high as 3km^3 above the supply [114], but uncertainties remain high and official data (Fig. 2-9) indicate that supply and demand are about equal. What is certain, however, is that Morocco's water surplus has been decreasing fast, all the more so in fact because the national water strategy was largely devised in the 1960s, a time of historically high precipitation (Fig. 2-3). As a consequence, much of the original infrastructure (dams and irrigation equipment) was sized for water volumes that have never been reached again since. For example, it was recently estimated by the Moroccan Ministry of Agriculture that actual utilizable volumes were about a third lower across Morocco's major basins than what was originally planned for in the 1960s and early 1970s. A critical point occurred in the 1980s, as the country went through a major,

decade-long drought which took a heavy toll on agriculture and the economy. For several years in a row, precipitation was near its lowest levels on record (Fig. 2-3). The large drought of the 1980s-1990s was associated with a persistent positive winter NAO phase (Fig. 2-4) that caused declines in precipitation over much of Spain and Portugal as well. Since then, precipitation has recovered, but only partly: station data indicate a tendency to long-term precipitation decline over the last few decades over most of Morocco [237] (Fig. 2-12). About 58% of stations have negative trends. Most trends (75%) are not significant, which is unsurprising in a region with such high inter-annual variability (low signal-to-noise ratio), but of the 13 stations where they are significant, 10 have experienced decreases in precipitation. On average, a decline of about 1% per decade is observed across stations. Similarly, discharge observations point towards declining runoff, and the frequency of dry years may be increasing as well [51].

As is often the case in semi-arid regions, the lack of surface water supply has been compensated by aquifer withdrawals. Since the 1980s, many aquifer levels have dropped by 1.5-3m per year [255] (Fig. 2-13), and the depletion rate has even increased since the late 1990s even though the country transitioned out of the drought into more average conditions. Today, an estimated 0.85km^3 of unsustainable groundwater is extracted and consumed every year [123].

2.4.2 Climate change and the "Mediterranean Hotspot"

The observed drying in Morocco has occurred in the context of a widespread regional precipitation decline across the Mediterranean Basin. Station-based observations show a consistent drying signal along much of the Mediterranean shoreline, particularly south of 40°N (Fig. 2-14-a) [118]. This pattern is also present, although with smaller magnitude, in Global Climate Model (GCM) simulations forced with observed greenhouse gas concentrations (Fig. 2-14-b). The large inter-annual and decadal variability in winter precipitation in the Mediterranean makes it difficult to assess the significance of observed trends, but evidence points to the existence a forced long-term drying signal superimposed on the decadal variability during the last few decades [118, 142]. In addition, models robustly project that these trends will continue into the future [101, 278, 142, 225], to a point where 40% of annual precipitation could be lost

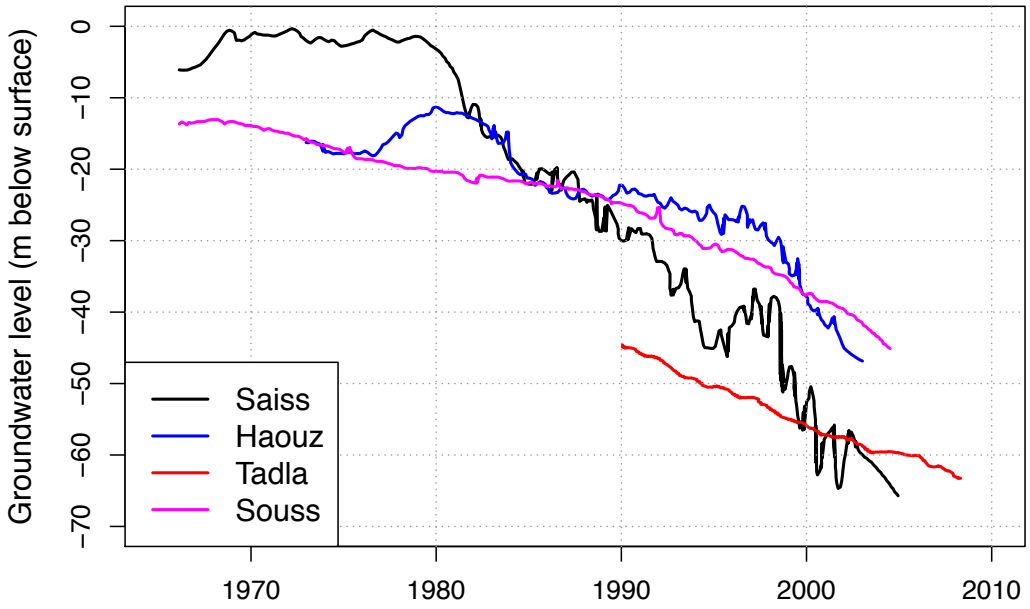

Figure 2-13: Groundwater level (in meters below surface) in four of Morocco's major aquifers (Saiss in the Sebou basin, Tadla in the Oum-Er-Rbia basin, Haouz in the Tensift basin around Marrakech and Souss in the Drâa catchment on the southern slopes of the High Atlas). Data from Hssaisoune et al. (2020) [123].

in Morocco by the end of the 21st century (Fig. 2-15-a) [133]. The Mediterranean Basin as a whole has consequently stood out in successive generations of models as a major hotpot of climate change [99, 59] (Fig. 2-15).

The robustness of the drying signal across GCMs, and its similarity with observations, suggests that models may be generally correct in their precipitation projections in this region. Still, the mechanisms responsible for such high inter-model agreement remain, for the most part, unclear. Just because models strongly agree in this region does not mean we must necessarily have high confidence in their projections. Sound physical explanations are needed to complement model results. Given the economic, cultural and geopolitical importance of the region, many studies have attempted to diagnose projected Mediterranean trends and understand their origin [168, 195, 65, 225, 278, 279, 226], but so far a clear and detailed picture has not emerged. The Mediterranean Basin is a unique region due to its geographical position which brings it under the influence of mid-latitude westerlies during winter, while large-scale descent forced by the Hadley circulation and Indian monsoon prevails during summer [26]. The variabiility between these two regimes, coupled with the influence of the Mediterranean Sea

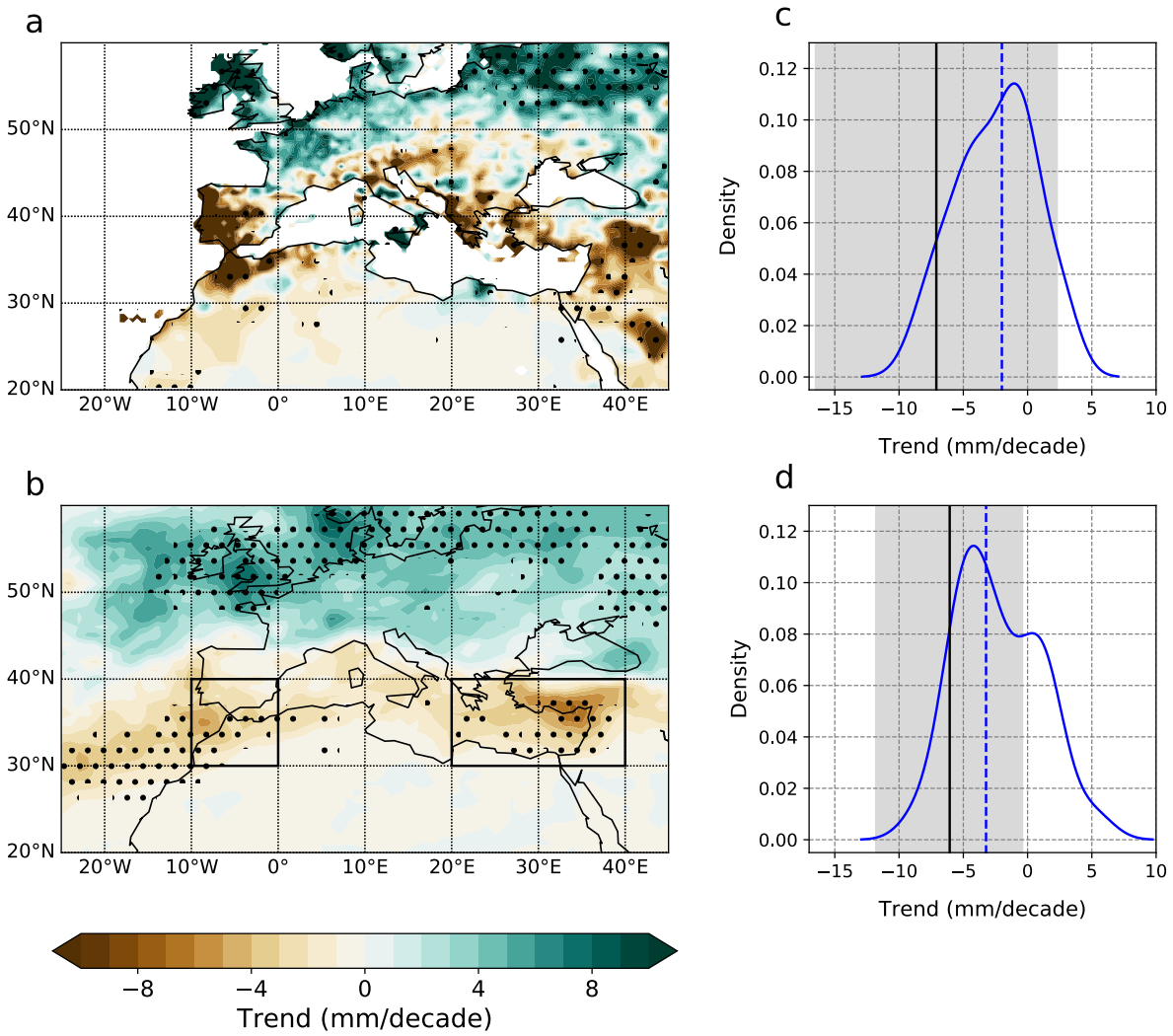

Figure 2-14: (a-b) 1950-2015 trends in November-to-April precipitation in the Mediterranean region in (a) GPCC and (b) CMIP5 GCMs (1950-2005: historical scenario; 2005-2015: RCP8.5 scenario). Dots indicate 10% significance. (c-d) 1950-2015 land precipitation trends in observations (GPCC; median: solid black line, 95% range: gray shading) and CMIP5 simulations (density: solid blue line; median: dashed blue) of (c) Western Mediterranean (10°W-0°/30-40°N, see box in (b)) and (d) Eastern Mediterranean (20-40°E/30-40°N) November-April precipitation.

and the intricate topography, make the regional climate particularly complex, subject to large inter-annual variability and strong spatial gradients. Early research highlighted the importance of poleward shifts of the large-scale circulation in explaining drying trends in subtropical and mid-latitude regions like the Mediterranean [160, 222]. The combined poleward expansion of the Hadley circulation [160] and shift of mid-latitude storm tracks, like the North Atlantic storm track [275, 195, 16], were believed to be the major drivers behind Mediterranean drying.

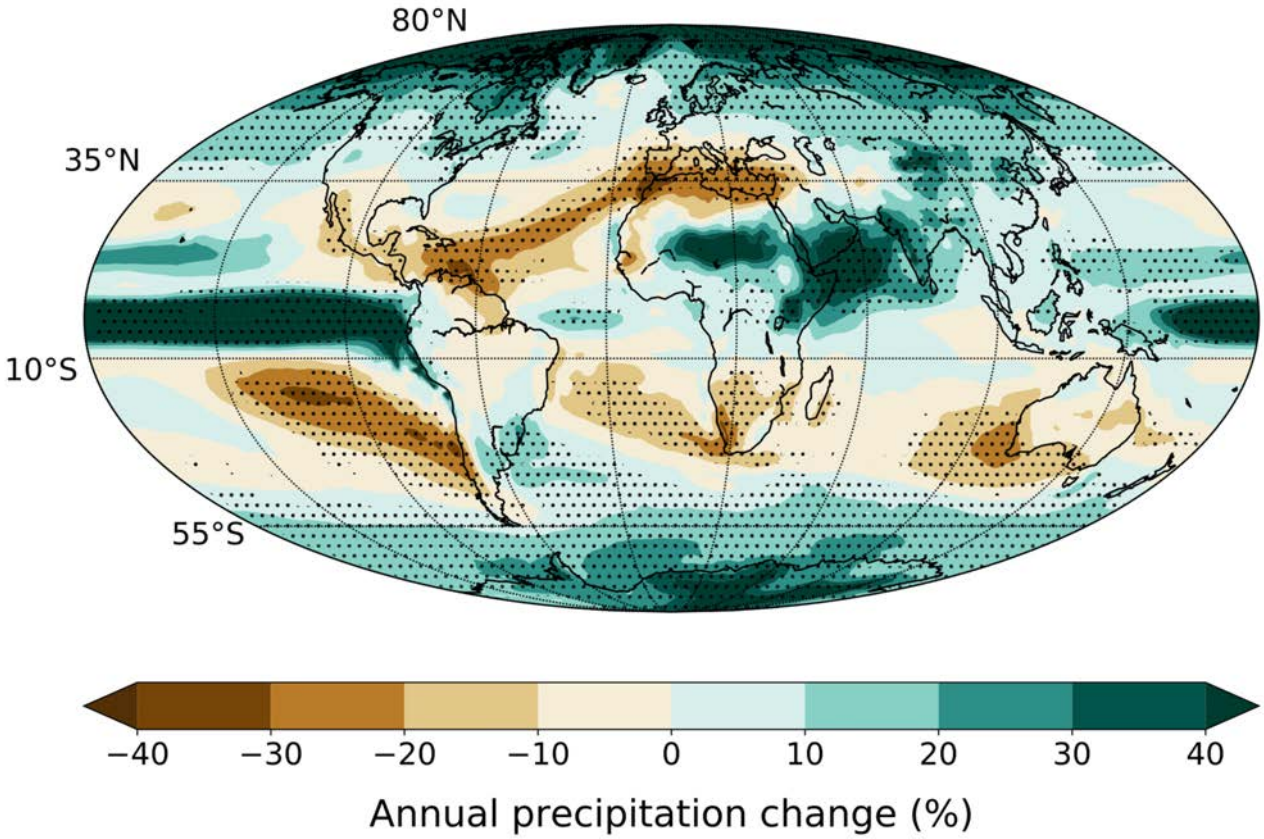

Figure 2-15: CMIP5 mulit-model mean relative change in annual precipitation (%) under RCP8.5 by the end of the 21st century (2071-2100 minus 1976-2005). Dots indicate agreement by more than 80% of models on the sign of the change.

While their impact has been confirmed for Southern hemisphere Mediterranean-like climate regions (Chile, South Africa and southwestern Australia), recent studies questioned their role in explaining hydroclimatic trends in the Mediterranean Basin [226]. Attention turned to Mediterranean regional-scale changes in atmospheric circulation as direct causes of the winter precipitation decline [225, 278, 279, 16, 36], but their origin has remained obscure [226]. In addition to scientific interest, water planning and management, as well as climate mitigation strategies in this region, would benefit from a better physical understanding of the projected drying. The latter may also be particularly useful to reduce inter-model spread in projections, which remains high despite the quasi-unanimous agreement on the sign of future precipitation trends. In the case of Morocco, for instance, winter precipitation declines by the end of the 21^{st} century range from -5 to -60% across models from the IPCC Fourth Assessment report [133].

Due to the severity of projected regional trends, the downscaling of climate projections for the Mediterranean region and Morocco has been the focus of numerous studies [101, 225, 278, 80, 246, 282]. Regional-scale information is indeed critical to assess climate change impacts and develop concrete adaptation strategies. Downscaling allows a finer-scale assessment of climate impacts on temperature, precipitation, river flow, snowpack and agriculture, among others. This is especially important for Morocco where components of the water cycle can vary significantly across space. Latitude is a major factor, of course, with a cooler and wetter north, and warmer and drier south, but the complex topography also plays an important role that only high-resolution analyses can apprehend [223].

Two approaches to regional climate downscaling exist: statistical downscaling, which relies on empirical relationships between large-scale climate fields (geopotential, SSTs, etc.) and small-scale climate variables of interest (temperature, precipitation); and dynamical downscaling, which involves the use of Regional Climate Models (RCMs), which, like global models, solve the physical equations of atmospheric flow but at higher resolution, over a smaller domain, and are forced at the domain boundaries by output from a given global model. RCMs can also incorporate physical mechanisms not well-resolved at the GCM scale [90], particularly those connected to fine-scale topography. Statistical downscaling has been applied to northwestern Africa [116], but has remained marginal due to the overall scarcity of station data in the region; most studies have thus adopted a dynamical downscaling approach. Earlier dynamically-downscaled projections were characterized by rather coarse resolutions (50-60km) [64, 166], but the improvements in computational efficiency now allow resolutions below 15km. For Morocco and the Mediterranean, the Mediterranean Coordinated Regional Climate Downscaling Experiment (MED-CORDEX) initiative, an RCM intercomparison project over the Northern Africa/Europe region, has been extensively used to analyze local-scale climate trends and their impacts on water availability in Morocco and the Western Mediterranean [247, 80, 166, 246, 282], with a finest resolution to date of 12km (0.11°). Enhanced resolution has brought significant improvements to the simulation of seasonal patterns of temperature and precipitation, as well as of extreme events [247]. Consistent with the GCMs used as input, regional simulations have consistently shown severe declines in precipitation across the region and Morocco specifically [247, 80, 282]; coupled with simplified hydrological modules, they

were also used to project decreases in runoff [166] and dam storage [246].

No regional studies however have attempted to physically explain precipitation projections over Morocco and connect them with physical mechanisms acting at the regional scale. Regional simulations indeed offer the opportunity to evaluate the relevance of physical drivers of precipitation trends and assess the likelihood of coarse-resolution GCM hydroclimate projections. In addition, few studies have used regional simulations to improve our understanding of Morocco's water cycle, particularly its snow component. The simulation of snowpack in 200km-resolution models is obviously completely unreliable when snowfall occurs on spatial scales of a few dozen kilometers at most, as is the case in the Moroccan Atlas [165]. High-resolution simulations therefore make it possible to assess water fluxes at very small scales, compare with available ground data, and estimate their response under climate change.

2.5 Conclusion

Due to its scarcity and high variability, water has been a topic of active interest in Morocco and the Mediterranean. Much effort has been put into understanding the regional hydroclimate in the current period and for the upcoming century. Variability of precipitation at all time scales, from weekly to multi-decadal, as well as the substantial spatial variability in water availability and water cycle components, create major challenges to water management in Morocco and the surrounding regions. This thesis builds on the results presented in this chapter, and brings useful contributions to major obstacles facing water management in Morocco.

Chapter 3

Seasonal precipitation forecasts for Morocco

3.1 Introduction

Interannual variability of precipitation is a constant obstacle to efficient water management and agricultural planning in semi-arid Morocco, where droughts are common and take a heavy toll on agricultural production. A large fraction of Morocco's arable land (80%) is located in arid and semi-arid regions, mostly in the northeast (Moulouya Valley), central west (Casablanca, Beni Mellal, Marrakech) and southwest (Souss) of the country. These regions are characterized by limited and erratic precipitation, with a high risk of drought. In parallel, they account for 55% of the national cereal production, and support about half of the country's livestock [74]. As most of the cropland (85%) is rainfed, and because interannual water storage is limited, crop water demand must usually be satisfied by the same year's precipitation. Precipitation therefore strongly impacts agricultural production and crop loss can be significant in times of

[1]This chapter is a partial reproduction of Tuel and Eltahir (2018) [251]. The introduction and literature review have been reformatted, and real-time forecasts extended to 2020.

drought (Fig. 2-11).

We saw in the previous chapter (2) that seasonal forecasts, whether empirical or dynamical, have thus far displayed limited skill, which makes them unreliable in practice. Therefore, in the current decision-making system, planners base their decisions on climatological probabilities for precipitation. This compels them to adopt very conservative risk levels in order to avoid water shortages should severe droughts occur, basically assuming a worst-case scenario every year, and sticking to a one- or two-year horizon at most. This leads to high inefficiency since it is not optimal to hedge every year against a bad drought. This underlines the substantial need for precipitation forecasts in Morocco. Here, we focus on one particular region, the Oum-Er-Rbia watershed (Fig. 2-1), in central Morocco, an area of high economic importance for the country. It concentrates 30% of the country's irrigated land and half of its hydroelectric capacity, and supplies water to over seven million people (including two of Morocco's largest cities, Casablanca and Marrakech). Currently, 90% of all water is used for irrigation, and 95% of available water resources are mobilized each year.

Early and reliable forecasts of seasonal precipitation would be particularly useful to mitigate the impacts of droughts and make the most of wetter years. We propose here a simple statistical approach to seasonal forecasting of precipitation in Morocco. Statistical forecasting algorithms are plenty, like multiple linear regression (MLR) or Canonical Correlation Analysis (CCA), an approach similar to MLR but applied to multivariate pattern predictands [267]. All, however, require a series of predictor variables, or covariates. Forecasting a variable of interest thus requires first to identify such covariates, and then to implement a forecast model. Our methodology falls therefore into two parts (Figure 3-1): covariate definition on the one hand, and covariate selection with model fit on the other. Previous studies identified relevant areas of sea-surface temperatures teleconnected to wintertime weather over our region of interest [49, 191]. Building on these results, we implement a series of statistical methods to identify, within those regions, the areas most connected to Moroccan precipitation. Then, in a second step, we fit linear models and identify small groups of robust predictors to get the best forecasts of three-month precipitation totals, as compared to observations.

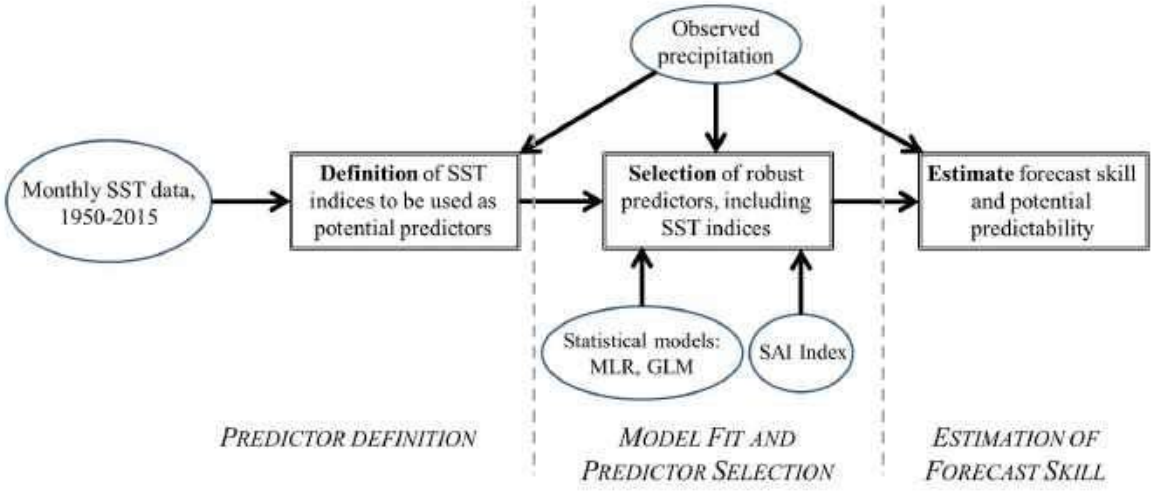

Figure 3-1: Summary of methodology followed in this chapter. The first step is to define potential precipitation predictors from monthly SST data and observed seasonal precipitation. Then, statistical models are fitted and the most robust, or informative, predictors are selected. Finally a traditional assessment of forecast skill is implemented.

3.2 Region of study

In the northwestern quadrant of Morocco, delimited by the Atlas and Rif ranges, which contains the Oum-Er-Rbia watershed, the climate is mediterranean – mild and wet in winter, and hot and dry in summer. Average annual precipitation varies significantly over this region, generally increasing with both latitude and elevation (Fig. 2-2). Thus, the low point is around Marrakech to the south, with only 200 mm of annual precipitation, while mountainous regions to the north receive well over 1000 mm. The wet season extends from November until April, when moist air is advected from the Atlantic ocean, located to the west and northwest. The wet season accounts for about 90% of annual precipitation. Precipitation events during this season tend to be short and irregular, occurring when mid-latitude weather systems, that formed over the Atlantic ocean, drift towards the coast, under the influence of prevailing winds. Typically, in the north-western Maghreb, a rain season consists of at most 10-14 single precipitation events [27].

A closer look at the annual precipitation cycle in the region reveals the presence of two modes in the distribution, with one peak in the early part of the wet season (around December) and a second in the later part, around March (Fig. 3-2). Precipitation thus appears to arrive in two independent waves, one in winter, the other in spring, with no apparent link between

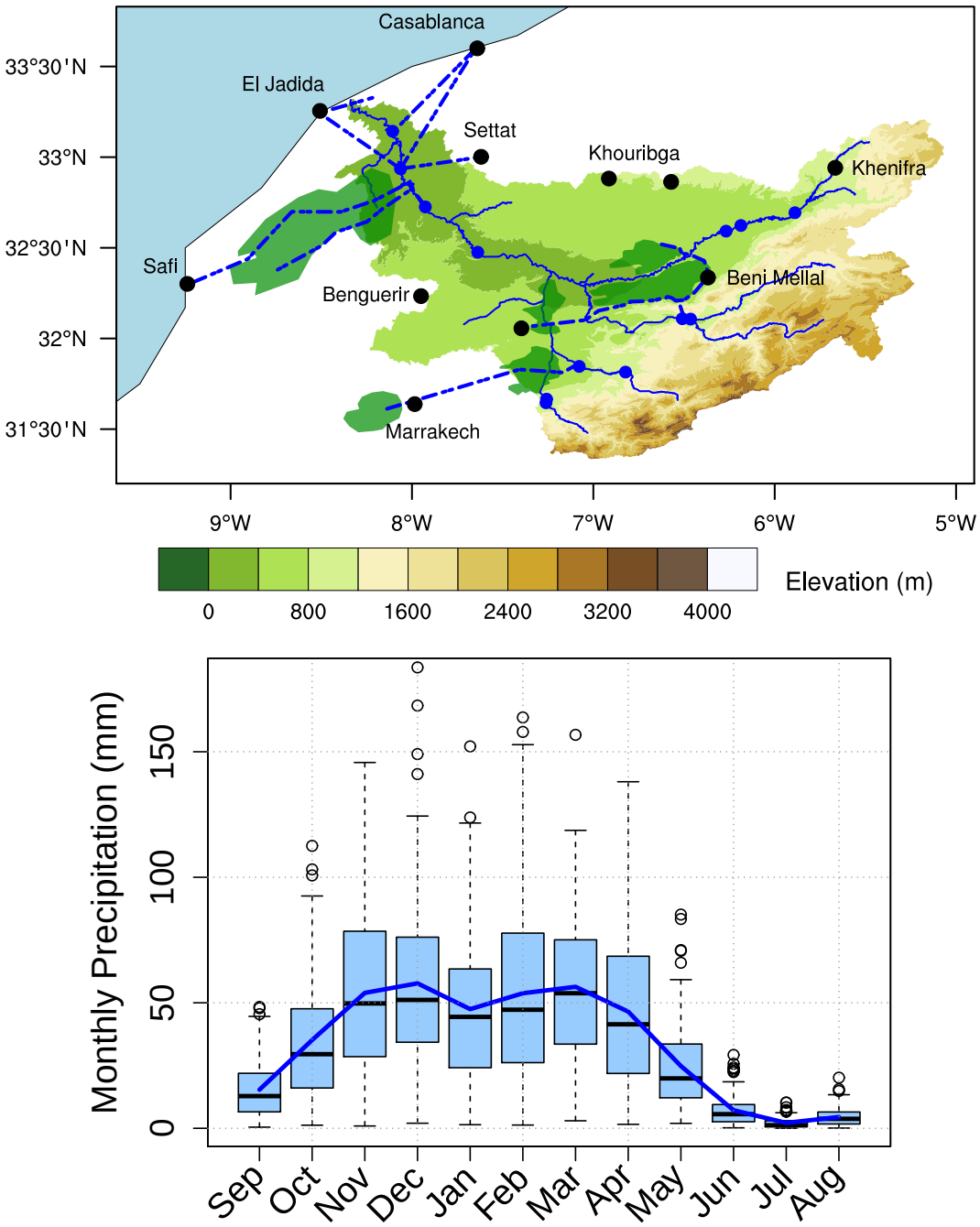

Figure 3-2: *Top*: Map of the Oum-Er-Rbia watershed, showing elevation (filled contours), main cities (black dots), dams (blue dots), channels (dot-dashed blue line) and irrigated perimeters (dark green). *Bottom*: Annual precipitation cycle over the Oum-Er-Rbia basin, from September to August (data: CRU TS4 [108]).

the two. For instance, Spearman's correlation coefficient between November-to-January and February-to-April precipitation is only 0.11 for the whole 1901-2015 period, and 0.17 for 1950-2015, both of which are insignificant at the 5% level of confidence. Similarly, knowing how

,uch precipitation fell from November to January brings now information about how much precipitation will fall from February to April (Table 3.1). This suggests that precipitation during the wet season may have different physical origins depending on the time of year, and that teleconnections for each "wave" will be different. This motivates us to divide the wet season into several subseasons and develop forecast models for each. We focus in this study on three precipitation series: November-to-January (NDJ), December-to-February (DJF) and February-to-April (FMA). A distinction is made between NDJ and DJF because, though the teleconnection of precipitation to the NAO usually steps in during November (Fig. 2-6), sub-monthly NAO variability may cause it to be delayed until early December, thus impacting predictability of precipitation. Separating NDJ and DJF also helps determine how predictable early-wet season precipitation is.

Coupled to its spatial variability, precipitation is also highly variable in time, both intra- and inter-seasonally. The annual coefficient of variation ranges from an average of 30% in the northwest to over 100% in the most arid areas. Local climate is characterized by long periods of droughts that tend to affect wide areas. Short-term seasonal lack of moisture is also common, either at the beginning (November-December) or the end (March-April) of the growing season.

NDJ / **FMA**	Dry	Avg	Wet
Dry	0.37	0.24	0.39
Avg	0.37	0.34	0.28
Wet	0.26	0.42	0.33

Table 3.1: Empirical probability table of FMA precipitation categories conditioned on NDJ precipitation (1950-2015 period). For instance, when NDJ precipitation was average, FMA precipitation was higher than average ("wet") 28% of the time.

3.3 Identified teleconnections

A large body of work exists on the teleconnections to wintertime western European and north-western African weather. As discussed in the previous chapter, precipitation over northwestern Morocco during late fall and winter (November-February) is strongly influenced by the North

Atlantic Oscillation (NAO). In the spring, however, as the SLP dipole drifts north, the connection to the NAO is gradually lost (Fig. 2-6). For that period, studies have suggested a stronger link to Pacific sea-surface temperatures (SSTs), in particular to the ENSO [167, 228] and the Pacific Decadal Oscillation (PDO) [167] phenomena. Seasonal lagged relationships have also been found by Knippertz et al. (2003) [147], who suggested a connection between winter ENSO conditions and spring rainfall over North Africa and the Iberian Peninsula. Overall, associations between Pacific SSTs and Mediterranean precipitation have been described during all seasons of the year [228].

Mechanistic explanations were lacking until the recent dynamical investigation by Shaman and Tzipermann (2010) [228], who suggested, based on an analysis of vorticity anomalies, that ENSO-related forcing of large-scale atmospheric circulation resulted in stationary barotropic Rossby wave trains propagating eastward from the eastern equatorial Pacific. This generates anomalous vorticity patches off the coast of Portugal and Morocco, which in turn impact winds in this region. This modulation of westerlies over southwestern Europe is found during fall (mainly over the Iberian peninsula) as well as spring (with a zone of influence displaced to the south). The physical mechanism behind it may be acting year-round, but remains marginal in summer – because the strong anticyclone acts as a blocking – and in winter, when the influence from North Atlantic pressure patterns is dominant. Spring and fall offer the opportunity for this mechanism to become more prevalent, since the Azores High is still weak and the storm-track has shifted north.

The teleconnection of winter precipitation to NAO is very strong, but the latter has proven remarkably challenging to predict. Many studies have suggested that a large fraction of NAO dynamics arose from internal, non-linear phenomena intrinsic to the atmosphere [78]. Nevertheless, while sub-seasonal variability of the NAO might arise from climate noise, external forcings likely play a significant role on longer timescales [233], most notably the ocean [24]. Given its large thermal inertia, ocean temperatures force the lower atmosphere over the course of months, making them very useful predictors for a wide range of climatic phenomena around the globe. Studies by Rodwell and Hoskins (199) [214] and Saunders and Qian (2002) [219] uncovered links between SST anomalies in the months leading to November and winter NAO. In particular, emerging in late spring and persisting until early fall is a noticeable North Atlantic

horseshoe pattern [49], with warm anomalies southeast of Newfoundland and cold anomalies to the northeast and southeast, which precedes positive phases of the NAO and could explain up to 15% of its variability. For the North Atlantic domain, SSTs likely play a role in determining the position, extent and strength of the meridional temperature gradient that in turn drives baroclinic instability and the storm track in the region. There is still debate about which specific region of the Atlantic is most strongly linked to winter NAO, from tropical and subtropical regions [50] to areas off the UK or Newfoundland [219]. Connections to other major ocean basins have been proposed as well, such as the southern Atlantic [209] or the tropical Indian and Pacific oceans [240]. Models and regression analyses suggest however that the oceanic influence on North Atlantic climate is nonstationary and appears to have varied, sometimes significantly, over the last two centuries [119].

Other climate variables, like Arctic sea-ice concentrations, are also believed to force winter atmospheric circulation [245], but their record is often limited to the satellite age (usually post-1980). This limits considerably the number of points that can be used to develop forecast models, adding more uncertainty to the process. Therefore, the focus here will be on SSTs, which have a long and reliable record going back to at least 1950 [144]. We consider only one other type of predictor, the Snow Advance Index (SAI) defined by Cohen and Jones [46] from the growth rate of October Eurasian snow cover. They found it to be strongly related to the winter NAO index since 1972, and suggested a convincing mechanistic explanation [46] (section 2.2.3). This index is available starting in 1972, a period long enough to make it worth considering in our models (Fig. 3-3).

Finally, in recent years, attention given to climate and weather models has also grown considerably. The improvement of computational capacities made it possible to simulate winter weather of the North Atlantic in much better detail, and some of the latest forecasts from Numerical Weather Models (NWMs), though they underestimate the variability of the NAO, show good skill at predicting its phase at the seasonal time scale [69].

3.4 Data

Precipitation data are taken from the CRU TS4.00 database [108], which extends from January 1901 to December 2015. The GPCC dataset [281] is also used for comparison and to get estimates of precipitation (for 2017 onwards, which were missing from CRU TS4 when forecasts were first developed).The most skillful numerical NAO hindcasts at a one-month lead are the ones published in Dunstone et al. (2016) [69], covering the winters 1981-82 to 2015-16. To be consistent with that study, observed NAO values are computed from the HadSLP2 database [7] as the difference in monthly sea-level pressure (SLP) between the Azores (28°-20°W, 36°-40°N) and Iceland (25°-16°W, 63°-70°N). In addition, we use as predictor fields the SST data from the Hadley Centre Sea Ice and Sea Surface Temperature (HadISST) dataset [205] at 1° resolution, covering the period 1870 to present. Because SST data before the 1940s have been shown to be less precise and to have generally larger uncertainty [144], and because station data for precipitation display several missing years throughout the 1920s and 1930s, we choose to focus on the period 1950-2015. We restrict our analysis to the North Atlantic (0°N to 65°N; 80°W to 6°W), Pacific (50°S to 65°N; 120°E to 65°W) and Mediterranean (30°N to 46°N; 6°E to 37°E) domains, as the literature suggests that they may be important [214, 49, 219, 240, 50]. Finally, the 1972-2015 Snow Advance Index (SAI) is taken from *Cohen and Jones* [2011].

3.5 Defining potential predictors

The first step in developing statistical forecasting models for any variable of interest is to select likely predictors. But how to select among millions of potential covariates at many different lead times? Many studies rely on previously identified predictors – for instance, ENSO or the Southern Oscillation Index to forecast precipitation. Still, in our case, there is little a priori knowledge of specific predictors to include in the models. Previous studies, however, have identified potential sources of skill in forecasting atmospheric teleconnection patterns at seasonal timescales (see section 3.3). In particular, Sea-Surface Temperatures (SSTs) in given ocean basins have been shown to constitute a substantial source of information.

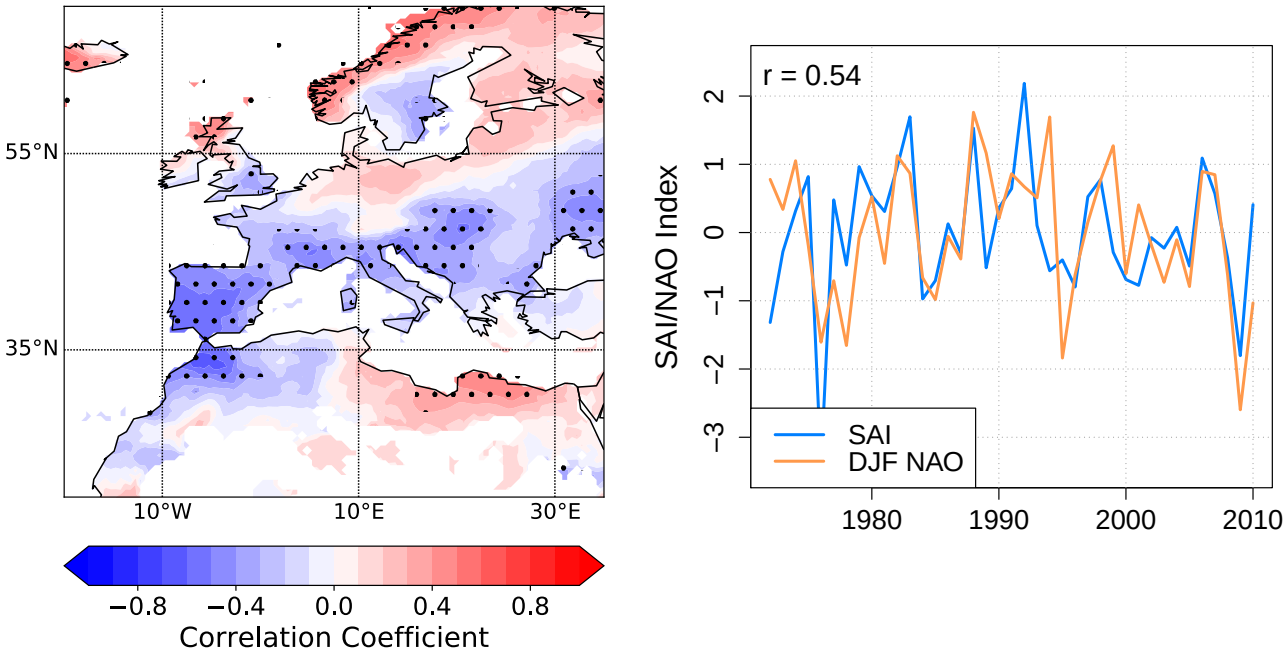

Figure 3-3: Pointwise correlation maps between DJF precipitation (from PERSIANN dataset [11]) and the weekly Snow Advance Index (SAI) [46], for the period 1972-2010. The correlation pattern is very similar to that of the NAO index (Fig. 2-6).

3.5.1 Methods

SST fields, however, are complex and highly multidimensional. To extract meaningful indices from those thousands of potential covariates at various different lead times, we display maps of several measures of statistical relationships between precipitation series and lagged SSTs. We go back as far as nine months in advance (May of the preceding hydrological year), as Czaja and Frankignoul (2002) [49] suggested that North Atlantic spring SSTs may force wintertime atmospheric circulation.

We first identify links between SST fields and precipitation series using well-known statistical methods, on a point-by-point basis, *i.e.* by considering the SST at each point in space as a potential predictor. In addition to correlation maps, we look at SST anomalies preceding a dry, average or wet season (composite maps). We also implement an Analysis-Of-Variance (ANOVA) procedure and calculate maps of mutual information (MI) between SSTs and precipitation time series, both of which measure how well the variability of a predictor explains that of the predictand. To take into account the strong spatial covariance of SST fields, we also

rely on Canonical Correlation Analysis (CCA), a statistical technique similar to multilinear regression, that identifies maximally-correlated patterns in the predictand and the predictor. Overall, these varied methods can highlight a wide spectrum of potential relationships. Their comparison helps separate spurious predictors from those with high potential skill. Using different methods also avoids being constrained by the assumptions behind a single one, nor by any p-value thresholds.

Predictor significance is based on bootstrap confidence intervals. Each method is applied to 5000 random ordering of years for SSTs, while the ordering of the precipitation series is kept constant. This allows to estimate confidence intervals at any given level of significance, and potential SST predictors are then defined by encapsulating the areas of highest significance, selected among those extending at least 15° in each dimension. We end up with lists of about two dozen potential indices for each season, at many different lead times (see Table3.2).

Similarly to [49],the question of whether there is a physical connection between the two fields is addressed by adopting the null hypothesis that there is none. If true, then temporally shuffling the sequences of the two fields (each shuffled differently) and applying one of the statistical methods should not lead to a statistically different outcome. Areas of statistical significance are therefore identified by generating 1000 maps for each method (excepted for MI, which is more computationally demanding, and for which we only look at the results for the historically ordered data), each time shuffling the precipitation series randomly, and comparing at each grid point the 2.5% and 97.5% quantiles to the values obtained with the original series.

Correlation maps

The correlation coefficient is undoubtably one of the easiest ways to highlight statistical links between two variables. Its interpretation must be done carefully, however. Depending on the method, the results may suggest non-existent relationships or over-estimate existing ones. The three most widely used correlation measures are Pearson's (r_P), Spearman's rank (r_S) and Kendall's tau rank (r_K) correlation coefficients. While r_P explicitly looks for linear relationships between two data series, and is thus only a measure of their linear correlation, r_S and r_K both measure the similarity of the ordering of the two data series. r_S is defined as Pear-

son's correlation coefficient between the ranks of observations of the two variables. Kendall's τ, for its part, is computed by looking at how often the respective rankings of two pairs of observations are in agreement. Thus, both r_S and r_K are more robust to outliers and, more importantly, can detect certain non-linear relationships that r_P would fail to highlight.

Composite maps

One other way to identify potential predictors of seasonal precipitation is to look for variables whose distribution is significantly different between years when precipitation is rather low and years when it is rather high. This is the basis of composite maps. First, years are divided into three categories according to the precipitation observed during the season of interest: below-, near- and above-average, as defined by the 33% and 67% percentiles of the precipitation series. SSTs are then averaged for each group of years, and the resulting maps are evaluated against confidence intervals to identify areas of significance.

ANOVA

Similarly, we can look at the problem the other way and look for variables such that the distributions of seasonal precipitation when those variables are low or high are significantly different. An Analysis-of-Variance (ANOVA) procedure is implemented for each SST grid point by dividing the years in the record into three categories, based on the 33% and 67% percentiles of the corresponding SST time series. The ANOVA method then tests whether the mean precipitation values for each of those three categories are significantly different. In other words, it evaluates how much of the variability in the predictor can be attributed to variability in the predictand. The significance of the decomposition is given by the F-statistic, defined as the ratio of between-categories variance over within-category variance for the precipitation data. The higher the F-statistic, the more the predictor is able to "separate" the predictand and reduce its uncertainty.

Mutual information

Mutual information (MI) belongs to the field of information theory as developed by Shannon and is conceptually linked to the notion of entropy. For two random variables X and Y of a joint probability distribution p, their mutual information is defined as

$$I(X,Y) = \iint_{x,y} p(x,y) \log\left(\frac{p(x,y)}{p(x)p(y)}\right)$$

which can be reformulated as the difference between the entropy of Y and that of $Y|X$. If X explains a lot about Y, then we can expect the entropy of $Y|X$ to be low, and the mutual information to be high. Similarly to ANOVA, it gives information on the residual uncertainty on the predictand when the value of the predictor is known. In other words, the higher MI, the larger the reduction in uncertainty on the predictand when the predictor is known. One of the main advantages of this method is its being non-parametric, meaning that it can easily detect non-linear relationships in the data. On the other hand, it is computationally intensive; the main practical difficulty here is the estimation of the joint density $p(x,y)$ and of the marginal densities $p(x)$ and $p(y)$. Non parametric density estimation methods are costly in high dimensions and necessitate a large amount of data.

Canonical Correlation Analysis (CCA) and composite maps

Since the previous methods are independently applied at each grid point, they do not take into account the substantial spatial covariance of SST data. To remedy this, we turn to Canonical Correlation Analysis (CCA), a statistical technique similar to multilinear regression, that identifies maximally-correlated patterns in the predictor and predicted fields. Each field is seen as a multivariate vector, and the analysis yields linear combinations of the two sets of variables whose correlation is maximal. In other words, if $X_t(s)$ denotes a vector of predictors (SST spatial field, index by location s), and y_t is the observed precipitation for the same year, CCA will output a vector $\xi(s)$ such that corr $(\sum_s \xi(s)X_t(s), y_t)$ is maximized. The procedure can be repeated by looking for linear combinations of X_t and y_t that are uncorrelated to the

previous combinations, but here we choose to stop after the first step. Instead of taking the full SST field $X_t(s)$ (several thousand grid points), which would make CCA too computationally demanding and its results quite unstable [267], SST fields at each time lead are filtered using a latitude-weighted Principal Component Analysis. Only the first principal components that explain at least 90% of variability are retained, and used as input for the CCA analysis.

3.5.2 Results

Applying the above methods to SST fields at different time leads yields a large number of potential predictors, displayed in Table 3.2. The most important ones (selected during model fit, see section 3.6), are highlighted on Figure 3-4 (left). Both the NDJ and DJF precipitation series appear to be most influenced by extratropical North Atlantic SSTs, from late spring until late fall. This is in keeping with previous results highlighting specific SST patterns in the same area linked to wintertime storm track position and strength, and thus to the NAO [214, 119, 219] (section 3.3).

Regarding the FMA series, the connection to the North Atlantic is overall weaker than for the other two series, though a horseshoe-like structure does appear in spring SSTs as well. The concurrent NAO still impacts spring precipitation, albeit much less so than in winter. The pattern of statistical links with winter (November to January) SSTs resembles that of the winter NAO itself, hinting at some potential feedback mechanism between winter NAO, winter SSTs and spring atmospheric circulation. A wide region of positive correlations stretches from the eastern seaboard of the US to northwestern Europe, linked to two areas of negative correlation values. FMA precipitation is most signigicantly linked, however, to Pacific SSTs, from early summer to December. The pattern found by all methods is very similar to that of the Pacific Decadal Oscillation (PDO), one of the major modes of SST variability in the Pacific ocean [248].

A comparison of some results from three methods is shown on Figure 3-4 (right). Overall, the different approaches to predictor definition highlighted above agree quite well on what areas are significantly linked to precipitation over the Oum-Er-Rbia, though the magnitude of the link and exact geographical delimitations vary somewhat between methods. The list of

potential predictors therefore includes many highly correlated predictors, from which the best are selected during model fit (section 3.6.1).

NDJ					
#	Month	minLon	maxLon	minLat	maxLat
1	May	-68	-35	30	45
2	May	-73	-58	35	50
3	May	-66	-41	28	46
4	MJJ	-60	-40	5	25
5	Jun	-63	-36	28	46
6	Jun	-63	-40	0	20
7	Jul	-83	-63	8	30
8	Aug	-28	-8	41	61
9	Sep	-28	-8	41	61
10	Oct	-23	-6	41	58
11	Oct	-56	-36	41	61
12	Oct	8	25	28	45
13	JJASO	-30	-8	41	56
14	JJASO	-62	-45	10	25
15	ASO	-28	-8	41	56
16	ASO	-25	-5	45	63
17	ASO	-83	-63	8	30

DJF					
#	Month	minLon	maxLon	minLat	maxLat
1	May	-75	-53	35	53
2	May	-60	-38	28	43
3	May	-63	-43	25	43
4	Sep	-63	-43	33	56
5	Sep	-101	-81	16	36
6	Sep	-75	-55	33	50
7	Sep	-65	-40	38	55
8	Oct	-30	-10	38	55
9	Oct	-61	-41	38	56
10	Oct	11	26	31	46
11	Oct	-58	-40	38	53
12	Oct	-160	-130	35	55
13	ASO	-60	-40	38	55
14	ASO	-160	-130	35	55
15	ASO	-60	-40	35	55
16	Nov	-40	-20	13	31
17	SON	-60	-40	38	55
18	SON	10	30	30	45
19	SON	-160	-130	35	55
20	SON	-60	-45	40	55

FMA					
#	Month	minLon	maxLon	minLat	maxLat
1	May	-60	-30	30	45
2	May	-70	-50	35	53
3	May	-105	-75	-20	10
4	May	-160	-135	35	55
5	Jun	-63	-40	30	50
6	Jun	-120	-65	-20	5
7	Jun	-70	-50	38	53
8	MJJ	-65	-40	30	50
9	Jul	-155	-65	-20	0
10	Aug	-155	-65	-20	0
11	Aug	-60	-35	36	56
12	Sep	-145	-70	-20	0
13	Sep	-175	-140	40	60
14	Oct	-170	-130	40	60
15	Oct	-150	-75	-20	5
16	Oct	160	185	25	50
17	ASO	-125	-65	-18	3
18	Nov	-145	-85	-20	0
19	Nov	-165	-130	40	60
20	Nov	-160	-85	-20	0
21	Dec	-155	-65	-20	5
22	Dec	-25	-3	36	61
23	Dec	150	175	-40	-15
24	Dec	-150	-125	40	60
25	OND	-155	-125	40	60
26	OND	-145	-85	-20	10
27	Jan	-68	-35	23	43
28	Jan	-155	-125	43	65
29	Jan	-130	-105	10	35
30	Jan	-145	-65	-20	5
31	Jan	-65	-35	23	43
32	NDJ	-140	-90	-20	0

Table 3.2: List of potential SST predictors defined for each precipitation series. Yellow highlight denotes best predictors selected by the models (see Figure 3-4, left). Bounds are given by minimum/maximum longitude and minimum/maximum latitude of the areas defining the SST indices.

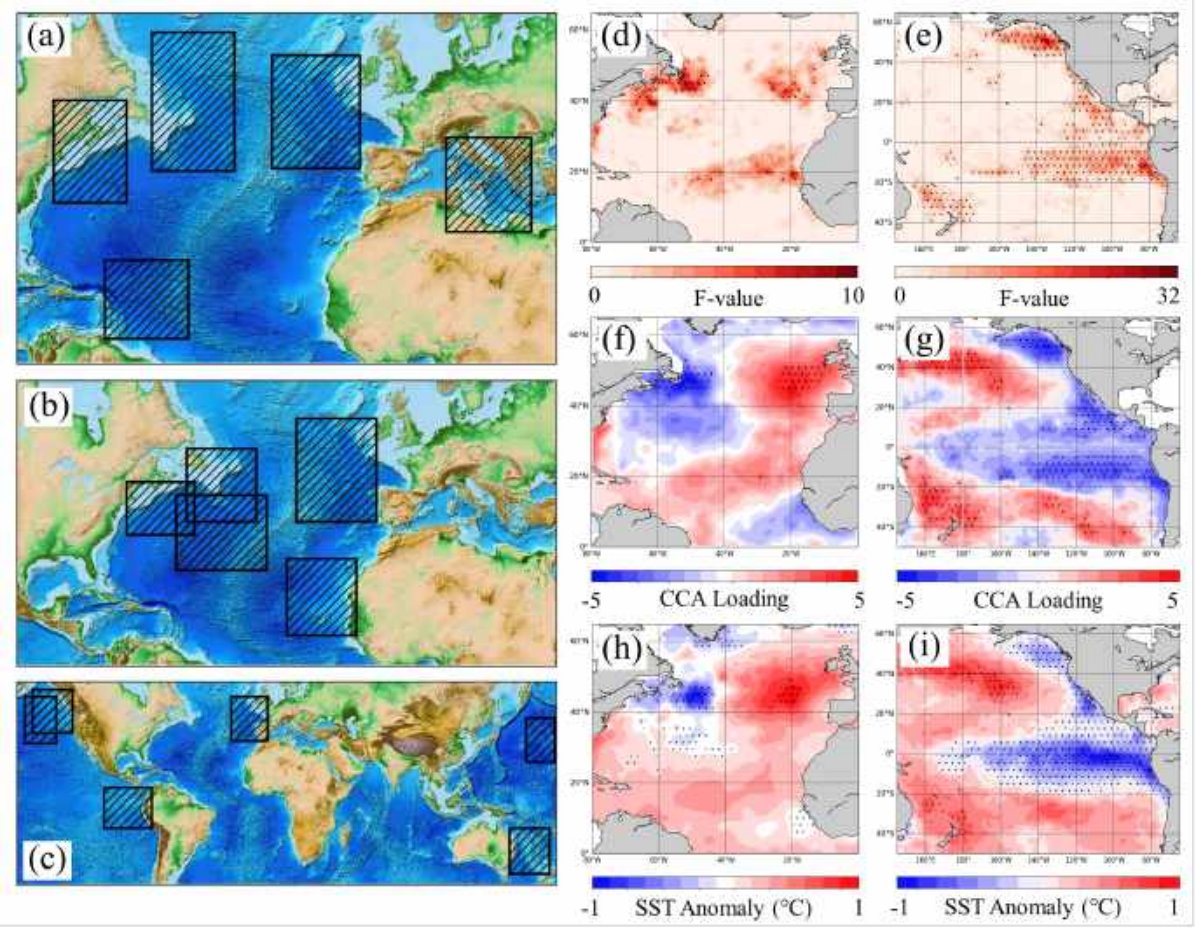

Figure 3-4: *Left*: Maps of each season's robust precipitation SST predictors: NDJ (a), DJF (b) and FMA (c). Robust predictors are defined as the ones selected most often during the cross-validation process (see section 3.6). The predictors shown on the above maps were selected in the models at least 90% of the time. *Right*: Example of results from three predictor identification methods (d,e: ANOVA; f,g: CCA; h,i: composite maps) between the DJF precipitation series and October North Atlantic SSTs (d,f,h) and the FMA precipitation series and December Pacific SSTs (e,g,i). Stipling corresponds to significance of the results with 95% confidence, as explained in the body of the article. Potential predictors were selected from such maps, drawn for every possible SST domain/lag time/precipitation series combination, and keeping areas found significant by all methods and extending at least 5° in each dimension.

3.6 Forecast models and predictor selection

3.6.1 Methods

Statistical models

Empirical forecast models are built for each precipitation series (NDJ, DJF and FMA) by relying on the information contained in the SST indices defined in section 3.5. Two main models are considered: Multiple Linear Regression (MLR) and the Generalized Linear Model (GLM) [61] with a logarithmic link function. The latter is considered because it brings a slight improvement in fit when regressing winter precipitation against the concurrent NAO index (see Discussion). In MLR, the expected value of seasonal precipitation y is modelled as a linear response of given covariates X : $\mathbb{E}[y] = X\beta$, while the log-link GLM model assumes $\ln(\mathbb{E}[y]) = X\beta$. In addition to the exact value of precipitation, we are interested in forecasting discrete events, like droughts. To that end, we define precipitation categories (below-, near- and above-average) based on the terciles $Y_{33\%}$ and $Y_{67\%}$ of each series. Thus, years for which the seasonal precipitation was below its 33% percentile ($Y_{33\%}$) were categorised as "dry". For each year t, by sampling regression coefficients and residuals, an empirical distribution $p(y,t)$ of the forecasted precipitation is estimated, from which we determine confidence intervals and probabilistic categorical forecasts; the probability of a dry year being equal to $\int_0^{Y_{33\%}} p(y,t)dy$. The predictive potential of the best NAO forecasts [69] is estimated via MLR using two cross-validation mathods. In the first, the model is trained on observed NAO and precipitation from 1901-1980, and validated using NAO forecasts over 1981-2015, rescaled to have the same mean and variance as observations. The second only relies on 1981-2015 hindcasts and a leave-one-out approach is selected.

Feature selection and cross-validation

The large number of potential predictors defined in section 3.5 must be narrowed down to avoid overfitting, given the limited length of the time series. We do this in two steps: the first,

based on LASSO regression using the R package `glmnet` [86], helps select a small subset of robust potential predictors (typically 12-15) out of the many initial ones. LASSO is a well-known, useful technique that performs feature selection by adding to the error a penalty term to favour a sparse vector of regression coefficients (details and references can be found in [86]). In a second step, the most informative predictors are selected by a combined forward and backward variable selection process, also known as stepwise regression. Starting from a model with no covariates, predictors are added, one at a time, to a list of "best" predictors leading to an "optimal" model. At each step, a new predictor is considered: it can either be added to the list of currently retained predictors, or replace one of them. Goodness-of-fit is estimated based on the Akaike Information Criterion (AIC), equal to twice the difference between the number of covariates included in the model and the model log-likelihood. A smaller AIC indicates a better fit; models with more parameters are penalised, and in that way the AIC is similar to the adjusted coefficient of determination. Predictors stop being added when no more improvement in AIC is possible. We also check that randomly shuffling the predictors at first does not significantly impact the stepwise regression.

In addition, a cross-validation procedure must also be implemented to assess model skill in the most objective way possible. Because feature selection implies looking at the data to extract the most relevant predictors, in order to avoid any bias in skill, both predictor screening and model building must be cross-validated simultaneously [173].

We adopt a k-folds cross-validation, by dividing the sample into subsamples of size k. Each of those is withheld in turn for validation, with all remaining years serving as training set. Thus, if k=10, forecasts for the years 2006-2015 are issued by models trained on 1950-2005. The value of k is varied from 5 to 25, to examine the robustness of the models. After separating the dataset into training and validation sets, the two feature selection steps (LASSO and stepwise regression) are conducted on the training set only, and model skill is assessed for the left-out validation data. This cross-validation methodology ensures that the data against which model skill is evaluated is never used at any step of the model building process.

Our predictor definition methodology described in the previous section did involve using all data points to compute ANOVA maps, CCA coefficients, etc. Still, because this process is time-consuming and involves a lot of selection by hand, it could not be repeated independently at

every step of the cross-validation. A few trials have however shown no significant differences when selecting different subsets of the observed data. Most relationships appear strong and stable enough so that similar predictors would have been selected in any case.

Based on this procedure, different optimal combinations of predictors may be – and in fact, are – selected to build the models, depending on the training set. This variation should not be seen as an attempt to maximize skill at the expense of physical interpretability; to the contrary, it helps avoid under- or overfitting of the models for given years and accounts for the uncertainty both in the importance of each predictor and in the number of optimal predictors. This approach can be considered more realistic and should better reflect the actual skill of the models, since forecasted years are clearly separated from the model-building process.

Skill Scores

For continuous forecasts, we use the coefficient of determination r^2 and root mean-square error (RMSE) to evaluate the accuracy of the models. For categorical forecasts, we rely on the hit score HS, equal to the percentage of correct hits (*i.e.* when the right category is predicted): if $z(t)$ is the observed category and $\hat{z}(t)$ is the forecasted one,

$$\mathrm{HS}(\mathcal{M}) = \sum_{t=1}^{T} \mathbb{1}\left\{\hat{z}(t) = z(t)\right\}$$

We also consider the forecast index FI, defined as the average probability forecasted for the realized category. With $p_j(t)$ the assigned probability of category j in year t:

$$\mathrm{FI}(\mathcal{M}) = \sum_{t=1}^{T} p_{z(t)}(t)$$

A perfect model would have both FI=HS=1 (all categories are forecasted correctly, with a probability of 1) and a no-skill model would have FI=HS=1/3 (random category is forecasted). To assess how well the models warn against specific events – for instance, droughts, we also look at the Relative Operating Characteristic score (ROC) score, based on the comparison of

hit- and false alarm-rates for different warning thresholds. For a category $j \in \{1, 2, 3\}$, and for a given threshold p_w, a warning is delivered if the forecasted probability $p_j(t)$ for category j is greater then p_w. The Hit Rate (HR) and False Alarm Rate (FAR) are estimated as follows:

$$\begin{cases} \text{HR} &= \frac{\sum_t \mathbb{1}\{\hat{w}(t)=1, w(t)=1\}}{\sum_t \mathbb{1}\{w(t)=1\}} \\ \text{FAR} &= \frac{\sum_t \mathbb{1}\{\hat{w}(t)=1, w(t)=0\}}{\sum_t \mathbb{1}\{w(t)=0\}} \end{cases}$$

From a sequence of thresholds p_w between 0 and 1, one can estimate the corresponding sequences of HR and FAR values, and the ROC is defined as the area under the curve in the HR-vs-FAR plot (estimated here by the trapeze method). Models with ROC$>$ 0.5 display skill (hit-rate is higher than false-alarm rate) while a no-skill forecast will have ROC$=$0.5 (hit-rate and false-alarm rate are equal).

3.6.2 Results

Historical hindcasts

The approach based on NWM NAO hindcasts [69] shows little skill, with the classifier trained on hindcasts only yielding FI$=$ 0.36 and HS$=$ 0.40. The model trained on 1901-1980 observations and validated on 1981-2015 hindcasts doesn't do as well as the one validated using NAO observations, as expected, but still shows some predictability ($r = 0.37$ against $r = 0.56$, $FI = 0.35$ against $FI = 0.38$ and $HS = 0.37$ against $HS = 0.41$). One issue may be that the classical definition of the NAO index may not be optimal to forecast winter weather in Northwestern Africa. Studies have shown that the southern pole of the NAO between the Azores and Gibraltar had significantly more influence on that region than SLP conditions over Iceland [147]. Instead of summarising the whole SLP field in the NAO index, it may be better to look at more specific SLP domains.

Models are built and fitted for all three seasons; for the DJF and FMA season in particular, we issue forecasts at four different lead times: on the first day of the season, and one to three months before the start of the season. As an example, for DJF, models are built using all

information up to September 1st, October 1st, November 1st and December 1st. The NDJ and DJF seasons are also analysed independently over the 1972-2015 period to estimate the improvement in skill brought by the SAI index. It must be noted, though, that because of the time required for processing the data, the full SST analysis fields are only available more than a month after the month of interest, i.e. July SST data are available in early September. However, that delay is mainly due to the sea-ice homogeneization process, and a preliminary SST field is made available on the 10th of the month after the month of interest (10th of August for July SSTs). For all models, 5-7 predictors are retained after feature selection. Figure 3-4 (left) shows the robust SST predictors that were selected most often by each model.

Results are shown in Table 3.3. Two main observations can be made. First, forecast skill is low for NDJ, but much higher for the other two series, for which model skill can safely be said to be significantly above that climatology. DJF is more predictable than NDJ, possibly because the NAO pattern during November is less stabilized, and thus less predictable, or because the beginning of the wet season in Morocco may shift by several weeks, thus adding noise to the NDJ data. DJF predictability is also more robust that that of FMA, since, when increasing k in the cross-validation, r^2 remains close to 0.40 for DJF but drops to 0.27 for FMA (Figure 3-7, left). Second, the GLM model performs better than the MLR model for all seasons. Both the increase in r^2 and the reduction in RMSE are significant, though the skill is more mixed when it comes to categorical forecasts (Table 3.3). This may be due to the asymmetry in the confidence intervals caused by the log-transformation.

Regarding lead times, the skill of one-month-ahead forecasts is about the same as that of models fitted on the first day of the season. For both DJF and FMA, forecast skill drops fast as lead time increases (Fig. 3-5), but remains somewhat higher for FMA (r^2 =0.15 three months ahead, compared to 0.05 for DJF). Table 3-5 presents more details on forecast skill vs. lead time for the DJF season. Forecast skill drops precipitously before November 1st, and remains about constant after October 1st.

Figure 3-4 (left) shows that for both the NDJ and DJF series, forecast skill mainly relies on North Atlantic SST data, essentially corresponding to the horseshoe pattern between May and November. The central Mediterranean basin is also selected for NDJ, although given the

	MLR					GLM				
	r^2	RMSE	FI	HS	ROC	r^2	RMSE	FI	HS	ROC
NDJ	0.12	58.2 (0.95)	0.44	0.51	0.67	0.14	55.5 (0.93)	0.44	0.49	0.64
DJF, Nov 1	0.34	62.1 (0.83)	0.45	0.51	0.68	0.37	57.1 (0.76)	0.46	0.53	0.76
DJF, Dec 1	0.37	60.5 (0.81)	0.46	0.56	0.73	0.41	55 (0.72)	0.47	0.54	0.80
FMA, Jan 1	0.33	52 (0.81)	0.50	0.59	0.71	0.36	51 (0.8)	0.48	0.58	0.74

Table 3.3: Regression (r^2, RMSE in mm) and classification (FI, HS, ROC) skill scores for the three precipitation series at different time leads, for the MLR and GLM models, over the 1950-2015 period. We use a k-folds cross-validation strategy with k=10. The number in brackets in the RMSE column corresponds to the percentage of the standard deviation of the corresponding time series that the forecast RMSE is equal to.

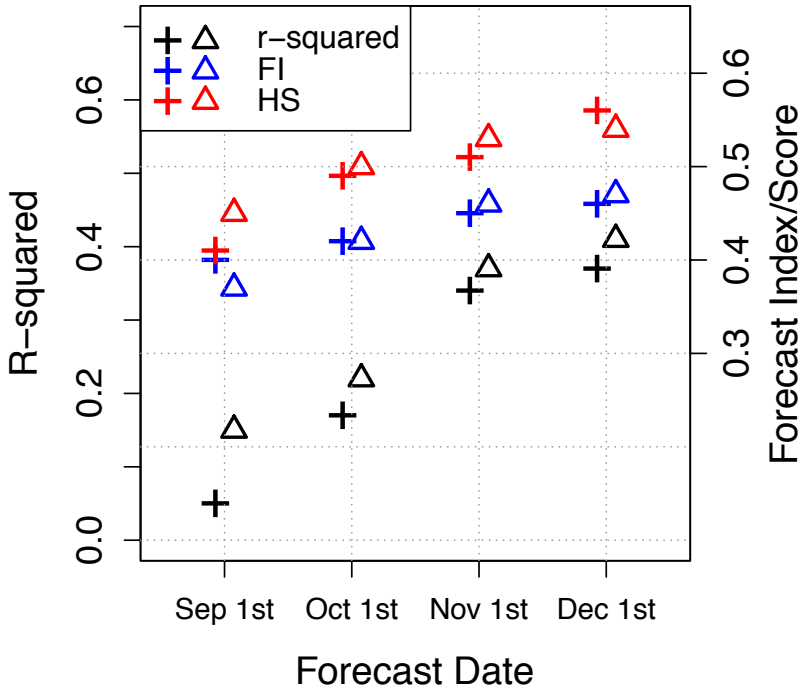

Figure 3-5: Model skill scores for DJF forecasts at various lead times with the GLM (triangle) and MLR (cross) models.

weak predictability of this series, the interpretation is subject to caution. The FMA series, however, is much more strongly connected to the Pacific basin, with much of the skill coming from the three poles of the PDO-like correlation structure. Robust predictors are highlighted in Table 3.2. Generally, most of the optimal predictors were defined with the CCA method. Unlike the other methods, CCA is not performed at the grid point level but takes into account the spatial coherency of the SST fields. This may explain why predictors defined based on CCA result perform better than others.

Skill improvement between the first DJF forecast (issued November 1st) and the second (issued December 1st) is small, though detectable (Tables 3.3 and 3.4). The additional November SST information may reflect the ocean-atmosphere forcing feedback, with November SSTs giving information about the NAO pattern more likely to get established for the winter. In the case of FMA, however, adding January SST information brings no predictability gain, in keeping with our observation that the teleconnection to the Pacific ocean peaked in December.

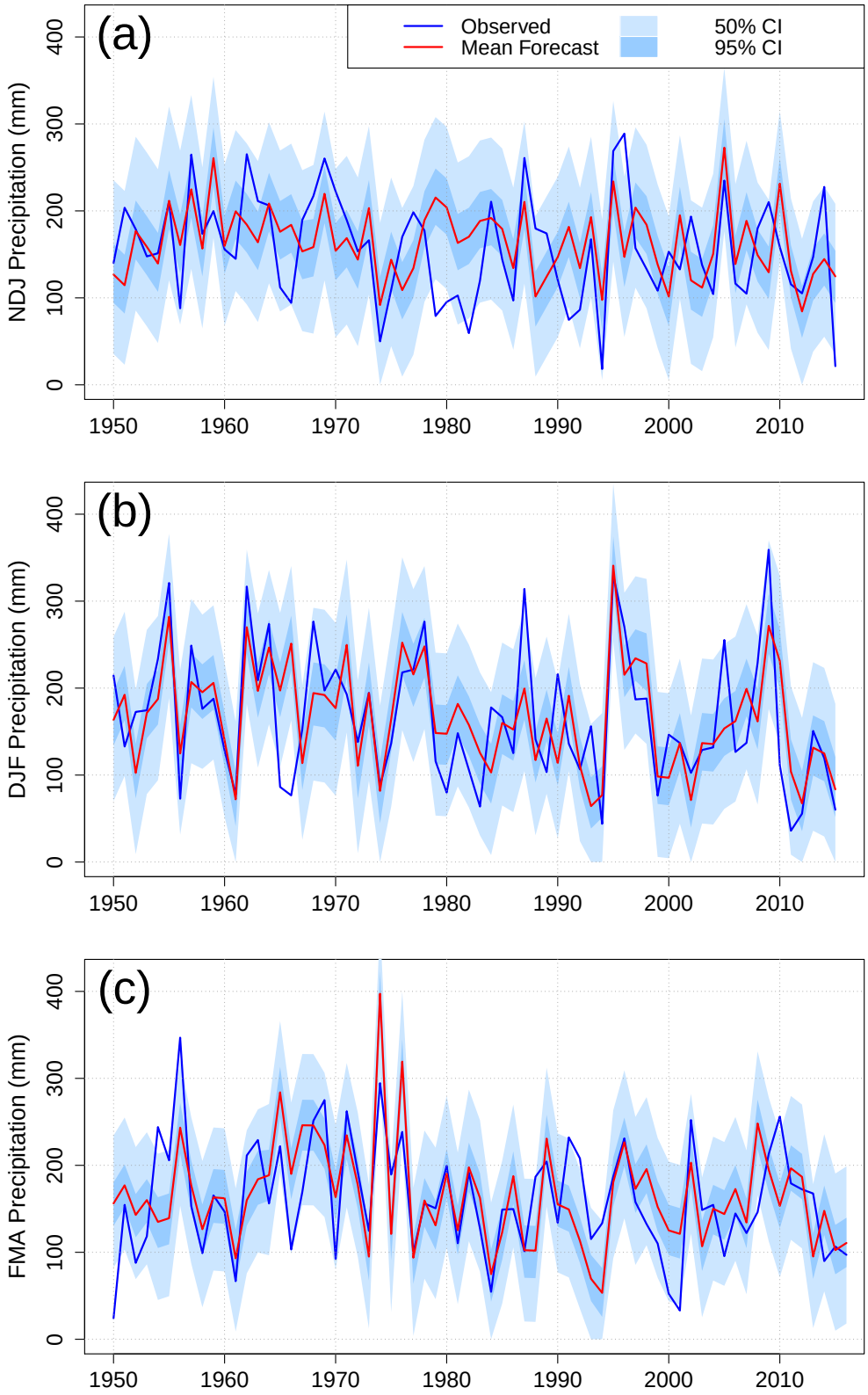

Figure 3-6: Results of GLM precipitation forecasts for (a) NDJ issued on November 1st, (b) DJF issued on December 1st and (c) FMA issued on January 1st. The mean forecast is shown by the red line, observed precipitation by the blue line, alongside 50% (shaded blue) and 95% (shaded light blue) confidence intervals.

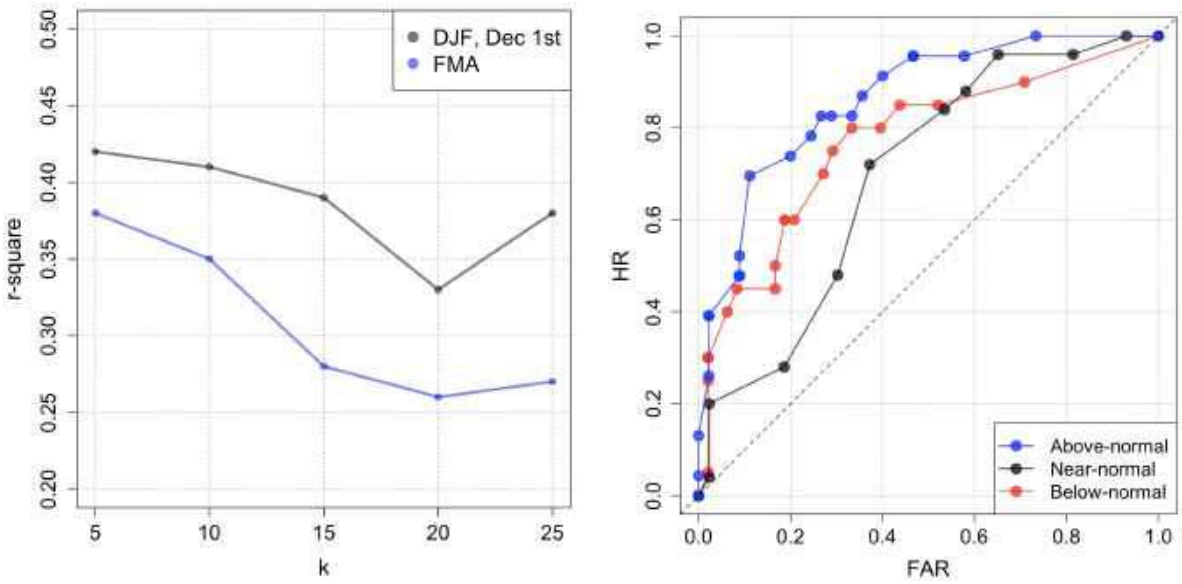

Figure 3-7: *Left*: Coefficient of determination (r^2) from the k-folds cross-validation, for the DJF and FMA forecast models, as a function of k. *Right*: ROC curves computed from the results of the GLM model applied to the DJF series. Curves are shown for all precipitation categories: near-normal (black), above-normal (blue) and below-normal (red).

The impact of the Snow Advance Index (SAI, section 3.3), detailed in Table 3.4, is on the whole positive, although very limited, and higher for NDJ than for DJF, even if the shortness of the record is a cause for caution. There is a decrease in all skill scores except for NDJ compared to the full record, as expected from the fact that we are fitting the models on a shorter time period. The small improvement due to the SAI suggests that the series brings independent additional information. Eurasian snow cover may indeed play a complementary role to SSTs in forcing wintertime atmospheric circulation: whereas SSTs impact the strength and extent of the meridional temperature, the SAI would reflect a land-atmosphere forcing process over Siberia that also influence the state of the winter NAO [46]. In recent years, however, the link between the SAI and NAO has degraded. It is a question whether climate-change induces trends in the snow cover might disrupt this link, a question that requires more analysis and is beyond our scope.

Examination of the ROC score shows that models show on average a good ability to predict droughts, with values of $0.75 - 0.8$ achieved for DJF and FMA. The ROC score can also be computed on each precipitation category taken separately, to estimate how well the model is able to predict it against the other two (see Figure 3-7 (right) for the ROC curves obtained

	GLM Model				
	r^2	RMSE (mm)	FI	HS	ROC
NDJ	0.12	60.2 (1.0)	0.42	0.46	0.58
NDJ+SAI	0.28	56.4 (0.94)	0.43	0.51	0.69
DJF, Nov 1	0.22	70.3 (0.96)	0.39	0.46	0.62
DJF+SAI, Nov 1	0.25	68.1 (0.92)	0.43	0.50	0.67
DJF, Dec 1	0.25	67.6 (0.91)	0.41	0.44	0.65
DJF+SAI, Dec 1	0.27	64.2 (0.86)	0.43	0.51	0.71

Table 3.4: GLM model skill scores for the 1972-2015 period, with and without the inclusion of the SAI index. We use a k-folds cross-validation with $k = 10$. The number in brackets in the RMSE column corresponds to the percentage of the standard deviation of the corresponding time series that the forecast RMSE is equal to.

with the GLM model for the DJF season). The near-normal category systematically has a lower ROC score, which is due to the fact that its probability is much less sensitive to the potential predictability of the underlying phenomenon [145]. A ROC score of about 0.8 for the DJF season corresponds to a potential predictability (r^2) of about 0.4, in keeping with the findings of Kharin and Zwiers [2003] in the case of a Gaussian setting. One must be careful while interpreting those results, though, as the ROC score is relatively independent of forecast calibration. This means that two forecasts of different biases will have equal ROC scores [145]. In consequence, the ROC tends to overestimate the skill that that be achieved in practice.

Real-time forecasts

For additional validation of our approach, we have also made "real-time" forecasts of DJF and FMA precipitation over the last four years, using SST data as soon as it was provided. Results are shown in Table 3.5. Our approach has performed rather well. In 2016-2017, conditions were generally average while the model pointed to a slightly wet DJF and dry FMA. The wet 2017-2018 year was correctly predicted, as well as the dry 2018-2019 season. Dry conditions of the last season (2019-2020), however, were missed for DJF, but correctly forecasted for FMA. Overall, the approach has been able to exclude the correct category in all eight cases excepted DJF 2019-2020.

DJF		1-Sep	1-Oct	1-Nov	1-Dec	Obs Qu.
2016-17	*Dry*	0.566	0.267	0.293	0.236	0.63
	Avg	0.126	0.246	0.272	0.31	
	Wet	0.308	0.487	0.435	0.454	
2017-18	*Dry*	0.395	0.5	0.302	0.221	0.70
	Avg	0.124	0.225	0.264	0.31	
	Wet	0.481	0.275	0.434	0.469	
2018-19	*Dry*	0.73	0.616	0.581	0.548	0.11
	Avg	0.086	0.199	0.229	0.29	
	Wet	0.184	0.185	0.19	0.162	
2019-20	*Dry*	0.09	0.27	0.33	0.35	0.33
	Avg	0.07	0.13	0.22	0.19	
	Wet	0.84	0.6	0.45	0.45	
FMA		**1-Nov**	**1-Dec**	**1-Jan**	**1-Feb**	**Obs Qu.**
2017	*Dry*	0.569	0.584	0.627	0.627	0.56
	Avg	0.239	0.232	0.202	0.202	
	Wet	0.192	0.184	0.171	0.171	
2018	*Dry*	0.098	0.165	0.037	0.037	0.83
	Avg	0.148	0.188	0.081	0.081	
	Wet	0.754	0.647	0.882	0.882	
2019	*Dry*	0.49	0.532	0.708	0.708	0.33
	Avg	0.251	0.261	0.161	0.161	
	Wet	0.259	0.297	0.131	0.131	
2020	*Dry*	0.37	0.41	0.59	0.59	0.28
	Avg	0.2	0.27	0.17	0.17	
	Wet	0.43	0.32	0.24	0.24	

Table 3.5: Results of GLM probabilistic categorical precipitation forecasts for the DJF and FMA seasons of the last four hydrological years (2016-2017 to 2019-2020), at different lead times. The last column on the right shows the observed percentile, and yellow highlighting indicates the observed precipitation category.

3.7 Discussion

3.7.1 Physical mechanisms and forecast skill

Though the models display a good ability to predict precipitation with a limited number of robust predictors, it remains to determine whether those predictors actually represent the underlying physical processes associated with seasonal variability over Morocco. Precipitation in Morocco almost systematically comes from the northwest (see section 2); the determining factor is the direction of the winds [147]. Mechanisms connecting SST patterns and large-scale atmospheric circulation over the North Atlantic have already been discussed in previous studies, whether for the winter NAO [191, 49] or for a fall teleconnection to the Pacific Ocean [228]. North Atlantic SSTs, in particular the horseshoe pattern, have long been believed to force the winter NAO, via direct diabatic heating or transient eddy-mean flow interactions. Peng et al. [2003] suggest that an anomalous flow is associated with heating from sea-surface temperature anomalies, in turn creating an anomalous eddy forcing which drives an anomalous eddy-forced flow. In other words, North Atlantic SST anomalies, especially off of Newfoundland, impact heat release in areas of maximum eddy-growth for the North Atlantic stormtrack [93]. This may weaken baroclinicity and in turn impact the strength and position of the stromtrack, which influences the NAO index.

For DJF, composite precipitation and circulation anomalies, associated with high (above the 67% percentile) and low (below the 33% percentile) values of each robust SST predictor from Figure 3-4, display significant changes in the westerlies around 30°N and 50°N (see Figure 3-8, a-f). Strengthened (respectively weakened) westerlies to the south are linked to weakened (respectively strengthened) westerlies to the north. Precipitation anomaly fields are consistent with this picture, with positive precipitation anomalies linked to strengthened westerlies (and vice-versa). Overall, this signature is very similar to that of the NAO, albeit of smaller magnitude, and the analysis corroborates the relevance of the selected predictors as forcing variables for winter atmospheric circulation.

Regarding teleconnections to FMA precipitation, current knowledge is less specific. Though

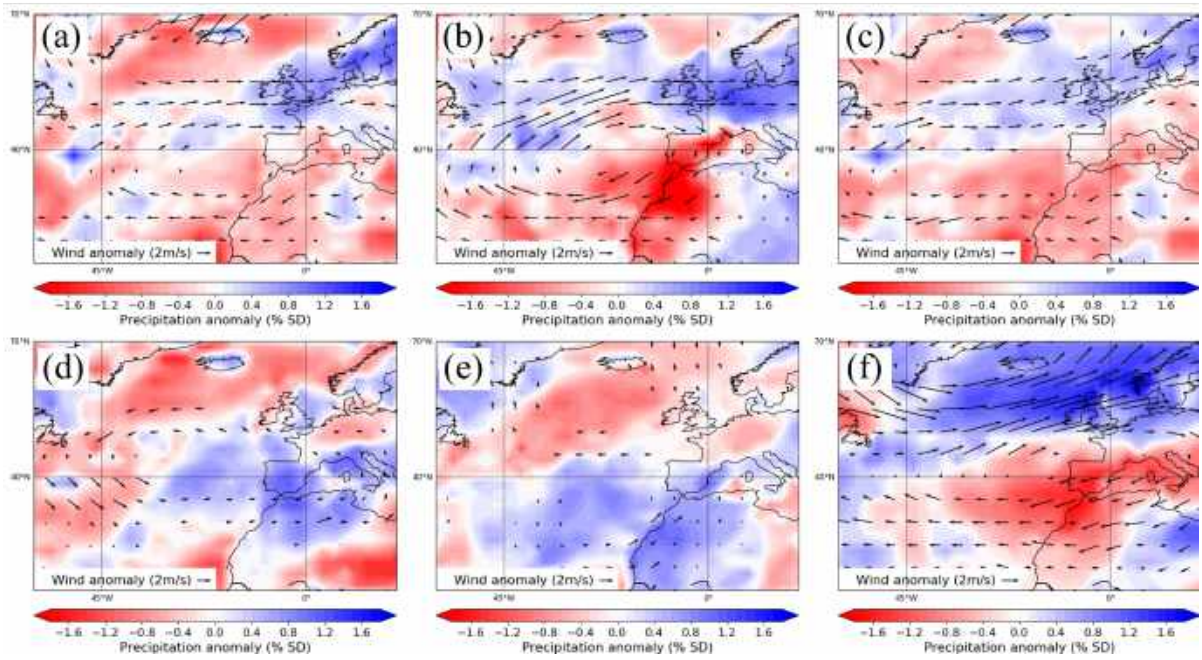

Figure 3-8: Composites of DJF GPCC precipitation (filled contours) and NCEP-NCAR reanalysis 850hPa winds, based on (a-e) the five SST predictors defined on Figure 3-4 (middle row) and on the DJF NAO index (f). Units for precipitation are percent of grid point standard deviation; units for circulation are m/s. Only areas significant at the 90% level are shown, based on a bootstrap estimation of confidence intervals.

a number of studies have identified teleconnections between tropical Pacific SSTs and European precipitation [228], physical explanations remain debated. Positive precipitation anomalies are still linked to strengthened westerly low-level winds, but there is no large dipolar structure over the North Atlantic. Both Park and Leovy (2004) as well as Shaman and Tziperman (2010) suggest that the connection is explained by Rossby wave trains originating from the Pacific, which cause vorticity anomalies over Western Europe and the Mediterranean [189, 228]. Figure 3-9 shows 500hPa vorticity anomalies associated with high/low values of the SST predictands, over the Eastern Pacific and North Atlantic sector. Pacific SST indices are associated with large-scale alternating vorticity anomalies extending from the Pacific to the North Atlantic. A patch of vorticity anomaly consistently appears west of the Iberian Peninsula (its sign depending on the selected SST index), accompanied by a change in westerlies around 40°N that impacts precipitation over the region. The time lag between predictors and predictands here is too long for the teleconnection to be due to direct Rossby wave trains [228]. The link may however arise from the persistence of Pacific SSTs over the course of several months. As

to the single North Atlantic SST predictor (Figure 3-9, f), it comes with a comparable vorticity anomaly field, but limited to the North Atlantic only.)

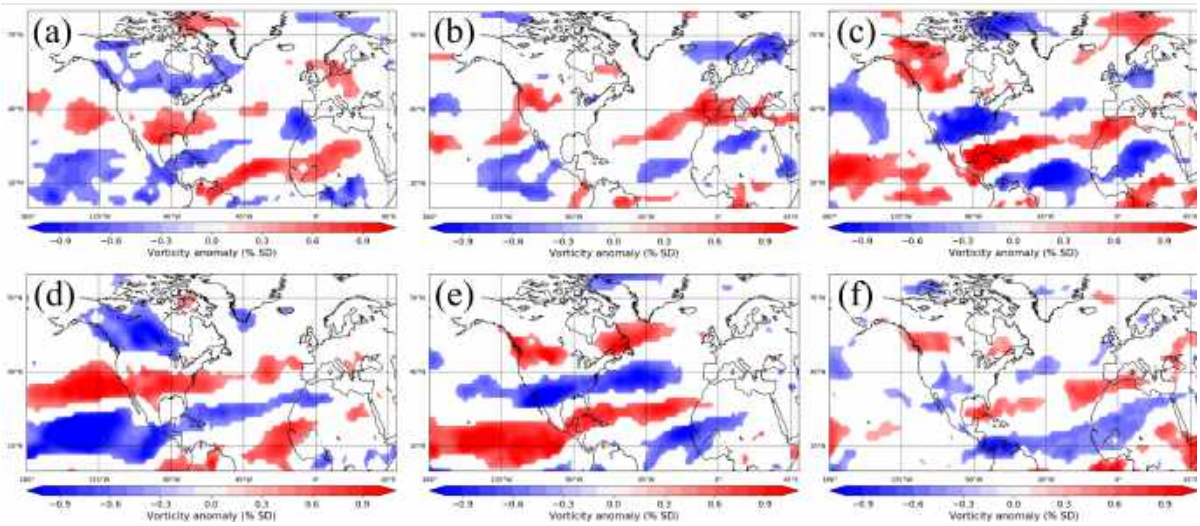

Figure 3-9: Composites of FMA 500 hPa vorticity from the NCEP-NCAR reanalysis, based on the six SST predictors defined on Figure 3-4 (bottom row). Units for vorticity are percent of grid point standard deviation. Only areas significant at the 90% level are shown, based on a bootstrap estimation of confidence intervals.

3.7.2 Some limitations

A criticism that can be made is that the whole record (1950-2015) is used to identify potential predictors, which, in spite of the double cross-validation strategy, possibly introduces artificial skill into the models. However, doing this procedure for every step of the cross-validation is impossible in practice and would probably have yielded similar results. This we checked for several SST-precipitation combinations, and found on the whole little variability, even if only 75% of the record was used (Figure 3-10). Selecting a wide range of potential predictors (see Table 3.2) should help deal with probable non-stationarities in the ocean-atmosphere feedback, and evident decadal scale variability in the relationships involved. The cross-validation process implemented here is also intended to prevent overfitting.

Yet, the main drawbacks of hand-engineered covariates is that they are time consuming and not scalable in practice. We attempted to define predictors based on the whole information contained in each monthly SST field, by decomposing the latter into EOFs and performing an

SVD decomposition on them, along with the precipitation series. This algorithm should select on its own the most relevant SST variables and patterns without any need to define by hand specific predictors. However, this approach turned out to be highly unstable and displayed little skill in practice. This may be due to our trying to predict a single, noisy time series and not a more stable multivariate field, as for instance in Totz et al. [2017], where the authors tried to predict European winter precipitation anomaly maps. But SST EOFs themselves can be rather unstable, even with more than 65 years of data. Principal components and the associated time series may be quite different depending on which portion of the data was used to obtain them – a bias rarely taken into account in most studies relying on EOF time series as predictors. Though these may vary, the spatial reconstructions of CCA coefficients are stable enough to confirm the reality of the statistical links (Figure 3-10).

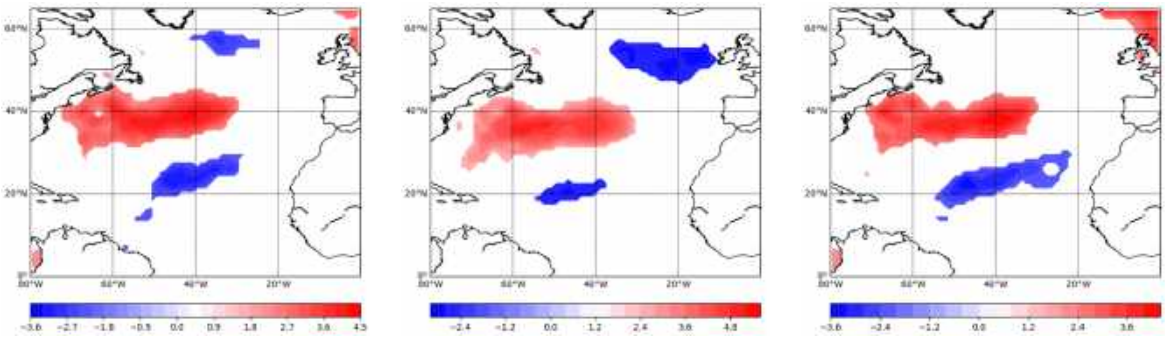

Figure 3-10: Three examples of filtered CCA coefficient maps for May-June-July North Atlantic SST anomalies, computed against DJF precipitation over the Oum-Er-Rbia. Each map was produced by selecting 50 random years in the period of observation, 1950-2015. Even when being rather conservative and keeping 75% of the available data, the obtained maps are very similar and the corresponding identified predictors would not differ much.

Considering a single time series (precipitation over the Oum-Er-Rbia) is indeed one of the limitations of our model. We know that, in winter, this series is strongly anticorrelated to precipitation over Scotland or western Scandinavia, which respond antisymmetrically to the same forcing by the NAO [129]. Thus, looking for predictors that show skill in predicting both of these series at the same time (in a multivariate setting) may bring robustness to the forecasts – by smoothing some of the noise in each of the series – and also help understand how differently, if at all, the northern pole of the NAO is affected by regional circulation. The continent-wide approach taken in Totz et al. [2017] may not yield very precise results for areas

as small as ours, but it can help shed some light on the dominant NAO state to be expected for the winter, an additional piece of information to include in the forecasts.

Finally, although we rely here on linear-based forecast models, the relationship between precipitation and large-scale flow is known to be non-linear [194]. Including a GLM model in this study was motivated by the fact that it allowed for some degree of non-linearity, and a log-link fit did show some improvement for the NAO-precipitation relationship (with the Akaike Information Criterion slightly smaller than that of a linear regression model, $\Delta AIC = 3.7$). It must be noted, however, that there is no physical basis for that choice, only statistical considerations. With such a short reliable record, and lacking advanced predictor selection methods, implementing non-parametric or non-linear forecasting algorithms to represent physical connections better remains a challenge.

3.8 Conclusion

Forecasting seasonal precipitation from NWMs will remain quite challenging for the foreseeable future. However, this study shows that a statistical approach, based on a careful identification and selection of SST predictors, allows for a skillful prediction of the interannual variability of seasonal precipitation. Early-season precipitation is much less predictable, however, even with no lead time. The accuracy suggested by the cross-validation is still higher than what teleconnection signals predicted from the most up-to-date NWMs imply. Despite the short length of the data record, 35–40% of interannual variability can be captured by a small set of robustly selected SST indices. The identified predictors are consistent with results from previous studies [49, 219, 191], and the analysis of composite circulation fields linked to these further supports the validity of the physical connections to precipitation.

While the proposed approach has demonstrated the potential for advance predictability of Moroccan seasonal precipitation, the results presented in this chapter are but the first step towards an operational implementation and use of the forecast algorithms. First, from a physical perspective, the large spatial variability in seasonal precipitation must still be quantified to better estimate the risk of local dry or wet conditions. Second, forecasts on their own are worthless if potential users do not know how to make use of them. Due to the high inter-annual vari-

ability and the general perceived lack in predictability of precipitation, most water-dependent actors (industry, water managers, farmers, etc.) in the region have adopted very conservative approaches to water management, usually assuming the worst (or close to that) to avoid bad surprises. Consequently, decisions tend to be made quite early in the season (typically over the summer, often before June), since there is no need to wait for information. This makes the current decision-making framework quite inflexible, and therefore any operational use of seasonal forecasts will have to begin by re-thinking how and when decisions are made.

Chapter 4

The Mediterranean Climate Change Hotspot

4.1 Introduction

Modifications of regional precipitation patterns will be one of the most critical consequences of climate change. Whereas theory and models all point to a clear increase in temperatures under continued emissions of greenhouse gases, there is much less agreement when it comes to changes in precipitation. Generally, constant or higher precipitation is expected over the world's land regions under climate change, except for a few specific regions where models project robust declines, mostly in the dry subtropics (Fig. 4-1-d). Among these regions, the Mediterranean Basin (10°W-40°E/30-45°N) stands out due to the magnitude and significance of its winter precipitation decline. Locally, up to 40% of winter precipitation could be lost by the end of the 21st century, setting strong limits on water resources that will constrain the ability of the region to develop and grow food, affecting millions of already water-stressed

[1]This chapter is an edited and partial reproduction of Tuel and Eltahir (2020) [252] and Tuel et al. (2020b) [254]. We combined material from the two papers and slightly expanded the discussion in sections 4.5.3 and 4.6.2.

people and threatening the stability of this tense and complex area.

Located at the border between the arid subtropics and the temperate mid-latitudes, the Mediterranean basin is characterized by low annual precipitation totals and high inter-annual variability, which impose a state of semi-permanent water stress across much of North Africa and the Middle East. Summers are warm and dry, dominated to the east by the influence of subtropical remote forcing triggered by the Indian monsoon, which cause intense subsidence across the region [213], and to the west by the subtropical high. In winter, however, the Mediterranean is largely outside the influence of such tropical teleconnections, and storms and rain are brought by mid-latitude westerlies. Consequently, winter precipitation is key to the region's agriculture and economy, with its future of paramount importance for the basin's countries. Regional- and local-scale processes, such as land-sea circulations, also play a significant part in shaping Mediterranean climate variability and climate change [26].

The Mediterranean has long stood out in successive generations of Global Climate Models (GCMs) as being particularly sensitive to rising concentrations of greenhouse gases. Models overwhelmingly project, across all scenarios, a large reduction in precipitation, more than in other land regions in relative terms (Fig. 4-1-b) [101, 59, 195]. A large part of that decline occurs during winter, south of 40°N (Fig. 4-1-d), with enhanced drying over northwest Africa (-30 to -40% in DJF precipitation) and the Eastern Mediterranean (-20 to -25%). In summer, significant warming and drying is also projected for the northern Mediterranean [35]. While the large inter-annual variability in wintertime Mediterranean climate makes the significance of past trends hard to establish [141], precipitation and sea-level pressure in observations and reanalysis products are in general consistent with those in historical simulations and projections for the upcoming century (Fig. 4-2-b). The Mediterranean has experienced substantial drying over the last century, part of which cannot be explained by simple internal variability [118, 141]. In fact, an unprecedented drought in the Eastern Mediterranean exacerbated the already tense situation in Syria which led to the outbreak of a civil war [143]. Further drying will inevitably exacerbate social and geopolitical tensions in this severely water-stressed region.

Changes in the regional low-level circulation have long been suspected to play a dominant role in the winter Mediterranean drying (e.g., [225, 278, 279, 250, 36]), in particular through the development of an anomalous surface anticyclone over the Mediterranean basin [226], a

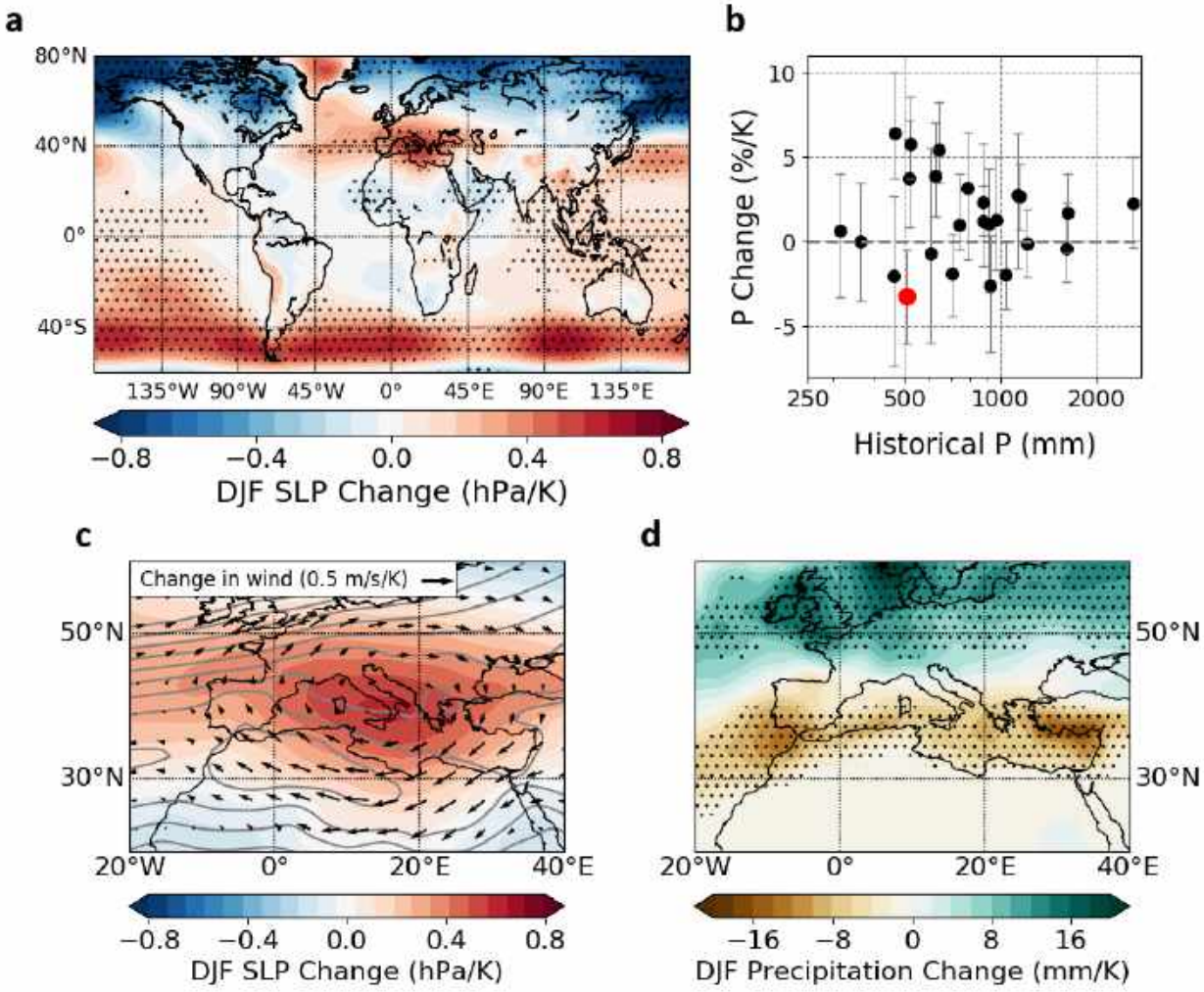

Figure 4-1: CMIP5 winter (DJF) multi-model mean projected change in (a) worldwide sea-level pressure (SLP), (c) Mediterranean SLP and 850 hPa winds, and (d) Mediterranean precipitation under RCP8.5 (2071-2100 minus 1976-2005). Historical DJF SLP contours also shown on (c) (from 1010 to 1024 hPa every 2 hPa; closed contour over North Africa is 1024 hPa). Dots (a,d) indicate that more than 80% of models agree on the sign of the change. (b) Median (black) and 90% inter-model spread (gray) of relative change in annual precipitation in CMIP5 models under RCP8.5 (2071-2100 minus 1976-2005), against annual mean historical (1976-2005) precipitation, for 25 land regions covering the whole globe [100]. The Mediterranean is highlighted in red. In (a-d), projections have been renormalized by each model's global projected temperature change.

striking feature of global climate projections (Fig. 4-1-a,c). This anomalous Mediterranean ridge extends from roughly November to April and has been consistently present in successive generations of models [101]. Its magnitude, and that of the associated wind field, is strongly correlated to the regional precipitation decline across models (Fig. 4-3) [278]. Observed trends

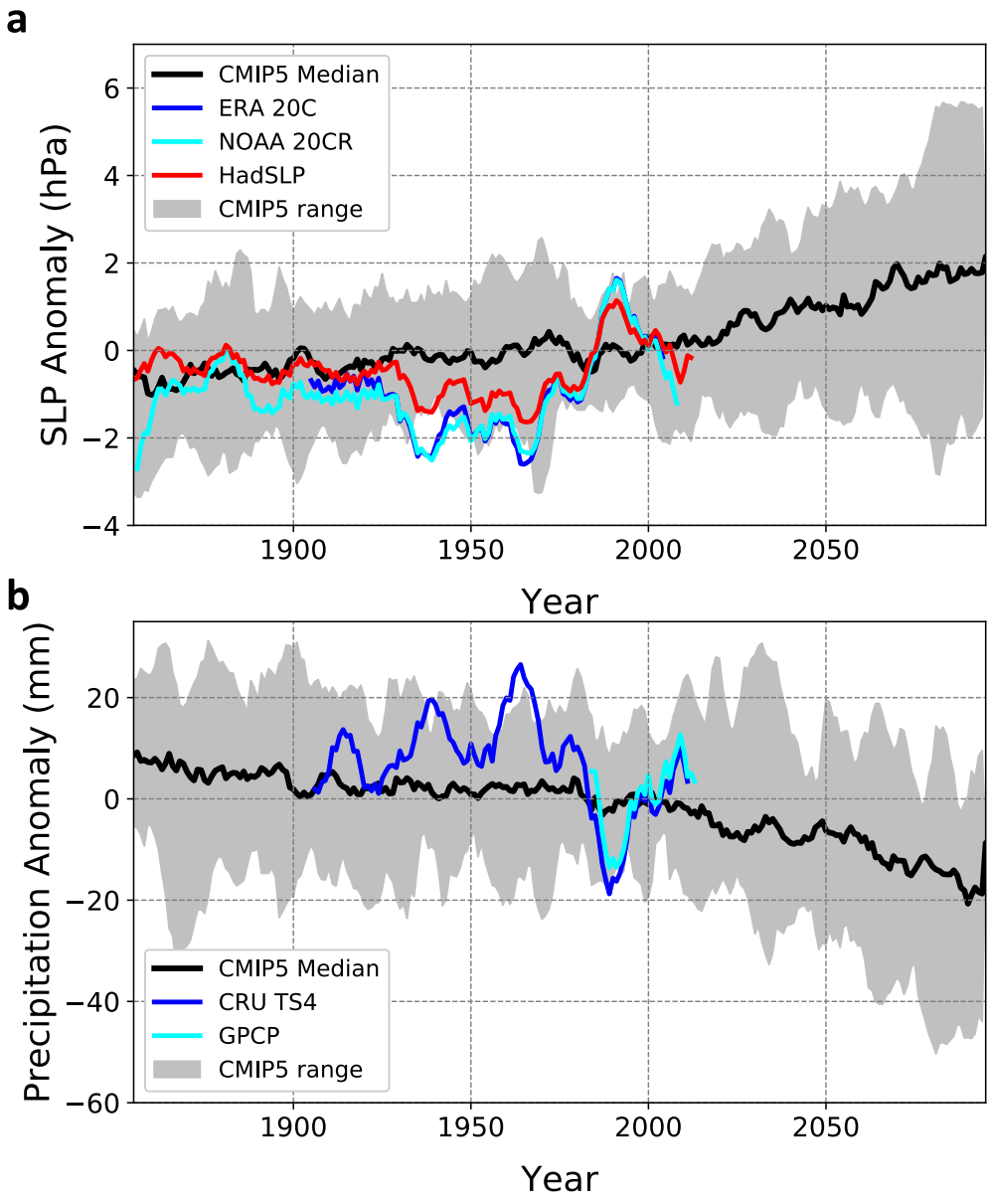

Figure 4-2: 5-year smoothed median (black line) and range (gray shading) of CMIP5 model simulations of DJF Mediterranean (a) sea-level pressure (0-30°E / 32-48°N) and (b) precipitation (20°W-40°E / 30-45°N) anomalies (map on Figure S1), alongside observations/reanalysis data from HadSLP2, NOAA 20CR and ERA-20C (in (a)) and GPCP and CRU TS4 v2 (in (b)).

have up to now been consistent with model projections (Fig. 4-2-a). Giorgi and Lionello (2008) [101] suggested that the anomalous high may drive the projected drying by increasing atmospheric stability in the region and suppressing Mediterranean cyclones, as discussed in later studies (e.g., [215, 277]). Subsequently, based on a three-dimensional analysis of the moisture

budget, Seager et al. (2014) [225] concluded that the Mediterranean precipitation decline was due to increased moisture divergence by the time-mean flow, due to anomalous anticyclonic circulation in the region. Zappa et al. (2015a) [278] additionally showed that the inter-model spread in precipitation change could be well-captured by a simple wind index reflective of the regional circulation, supporting the idea that future Mediterranean hydroclimate trends are primarily driven by changes in the regional atmospheric circulation (Fig. 4-3).

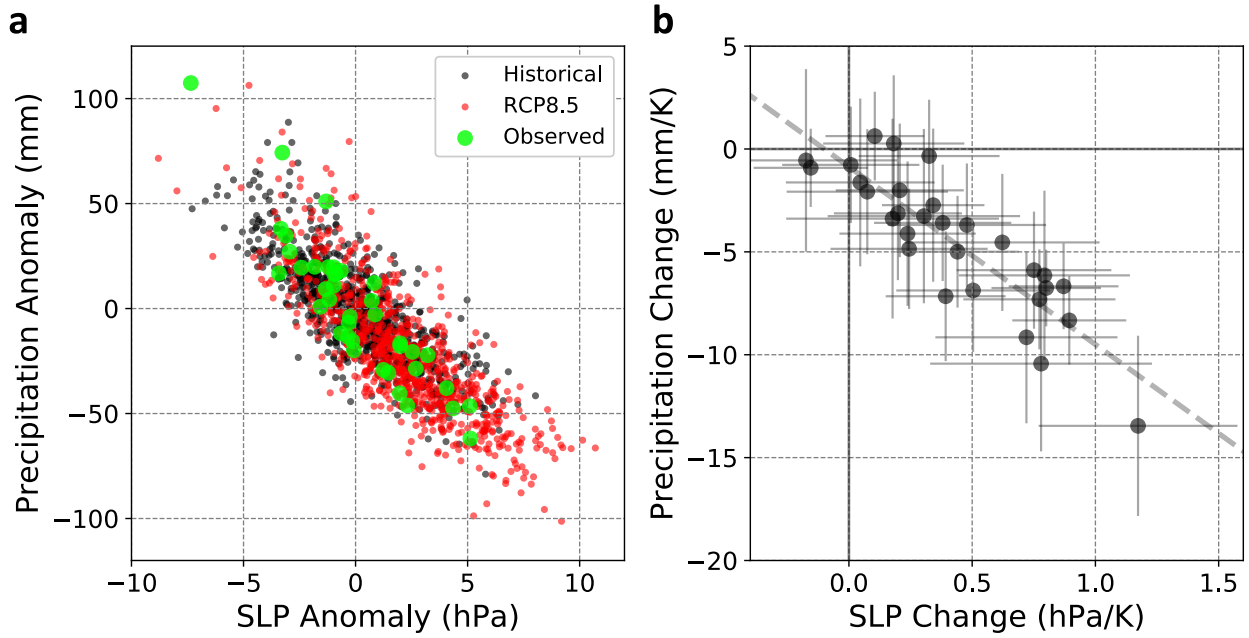

Figure 4-3: (a) DJF Mediterranean (20°W-40°E/30-45°N) precipitation against SLP (0-30°E/32- 48°N) anomalies in historical (1976-2005) and RCP8.5 (2071-2100) CMIP5 simulations, and observations (HadSLP2/GPCP, 1979-2017). (b) Change in DJF Mediterranean precipitation and SLP across CMIP5 models, with 95% confidence intervals and least-squares best fit. Changes are re-scaled by each model's projected global temperature change.

Why the anomalous high pressure develops in the first place, however, and how it connects to the robust pattern of the precipitation response remains unclear. Changes in the large-scale circulation, notably the expansion of the Hadley circulation [160] and the corresponding poleward shift of the North Atlantic storm track [275, 222, 271], the weakening of the Mediterranean storm track and changes in regional flow regimes [277, 215], have previously been suggested as driving mechanisms behind Mediterranean circulation trends. More recently, the role of shifts in Northern Hemisphere stationary waves was shown to modulate precipitation projections over California [231], and suspected to impact the Mediterranean as

well [226]. Tuel and Eltahir (2018) [250] also first suggested that the regional warming contrast between land and sea could play a role. Still, the specific contributions of those mechanisms to projected Mediterranean climate trends and their spread has not been clearly quantified. Additionally, the role of Hadley cell and storm track shifts has been challenged as they were found to occur, in abrupt-CO_2 experiments, on a much faster time scale than the Mediterranean drying (He and Soden 2017). The zonal symmetry in Hadley cell shifts is also at odds with the amplified Mediterranean SLP signal (Fig. 4-1-a), since it is not obvious why the Mediterranean would be particularly sensitive in climate projections.

Therefore, while much attention has been given to this region, a comprehensive theory for the wintertime Mediterranean precipitation decline is still lacking. This chapter seeks to answer the following two questions: what causes the anomalous high pressure over the Mediterranean? and how does regional circulation changes relate to the robust pattern of precipitation decline? We focus essentially on the winter period (December-to-February, DJF), but also discuss how identified mechanisms relate to spring and fall trends. In general, modifications to low-level circulation are governed by two main drivers: changes in the large-scale circulation, like storm tracks or the Hadley circulation, and changes in land-atmosphere interactions (surface energy budget, for instance). We use here results of simulations from the Coupled Model Inter-comparison Project phase 5 (CMIP5) and idealized simulations with the MIT Regional Climate Model to show that both drivers matter for the Mediterranean. Global-scale circulation changes originating near the tropopause, characterized by shifts in stationary waves, and the independent relative cooling of the Mediterranean Sea relative to the surrounding land, are found to greatly contribute to the development of the lower-tropospheric anticyclonic anomaly. Furthermore, we show how that anomaly leads to changes in moisture availability and energy balance in the Western and Eastern Mediterranean, triggering particularly sharp precipitation declines in these regions. Winter and summer trends are contrasted, as well as causes of inter-model spread in projections.

4.2 Data

We analyse recent surface temperature, pressure and precipitation trends in the Mediterranean region using various datasets. Observed surface temperatures are taken from the NOAA MLOST [258] (land and ocean, 1850-2018), and the CRU TS4.02 dataset [108] (land only, 1901-2018). Monthly precipitation over land from CRU TS4.02 is also used, and, for ocean coverage, we consider data from the Global Precipitation Climatology Project version 2.3 [3] as well (1979-2018). Sea-Surface Temperature (SST) data is taken from HadISST [205] and ERSST v5 [124]. SLP from the HadSLP2 dataset (1850-2018) is used [7]; for purposes of comparison, we also look at SLP in the NCEP-NCAR [138], NOAA 20CR [48] and ERA 20c [197] reanalyses. As estimate of the current climate, we consider the ERA-Interim reanalysis [55] over the 1979-2018 period. ERA-Interim is based on an atmospheric model and reanalysis system with a horizontal grid spacing of about 79 km. Here, we perform our calculations with data archived on a regular 1° grid with 17 pressure levels at monthly resolution.

Future climate trends are analysed using thirty Global Climate Models (GCMs) simulations from CMIP5 [241], under the historical and Representative Concentration Pathway 8.5 (RCP8.5) scenarios. We used all CMIP models that provided sea-level pressure (SLP), precipitation, surface temperature, and specific humidity, temperature, winds and pressure-velocity on pressure levels at monthly resolution for our reference (1976-2005) and future (2071-2100) periods. Ten models from the "Atmospheric Model Inter-comparison Project" (AMIP) [94], under the "amip" and "amipFuture" scenarios, are also considered. In "amip", the atmosphere is forced by observed time varying SSTs and sea-ice at present-day atmospheric composition, while a patterned SST anomaly is added in the "amipFuture" runs (sea-ice and CO2 being kept the same). The SST pattern is based on the CMIP3 multimodel-mean SST response to a quadrupling of CO2, where individual CMIP3 model responses are normalised to have a global-mean 4K warming [2]. For runs longer than 30 years, we keep only the last 30 years for analysis; otherwise, all available years are retained. The "amip" runs are used as reference. A detailed list of all selected models can be found in Tables 4.1 and 4.2. For each model, in case more than one ensemble member is available, only the r1i1p1 ensemble member is used.

[2]Details at https://www.earthsystemcog.org/projects/cfmip/cfmip2-cmip5

All model output is regridded to a common 1°x1° grid. Unless specified, all changes under RCP8.5 are defined as the 2071-2100 minus 1976-2005 average, and all anomalies (of SLP, precipitation, etc.) are defined with respect to the 1976-2005 reference period.

Name	**Resolution**	
	Atmosphere	Ocean
ACCESS1-0	144 × 192	300 × 360
ACCESS1-3	144 × 192	300 × 360
BCC-CSM1-1-m	160 × 320	232 × 360
BNU-ESM	64 × 128	–
CanESM2	64 × 128	192 × 256
CCSM4	192 × 288	384 × 320
CESM1-CAM5	192 × 288	384 × 320
CMCC-CESM	48 × 96	149 × 182
CMCC-CM	240 × 480	149 × 182
CMCC-CMS	96 × 192	149 × 182
CNRM-CM5	128 × 256	292 × 362
CSIRO-Mk3-6-0	96 × 192	189 × 192
FGOALS-g2	60 × 128	360 × 196
GFDL-ESM2G	90 × 144	210 × 360
GFDL-ESM2M	90 × 144	200 × 360
GISS-E2-R	90 × 144	144 × 90
GISS-E2-R-CC	90 × 144	144 × 90
HadGEM2-AO	144 × 192	216 × 360
HadGEM2-CC	144 × 192	216 × 360
HadGEM2-ES	144 × 192	216 × 360
INM-CM4	120 × 180	340 × 360
IPSL-CM54-LR	96 × 96	149 × 182
IPSL-CM54-MR	143 × 144	149 × 182
MIROC-ESM	64 × 128	192 × 256
MIROC-ESM-CHEM	64 × 128	192 × 256
MPI-ESM-LR	96 × 192	220 × 256
MPI-ESM-MR	96 × 192	404 × 802
MRI-CGCM3	160 × 320	368 × 360
NorESM1-M	96 × 144	384 × 320
NorESM1-ME	96 × 144	384 × 320

Table 4.1: List of selected CMIP5 models. Resolution is in latitude by longitude.

Name	Resolution	
	Atmosphere	Ocean
CanESM2	64 × 128	192 × 256
CCSM4	192 × 288	384 × 320
CNRM-CM5	128 × 256	292 × 362
HadGEM2-A	144 × 192	216 × 360
IPSL-CM54-LR	96 × 96	149 × 182
IPSL-CM5B-LR	143 × 144	149 × 182
MIROC5	64 × 128	192 × 256
MPI-ESM-LR	96 × 192	220 × 256
MPI-ESM-MR	96 × 192	404 × 802
MRI-CGCM3	160 × 320	368 × 360

Table 4.2: List of selected AMIP models. Resolution is in latitude by longitude.

4.3 Large-scale dynamics and planetary wave shifts

4.3.1 Changes in stationary planetary waves

Wintertime mid-latitude flow in the Northern Hemisphere is strongly modulated by atmospheric stationary waves, which arise from orographic and atmospheric diabatic forcing, land-sea thermal contrasts, as well as transient eddy heat and momentum fluxes [122, 113]. Stationary waves exhibit wavelengths ranging roughly from a few thousand to twenty thousand kilometers, and generate large-scale variations in the atmospheric circulation, leading to large longitudinal asymmetries in the distribution of temperature and precipitation. Global climate models robustly agree on the pattern of change in upper-tropospheric wintertime circulation in the Northern Hemisphere [231, 269], consisting of a strengthened jet stream and alternating cyclonic and anticyclonic circulation anomalies between 20° and 60°N. The magnitude of the projected circulation change for the 2071-2100 period is substantial, reaching up to 30% of historical values. The acceleration of the jet stream follows from the thermal wind balance

response to the increase in the equator-to-pole temperature gradient at upper levels, itself a consequence of enhanced warming in the middle and upper tropical troposphere and less warming in the upper troposphere at higher latitudes [208]. Given that the structure and amplitude of stationary waves is very dependent on the strength of the jet stream, changes in zonal and meridional winds are strongly related. The pattern of change in upper-tropospheric meridional winds can be understood from simple theoretical arguments [231]. Linear theory of barotropic Rossby waves on a zonal-mean zonal flow u_0 away from sources states that the total wavenumber for stationary waves is given by

$$K = \sqrt{k^2 + l^2} = \sqrt{\frac{\beta - \frac{\partial^2 u_0}{\partial y^2}}{u_0}} \tag{4.1}$$

where k and l are the zonal and meridional wavenumber, respectively (e.g., [121]). In the current climate, stationary waves with non-dimensional zonal wavenumbers smaller than 7 are largely prevalent [231]. As u_0 increases, K must decrease. Assuming unchanged l, the zonal wavenumber must also decrease, which leads to an increase in the wave- length of stationary waves. Because the wave sources are mainly tied to the Earth's topography and are therefore largely fixed in space, the change in wavenumber translates into a change in wave phase downstream from sources, where stationary waves extend further eastward in future climate projections (Fig. 4-4-a).

Meridional wind changes are somewhat stronger and more robust over North America than the Mediterranean, yet overall there is a pronounced zonal symmetry in the pattern of upper-tropospheric circulation change (Fig. 4-4-b). A direct consequence of the eastward shift is the development of an anomalous upper-level anticyclonic circulation over the Mediterranean. This anomalous pattern is also expected at lower levels due to the generally equivalent barotropic nature of winter stationary waves [112, 113]. The wave-like pattern is indeed still present at the 850 hPa level, but does not follow a simple dampening of the 300 hPa pattern. The largest circulation changes are now found over the Mediterranean and off the coast of North America, whereas meridional wind anomalies are quite weak over the tropical Atlantic, the Gulf of Mexico or the Arabian Peninsula. While there is clearly an overall equivalent barotropic

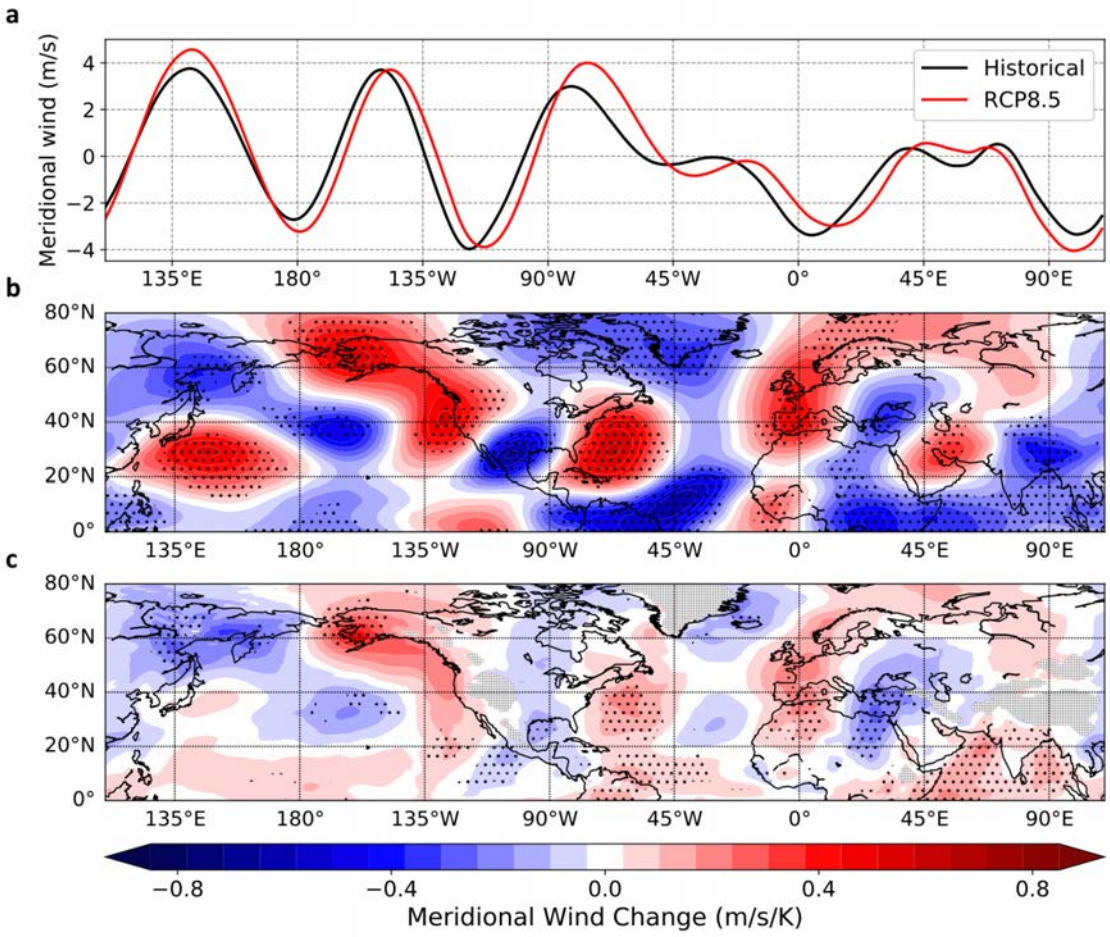

Figure 4-4: (a) CMIP5 multi-model mean 300 hPa meridional winds in the historical and RCP8.5 scenarios, averaged between 20° and 50°N. See Simpson et al., figures 1 and 4 [231]. (b-c) CMIP5 multi-model mean projected change in DJF meridional winds at (b) 300 hPa and (c) 850 hPa. For each model, projections were normalized by its mean annual global temperature change to roughly account for differences in climate sensitivity across models. Dots indicate that more than 80% of models agree on the sign of the change.

structure over the North Atlantic, Pacific and the Mediterranean, the pattern appears more baroclinic over Asia and North America.

Significant longitudinal variations in the vertical structure of Northern hemisphere winter circulation have been documented by Blackmon et al (1979) [21]. They found that over the central and eastern parts of the Atlantic and Pacific oceans, and Western Europe, the vertical mode is highly barotropic with strong vertical coherence. On the other hand, North America and Asia are characterized by a more baroclinic structure with little coherence between low- and upper-level fluctuations. It follows from this observation that lower-tropospheric flow over the large continental masses should be much less sensitive to stationary circulation changes

than over oceans, which is quite consistent with the comparison between 300 and 850 hPa meridional wind changes. To find the physical cause of this empirical finding, we turn to linear theory of mid-latitude dynamics.

4.3.2 The external mode

For atmospheric conditions typically prevailing in the mid-latitudes, there exists a single trapped vertical mode for Rossby waves propagating on a mean westerly zonal flow with vertical shear, referred to as the external mode [112]. Since this mode therefore connects the upper- and lower-tropospheric circulation, differences in the surface response to similar high-level circulation anomalies should be partly related to variability in the external mode itself. A lack of vertical coherence of the stationary circulation could also locally relate to vertically propagating Rossby waves over regions of topography, but here we focus on the structure of the external mode since it should be an important factor over all land regions as well as over ocean.

The vertical structure of the external mode can be calculated by solving the stationary quasi-geostrophic potential vorticity and thermodynamic equations on a beta-plane of infinite zonal extent, linearized about a mean zonal flow $\bar{u}(p)$, between the surface and the 50 hPa level:

$$\frac{\partial q}{\partial t} + \bar{u}\frac{\partial q}{\partial x} + \frac{\partial \psi}{\partial x}\left(\beta - \frac{\partial}{\partial p}\left(\frac{f^2}{\sigma}\frac{\partial \bar{u}}{\partial p}\right)\right) = 0 \tag{4.2}$$

where $q = \Delta\psi + \frac{\partial}{\partial p}\left(\frac{f^2}{\sigma}\frac{\partial \psi}{\partial p}\right)$ is the anomalous quasi-geostrophic potential vorticity, ψ is the anomalous stream function, f is the Coriolis parameter, β is its meridional gradient, $\omega = \frac{Dp}{Dt}$ and $\sigma = -\frac{RT}{p}\frac{d\log(\theta)}{dp}$ is the static stability parameter. At the surface and at 50 hPa, we obtain boundary conditions from the thermodynamic equation

$$\left(\frac{\partial}{\partial t} + \bar{u}\frac{\partial}{\partial x}\right)\frac{\partial \psi}{\partial p} - \frac{\partial \psi}{\partial x}\frac{\partial \bar{u}}{\partial p} = -\frac{\sigma\omega}{f} \tag{4.3}$$

by enforcing $\omega = 0$. Looking for stationary solutions of the form $\psi(x, y, p) = \mathrm{Re}\left[\hat{\psi}(p)e^{i(kx+ly)}\right]$,

equations (4.2-4.3) become

$$\frac{1}{\bar{u}}\left(\bar{u}\Gamma + \beta - \Gamma\bar{u}\right)\hat{\psi} = K^2\hat{\psi} \tag{4.4}$$

where $\Gamma = \frac{\partial}{\partial p}\left(\frac{f^2}{\sigma}\frac{\partial}{\partial p}\right)$ and $K^2 = k^2 + l^2$, and equation 4.3 becomes

$$\bar{u}\frac{d\hat{\psi}}{dp} = \frac{d\bar{u}}{dp}\hat{\psi} \tag{4.5}$$

Equations (4.4-4.5) form an eigenvalue problem with eigenvalue K^2, and the eigenvector associated with the most positive eigenvalue corresponds to the external mode. Solutions to (4.4-4.5) are computed numerically using centered finite differences in pressure. We checked that a single positive mode ($K > 0$) was always found, although setting the lid at a higher level (pressure below 50 hPa) sometimes yields additional spurious modes as discussed in Held et al. (1985) [112]. We normalize the external mode by its value at 300 hPa which is usually close to the level where it reaches its maximum amplitude.

The external mode is conventionally computed at a given latitude from zonal- and time-mean wind and temperature data [112]. Here, however, we are particularly interested in the variability of the external mode with longitude, and as noted in the introduction to Held et al. (1985) it is possible to define a zonally localized external mode if the time-mean flow is sufficiently slowly varying in longitude. Therefore, we calculate the DJF external mode along the 40°N latitude circle, for ERA-Interim data and each CMIP5/AMIP model in the two corresponding scenarios, by averaging atmospheric data between 35°N and 45°N and then taking a running mean over 60-degree longitude intervals. We choose a 60-degree width as a compromise between a width large enough to correctly represent the mean state across the stationary wave length that dominates the climate-change response (waves with non-dimensional zonal wavenumber 5 account for most of the projected 300 hPa meridional wind change [231], Fig. 4-4) and a width small enough to capture zonal variability in the mean state. Subsurface values are discarded based on each model's mean surface pressure; for each 60-degree interval, the surface level used in (4.4) is chosen as the highest pressure level with at least 50% of valid data. We refer to the zonally-varying external mode as $\hat{\psi}(p, \lambda)$ where λ is longitude. For

comparison, we also calculate the external mode using zonally-averaged fields, and refer to it as $\hat{\psi}_0(p)$.

The external mode allows us to estimate the near-surface component of the stationary wave response using only as input the flow response in the upper troposphere. We compute estimates of the 850 hPa meridional wind change at 40°N (35-45°N average) in the RCP8.5 (for CMIP) and "amipFuture" (for AMIP) scenarios by multiplying, at each longitude, the mean 300 hPa meridional wind by the external mode component at 850 hPa, and taking the difference between the two scenarios. So, for CMIP models, this corresponds to:

$$\Delta v^{850}_{\text{est}}(\lambda) = \hat{\psi}^{850}_{\text{RCP8.5}}(\lambda) v^{300}_{\text{RCP8.5}}(\lambda) - \hat{\psi}^{850}_{\text{hist}}(\lambda) v^{300}_{\text{hist}}(\lambda) \tag{4.6}$$

where historical values are averaged over the 1976-2005 period and RCP8.5 values over the 2071-2100 period. Using only the historical external mode leads to local differences of less than 5%, and therefore differences in external mode amplitudes between scenarios is of minor importance in our problem.

4.3.3 Results

Zonal variability of the external mode is shown on Fig. 4-5-a. Consistent with the findings of Blackmon et al. (1979), the structure of the external mode exhibits a substantial zonal variability. Eastern ocean basins and western continental margins are characterized by much stronger vertical coherence, with larger amplitudes in the lower troposphere, than continents. In particular, the external mode amplitude at 850 hPa is maximal over the Western Mediterranean (≈ 0.43 when averaged over 10°W-0° in ERA-Interim). Over western North America (125°W-115°E), that amplitude is only 0.32.

The variations with longitude in Fig. 4-5-a essentially reflect the variability in the vertical structure of the zonal wind profile. Indeed, estimates of the vertical mode based on zonal-mean static stability values show little difference with the values in Fig. 4-5-a. The external mode tends to have similar vertical structure as the mean zonal wind [113], and thus the ex-

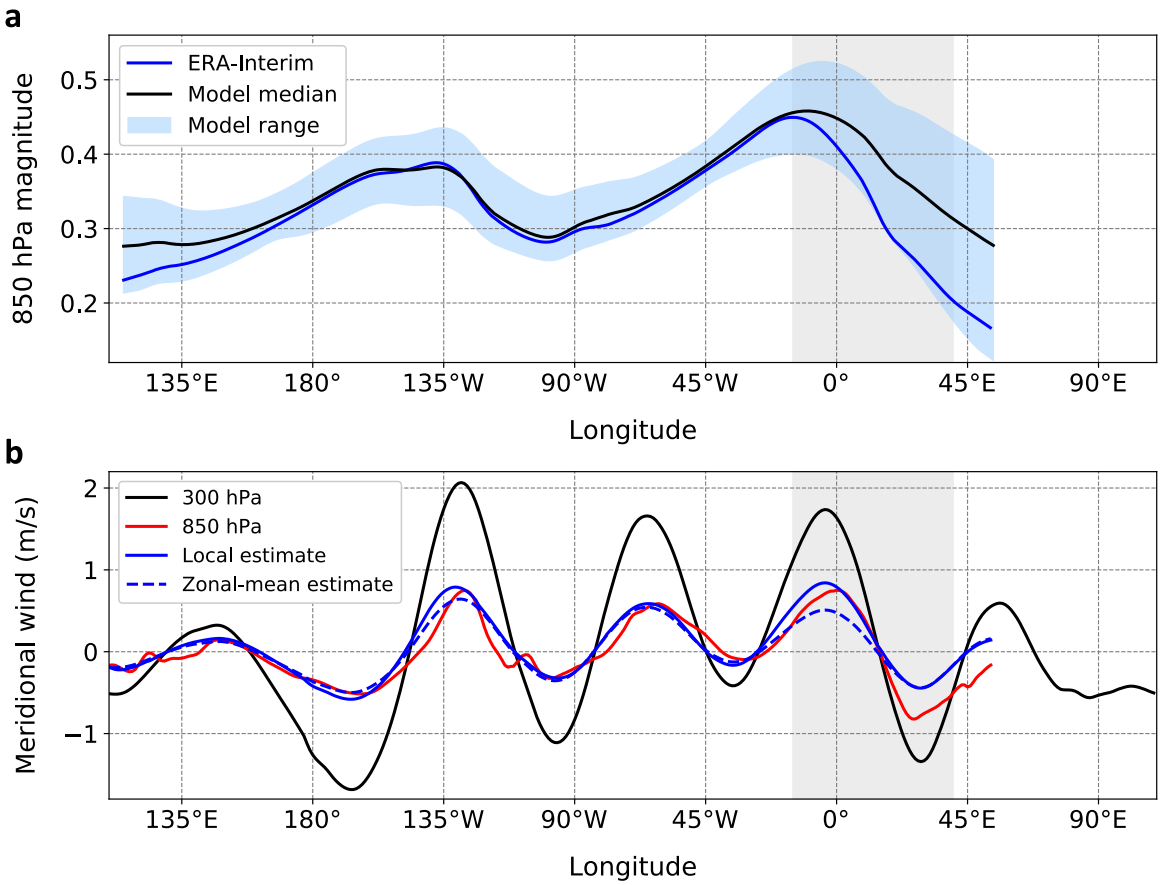

Figure 4-5: (a) Value of the DJF external mode at 850hPa and 40°N as a function of longitude (normalized by its 300 hPa value): CMIP5 median (black), 95% range (light blue shading) and ERA-Interim (blue). The external mode is normalized so that it is equal to 1 at 300hPa. (b) CMIP5 multi-model mean DJF meridional wind change (35-45°N average) at 300 hPa (black), 850 hPa (red), the estimate based on the external mode structure (solid blue) and the estimate based on the zonal-mean external mode (dashed blue). In both panels, the Mediterranean region (15°W-40°E) is highlighted in light gray.

ternal mode is more barotropic the smaller the vertical shear of the mean zonal wind. This vertical shear is strongest on the western side of ocean basins and adjacent land in the storm track entrance regions (corresponding to a weak external mode at 850hPa) and weakest on the eastern side of ocean basins and adjacent land (corresponding to a strong external mode at 850hPa). Differences in friction between land and ocean can also affect the vertical structure of the mean zonal wind and thus the zonal variability of the external mode. In particular, the Mediterranean has relatively weak wind shear and a strong external mode at 850hPa since in winter it lies to the east of the North Atlantic jet and to the north of the subtropical jet over Africa (see e.g. Fig. 1b of Harnik et al. (2014) [107]). In the Pacific storm track, between

135°E and 135°W, large 300 hPa winds and weak near-surface winds generate strong shear, resulting in a smaller 850hPa external mode magnitude compared to the North Atlantic.

It is interesting to notice from Fig. 4-5-a, however, that although the external mode amplitude is generally well-reproduced in models, across the 40°N latitude circle, the single area of significant discrepancy is the Central and Eastern Mediterranean, up to the beginning of the Central Asian mountain chains (10-55°E). There, models almost systematically overestimate the low-level external mode amplitude, on average by 40%. This suggests that, even if the upper-level circulation change projected by models is realized, the regional surface circulation response will be weaker than in model projections. In addition, inter-model scatter in external mode magnitude in this region is much larger than elsewhere, which may point to differences in the resolution of orography and in the effect of orography on the large-scale flow. The overestimation of the external mode component over the Eastern Mediterranean seems related to a large underestimation of zonal wind shear by GCMs over northern Africa and the Middle East, along the northern border of the North Africa jet (Fig. 4-6). Weaker shear is consistent with an overestimation of external mode magnitude at low levels, although biases in mean 300 hPa zonal wind may also matter (see equation (4.4)).

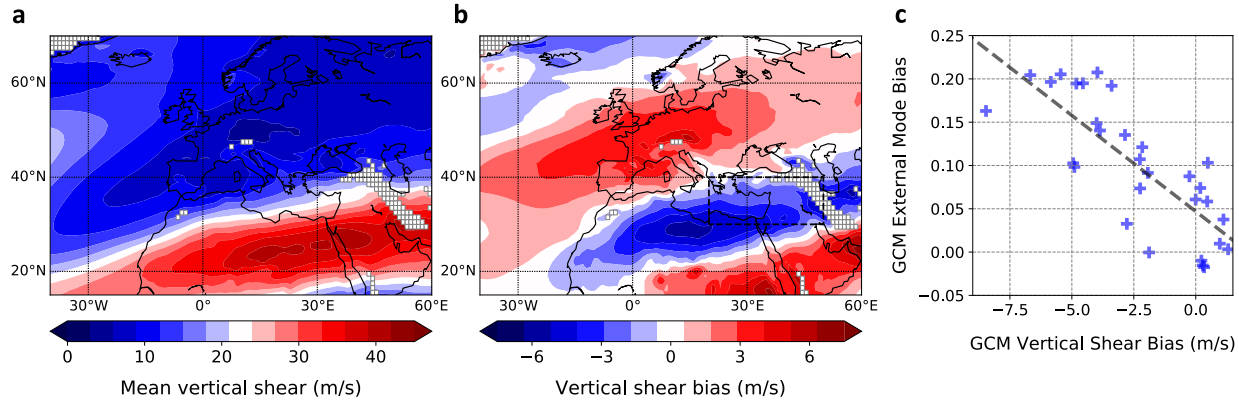

Figure 4-6: (a) DJF Mediterranean mean vertical wind shear, from ERA-Interim. (b) CMIP5 multimodel-mean bias in DJF Mediterranean vertical wind shear. (c) Bias in vertical wind shear over the southeastern Mediterranean region (20-50°E/30-40°N, see rectangle in (b)) against bias in Eastern Mediterranean (16-46°E) external mode magnitude at 40°N across CMIP5 models. The best-fit linear regression line is shown in dashed black. In (a-c), vertical wind shear is defined as 300 hPa minus 850 hPa zonal wind.

This zonal variability has important implications for the low-level response. Fig. 4-5-b shows the two estimates of the 850 hPa meridional wind change, using either the zonally-

varying or the constant external mode, averaged across all models. Generally, the two estimates are very consistent with the 300 hPa model response. The magnitude of the 850 hPa change is correctly captured, even with the zonal-mean external mode, except over the Mediterranean. In the Western Mediterranean, the peak in 850 hPa external mode amplitude coincides with a peak in 300 hPa meridional wind change, so that it is necessary to use the local external mode value to account for the full magnitude of the 850 hPa wind change. The Western Mediterranean is the only region where this coincidence occurs – near all the other peaks in the 300 hPa series, the local external mode value is close to its zonal average, so that the two estimates do not differ significantly. In the Eastern Mediterranean, both estimates account for only half or so of the observed wind change in models (the difference is, on average, 0.3 m/s). In addition to the multi-model mean, inter-model spread is also well explained by this approach. Fig. 4-7 shows the values of the local external mode-based estimate of 850 hPa wind change against those given by models. We consider both the average and the maximum change. There is excellent agreement in both cases, although for models falling at the extremes the external-mode based estimate tends to underestimate the wind response, particularly in the Eastern Mediterranean (see the next section). The larger changes found in the AMIP simulations are also well accounted for by this method, *i.e.* they mainly result from larger circulation changes in the upper-troposphere in AMIP simulations. Differences in external mode magnitude across models are found to play no role in the spread of 850 hPa meridional wind projections, which is almost exclusively dictated by the scatter in upper-tropospheric trends.

This analysis can be repeated on a monthly basis to assess the role of large-scale stationary wave shifts on near-surface Mediterranean dynamics. Figure 4-8 shows results obtained when calculating the external mode for each month of the year and estimating the 850 hPa meridional wind change based on that external mode and 300 hPa meridional wind trends. The connection between near-surface and upper-tropospheric changes peaks in January, at the same time as stationary wave activity in the Northern Hemisphere [113, 269]. Significant correlations are found between October and April, which suggest that our argument applies to dynamical Mediterranean trends both in the second half of fall and the first half of spring, when GCMs still project anticyclonic anomalies over the Mediterranean.

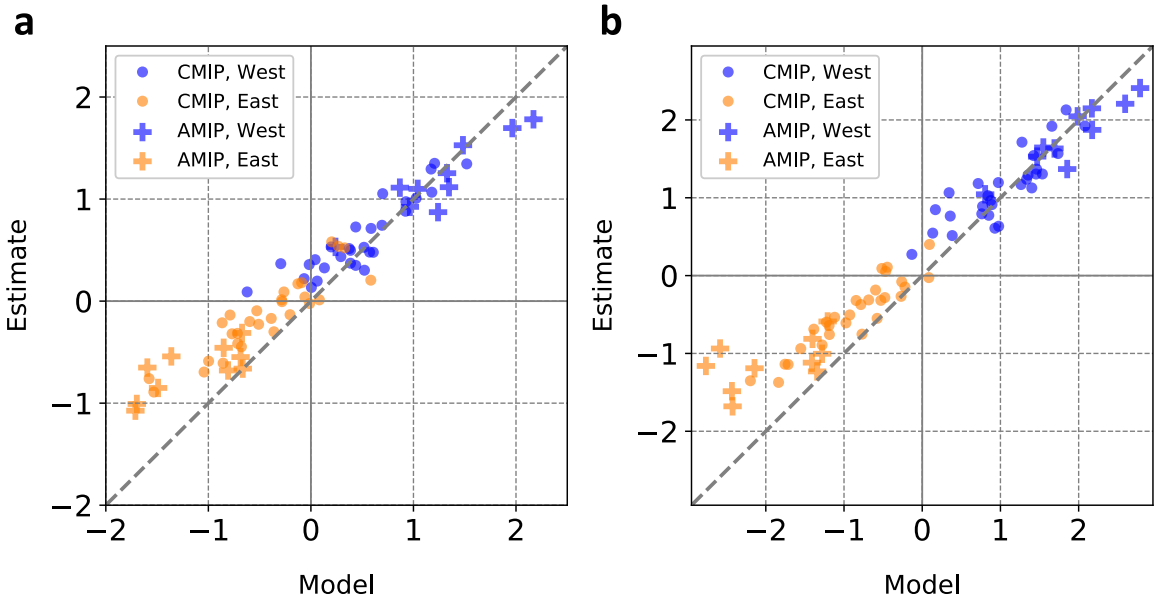

Figure 4-7: 850 hPa meridional wind change (35-45°N average) in the Western (15°W-15°E, blue) and Eastern (16-46°E, orange) Mediterranean in CMIP5 (circles) and AMIP (crosses) models. The changes estimated through the external mode (equation 4.6) are plotted versus the changes in the models. Panel (a) shows wind values averaged over the respective intervals, while (b) shows the maximum values in those intervals.

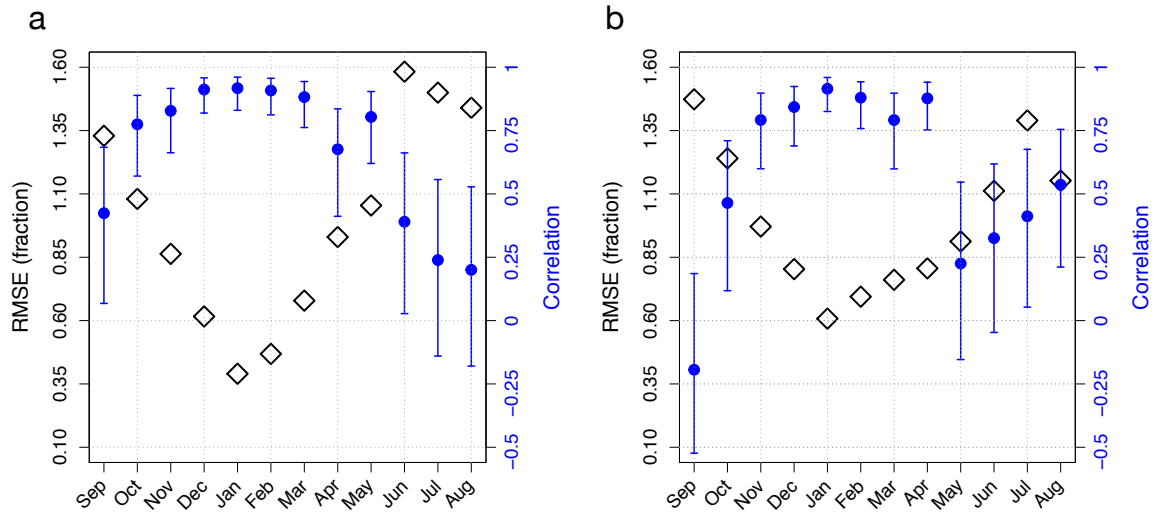

Figure 4-8: Annual cycle of monthly inter-model correlation (blue) and root mean-square error (black) between CMIP5 850 hPa meridional wind change and the external-mode based estimate, for (a) the Western (15°W-15°E) and (b) the Eastern (16-46°E) Mediterranean. Blue whiskers indicate 95% confidence intervals for the correlation coefficients.

4.4 Quantifying the SLP response to upper-level circulation change

The upper-level anticyclonic anomaly over the Mediterranean that results from robust shifts in the winter stationary circulation therefore translates into an anticyclonic anomaly at low levels, and therefore higher pressure. Quantifying the SLP anomaly associated with the projected low-level ridge is not straightforward, in particular because SLP is also determined by surface friction, whose parametrization differs between GCMs. One possibility would be to remain at low levels (850 hPa), away from the surface, and estimate the geopotential gradient needed to balance geostrophically the projected anomalous wind field. Here, we take a different approach, purely empirical, based on identifying circulation analogues and reconstructing associated SLP fields. This method allows us to infer SLP directly, for any GCM, without the need to consider resolution, topography or friction. We show that, consistent with the theoretical results discussed above, the projected shift in upper-level circulation over the coming decades (Fig. 4-4) does lead to an enhanced SLP response over the Mediterranean compared to regions at the same latitude, but fails to explain the full magnitude of GCM projections under RCP8.5.

4.4.1 Methods

To quantify the impact of trends in upper-tropospheric flow on Mediterranean low-level circulation, we apply to each selected GCM an analogue-based "dynamical adjustment" model. We give here a brief overview of the method presented in Deser et al. (2016) [58] and refer to their paper for further mathematical details. We consider two physical fields, a predictor field $\mathbf{X} \in \mathbb{R}^p$, and a predictand field $\mathbf{Y} \in \mathbb{R}^q$, linked by some physical relationship (variability in $\mathbf{X}$ influences variability in $\mathbf{Y}$). p, q refer to the space dimension. We assume that a "training" series of concurrent values of $\mathbf{X}$ and $\mathbf{Y}$, of length n, is available, which we note $(\mathbf{X}_i)_{0\leq i\leq n}$ and $(\mathbf{Y}_i)_{0\leq i\leq n}$. The goal of dynamical adjustment is to estimate the amplitude of the field $\mathbf{Y}_t$ associated with the predictor field $\mathbf{X}_t$, observed at a time $t > n$. To that end, we select the $N = 50$ closest analogues of field $\mathbf{X}_t$ among the $(\mathbf{X}_i)_{0\leq i\leq n}$, with Euclidean distance used as the metric. Among these N fields, we randomly select a subsample of $M = 30$ fields, which

are assembled in a $p \times M$ matrix $\mathbf{X}_c$. The corresponding $\mathbf{Y}$ values are similarly put in matrix $\mathbf{Y}_c$. Then, optimal linear combination weights β are estimated such that

$$\mathbf{X}_t \approx \beta \mathbf{X}_c \tag{4.7}$$

$\beta \mathbf{X}_c$ represents a "constructed analogue" of $\mathbf{X}_t$. Finally, the same weights β are applied to $\mathbf{Y}_c$ to estimate the component of $\mathbf{Y}_t$ induced by predictor $\mathbf{X}_t$: $\hat{\mathbf{Y}}_t = \beta \mathbf{Y}_c$. The procedure is then repeated 1000 times, each time with a new random subsample of 30 analogues. The purpose of this subsampling is to increase robustness of the results and better quantify the variability in the reconstructed estimates [58]. The results are not particularly sensitive to the specific choice of N and M, over the range $30 \leq N \leq 60$ and $M \approx \frac{2N}{3}$.

The method is applied to each GCM separately, using for $\mathbf{X}$ the DJF meridional wind field anomalies at 200 hPa in the 20-80°N latitude range, and for $\mathbf{Y}$ the Northern Hemisphere DJF SLP anomaly field. Seasonal anomalies are computed by subtracting from each field its 1976-2005 mean. The historical (1850-2005) simulations are used as "training" series (thus n=155 winters), and we calculate constructed analogues for all winters between 2070 and 2100. Our choice of predictor is motivated by the results of Simpson et al. (2016) [231], which implied that projected upper-level meridional wind anomalies were reflective of the shifts in mean stationary wave structure. Results are not significantly different when using the zonal wind component, or even the stream function, since upper-tropospheric flow is essentially non-divergent at seasonal timescales.

An important assumption of this approach is that, at first order at least, the surface circulation response to upper-level wind pattern change is linear. To test that hypothesis, we also reconstruct annual SLP anomalies in the historical runs: for each of the 155 winters in 1850-2005, the other 154 winters are used to look for analogues. This helps determine whether inter-annual variability of Mediterranean SLP is correctly reconstructed in both historical and future simulations.

4.4.2 Results

Most of the year-to-year variability in DJF Mediterranean SLP is well reconstructed based on upper-tropospheric flow anomalies, in both historical and RCP8.5 runs (Fig. 4-10-c). The model-mean squared correlation coefficient is about 0.75 for each scenario (model range is 0.55-0.85), and the average root mean square error is 1.2 hPa (model range 0.95-1.5 hPa). SLP anomalies are correctly approximated over the whole range of inter-annual variability; only very low SLP values seems to be slightly overestimated. Over the Northern hemisphere, we find that SLP reconstructions from upper-tropospheric circulation are valid only over the ocean basins, and particularly on their western margins, consistent with the difference in wind shear between the eastern and western margins mentioned above. Despite the mean shift towards positive Mediterranean SLP anomalies in future projections, the range of values of RCP8.5 anomalies is not substantially different from historical ones. This increases our confidence that the method will correctly capture shifts in the distribution of SLP anomalies connected to projected changes in upper-level wind fields.

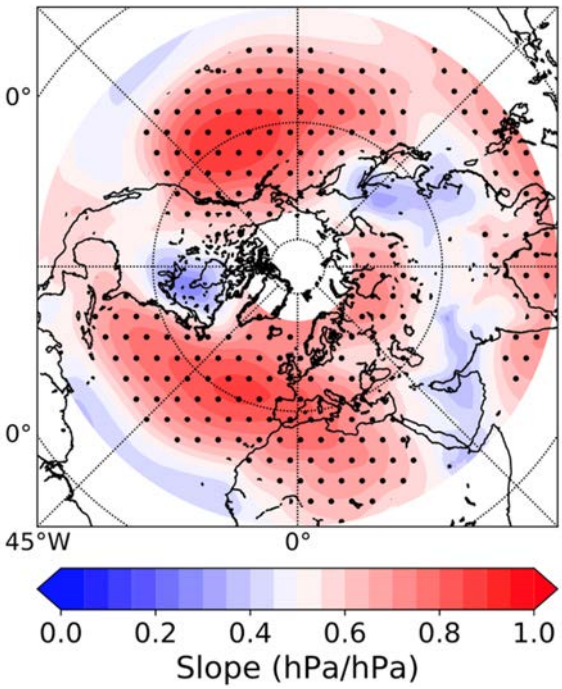

Figure 4-9: CMIP5 multi-model mean best fit linear slope of target-vs-reconstructed DJF SLP. Dots indicate 1% sifnificsance of the corresponding correlation coefficient.

Looking ahead, we find that future upper-tropospheric wind patterns are consistent with an amplified SLP response over the Mediterranean, and also east of Japan (Fig. 4-10-a,b). They also account for 80% of inter-model spread in Mediterranean projections (Fig. 4-10-d), in keeping with the external mode analysis which highlighted upper-tropospheric trends as the major contributor to uncertainties in low-level circulation projections. The decrease in

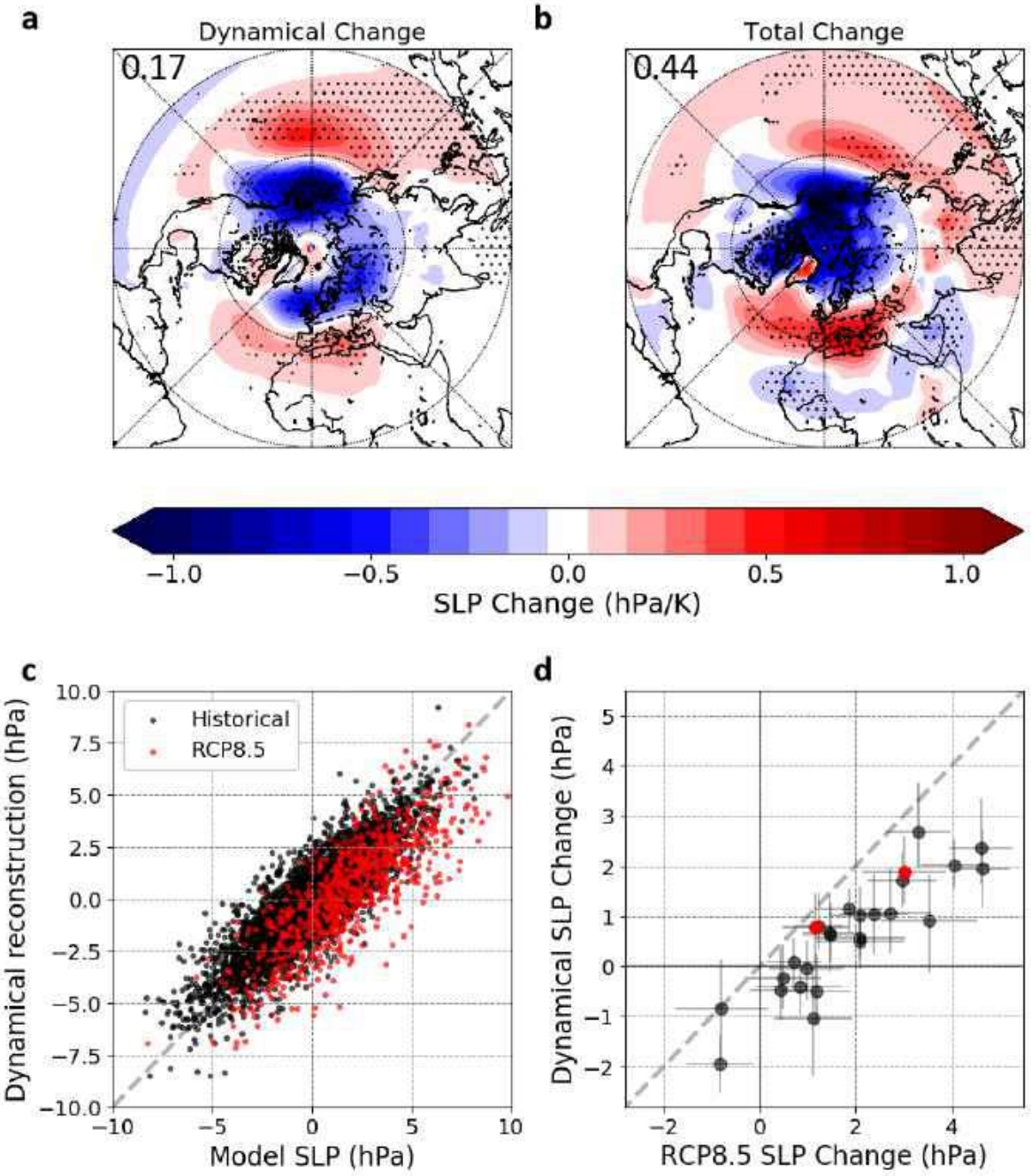

Figure 4-10: Northern Hemisphere CMIP5 multi-model mean change in DJF SLP (a) estimated by dynamical adjustment, and (b) projected by CMIP5 models. Stippling shows agreement on the sign of the change by 80% of models. Numbers indicate average value within the box (dashed). (c) Model vs. dynamically-reconstructed DJF Mediterranean (0-30°E/32-48°N) SLP anomalies in historical (black) and RCP8.5 (red) simulations, for all 30 CMIP5 models. (d) Mediterranean (0-30°E/32-48°N) CMIP5 inter-model change in DJF SLP estimated by the dynamical adjustment model along with 90% confidence intervals. The two models used in Brogli et al. (2019) are highlighted in red (see also section 4.7.3).

SLP over the North Pacific is also approximated, but not so much over North America, the North Atlantic and Siberia, where other factors, notably linked to thermodynamic forcing (e.g., Arctic amplification, North Atlantic Warming Hole) likely play a role [95]. However, only 40% of the mean GCM response is accounted for (0.7 hPa compared to 1.7 hPa in the multi-model mean). Similarly, during the "extended" winter season, outside of DJF, future upper-tropospheric circulation anomalies are still connected to an increase in SLP over the Mediterranean, but only explain about 30-40% of the whole signal.

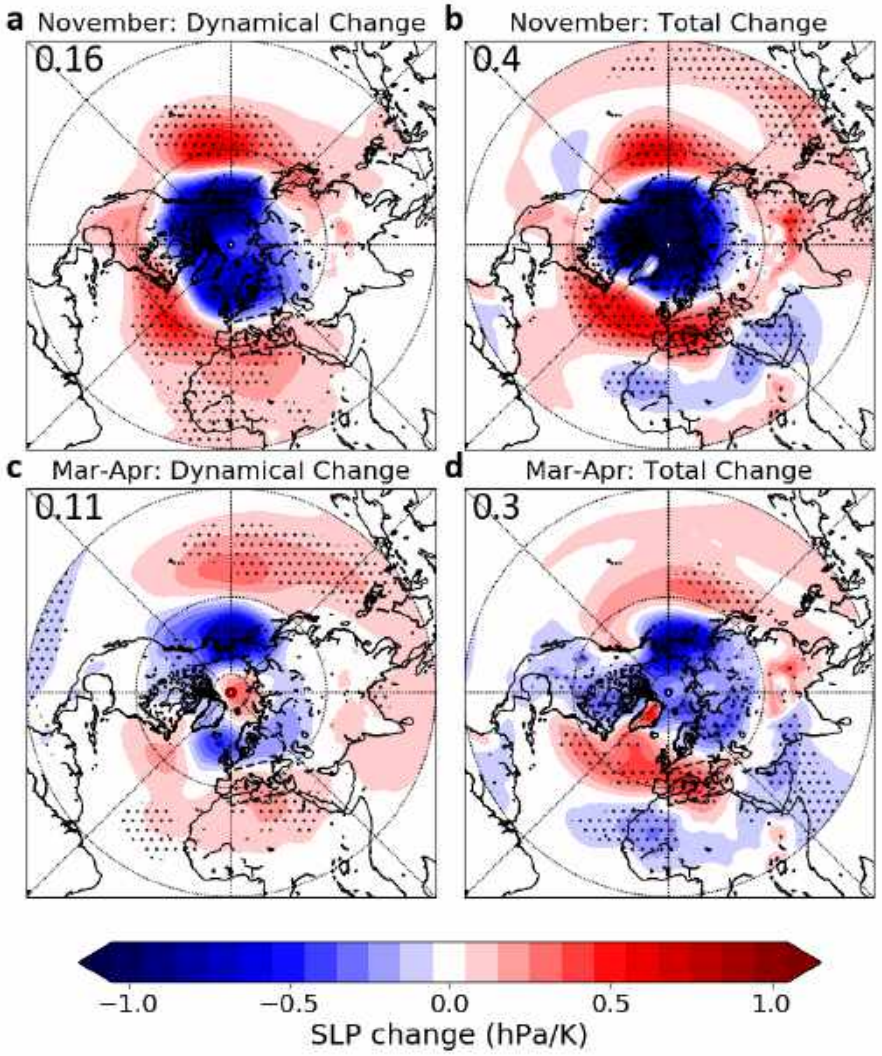

Figure 4-11: Northern Hemisphere CMIP5 multi-model mean change in (a,b) November and (c,d) March-April SLP (a,c) estimated by dynamical adjustment, and (b,d) projected by CMIP5 models. Stippling shows agreement on the sign of the change by 80% of models. Numbers indicate average value within the box (dashed).

4.5 Surface thermodynamical forcing

Trends in the large-scale circulation therefore do not seem to fully account for projected 21st century low-level dynamical trends over the Mediterranean. We now turn to the surface and investigate whether changes in surface-atmosphere interaction terms may explain the rest. The geography of the Mediterranean Basin is quite unique, characterized by the existence of a large sea enclosed by continents on almost all sides. During winter, due to water's larger thermal capacity, the Mediterranean Sea is on average warmer than the surrounding land. However, due to enhanced warming over land under climate change [239, 39], future climate projections exhibit a robust and gradual relative cooling of the Mediterranean Sea with respect to surrounding land (Fig. 4-12-a). We define a simple sea-land temperature difference index as the difference between mean DJF temperatures over sea and over land in the Mediterranean region (5°W-38°E/28°-48°N, Fig. 4-12-a). In historical CMIP5 simulations and ERA-Interim, that difference reaches about 5°C; by 2100, RCP8.5 simulations project a 0.5°C decrease, with little spread across models (Fig. 4-12-b). Th magnitude of the projected index change is similar to its historical inter-annual standard deviation, suggesting a potentially important role of sea-land temperature change in shaping future regional circulation. Up to now, the projected decrease has been consistent with a range of observational datasets (Fig. 4-12-c).
The impact of surface SST anomalies on regional circulations has been investigated, both from a theoretical perspective [122] and in model projections for the coming century (e.g., [95]). At leading order, using geostrophic balance, a shallow relative cooling over the Mediterranean should result in anomalous surface anticyclonic circulation, since the land-sea warming contrast disappears in the mid-troposphere [38]. Linear theory similarly suggests a baroclinic response to a Mediterranean negative SST anomaly characterised by a downstream SLP high [122]. A similar result has been obtained while investigating the atmospheric response to the relative cooling of the North Atlantic Warming Hole in a realistic model [95].

4.5.1 Model simulations

We investigate the impact of the land-sea warming contrast on Mediterranean circulation using regional climate simulations with the Massachusetts Institute of Technology (MIT) Re-

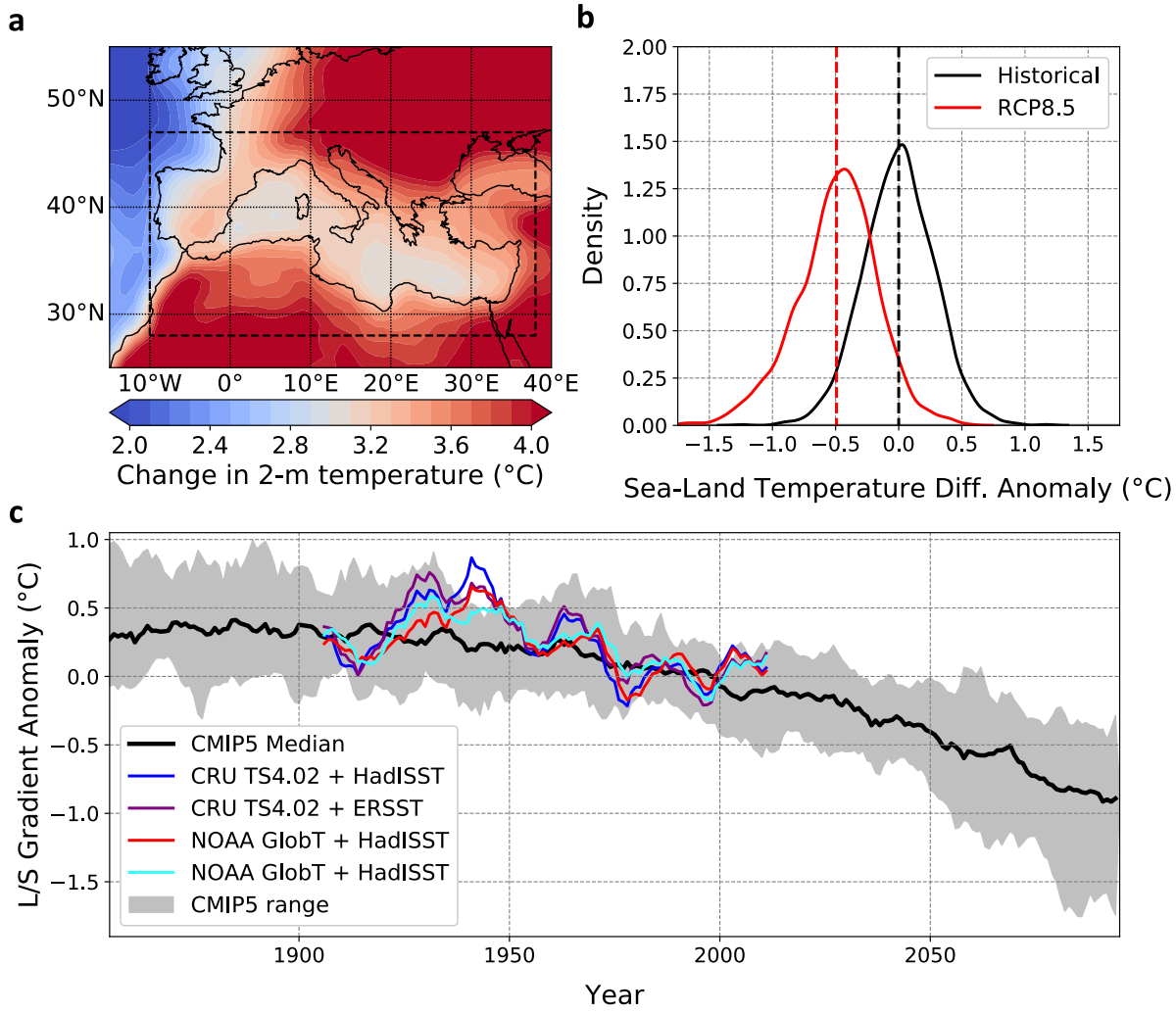

Figure 4-12: (a) CMIP5 multi-model DJF 2-meter temperature change under RCP8.5 (2071-2100 minus 1976-2100). The box encompasses the area used to calculate the sea-land temperature index. (b) Distribution of historical (black) and RCP8.5 (red) DJF sea-land temperature index anomalies across CMIP5 models. (c) 5-year smoothed median value (black line) and range (gray shading) of CMIP5 model annual values (1850-2095) of DJF sea-land temperature index anomalies, alongside observations from CRU, NOAA Global Surface Temperature, ERSST and HadISST. In panel (c) only, the temperature index is defined using SST over the sea, not 2-meter temperature, since the latter has limited availability over sea areas in observations.

gional Climate Model (MRCM). MRCM is based on the Abdus Salam International Centre for Theoretical Physics Regional Climate Model Version 3 (RegCM3) [187], and includes several improvements [270, 98, 96, 97] achieved through incorporation of new physical schemes or modification of original schemes. MRCM has been rigorously tested against observations, in its ability to simulate key observed climate features, across several regions (e.g., North America

[270], West Africa [131], the Maritime Continent [130] and Southwest Asia [186]).
We conduct two sets of simulations to assess the impact of the Mediterranean relative cooling over a domain that encompasses the whole Mediterranean and Black seas (Fig. 4-14), at a horizontal resolution of 35 km and using 40 vertical levels. The first set is driven by the 1.5°x1.5° 6-hourly ERA-Interim reanalysis [55] as lateral boundary conditions and 1°x1° weekly NOAA OISST v2 [206] for the ocean surface, over the 1981-2011 period. In the second, we use the MPI-ESM-MR model [276] under the RCP8.5 scenario as boundary conditions, over the 2070-2100 period. The MPI experiments are intended to assess the impact of a relative Mediterranean cooling in a climate change context as surrounding continents warm. Still, any GCM presents a number of biases in its background climate, which may modulate the impact of the relative cooling. The ERA experiments thus allow us to assess the circulation impact of a relative cooling in the current Mediterranean climate, with no land warming.

Each set consists of a reference simulation ("0C") and a perturbed simulation ("+1.5C"), in which Mediterranean SSTs are artificially increased by 1.5°C. The essence of the "+1.5C" simulations is to force the Mediterranean to warm as much as if it were land. We choose an SST difference of 1.5°C because it translates in the simulations into a 0.5-0.6°C change in the sea-land temperature index, consistent with the shift projected by CMIP5 models (Fig. 4-12 and Fig. 4-13). The difference between the reference and the perturbed simulations ("0C" minus "+1.5C") corresponds to the impact of the relative Mediterranean cooling on regional circulation. The first set of simulations is referred to as "ERA" ("ERA0C" and "ERA+1.5C"), and the second as "MPI" ("MPI0C" and "MPI+1.5C"). In all simulations, the first year is discarded as spin-up. Long-term averages are computed over 1982-2011 for ERA and 2071-2100 for MPI experiments.

4.5.2 Results

Compared to the +1.5C experiments, the 0C experiments exhibit a roughly 0.6°C relative cooling of the sea-land temperature index (0.62°C for ERA and 0.57°C for MPI, Fig. S4). The magnitude and spatial pattern of this relative cooling is similar to that projected by CMIP5 models (Fig. 4-14). Fig. 4-16 shows the difference, between the two experiments (0C minus +1.5C), in mean DJF SLP, 850 hPa wind and precipitation fields over our simulation domain. Compared to +1.5C, the 0C simulations exhibit a substantial anticyclonic flow in the boundary layer with a strong anomalous ridge generally located downstream of the SST anomaly. Both anticyclonic anomalies are accompanied by anomalous easterlies and north-easterlies over North Africa and the Middle East, of about 0.5 m/s magnitude, and a much weaker circulation response to the north. The pattern of the wind response south of 40°N is similar to that of the CMIP5 multi-model mean under RCP8.5, especially for the ERA experiments, even if of smaller magnitude (see Fig. 4-1-c, noting that wind change is normalized by global temperature change, i.e. divided by a factor of ≈4). The relative Mediterranean cooling is also associated with a pronounced regional precipitation decline (Fig. 4-16-b,d). In absolute terms, this decline is strongest over the eastern half of the basin, particularly along the Turkish and Middle Eastern coastline. Precipitation is less impacted west of 10°E, except along the Algerian coastline.

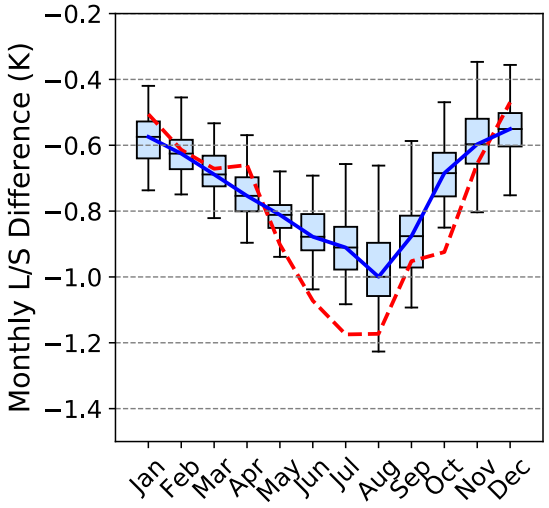

Figure 4-13: Annual cycles of sea-land temperature index difference between "0C" and "+1.5C" experiments, for ERA and MPI experiments combines. Boxes represent the 50% inter-annual range, and whiskers the full range of inter-annual variability. "Sea" and "land" values are defined by the box on Figure 4-12-a. The corresponding cycle for the CMIP5 multi-model mean is shown by the dashed red line.

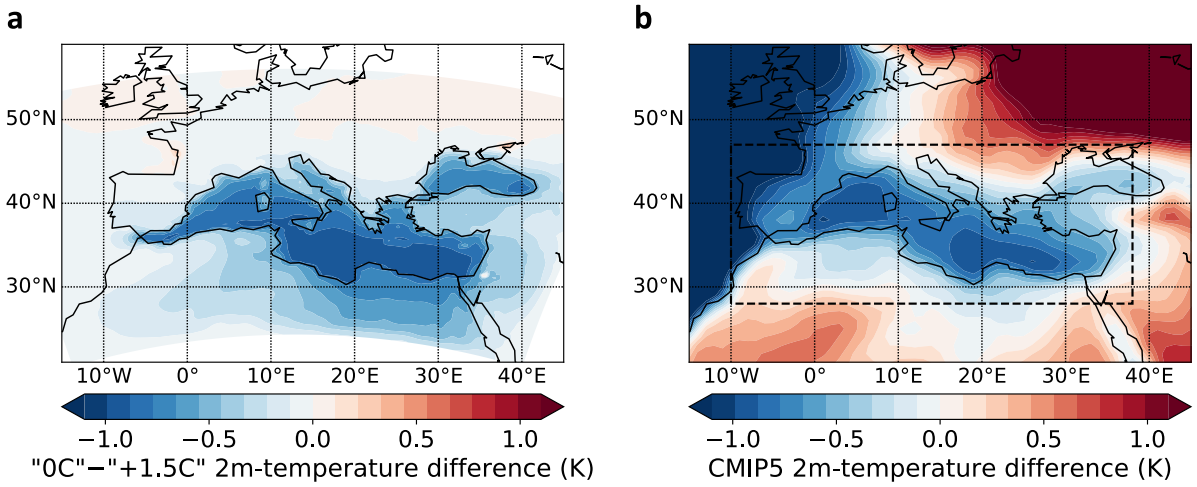

Figure 4-14: (a) Difference in DJF mean 2-meter temperature between the "0C" and "+1.5C" experiments (average of ERA and MPI simulations). (b) Change in DJF 2-meter temperature under RCP8.5 (2071-2100 minus 1976-2005), to which the average Mediterranean land warming (3.9K) was subtracted to highlight the relative cooling over the sea.

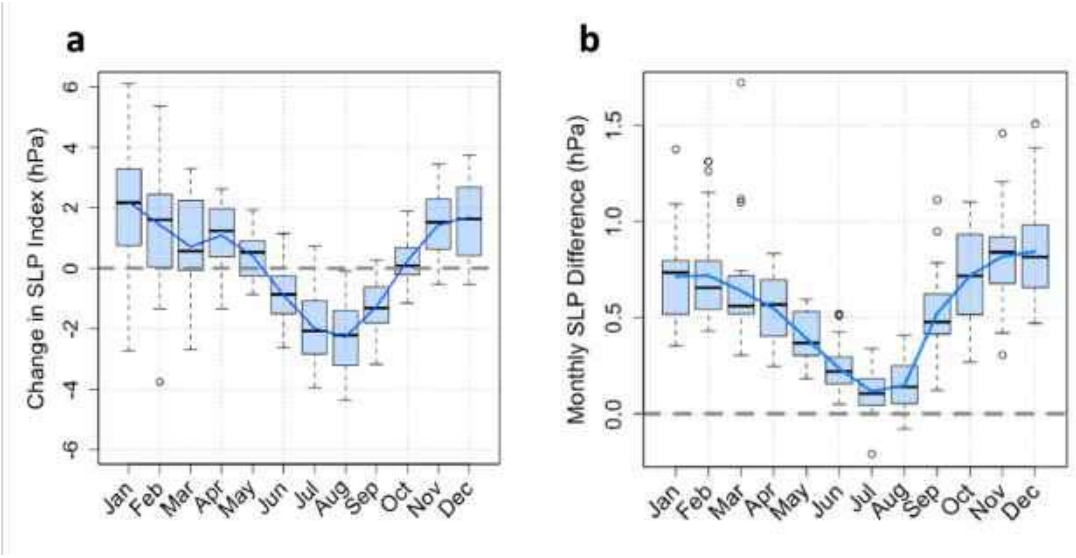

Figure 4-15: (a) Annual cycle of monthly Mediterranean (0-30°E/32-48°N) SLP change under RCP8.5 (2071-2100 minus 1976-2005) across CMIP5 models. (b) Annual cycle of monthly difference in Mediterranean SLP between the "0C" and "+1.5C" experiments ("0C" minus "+1.5C"), ERA and MPI combined. In both panels, boxes represent the 50% range and whiskers extend to the full range of values, across all GCMs (in (a)) and all simulation years (in (b)). Median values are shown by thick blue lines.

The main difference between the ERA and MPI simulations is the location of the anomalous high. It is centered south of Greece and peaks at about 1.1 hPa in ERA, whereas it is slightly weaker (≈1 hPa) and shifted south-east in the MPI experiment (Fig. 4-16-a,c). Averaging

over the 0-30°E / 32-48°N domain, we find a 0.76 hPa SLP difference between ERA0C and ERA+1.5C, and 0.62 hPa between MPI0C and MPI+1.5C. Additionally, the baroclinicity of the response is much more pronounced in the MPI simulations. However, the background climates in the two reference (0C) simulations are different, notably the low-level zonal wind and static stability (Fig. S5). Those two fields are critical in determining the atmospheric circulation response to shallow heating anomalies in the mid-latitudes [122, 106]. The MPI reference state displays a slightly larger static stability over the Mediterranean and a stronger zonal wind field, both of which are consistent with a weaker circulation response to the imposed surface temperature anomaly in the MPI experiments. A larger static stability limits the expansion of the heating anomaly in the lower troposphere, while the enhanced zonal wind reduces the circulation response required to compensate for the heating anomaly [122]. Furthermore, the MPI simulations also include long-term, circulation trends induced by greenhouse gas forcing. Despite this, the circulation and precipitation responses to the relative cooling are very similar between ERA and MPI. This points towards a robust anticyclonic circulation response triggered by the relative Mediterranean cooling.

4.5.3 Contrasting winter and summer

Reduced rates of warming over oceans are a year-round feature in future simulations [39]. Therefore, the Mediterranean relative SST cooling occurs in all seasons and not only winter. However, GCM projections for summer clearly show a robust decrease rather than an increase in Mediterranean SLP [101] (Fig. 4-15). Our regional simulations also clearly show that, although the relative SST cooling is applied year-round, the dynamical response is concentrated between October and April, with a negligible SLP signal in summer (Figs. 4-15,4-17). This raises the question of why the winter circulation might be more sensitive to surface thermodynamic forcing than the summer one.

Fig. 4-17 shows the mean SLP and 850 hPa wind difference between the perturbed ("+1.5C") and the reference ("0C") simulations (which represents the impact of the relative sea cooling) for winter (DJF) and summer (JJA), averaged for the two sets of simulations (ERA and MPI). First, the winter circulation response to relative SST cooling is evidently much larger than

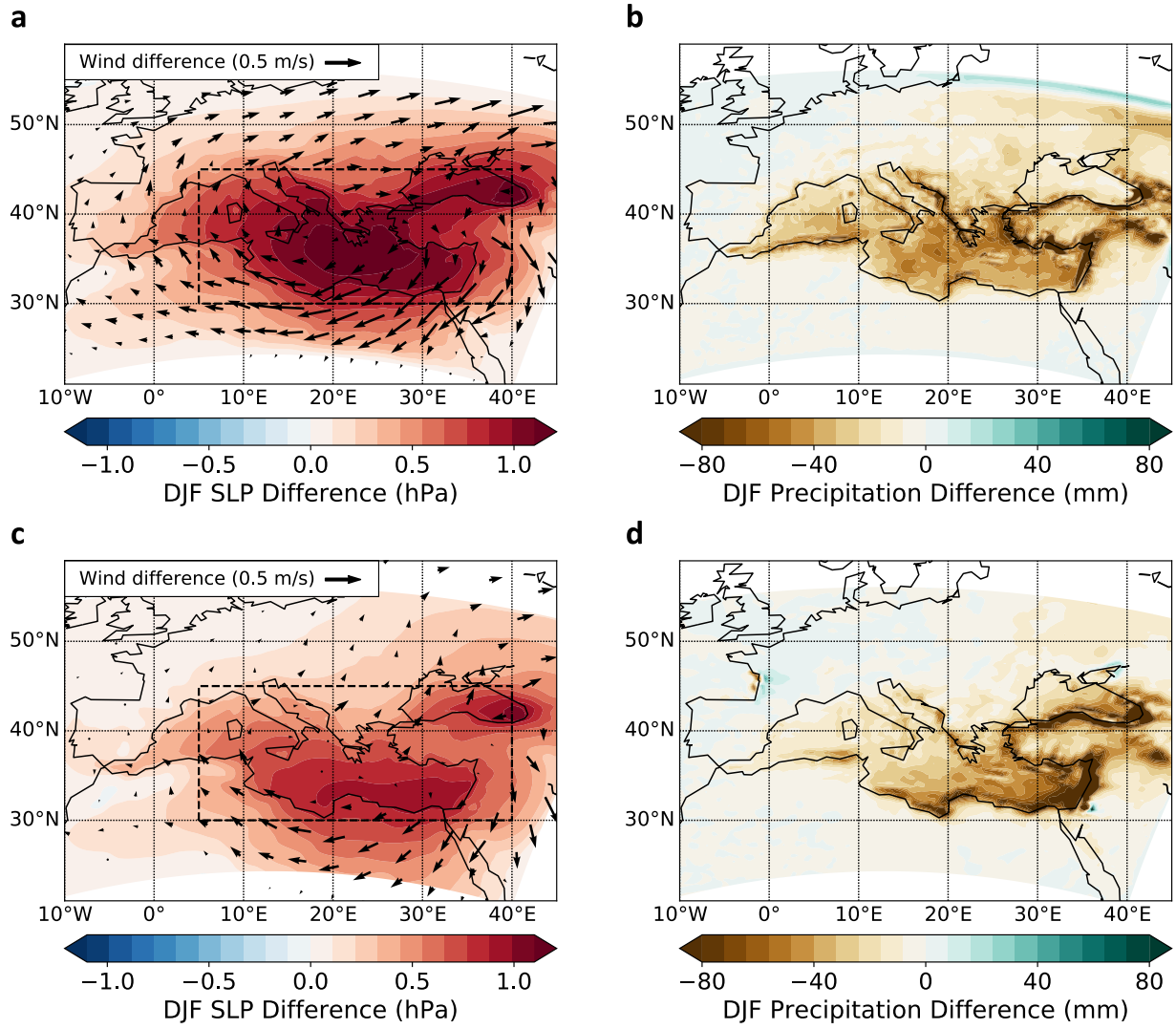

Figure 4-16: Difference in DJF (a,c) SLP and 850 hPa winds and (b,d) precipitation between the +1.5C and 0C experiments (0C minus 1.5C) in the (a,b) ERA and (c,d) MPI simulations.

the summer one: though SLP tends to increase in both seasons, the increase during winter is about 3.5 times larger than during summer (Fig. 4-17-a,c). Additionally, the winter response consists of a well-defined anticyclonic anomaly centered south of Greece, while in summer, the SLP change exhibits a more uniform increase over the Mediterranean. The associated circulation response is everywhere negligible. For further analysis, we look at the temperature and circulation response on pressure levels (Fig. 4-17-b,d). The striking difference is that during winter, the relative cooling extends much higher into the lower troposphere (up to 850 hPa, and even weakly above that) than in summer, when it is confined to the very lowest model level. As expected, there is little to no circulation response below 800 hPa in summer, whereas

at these levels in winter there is significant divergence and weak descent.

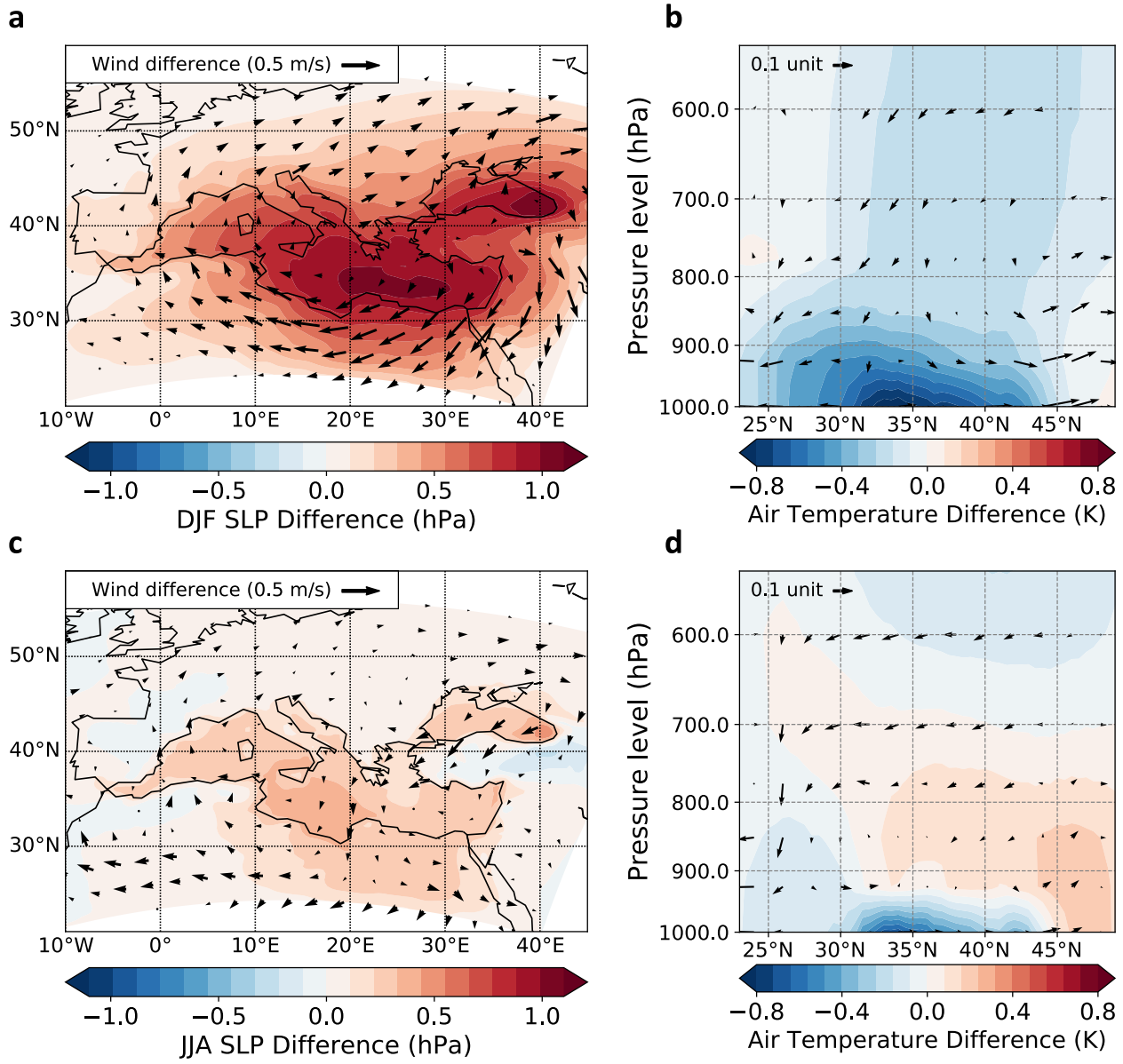

Figure 4-17: Difference in (a,c) SLP and 850 hPa wind, and (b,d) zonally-averaged (0-40°E) air temperature, meridional wind and pressure velocity, between the "0C" and "+1.5C" simulations ("0C" minus "+1.5C", average of ERA and MPI runs), for winter (DJF, a-b) and summer (JJA, c-d). In (b,d), circulation vectors are scaled such that 1 horizontal unit = 1 m/s; 1 vertical unit = 0.2 hPa/h.

To determine why the winter circulation is more sensitive to relative SST cooling, we now turn to near-surface static stability σ. Its annual cycle at 925 hPa averaged over the Mediterranean Sea is shown on Fig. 4-18-a. There is a strong winter/summer contrast, with static stability twice as large in summer than in winter. This seasonal contrast is consistent with the smaller amplitude of the annual cycle of SSTs compared to low-level air temperature. In winter, SSTs and near-surface air are warmer than overlying air layers, which is conducive to low static stability, also translated into enhanced lightning frequency [148], while in summer the situation is reversed: relatively cooler SSTs are associated with enhanced static stability. The large summer static stability prevents communication of the relative cooling to levels higher than the near-surface.

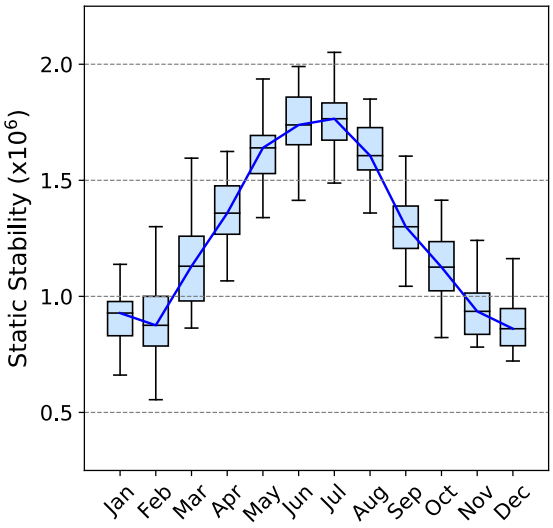

Figure 4-18: Annual cycle of 925 hPa Mediterranean-average (10°W-45°E/30-45°N) static stability, from ERA-Interim (1979-2018). Boxes represent the 50% range over the 40 years of data, and whiskers show the full range.

It is important to put this analysis in the context of the regional circulation. The latter is dominated during summer by the large-scale descent forced by the Indian monsoon to the east [213], which contributes to enhanced static stability of the whole air column, not just the lower levels. There is no such forced signal during winter: the area of strong descent near the regional Hadley cell edge is over the Sahara Desert, well to the south of the Mediterranean (Fig. 4-19). Therefore, the Mediterranean Sea is located enough to the north of the Hadley cell such that the warm SSTs can trigger large-scale ascent over the sea, a striking feature of the vertical circulation (Fig. 4-19-a). This large-scale ascent during winter in turn helps propagate the cooling anomaly upwards into the troposphere in our simulations, whereas it remains confined near the surface during summer (Fig. 4-17-b,d). The combination of the descent and large static stability in summer explains why there is no associated anomalous circulation above the surface since there is no heating anomaly to compensate [122].

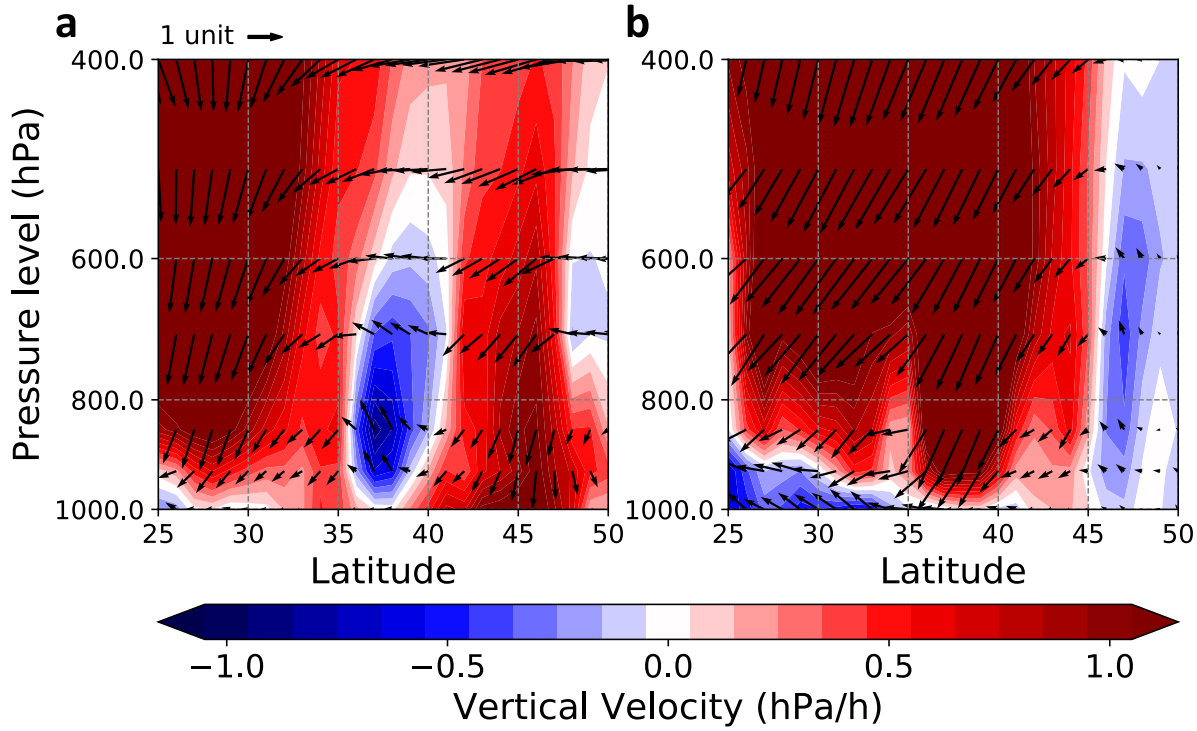

Figure 4-19: Mediterranean (10°W-45°E) zonal-mean DJF (a) and JJA (b) vertical and meridional circulation: vertical velocity (shaded) and wind in the meridional-pressure plane (arrows), in ERA-Interim (1979-2018). Circulation vectors are scaled such that 1 horizontal unit = 3 m/s; 1 vertical unit = 1 hPa/h.

4.6 Precipitation response

The consequence of the development of the anomalous Mediterranean ridge is an increase in mass and moisture divergence by the mean flow, which drives a regional precipitation decline [225]. However, the impacts are felt differently across the basin: the decrease in precipitation is most pronounced over southern Turkey to the east and over Morocco and the Iberian Peninsula to the west, away from the high-pressure anomaly (Fig. 4-1). The anomalous ridge is accompanied by a strong low-level wind field, that disrupts the relatively weak average circulation south of 40°N, and locally modifies the energy and moisture balance.

4.6.1 Eastern Mediterranean

To the east, thermal balance implies that subsidence will develop on the eastern margin of the Mediterranean ridge to compensate for cold advection from anomalous northerlies [225], which will tend to suppress precipitation. This view is consistent with the particularly large anomalous downward motion centered over that region in future projections (Fig. 4-21-a). The time-mean regional energy balance can be written in pressure coordinates as [213]

$$\overline{\frac{\partial T}{\partial t}} = \underbrace{\frac{\overline{Q}}{c_p}}_{\text{A}} \underbrace{- \left(\frac{p}{p_0}\right)^{\kappa} \overline{\omega} \frac{\partial \overline{\theta}}{\partial p}}_{\text{B}} \underbrace{- \overline{\mathbf{u}} \cdot \nabla_p \overline{T}}_{\text{C}} \underbrace{- \left(\frac{p}{p_0}\right)^{\kappa} \frac{\partial}{\partial p} \overline{(\omega' \theta')}}_{\text{D}} \underbrace{- \nabla_p \cdot \overline{(\mathbf{u}' T')}}_{\text{E}} \tag{4.8}$$

where t is time and p pressure, T is temperature, Q is diabatic heating/cooling, c_p is the specific heat of dry air at constant pressure, p_0 is a reference pressure (1000 hPa), R is the specific gas constant for dry air, $\kappa = R/c_p$, ω is pressure velocity (Pa/s), θ is potential temperature and $\mathbf{u}$ is the horizontal wind vector. Time means are denoted with overbars, and their deviations with $'$. Time means are computed in CMIP5 models for the 1976-2005 (reference) and 2071-2100 (future) periods. For long-term averages, the term on the left ($\overline{\frac{\partial T}{\partial t}}$) is about zero.

The last two terms on the right-hand side (D and E, transient terms) are also small (Fig. 4-20), and the balance is between diabatic forcing (A), vertical advection (B) and horizontal advection (C). Those three terms also dominate changes in the long-term balance. Downward motion compensates for the cooling from anomalous northerlies; yet, because it also suppresses precipitation, it indirectly leads to diabatic cooling of the air column (less vertical latent heat flux), and therefore reinforces itself. This likely explains why the cooling from horizontal advection is only about two-thirds of the change in adiabatic warming (Fig. 4-21-b). Models correctly reproduce the inter-annual link between winter Eastern Mediterranean precipitation and vertical velocity anomalies (Fig. 4-21-c). Across models, the change in seasonal precipitation is well correlated to that in pressure velocity (Fig. 4-21-d).

Topography in this region also likely plays a role in driving subsidence. Anomalous northerlies will tend to flow downslope from the Anatolian Plateau that extends over most of Turkey,

thus leading to a localized strengthening of trends in downward motion (Fig. 4-21-a) and in precipitation decline (Fig. 4-1-d). The resolution of orography in GCMs is however quite poor and a better assessment of the interaction between wind trends and mountains in the Eastern Mediterranean requires dynamical downscaling. In addition, during winter, evaporation from the Mediterranean Sea provides, especially in its eastern regions, a significant fraction of the water that falls as precipitation [26]. The western end of the basin depends rather on Atlantic evaporation. Therefore, the relative cooling of Mediterranean SSTs may act to decrease precipitation not only through it effect on regional circulation, but also by limiting the increase in evaporation and therefore moisture fluxes towards land. This might be an important factor for the Eastern Mediterranean, which receives much of its winter precipitation from Mediterranean cyclones [277].

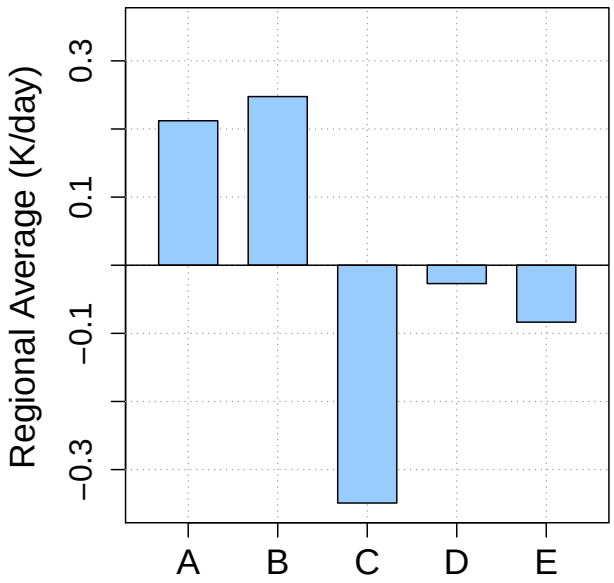

Figure 4-20: Energy budget equation terms for the Eastern Mediterranean (20°-35°E/30°-40°N), estimated from ERA-Interim 6-hourly data (1980-2018). See equation 4.8 for details.

4.6.2 Western Mediterranean

To the west of the basin, the energy balance argument does not hold. There, while precipitation still declines, the trend is rather towards upward motion (Fig. 4-21-a). Because anomalous winds associated with the low- level pressure high are predominantly easterly, they do not

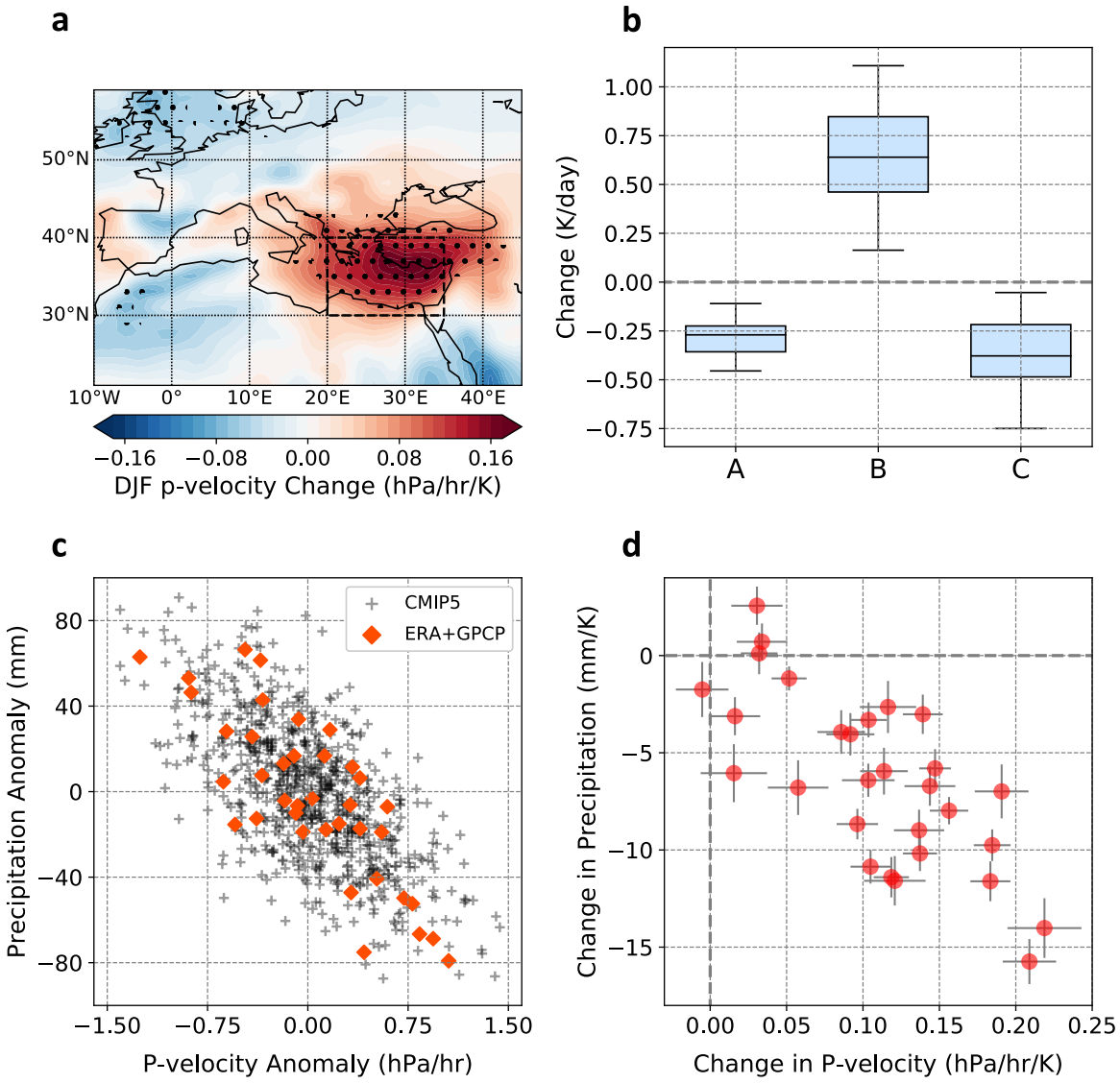

Figure 4-21: (a) CMIP5 multi-model mean change in DJF 500 hPa pressure velocity, under the RCP8.5 scenario. For each model, projections were normalized by its mean annual global temperature change. Dots indicate that more than 80% of models agree on the sign of the change. (b) Change in column-integrated energy budget terms across CMIP5 models, averaged over the Eastern Mediterranean (see box in (a)) (A: diabatic warming; B: vertical advection; C: horizontal advection, see equation 4.8). (c) Eastern Mediterranean (20°-35°E/30°-40°N, see box in (a)) DJF precipitation and p-velocity anomalies in historical (1976-2005) CMIP5 models and the observed record (1979-2018: ERA-Interim p-velocity and GPCP precipitation). (d) Change in Eastern Mediterranean DJF precipitation and pressure velocity across CMIP5 models, normalized by each model's mean annual global temperature change. 95% confidence intervals are shown by light gray bars.

change the energy balance as much as they do over the Eastern Mediterranean. However, they have a substantial impact on the moisture budget. Atlantic westerlies are the direct

source of precipitation for the Western Mediterranean [128]. Projected circulation trends not only act to weaken this moisture influx, they also tend to advect much drier air from the Sahara Desert (Fig. 4-22-c). Future projections show a consistent stagnation or weak increase in low-level specific humidity in the area (Fig. 4-22-a) which, combined with warming, leads to a pronounced increase in dew point depression (Fig. 4-22-c) well correlated with the regional precipitation decline across models (Fig. 4-22-b).. Lower relative humidity in the low troposphere decreases convective instability, meaning that uplift and associated condensation of water vapor become less likely. In addition, a decline in relative humidity higher up in the atmospheric colum, although less pronounced than at 850 hPa, can also act towards reducing precipitation through entrainment.

The results from our regional simulations (Fig. 4-16-a,c) as well as the analysis based on the external mode (Fig. 4-5-b) show that the relative Mediterranean Sea cooling plays a limited role in dynamical trends over the Western Mediterranean. Most of the wind change responsible for the dry advection and precipitation decline is forced by changes in the large-scale circulation. Therefore, the precipitation response to the relative SST cooling (Fig. 4-16-b,d) is much weaker over the Western Mediterranean, in particular over Morocco.

The impact of the anomalous Mediterranean ridge on specific humidity trends can be quantified using the analog method described in section 4.4. Using the Mediterranean SLP field as predictor and specific humidity as predictand, we estimate the specific humidity anomalies associated with future SLP patterns in each CMIP5 GCM. Multi-model averages for DJF and MAM are shown in Figure 4-23. The drying effects of the SLP anomaly over northwestern Africa and the Iberian Peninsula are evident, and compare well to the trend anomalies obtained by subtracting the regional average increase in specific humidity due to the background warming. These physical insights are confirmed by the mechanistic analysis of high-resolution climate projections over the Western Mediterranean (see Chapter 5). Similarly, the anomalous high is associated with slight atmospheric drying over southern Turkey, which may also contribute to the precipitation decline in this area. This is due to the anomalous northerlies advecting colder and drier air from central Europe and the Anatolian Plateau. The wetting effect of the pressure high over Egypt and Lybia is also clear in DJF, and absent in spring as the region of high pressure weakens and shifts westwards, away from this region. The region

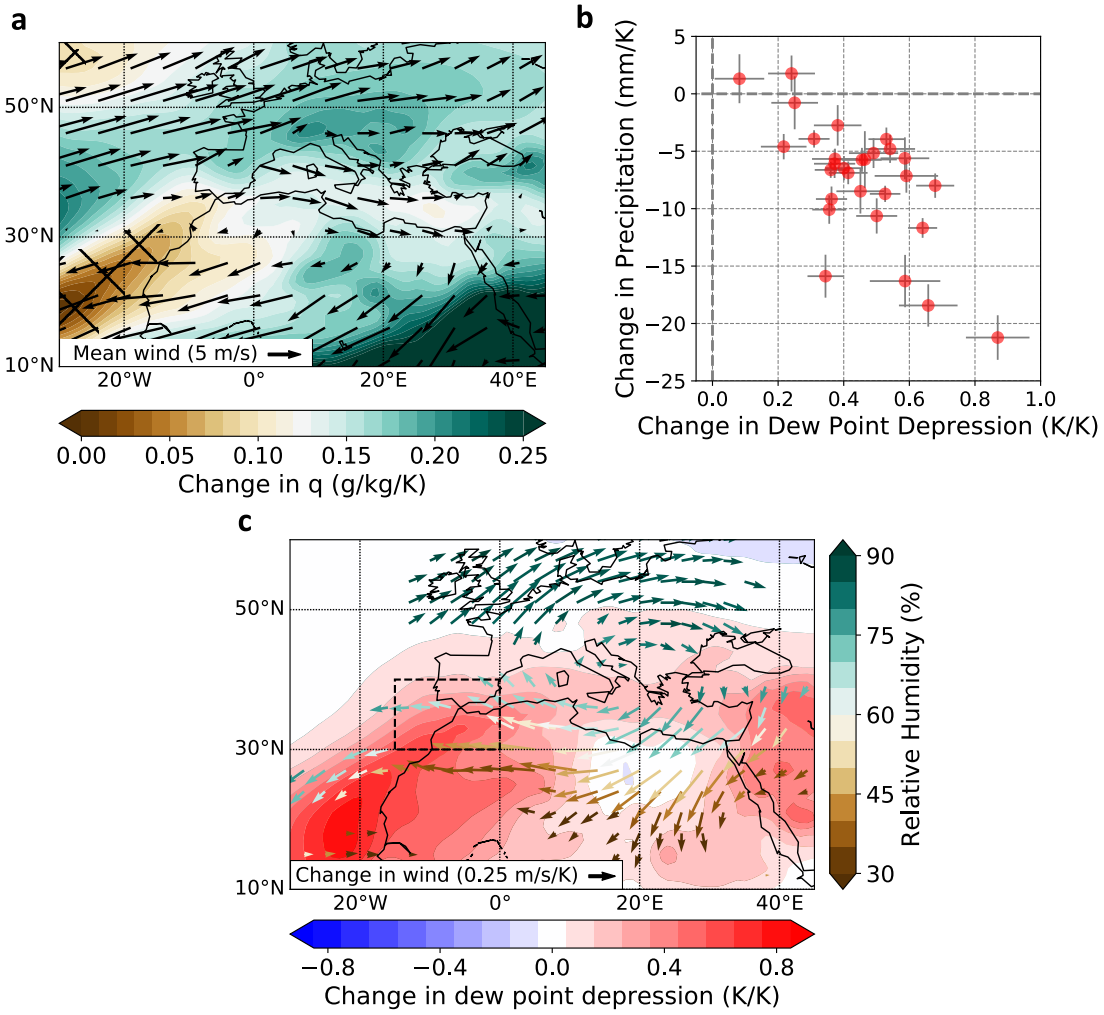

Figure 4-22: CMIP5 multimodel mean change in DJF 925-850 hPa averaged specific humidity (a) and dew point depression (c), normalized by each model's annual global-mean temperature change. Arrows indicate DJF (a) historical and (c) change in 925-850 hPa averaged winds. Wind arrows in (c) are colored according to mean historical relative humidity at each point and shown only where 80% of models agree on the sign of the change. (b) Western Mediterranean (15°W-0°/30°-40°N, box in (a)) DJF precipitation and dew point depression change across CMIP5 models, normalized by each model's mean annual global temperature change. 95% confidence intervals are shown by light gray bars.

directly west of the Sahara Desert at 20-25°N is also characterized by intense drying in both winter and spring. This trend is part of a global phenomenon of weak increases in atmospheric humidity at the eastern margins of the oceanic subtropical highs, where mean subsidence is strong [127]. Background easterlies blowing from the Sahara Desert may also prevent any increase in specific humidity in this region, since the Sahara, even in a warmer and wetter climate, will not provide much more atmospheric moisture since evaporation will not increase

significantly in this region. The effects of this feature are mainly concentrated south of 30°N, where little winter precipitation occurs. Still, it may help partly strengthen the drying trend caused by the anomalous Mediterranean pressure ridge. Another potentially important consequence is on spring precipitation on the southern slopes of the Atlas Mountains, which, though scarce, critically depends on moisture transport from the tropical Atlantic [27].

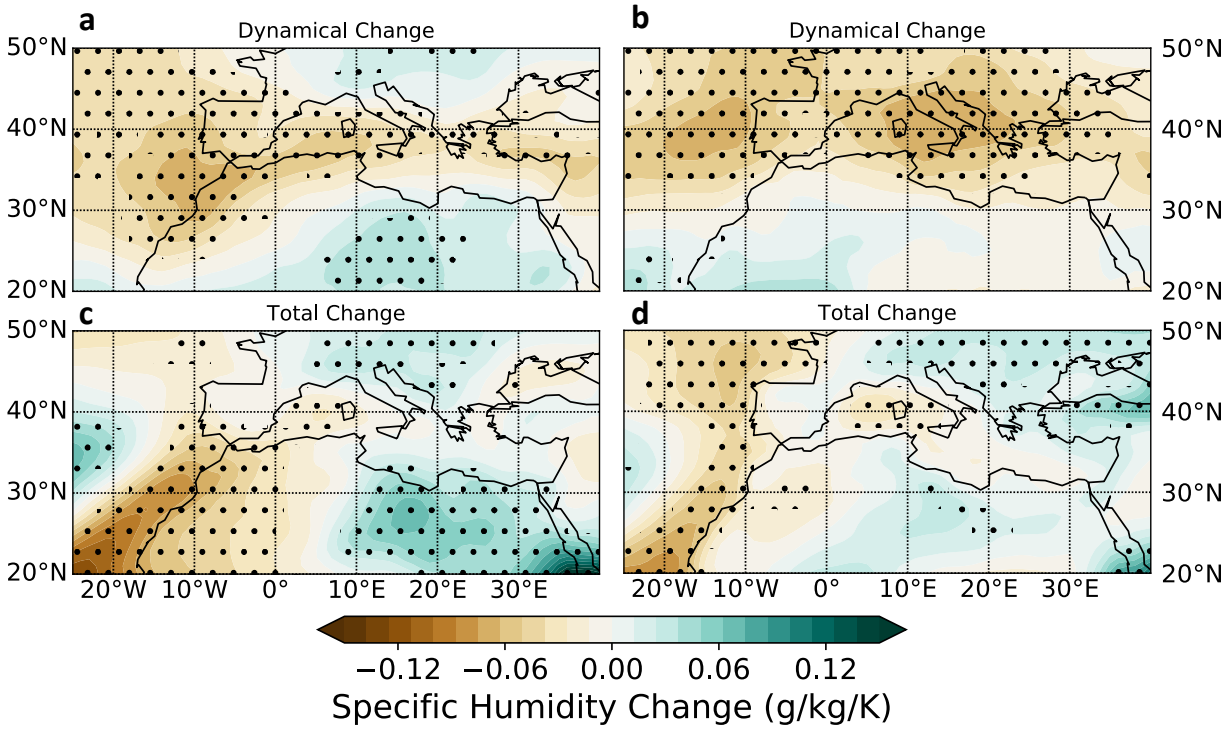

Figure 4-23: RCP8.5 change (2071-2100 minus 1976-2005) in Mediterranean 925-850 hPa averaged specific humidity (a,b) estimated by dynamical adjustment based on concurrent seasonal SLP anomalies and (c,d) CMIP5 multi-model mean, during (a,c) DJF and (b,d) MAM. In (c,d), the zonal mean change was subtracted at each latitude to make the range of values correspond to that in panels (a,b).

From this perspective, it is straightforward to understand the high correlation between the magnitude of anomalous SLP and Mediterranean-wide precipitation change (Fig. 4-3). Even though the physical mechanisms behind the drying are different in the Eastern and Western Mediterranean, the change in SLP determines the strength of the anomalous circulation that drives the decline in precipitation at each end of the basin. While these elements seem to explain precipitation trends in GCMs, it is important to remember that both the Eastern and Western Mediterranean exhibit in reality complex orographic features, which play an

important role in regional precipitation patterns. As noted previously in the case of the Eastern Mediterranean, their interaction with large-scale circulation trends may also impact future precipitation changes. Over southern Turkey, anomalous northerlies forced down the Anatolian plateau will cause subsidence and suppress precipitation. A similar phenomenon can be expected to occur north of the Atlas Range in Morocco and Algeria. These features are not well-resolved by GCMs; at the relatively finer resolution of our regional simulations (35 km), the orographic signal is much more detectable (see also Chapter 5), and the enhanced precipitation decline south of Turkey may indicate further drying following subsidence induced by topography (Fig. 4-16-b,d) [139].

4.7 Discussion

4.7.1 Uncertainties in the thermodynamical response

The estimate of the SLP response to surface thermodynamical forcing is based on a roughly 0.5°C change in the land-sea temperature contrast, with limited variance across models. That change is in no small part determined by Mediterranean SST trends under continued greenhouse gas forcing, which in turn depend, among others, on Mediterranean Sea circulation. The latter, however, is not well-resolved in GCMs [195]. Reasons are to be found among the region's complex geography, its small size relative to model resolution and the very small extent (15km) of the Gibraltar Strait, which plays a major role in the mass and energy balance of the Mediterranean [217]. Energy exchange with the Atlantic Ocean at Gibraltar must be parametrized in GCMs, which of course leaves room for substantial errors in long-term SST trends. In some models, the Mediterranean is even represented as a closed sea, which may tend to overestimate the SST response, with implications for the regional circulation change. Despite obvious differences, the impact of the Mediterranean relative cooling on regional circulation and precipitation is relatively similar between the ERA and MPI experiments: a general increase in SLP of about 0.6 hPa, peaking over the Eastern Mediterranean at around 1 hPa. This suggests that the response to relative cooling may also be similar when using other

CMIP5 models as lateral boundary conditions.

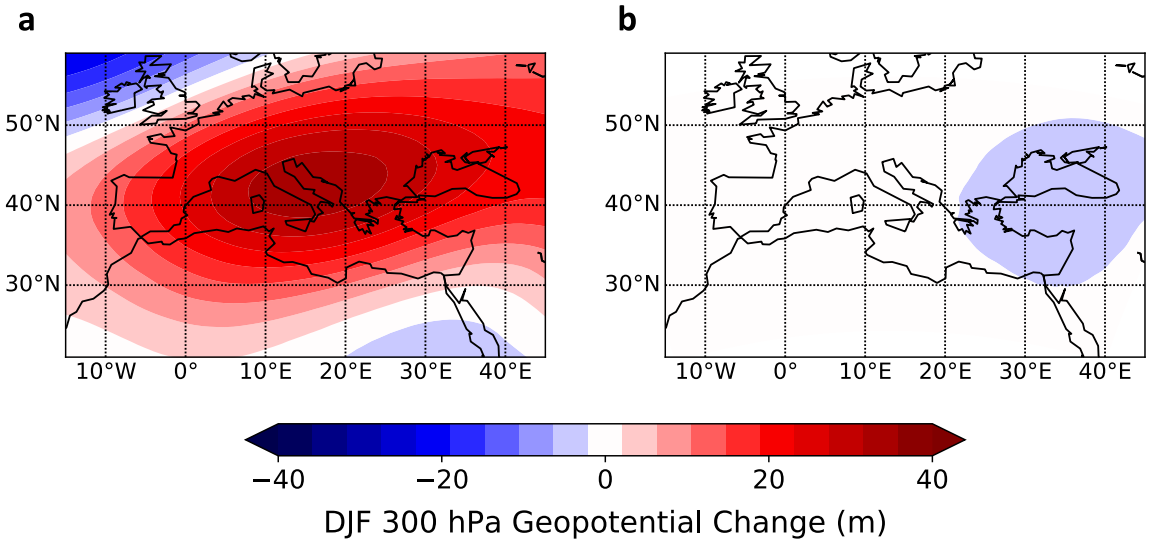

Figure 4-24: (a) CMIP5 multi-model mean Northern Hemisphere 300 hPa geopotential height change under RCP8.5 (2071-2100 minus 1976-2005). The zonal-mean change is subtracted at each latitude to highlight zonal variability. (b) Difference in 300 hPa geopotential height between the "0C" and "+1.5C" experiments.

4.7.2 Combining mechanisms and other explanations

The "dynamical" SLP response is higher over the Western Mediterranean, which can be seen as an eastward shift of the North Atlantic subtropical high, consistent with the eastward shift of the stationary waves themselves [231]. Contrarily, the SLP anomaly due to relative Mediterranean cooling peaks downstream of the anomaly, *i.e.* to the south and east of the anomalous high in the mulimodel CMIP5 simulations (compare Fig. 4-1-a with 4-17-a). Although assessed within different modelling frameworks, our approach suggests that the two mechanisms may individually contribute somewhat equally to the Mediterranean SLP increase (about +0.6-0.7 hPa, or 35 to 40% of the mean projected response), and therefore to the precipitation decline. The dynamical SLP anomaly nevertheless clearly dominates in a number of models, in addition to being responsible for most of the inter-model spread. The strong geopotential ridge projected at upper levels above the Mediterranean by CMIP5 models [225]) is also clearly associated with the planetary wave shift, not with the surface relative cooling, whose effect is

limited to the lower troposphere (Fig. 4-24).

In our regional simulations, we find associated with the relative cooling strong anomalous northerlies to the east of the basin, around 30-35°N (Fig. 4-17-a). To the west, the meridional wind response is weaker, consistent with the fact that the stationary wave response explains almost all of the magnitude in meridional wind trends west of 15°E (Fig. 4-5-b). Repeating the external mode calculation of section 4.3.3 for 35°N rather than 40°N and making an estimate of the change in meridional winds at 850hPa leads to a similar conclusion that the external mode cannot explain the total response in the east of the basin. Similarly, adding the SLP trends induced by the two proposed mechanisms accounts for only 80% of the model-mean projected change, leaving a sizeable part unexplained. Therefore, we conclude that while the surface forcing helps to explain the inability of the external-mode estimate to account for the full 850 hPa meridional wind response in GCMs at that latitude, the absence of a circulation anomaly at 40°N, following the relative SST cooling (Fig. 4-17-a), suggests that simply adding the two mechanisms may not be sufficient to explain the total circulation response at 40°N. A non-linear superposition of the dynamical responses to each forcing may explain part of that discrepancy, and also enhance the SLP total response. Additionally, the use of a different modeling framework, the finer representation of topography, the influence of friction and high topography on the mean all possibly contribute to shaping the low-level circulation response and may explain why a larger wind anomaly is not seen around 40°N. Surface friction in particular responds non-linearly to surface winds, which may be relevant in this region of complex topography. A smoother orography in GCMs may for instance underestimate the reduction in wind speed anomalies consecutive to surface friction, and overestimate SLP trends compared to finer-resolution RCMs. Further investigation is warranted, particularly since GCMs probably overestimate the dynamical response to upper-level forcing in the first place.

One other prominent feature of the mid-latitude circulation change is an increase of SLP in the North Atlantic, between 45°W and 0° (Fig. 4-1-a). We find that part of this increase, along the 40°N parallel, where CMIP5 SLP trends are robust, may also be a response to upper-level circulation changes (Fig. 4-a). North of there, the SLP change, though less robust, may be the downstream response to the North Atlantic Warming Hole (NAWH), an area of relative

SST cooling [95], though this remains far from certain. Despite weaker inter-model agreement in this region during winter, a downstream increase in SLP extending to the Mediterranean is possible. Though it would not explain the robustness of the Mediterranean hotspot, it may combine with the robust anomalous positive SLP from our two proposed mechanisms. Model agreement in this region is stronger in spring and fall, and this phenomenon could therefore also enhance the Mediterranean SLP response in those seasons, especially given the weaker projected upper-level flow changes in early spring and late fall (compare for instance Figs. 4-10 and 4-11 and associated reconstructed SLP anomalies, largest in DJF). Simulation results of Gervais et al. (2019) [95] suggest that the impact is small, but not zero (their figures 3 and 5). They also used only one model. Analyzing, within a coherent modelling framework, the contributions of upper-level flow changes, the Mediterranean relative cooling and the NAWH to future Mediterranean circulation trends may shed more light on this.

4.7.3 Consistency of mechanisms with other studies

We end by discussing the consistency of our results with those of previous studies. Among the various mechanisms proposed to explain the anomalous ridge, discussed in the introduction, we show in this chapter that changes in stationary wave structure discussed by Simpson et al. (2016) [231] play a crucial role, both for the model mean and inter-model spread (Fig. 4-10). Consequently, poleward shifts of the Hadley circulation and storm tracks, already shown to be limited in the Northern Hemisphere during winter, probably have limited direct influence. Recently, Brogli et al. (2019b) [36] concluded that large-scale circulation changes were the main driver the Mediterranean precipitation decline, and that regional effects were minimal. Their simulations that focus on the relative cooling of the Mediterranean also find a decrease in precipitation in the Eastern Mediterranean compared to a scenario where SSTs warmed as much as the land (their figure 4). Yet, their conclusions were based on two models (MPI-ESM-LR and HadGEM2-ES) in which the contribution of upper-tropospheric forcing happens to dominate (Fig. 4-10-d). As we show here, however, large-scale dynamics have a wide range of effects across models; although they account for much of the spread in the precipitation response, large-scale circulation trends are not sufficient to fully explain regional projections.

In terms of precipitation response, our results agree with the perspective offered by Seager et al. (2014) [225]. In CMIP5 models, the Mediterranean drying is connected to changes in moisture convergence by the mean flow, but the drivers behind those changes vary from east to west. To the west, moisture convergence declines due to a weakening of the Atlantic moisture supply through increased advection of dry air from the Sahara. To the east, large-scale subsidence is the main cause of the precipitation decrease. In reality, however, precipitation is strongly linked to prominent topographic features that are, to a large extent, not resolved by GCMs. Orographic lifting and the interaction of mountains with large-scale circulation changes predicted by CMIP5 models will impact precipitation projections.

Our results also shed some light on the conclusions of Zappa et al. (2015b) [277], who found the Eastern Mediterranean precipitation decline to be associated with large reductions in cyclone frequency and intensity. We find that regional circulation and its changes control precipitation variability and change in the basin (Figs. S2, 4-21 and 4-22), and therefore should control cyclonic activity, which is responsible for most of winter precipitation [277]. The decrease in mean storm precipitation and dynamical weakening of cyclones they identified is consistent with the substantial anomalous regional downward motion over the region (Fig. 4-21-a). In addition, anomalous northerlies advecting drier higher-latitude air and the relative Mediterranean cooling both act to constrain humidity trends, which likely cause the projected local minimum in specific humidity change near Cyprus (Fig. 4-22-a). The weakening of the storm track is consistent with a weakening of the meridional temperature gradient between the Mediterranean Sea and the continent to its north, and the reduction in baroclinicity it may lead to. Future research should focus on understanding how the large-scale drivers we identified control storm genesis in the Mediterranean.

4.8 Conclusion

In conclusion, we find that future winter Mediterranean circulation and hydroclimate trends in the CMIP5 multi-model mean are primarily determined by large-scale circulation changes and regional thermodynamical forcing. The combination of shifts in winter stationary wave and asymmetries in their vertical structure lead to a pronounced anticyclonic anomaly over

the Mediterranean. In addition, the atmospheric response to reduced warming of the Mediterranean Sea compared to land also contributes to the anticyclonic anomaly. This analysis applies generally to the "extended" winter season (November-April). The dynamical response maximizes during winter, first because that is when stationary waves and their changes are at their strongest, and second, because at that time of the year, the Mediterranean Sea lies away from the Hadley cell edge and is warmer than the atmosphere above it, which leads to low static stability, thus allowing contrasting surface temperature trends to extend to the lower troposphere and trigger a major circulation response. These results offer a coherent and mechanistic picture of Mediterranean winter climate projections that is consistent with their robustness.

While much work remains to be done to understand the variability in SLP and precipitation change patterns across models, we find that the unique combination of the large-scale "dynamic" response and the independent, regional-scale "thermodynamic" response explain the robust regional maximization of wintertime climate change over the Mediterranean, making this region a major climate change hotspot for the coming decades. The contributions from each response appear comparable, though a non-linear superposition may contribute to enhancing the response even more in certain models. Robust physical mechanisms involving local circulation account for the coherence of regional precipitation change and a maximized response at each end of the basin. Complex topography in those two regions indicates however that detailed regional simulations are required for improved future climate projections.

Chapter 5

High-resolution climate change projections over the Western Mediterranean

5.1 Introduction

Previous chapters have described how the Mediterranean Basin stands out in global climate projections as a major climate change hotpot, notably due to a severe winter precipitation decline within this already semi-arid area. We discussed in chapter 4 why the western end of the basin, in particular, should experience a particularly sharp decrease in precipitation. However, we have so far limited our analysis to coarse-resolution GCMs and medium-resolution regional simulations. The complex topography and corresponding climate of the region are not well-resolved at such resolutions [90]. For instance, important mountain watersheds can stretch over just a few thousand square kilometers, a fraction of a GCM grid cell (∼15000

[1]This chapter is an edited reproduction of Tuel, Kang and Eltahir (2020) [253]. A discussion of MRCM performance compared to station data has been added, as well as a section on subseasonal extremes of temperature and drought.

km^2). Precipitation over Morocco and Andalusia is also strongly variable in space and time, and largely determined by the complex topography, with large maxima over the Rif and Atlas Range peaks, and over Spain's coastal plains and Sierra Nevada (Fig. 5-1-a, 3-a). For an accurate assessment of climate change risks and processes in Morocco and the surrounding areas, downscaling projections to a higher resolution is critical.

Regional Climate Models (RCMs) are well-suited to downscale projections when long and reliable records are not available, as is the case for most of our area of interest. They can provide detailed physical insights into the future climate of a region, down to scales that are relevant for water management applications. RCMs have been shown to bring significant improvements to the modelling of the complex North African climate [247, 216], where the correct simulation of precipitation is challenging due to its high spatio-temporal variability. Several studies have already evaluated climate change impacts at high resolution over this area. Most used horizontal grid spacings larger than 20km [90, 64], with a few studies going down to under 15km within the framework of the Coordinated Regional Climate Downscaling Experiment database (CORDEX) [247, 227, 166, 246].

Still, these past studies have a number of limitations. First, the choice of the forcing GCM is not discussed, whereas it is well-known that various GCMs have different biases and some are not able to correctly model the climate in given regions [242, 170]. Bias correction is the preferred option to tackle this problem, but some GCMs may not be able to accurately represent large-scale climate drivers and known teleconnections, thus diminishing our confidence in their projections. Second, the physical mechanisms behind projected regional climate changes are not discussed. It is important to put the regional drying in the context of larger-scale trends simulated by coarse-resolution GCMs. This chapter addresses these points. We evaluate the performance of the MIT Regional Climate Model (MRCM) in simulating seasonal and inter-annual regional climatic features over the Western Mediterranean, and develop and interpret regional climate change projections over that same region. Our focus is on fine-scale changes in the seasonal means and sub-seasonal extremes of temperature and precipitation, and their physical interpretation.

5.2 Area of study

Fig. 5-1-a shows our simulation domain, centered at 34°N, 5°W, and which covers most of Morocco, Portugal and southern Spain; we refer to it hereafter as Northwest Africa and the Iberian Peninsula (NWAIP). It has 166×161 grid cells with a horizontal resolution of 12 km, sufficient to resolve much of the complex regional topography. Most of the precipitation occurs over Portugal, western Spain and northwestern Morocco, coastal regions which stand under the influence of North Atlantic storm systems [129, 147]. There, the climate is of the Mediterranean type: winters are mild and wet, and summers hot and dry. Average annual precipitation ranges from 50 mm south of the Atlas, up to about 800 mm over southern Portugal and Morocco's Rif Mountains. The vast majority of it falls during the wet season, from November to May. Storm events during this period are few, short and irregular [27], occurring as mid-latitude weather systems drifting south-eastward from the North Atlantic. Their frequency increases with latitude, as one gets closer to the storm track center. A large fraction of the winter precipitation falls as snow over the Atlas Range and Iberian sierras, building up a snowpack which slowly melts over spring, guaranteeing a prolonged water supply for the plains below. South and southeast of the Atlas, the Sahara Desert is characterized by a year-round hot and dry climate with less than 50 mm of rain. The Spanish sierras, like the Atlas Range, act as a barrier which slows down westerlies, forces orographic precipitation, and cuts off the moisture supply for regions to its east. This creates a rain shadow over southeastern Spain, much drier than the regions to its west.

Coupled to this spatial variability, rainfall is also highly variable in time, with an inter-annual coefficient of variation ranging from 25% along the Atlantic coast up to 100% in the most arid regions. The main driver of inter-annual winter precipitation variability in the NWAIP is the North Atlantic Oscillation (NAO), an oscillatory pattern of sea-level pressure between the Azores High to the south and the Icelandic Low to the north [129]. High values of the NAO are associated with a northwards-displaced storm track and dry conditions south of 40°N; negative values, on the other hand, lead to wetter-than-average conditions over southern Spain, Portugal and Morocco (see also Chapter 2). For a detailed characterization of rainfall and temperature changes across this complex region, we divide the land area in our domain into several sub-

regions. Relevant to precipitation projections, we select five major watersheds: the Tajo and Guadalquivir, in southern Spain and Portugal, and the Loukkos, Sebou and Oum-Er-Rbia watersheds in Morocco (Fig. 5-1-b). The last three provide about 70% of river discharge in Morocco [171] and their water resources are therefore critical for the country. We analyze both winter (DJF) and spring (MAM) seasons, since each accounts for 30-40% of annual rainfall over most of the NWAIP domain. For temperature projections, we focus on coastal and mountainous (above 1200m) regions in winter (DJF) and summer (JJA). Specifically, we consider the Atlas Range in Morocco and the Sierra Nevada in southern Spain, two areas characterized by an important winter snowpack and therefore highly vulnerable to warming (Fig. 5-1-c).

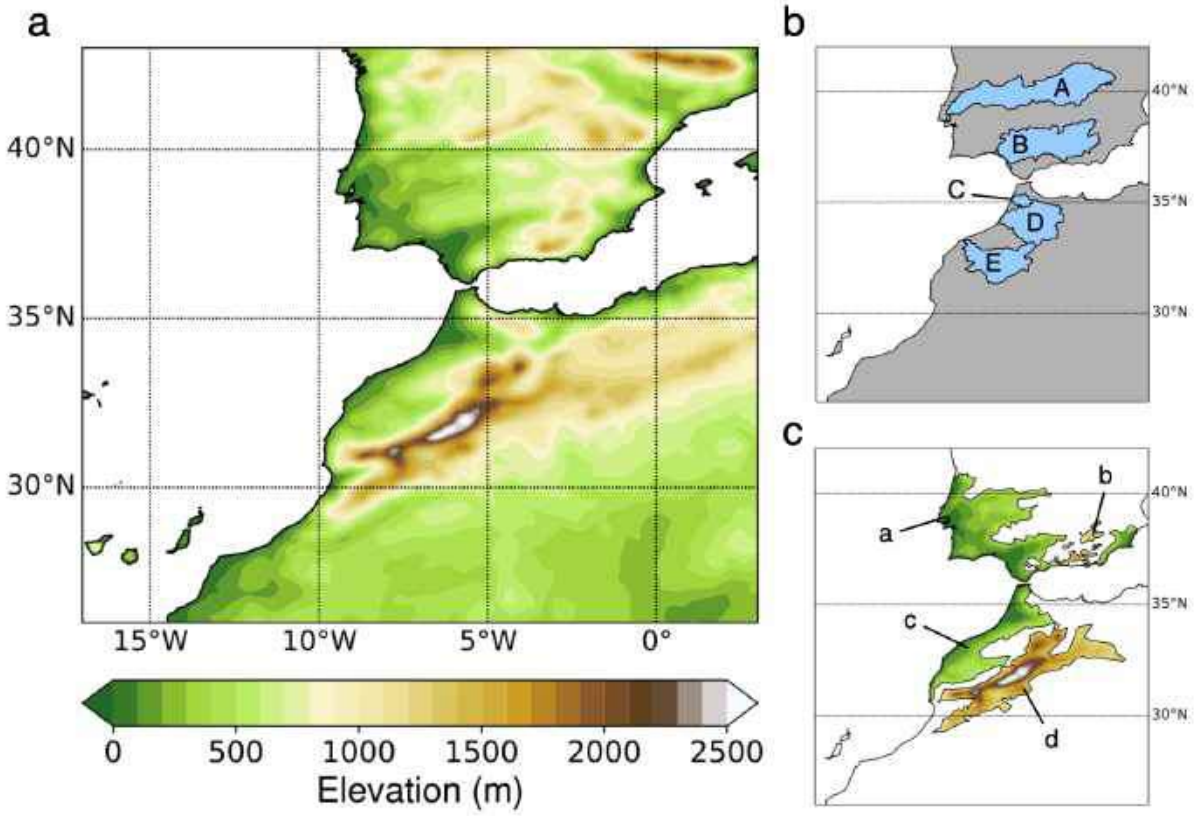

Figure 5-1: (a) MRCM simulation domain and topography. (b) Sub-regions used for regional analysis of precipitation projections: (A) Tajo, (B) Guadalquivir, (C) Loukkos, (D) Sebou and (E) Oum-Er-Rbia watersheds. (c) Sub-regions used for regional analysis of temperature projections: (a) Iberian coastal plain, (b) Sierra Nevada, (c) Moroccan coastal plain and (d) Atlas Range. (a,c) are defined by altitude <500m and (b,d) by altitude >1200m at the MRCM resolution.

Agriculture plays a major part in the region's economy, from the Spanish provinces of Andalusía and Murcia, to the fertile plains of Morocco north of the Atlas Range. Dry summers mean that winter rainfall is critical for agriculture, even in Spain where the penetration of technology in agriculture is higher and irrigation more widespread. We saw in Chapter 2 how inter-annual variability in seasonal precipitation dictated that in cereal yields (Fig. 2-11). Total precipitation during the growing season isn't everything, however. Sub-seasonal variability in weather also impacts crop productivity in rainfed agriculture. An average season with precipitation falling in just 3-4 storm events separated by long dry periods may be just as bad as a fully dry season. Fatna and Abderrahim (1997) identified for instance a very strong correlation ($r^2 = 0.92$) between Moroccan cereal production and cumulative rainfall deficits during December, January and February [76]. Jarlan et al. (2014) found in the case of wheat in Morocco, rainfall and temperature anomalies play a major role essentially at critical stages of wheat development [134]. Water stress at the early stage of growth in November-December can induce significant losses; even if more favorable conditions follow, the water deficit cannot be made up for and stressed plants have lower yields. High temperatures also tend to negatively impact yield, especially between March and May‘, during the critical stages of flowering and grain filling for cereals [151, 12, 134, 102]. Short (2-5 days) warm episodes around the time of flowering with average temperatures above 34°C can reduce wheat yield by 30-40% [12, 199]. Persistent >20°C nighttime temperatures also decrease wheat fertility and grain size.

Reported critical drought and temperature thresholds for wheat, the major rainfed crop in Morocco, vary in the literature [57]. For illustrative purposes, we simplify the problem by looking at two simple metrics for weather extremes: the maximum number of consecutive dry days within a growing season (November-April) and the maximum daily-average temperature between April and May. We assess the performance of MRCM in simulating the statistics of these extremes and infer future risks from such extremes for agriculture using the downscaled climate projections.

5.2.1 Station data

Additionally, available station data over Morocco are used, both to assess the skill of MRCM in downscaling "perfect" coarse-scale information from ERA-Interim, and to bias-correct future projections at the station scale to improve the assessment of risks from subseasonal extremes. A map of station locations is shown on Figure 5-2. Daily average temperature data are available from the Global Historical Climatology Network (GHCN) database [172] for our 1982-2011 simulation period (see next section) at 11 locations, all major Moroccan cities. Daily precipitation data at 90 stations was obtained from the Department of Water at Morocco's Ministry of Equipment, Transport, Logistics and Water. This data is concentrated in mountainous regions, where most of the precipitation occurs, hence the relatively small number of stations available over the plains. Coverage is also much higher over Morocco's northern regions (Rif) than over the Atlas.

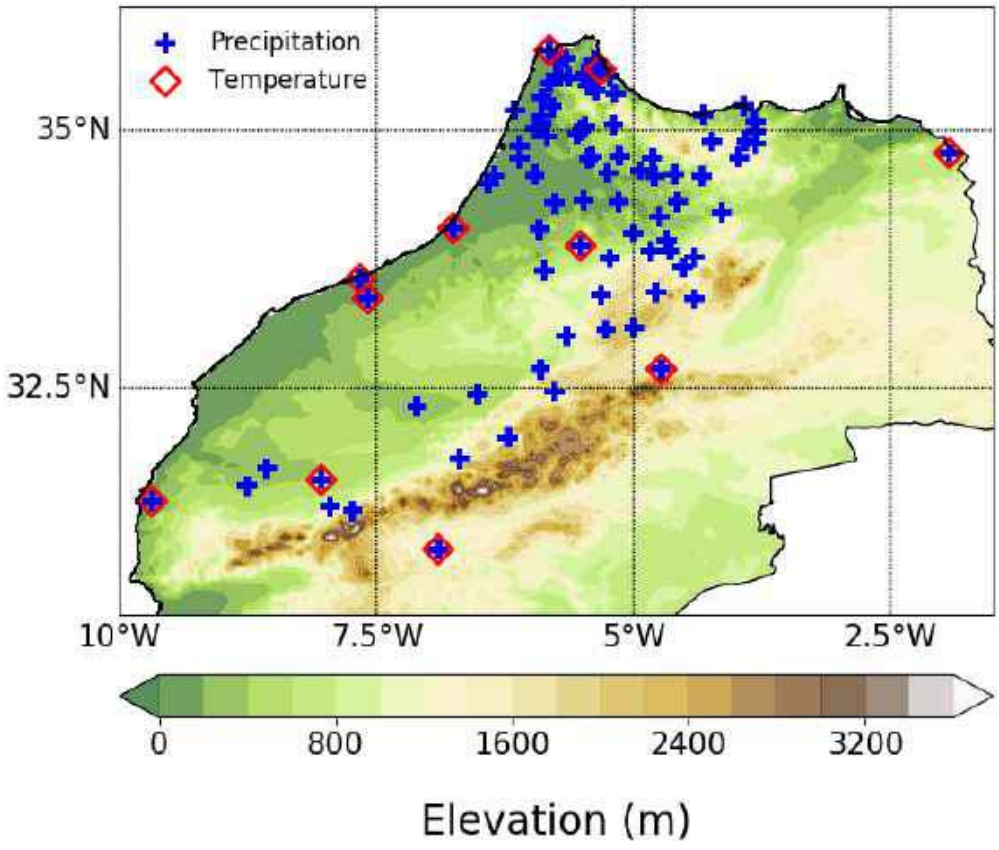

Figure 5-2: Location of ground stations with available precipitation (blue crosses) and air temperature (red diamonds) data in Morocco.

5.3 Model description and experimental design

5.3.1 The MIT Regional Climate Model (MRCM)

MRCM [132] is based on the ICTP-Regional Climate Model Version 3 (RegCM3, Pal et al 2007 [187]). MRCM maintains much of the same structure but incorporates several significant enhancements, including coupling of the Integrated Biosphere Simulator (IBIS) land surface scheme [270], a new surface albedo assignment [162], modified boundary layer height and boundary layer cloud schemes [98], an irrigation scheme [163], an improved convective cloud scheme [96] and a convective rainfall auto-conversion scheme [97]. With its incorporation of new physical schemes or modification of original schemes, MRCM has consistently showed comparable or better performance in simulating key climate features across various regions (e.g., North America, West Africa, Southwest Asia, and the Maritime Continent) compared to various regional climate models. In particular, Im et al (2014) demonstrated from simulations over West Africa that the use of IBIS as the land surface scheme results in better representation of surface energy and water budgets in comparison to RegCM3's BATS [132]. Additionally, Pal and Eltahir (2016) improved the skill of MRCM in simulating the key surface processes over the desert of southwest Asia, thanks to a new albedo prescription based on NASA/GEWEX Surface Radiation Budget (SRB) project and emissivity from NASA MODIS surface emissivity data [186]. In consideration of the good performances from these previous studies, we adopt the same combination of physical parameters and land surface conditions as in Pal and Eltahir (2016) except for the convection scheme. We run the model at a resolution of 12 kilometers. The choice of convective scheme is based on results of test simulations among several potential schemes and selecting the one that simulates observations best. The following physical schemes are employed in our experiment: the IBIS land surface scheme; the Grell convection scheme with Fritsch-Chappell closure assumption; the sub-grid explicit (SUBEX) moisture scheme [188]; the radiation package of the National Center for Atmospheric Research (NCAR) Community Climate Model, version 3 (CCM3) [146]; the nonlocal planetary boundary layer scheme [120]; and the ocean–atmosphere flux algorithm proposed by Zeng et al. (1998) [280].

	Boundary conditions	Scenario	Simulation period
Reanalysis downscaling	ERA-Interim + OISST	—	1982-2011
Climate change simulations	MPI-ESM-MR	Historical	1976-2005
		RCP4.5	2071-2100
		RCP8.5	2071-2100
	GFDL-ESM2M	Historical	1976-2005
		RCP4.5	2071-2100
		RCP8.5	2071-2100
	IPSL-CM5A-LR	Historical	1976-2005
		RCP4.5	2071-2100
		RCP8.5	2071-2100

Table 5.1: Summary of the ten MRCM simulations.

5.3.2 Experiment design

First, we evaluate the model's performance in simulating key processes of the regional climate by performing a dynamical downscaling of the ERA-Interim reanalysis dataset (Dee et al. 2011) with MRCM over the 30-year 1981-2011 period. In this experiment, MRCM is driven by the 1.5°×1.5° 6-hourly ERA-Interim data [55] as lateral boundary conditions and the 1°×1° weekly National Oceanic and Atmospheric Administration (NOAA) optimum interpolation sea surface temperatures (OISST, [206]) over oceans. We select the optimal convection scheme in this setting. This simulation is afterwards referred to as ERA/MRCM. Second, we perform climate change experiments using the same configuration of MRCM as in ERA/MRCM, but with 6-hourly output from three selected GCMs from the CMIP5 data archives ("r1i1p1" ensemble members) used as lateral boundary conditions. The selection process is described in section 5.3.3. The 1975-2005 period forced by historical greenhouse gas concentrations is taken as reference, and compared with the 2070-2100 period forced by the RCP4.5 and RCP8.5 emission scenarios [256]. In total, nine 31-year GCM runs are dynamically downscaled with MRCM. A summary of the ten MRCM runs is given in Table 5.1. In all simulations, the first year is discarded as spin-up, leaving 30-year projections (1976-2005 for reference, 2071-2100 for future and 1982-2011 for ERA/MRCM) to be analyzed. Different strategies are selected to

Name	**Resolution**	
	Atmosphere	Ocean
ACCESS1-0	144 × 192	300 × 360
BCC-CSM1-1-m	160 × 320	232 × 360
CanESM2	64 × 128	192 × 256
CESM1-CAM5	192 × 288	384 × 320
CMCC-CMS	96 × 192	149 × 182
CSIRO-Mk3-6-0	96 × 192	189 × 192
GFDL-ESM2M	90 × 144	200 × 360
INM-CM4	120 × 180	340 × 360
IPSL-CM54-LR	96 × 96	149 × 182
MIROC-ESM	64 × 128	192 × 256
MIROC-ESM-CHEM	64 × 128	192 × 256
MPI-ESM-MR	96 × 192	404 × 802
NorESM1-ME	96 × 144	384 × 320

Table 5.2: List of selected CMIP5 models. Resolution is in latitude by longitude.

correct the mean biases of surface temperature and precipitation in the MRCM simulations, at the monthly time scale for the whole simulation domain, and at the daily time scale at station locations (see section 5.3.4).

5.3.3 GCM selection

We select suitable GCMs to use as forcing boundary conditions for MRCM. GCMs are selected among all CMIP5 participating models for which 6-hourly data is available, according to the following methodology:

1. First, given the dominant role played by the NAO in driving inter-annual precipitation variability over our domain, we first retain thirteen models that are able to capture some of the main features of the NAO, based on the comprehensive analyses by Davini and Cagnazzo (2014) [53] and Wang et al. (2017) [264], and for which 6-hourly output data is available. The model list is given in Table 5.2.

2. Second, we exclude the GCMs that are unable to simulate the impact of the NAO on

southwestern Mediterranean precipitation (15°W–0°/30–40°N) during winter. This impact is quantified by the correlation of the DJF NAO index and concurrent precipitation (Fig. 5-3). Two procedures are tested to compute the NAO index in GCMs: first, as the time series of the first principal component of DJF sea-level pressure (SLP) over the North Atlantic (90°W–40°E and 20–80°N), and second, as the projection of annual DJF SLP fields onto the "observed" NAO pattern, defined as the first principal component of DJF SLP in the NCEP-NCAR reanalysis [138] (Fig. 5-3-a,b,c,d). Both approaches yield similar results, though each has its limitations, as discussed in Davini and Cagnazzo (2014). We also assess the ability of GCMs to reproduce the spatial patterns of DJF SLP correlation to Western Mediterranean precipitation (Fig. 5-3-e,f,g,h).

3. Finally, the historical simulations from the selected GCMs are evaluated over the domain, by looking at climate variables during winter and spring relevant for the present analysis: temperature, relative humidity and precipitation. Spatial patterns and regional means are compared to TRMM, ERA-Interim and TerraClimate to confirm that domain-average values and spatial patterns, particularly the dependence with elevation, are reasonably captured.

We select three GCMs at the end of this screening process: GFDL-ESM2M [68], IPSL-CM5A-LR [67] and MPI-ESM-MR [276]. Although they all suffer from an evident dry bias (common in fact to most, if not all, CMIP5 GCMs, partly connected to the poor representation of the regional orography, which plays an important role in forcing winter precipitation), they accurately reproduce the SLP-precipitation relationship during winter.

5.3.4 Bias correction

Output from regional climate modeling experiments contains systematic biases arising, among others, from lateral boundary conditions and imperfect representation of physical processes [153, 71]. To reduce this bias and improve the relevance of projections, MRCM output must be bias-corrected. To that end, we adopt two slightly different strategies, one for monthly-mean variables over the whole domain, and one for daily variables at station locations only.

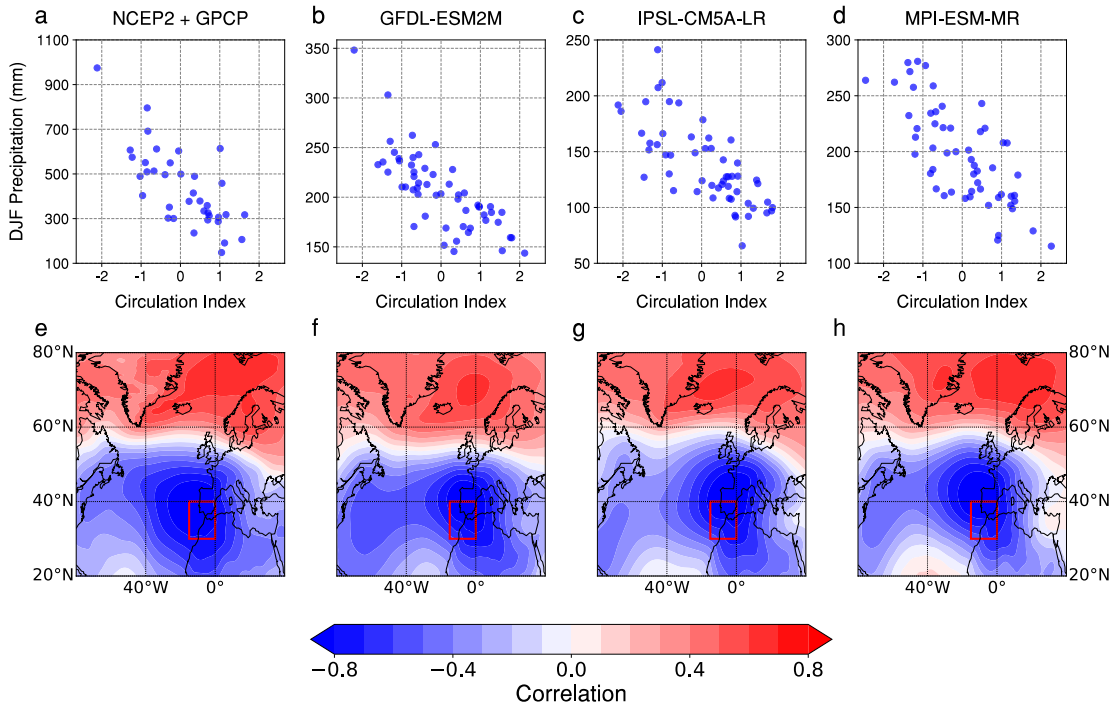

Figure 5-3: (a-d) DJF Western Mediterranean (15°W-0°/30-40°N) precipitation against concurrent NAO circulation index (see text for definition); and (e-h) Pearson correlation of DJF SLP to concurrent Western Mediterranean precipitation, in (a,e) GPCP and NCEP-NCAR reanalysis (1979-2017); (b,f) GFDL-ESM2M; (c-g) IPSL-CM5A-LR; and (d,h) MPI-ESM-MR. For (b-h) data covers the 1950-2004 period.

For monthly-average values, we apply at each grid point the cumulative distribution function transform (CDFt) method [174] which corrects the given (MRCM) CDF based on a target (observed) CDF by matching the quantiles of the first with those of the latter with an empirically-estimated transfer function (this technique is part of the family of methods known as quantile mapping [152]). As observations, we use data from the Tropical Rainfall Measuring Mission (TRMM, [126]) 3B43 version 7 for precipitation and, for temperature and precipitation as well, the TerraClimate dataset [1], a consistent, long-term and fine-scale gridded observation-based record. Both datasets are first regridded to the MRCM resolution. TerraClimate is available globally at monthly resolution after 1958, while TRMM is available only after 1998, but at a daily resolution. We consider both datasets for precipitation, because TerraClimate extends over a longer period, which allows for a better assessment of MRCM performance, and because TRMM is available at a daily time step, which we will require for the analysis of sub-seasonal drought extremes (see below).

Because we apply the CDFt method at each grid point and month separately, the 30 values this corresponds to are not sufficient to estimate the CDF non-parametrically. Therefore, we first fit parametric CDFs to monthly-mean values of temperature and precipitation, at each grid point, in model output and observations. We choose normal (gaussian) distributions for monthly-mean temperatures and gamma distributions for monthly-mean precipitation. As usual in bias correction methods, this transformation is assumed to remain valid in the future climate, so the same tranform function is applied to future temperature and precipitation.

For the analysis of subseasonal extremes, much more data are available since we now focus on the daily time step. For daily temperature, at each of the 11 available locations, we apply the same CDFt method to MRCM-simulated and observed data over their common period. For some stations, temperature observations are missing for a few years at the beginning of the 1980s, but overall, at each station, observations and MRCM ouput are both available for at least 25 common years. The bias correction is implemented for each month separately. For precipitation, since we are interested in drought periods (*i.e.*, days with no or negligible precipitation), there is no need to correct for the magnitude of precipitation on wet days. Rather, we calculate for each station its wet-day probability between November and April, the wet season, during which crops are grown. A wet day is here defined as a day with more than 0.5mm of precipitation. When the associated MRCM series overestimates the number of wet days, we calculate the daily precipitation threshold in the MRCM series that corresponds to the station-based wet-day probability, and set all daily precipitation values below this threshold to 0 in the MRCM series. This ensures that MRCM and station observations have the same wet-day probability (this does not correct, however, for potential biases in the temporal autocorrelation of precipitation). If the MRCM series has too few wet days compared to observations, this methodology obviously does not work. Other approaches are possible, like the random generation of additional wet days in the MRCM series to increase wet-day probability, but it is not straightforward to do so while preserving temporal autocorrelation, very important when considering drought periods. Out of the three GCMs, only IPSL-CM5A-LR is in this situation (the other two both simulate the same or a higher number of wet days at each station, see section 5.4.2); therefore, we discard it from our analyses of subseasonal drought extremes.

5.4 Simulation results

5.4.1 MRCM performance

We first assess the performance of ERA/MRCM by comparing the simulated precipitation to TerraClimate, focusing on the climatology over our domain and inter-annual variability for the winter season, which accounts for the bulk of water availability in this region. While the GCM ensemble mean (ENS/GCM) is able to broadly capture the overall precipitation gradient between the wetter regions over the Iberian Peninsula and the dry desert over northwest Africa, the small-scale maxima along the African coastlines and over the high mountainous regions are, unsurprisingly, missed (Fig. 5-4-a,b,c). The overall dry bias of GCMs over Morocco is evident Figure 5-4-c, expected since it is the unresolved high-altitude regions that receive the most precipitation. By contrast, ERA/MRCM is in good agreement with the observed distribution, both at large- and small-scales. There is a substantial overestimation of DJF precipitation over the Moroccan and Algerian coastlines, as well as central Spain. South of the Atlas Range, precipitation is also slightly overestimated, possibly a consequence of the incorrect representation of summer small-scale convective systems which bring a large fraction of annual precipitation in this region. Still, MRCM exhibits a pronounced precipitation downscaling skill, especially in regions where orographic forcing dominates.

As to annual cycles (Fig. 5-4-d,e), the ENS/GCM is quite able to capture the seasonal variation of precipitation over the Iberian Peninsula, with its maximum in winter and minimum in summer. The magnitude of wet-season precipitation is reasonably close to TerraClimate, despite a dry bias between October and December. Summer precipitation is quite overestimated, however. By contrast, over northwestern Morocco, GCMs fail to capture the seasonal cycle, showing instead a somewhat constant monthly precipitation rate. The dry bias during winter and spring is evident. Additionally, inter-GCM spread is quite large, especially between July and September when some GCMs produce copious amounts of precipitation, possibly the result of exaggerated tropical moisture transports typically responsible for much of the summer precipitation south of the Atlas Range [27], or of incorrect representation of summer convection. Compared to ENS/GCM, ERA/MRCM is in good agreement with TerraClimate,

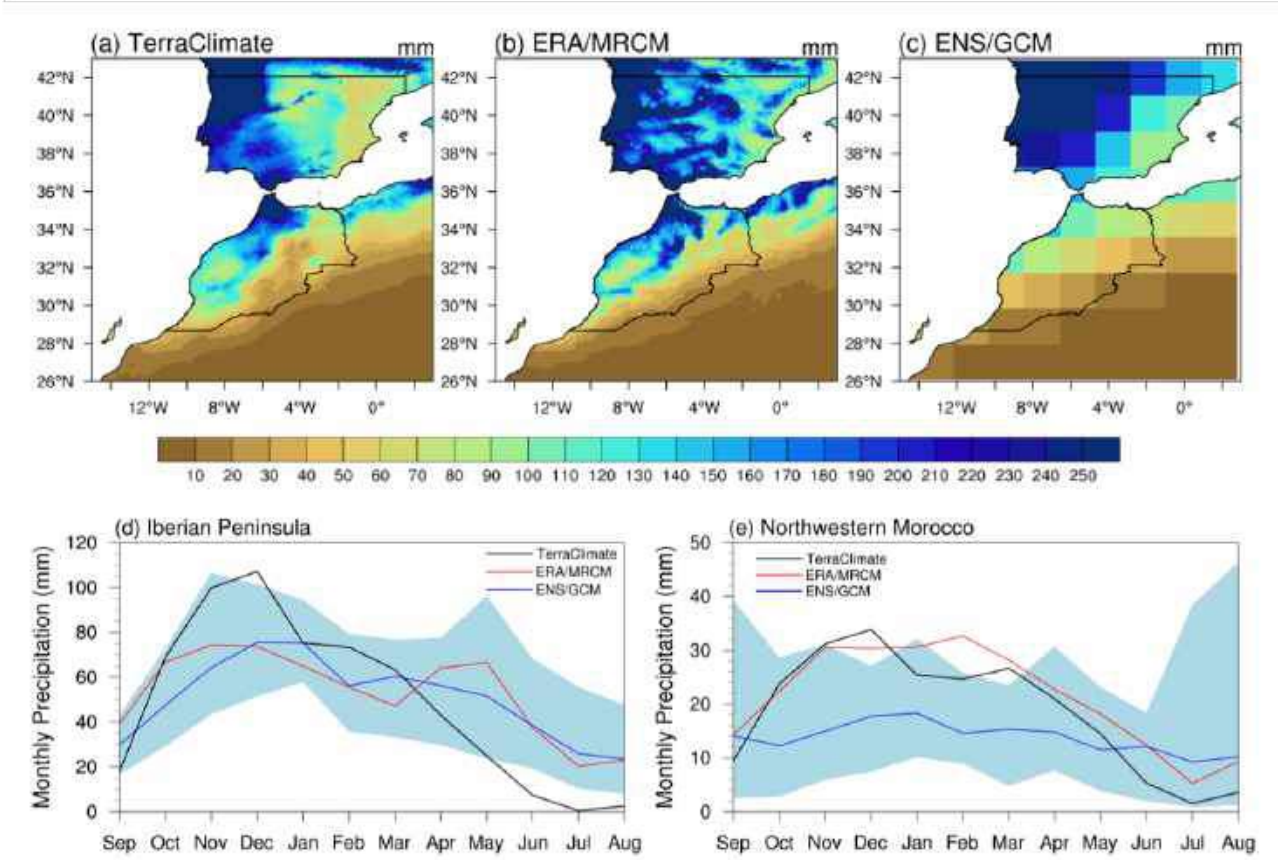

Figure 5-4: (a-c) Spatial distribution of 30-year climatology of average DJF total precipitation over the NWAIP: (a) TerraClimate, (b) MRCM-downscaled ERA-Interim (ERA/MRCM), (c) ensemble mean of 13 CMIP5 GCMs (ENS/GCM) (see Table S1). (d-e) Annual cycles of monthly land precipitation averaged over (d) the southern Iberian Peninsula and (e) northwestern Morocco (see black contours in (a-c)), in TerraClimate (black), ERA/MRCM (red) and ENS/GCM (blue). The light blue shading corresponds to inter-GCM spread in the 13-member GCM ensemble.

especially over northwestern Morocco, though it fails to fully capture the bimodal distribution with two peaks in December and March as evident in TerraClimate. GCM biases over the Iberian Peninsula, especially a peak in precipitation around May and the underestimation of late fall precipitation, are not fully corrected.

Inter-annual variability in precipitation is well captured by ERA/MRCM. Figure 5-5 shows the time series of DJF precipitation anomalies (defined with respect to each series' 1982-2011 mean), over the five selected watersheds (Fig. 5-1-b). Anomaly correlation coefficients range from 0.91 to 0.98, which shows that MRCM, for this domain and at the 12 km resolution, is

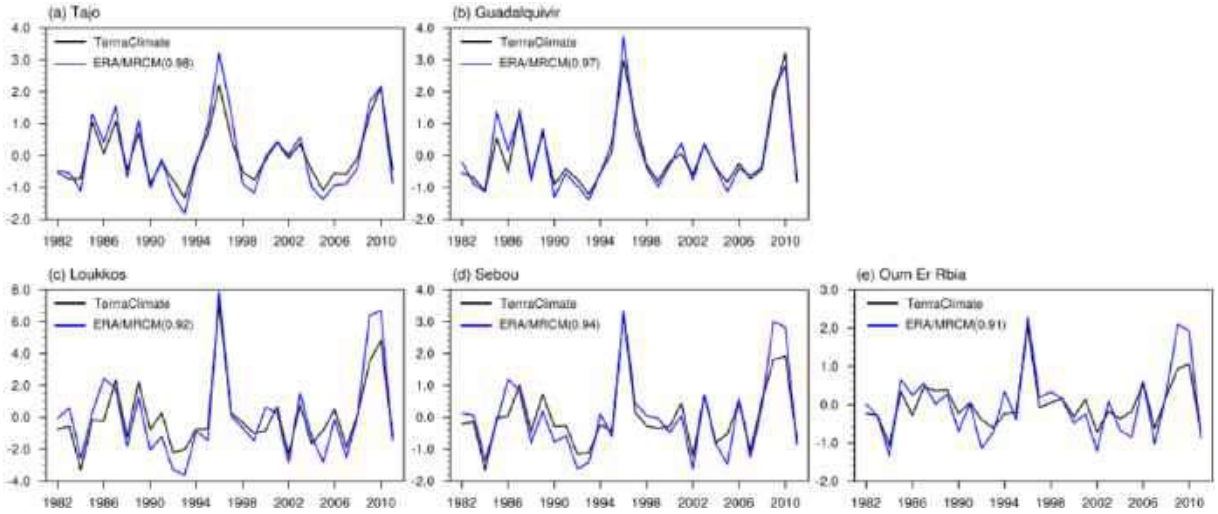

Figure 5-5: Annual DJF precipitation anomalies (mm/day) averaged over the five selected watersheds, in TerraClimate (black) and ERA/MRCM (blue). Anomalies are defined with respect to each series' 1982-2011 average.

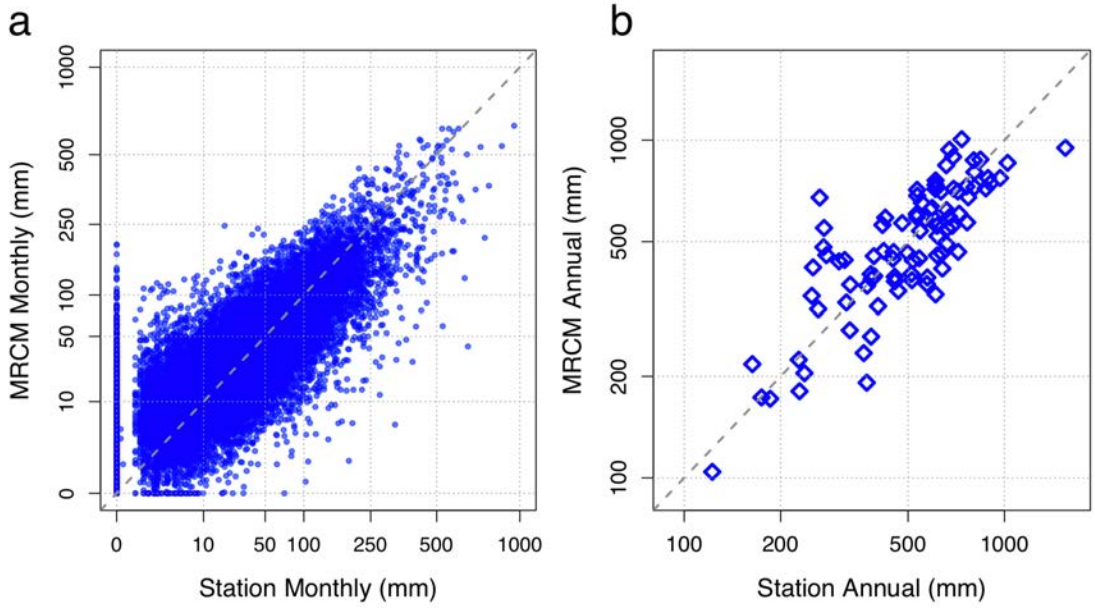

Figure 5-6: (a-b) (a) Monthly and (b) annual-average precipitation at stations and corresponding ERA/MRCM grid cells.

able to correctly simulate the precipitation response to large-scale, NAO-linked storm track shifts present in the boundary conditions. At the station scale, ERA/MRCM and station data also show reasonable agreement for monthly and annual-mean values (Fig. 5-6-a,b). MRCM has a slight wet bias for low precipitation values, and dry bias for high ones. The mean distribution of annual-average precipitation across stations is also satisfactory.

In summary, ERA/MRCM shows satisfactory performance in simulating both the average and the inter-annual variability of winter precipitation over the NWAIP domain. Even though GCM biases translate to the downscaled simulations, the improved representation of topography helps to compensate in part for GCM's dry bias during the wet season.

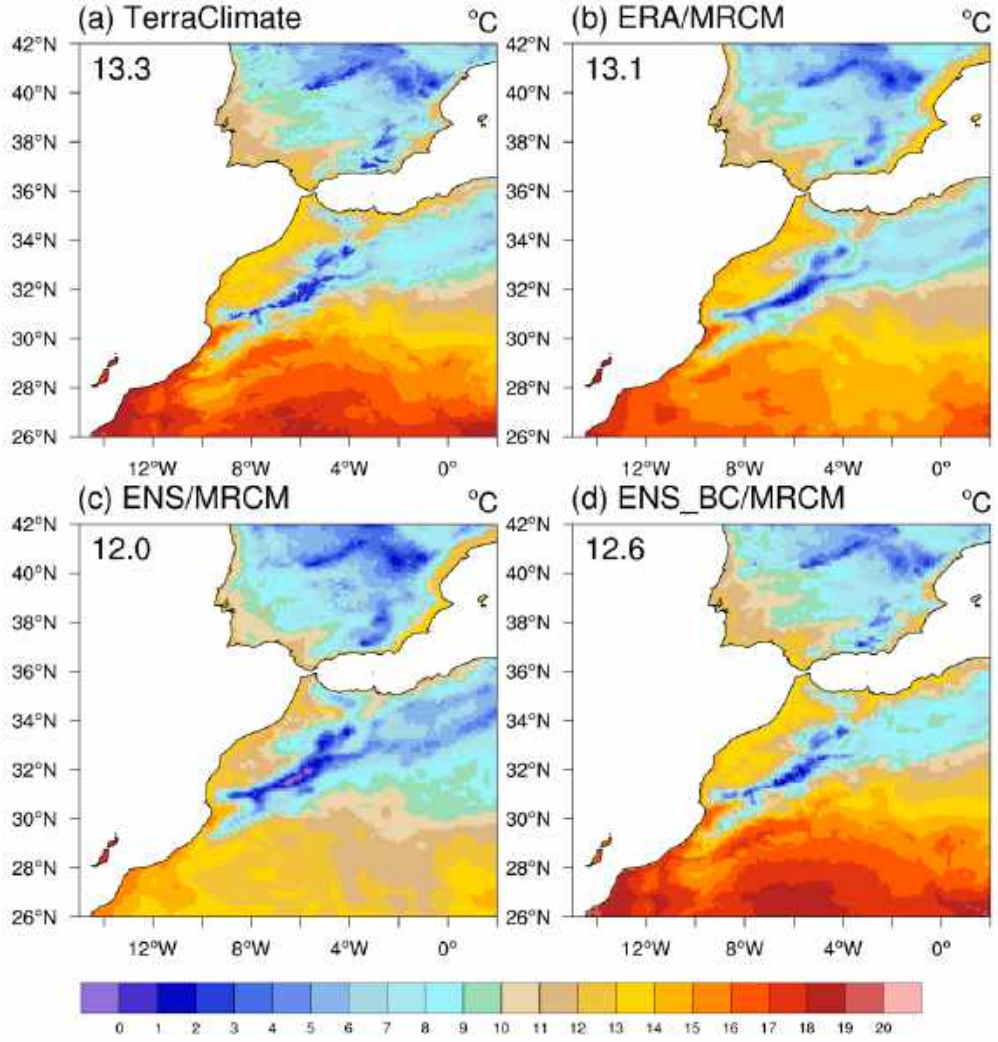

Figure 5-7: Spatial distribution of 30-year climatology of DJF average 2-meter air temperature in (a) TerraClimate, (b) ERA/MRCM, (c) ENS/MRCM (ensemble mean of MRCM simulations) and (d) ENS_BC/MRCM (ensemble mean of bias-corrected MRCM simulations). Domain-averaged values over land are indicated at the top left-hand corner of each plot.

The spatial distribution of winter surface temperature is correctly simulated over the domain, despite a slight warm bias along the coasts and cold bias over the desert (Fig. 5-7-a,b). Domain-wide averages are within each other's uncertainty bounds. The cold bias over desert areas has been pointed out by Pal and Eltahir (2016) in their analyses over the Arabian

Peninsula, a region of similar climate to the Sahara Desert. Although, like them, we force the surface albedo and emissivity in the MRCM runs to equal observed values inferred from NASA's SRB datasets, persistent residual biases over deserts are still possible. In addition, the land surface scheme IBIS used in MRCM also tends to underestimate ground temperature in dry areas free of vegetation. Daily temperature at available stations is also particularly well simulated, generally within the bounds of measurement error, and for both annual cycles and daily variability (Fig. 5-8). Performance in capturing day-to-day variability is slightly lower along the coasts (mainly the Essaouira, Tangier and Saniat Rmel stations), likely due to the strong gradients of weather variables between land and ocean at the 12km scale, particularly water vapor due to its important role in the radiative balance.

5.4.2 Verification of bias corrected MRCM runs

Before analyzing future projections, we also validate the performance of the bias corrected GCM-driven MRCM runs (ENS_BC/MRCM) for the reference period, by comparing their results with those from ERA/MRCM and with observations. Figures 5-9 and 5-7 show the spatial distribution of the 30-year monthly precipitation and surface mean temperature climatologies for the winter season (DJF) derived from TRMM and TerraClimate, ERA/MRCM, ensemble mean of three MRCMs (ENS/MRCM) and ensemble mean of three bias-corrected MRCMs (ENS_BC/MRCM).

For precipitation, ENS/MRCM shows good qualitative correspondence with the observed regional distribution (Fig. 5-9). However, the GCM-driven MRCM runs tend to produce excessive precipitation over higher mountainous regions, particularly over south-central Spain, like the ERA/MRCM run. Wet biases over mountainous areas are indeed a common deficiency in dynamical downscaling, as noted also in other studies [234, 98]. The exception here is IPSL-CM5A-LR, for which the dry bias evident in the GCM output (Fig. 5-3-c) is not fully compensated by the dynamical downscaling. Although it somewhat accurately reproduces long-term NAO dynamics and its relationship to Northern Hemisphere climate variability [264], IPSL-CM5A-LR suffers from an "anticyclonic" bias, with too strong a North Atlantic subtropical high that blocks cyclonic activity and leads to the observed dry bias [53]. Naturally,

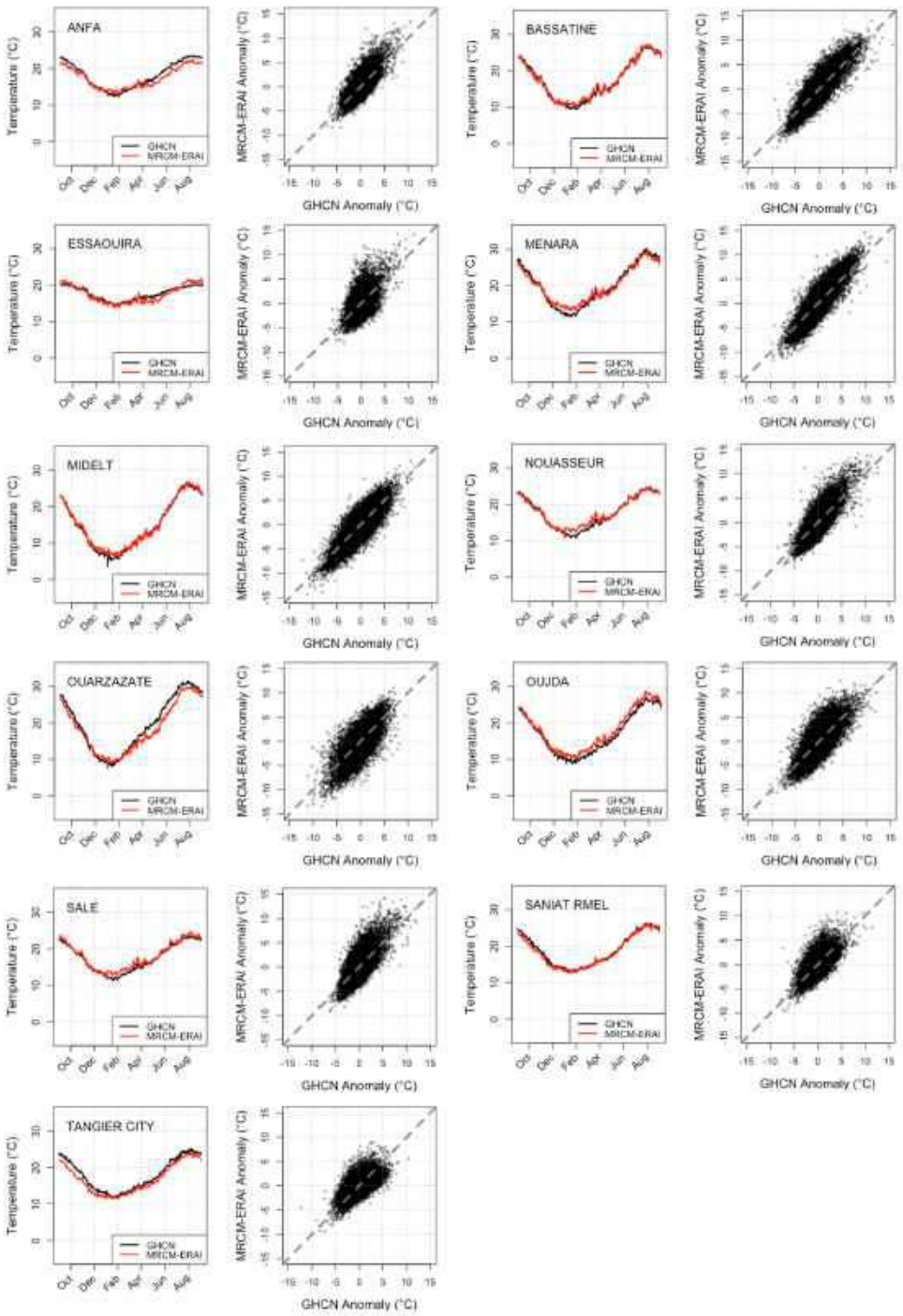

Figure 5-8: Annual cycle of daily temperature at GHCN stations and corresponding ERA/MRCM values, corrected for elevation difference with stations using a locally-estimated daily temperature lapse rate (first and third columns); Deviations from these annual cycles plotted against each other (second and fourth columns), for all 11 available GHCN stations. Station names are indicated in top-left-hand corners.

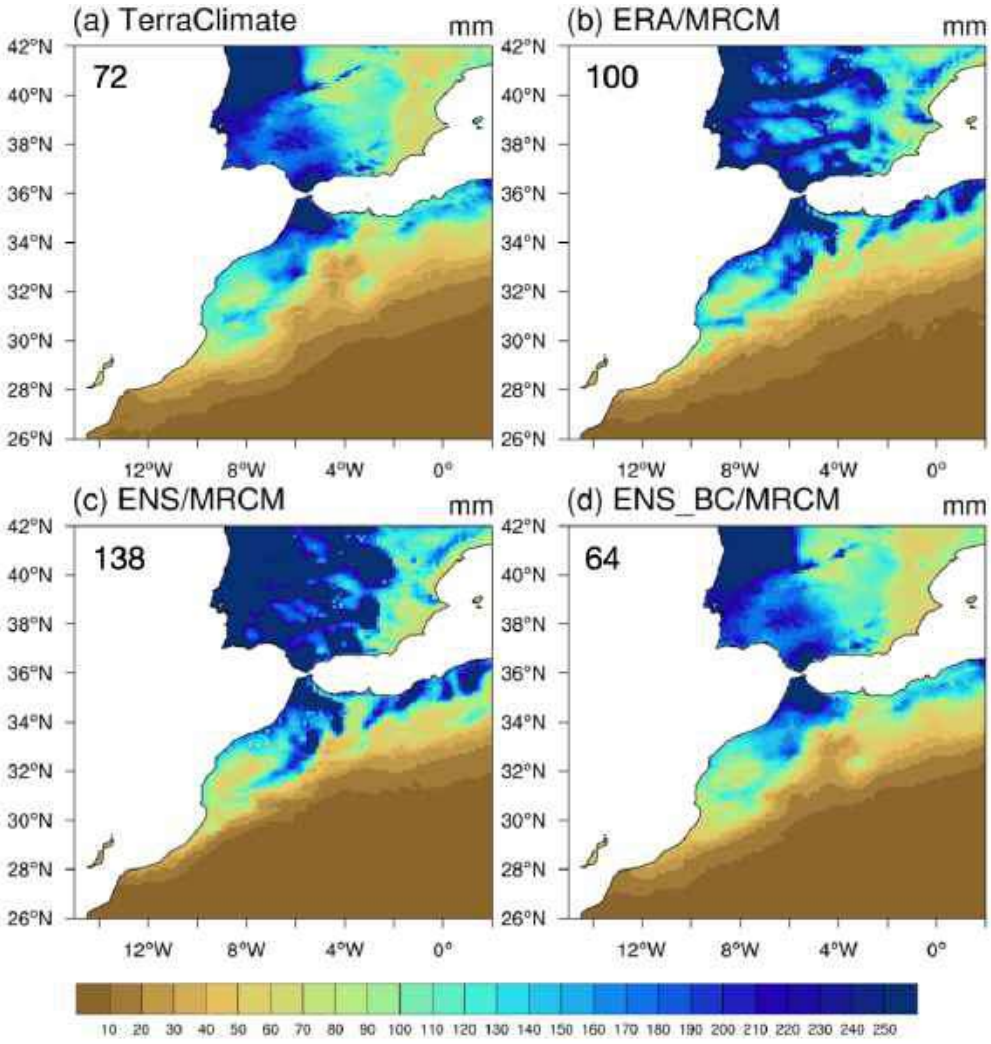

Figure 5-9: Same as Fig. 5-7, for precipitation.

regional downscaling cannot compensate for such biases in the large-scale circulation. By comparison with ERA/MRCM and ENS/MRCM, ENS_BC/MRCM is, as expected, in better agreement with TerraClimate in terms of the spatial pattern and area-averaged precipitation. Bias-corrected precipitation is still somewhat lower than observations over the High- and Anti-Atlas (around 8°W/31°N, see Fig. 2-1). Due to the sharp topographic gradients and the scarcity of station data, however, TerraClimate data is undoubtedly less robust in these regions. Regarding mean surface temperatures, the essential characteristics of the mean DJF pattern are accurately reproduced in both ERA/MRCM and ENS/MRCM, although again there is a pronounced cold bias in ENS/MRCM over much of the domain, highest over the desert. After bias correction, the cold bias still persists but still ENS_BC/MRCM successfully captures the

observed major characteristics in terms of regional variations and area-averaged values (Fig. 5-7).

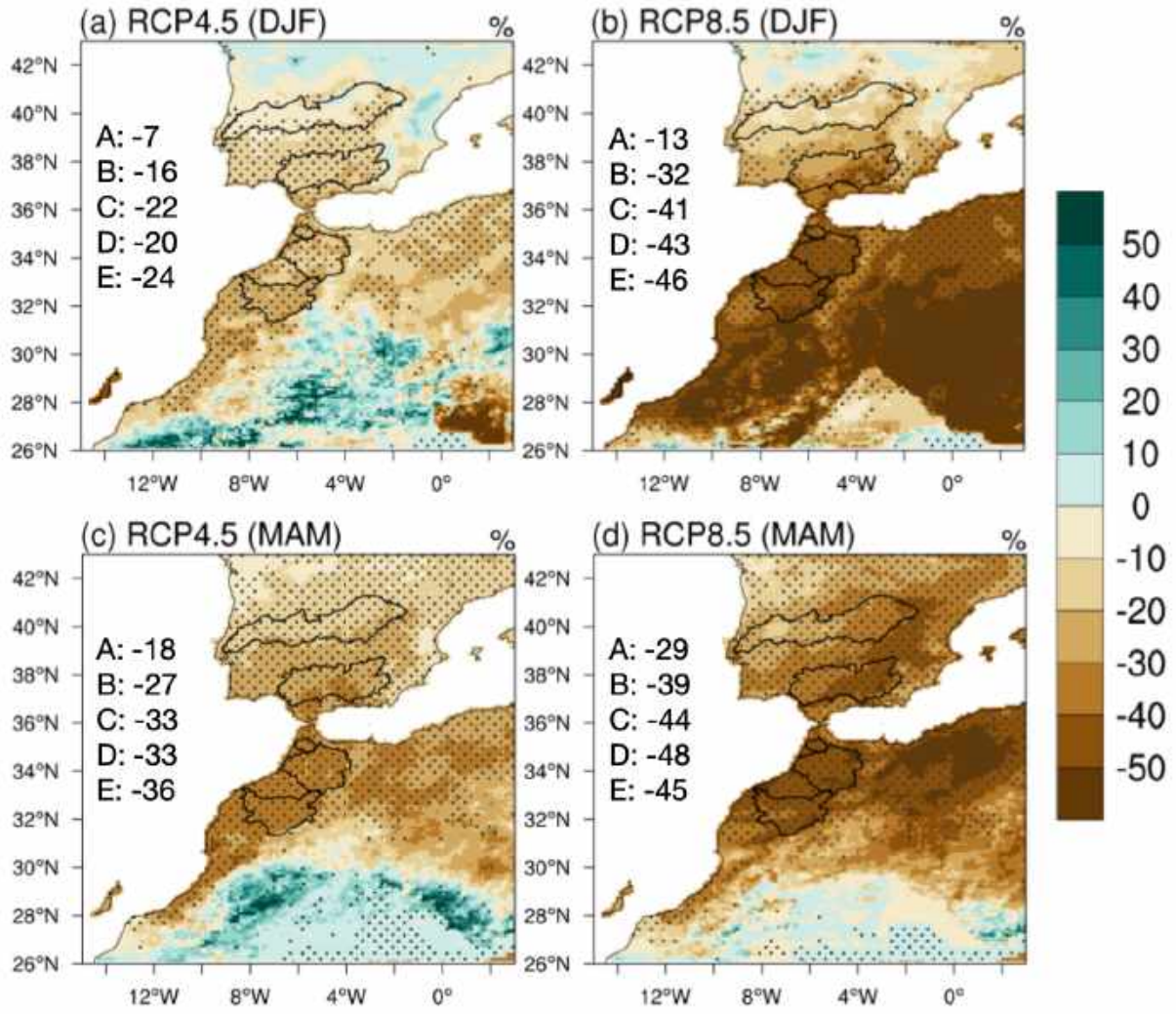

Figure 5-10: MRCM ensemble-mean percentage change in (a,b) DJF and (c,d) MAM precipitation, under (a,c) RCP4.5 and (b,d) RCP8.5, 2071-2100 minus 1976-2005. Mean values averaged over the five watersheds on Fig. 5-1-b are shown on the left-hand side of each plot. Dots indicate agreement by three MRCM simulations on the sign of the change.

5.4.3 Future projections

Precipitation

The spatial distributions of DJF and MAM relative precipitation change under RCP4.5 and RCP8.5 are shown on Figure 5-10. A pronounced and robust large-scale precipitation decline over the domain is evident under both scenarios and in both seasons, consistent with the CMIP5 multi-model mean [252] and earlier CMIP5 projections [101]. For the region as a whole, the drying gradually weakens from southeast to northwest. In winter, regions north of 40°N even show slight wetting trends, albeit not robust at all. The African coastline is projected to experience the largest drying by far (-40/45% under RCP8.5), and quite uniformly too: the three Moroccan watersheds show very similar changes in all cases (seasons/scenarios). The southern coast of the Iberian Peninsula is in an intermediate state, with a robust though weaker winter drying. Under RCP8.5, the drying is about twice as large everywhere compared to RCP4.5: from 7-24% to 13-46% (Fig. 5-10). In relative terms, the decrease in precipitation is generally larger during spring, at which time it also extends further north in the Iberian Peninsula. Indeed, projections suggest somewhat constant winter precipitation amounts over central and Eastern Spain, but a robust 10-30% decline during spring.

Temperature

Regarding temperature changes, mean surface temperature is unsurprisingly projected to increase over the whole domain under both RCP scenarios, roughly proportionally to the radiative forcing (Fig. 5-12). Similar to the precipitation change, the warming exhibits a pronounced meridional gradient during winter. Temperatures are projected to increase more over North Africa (by 0.5-1°C), a possible consequence of its more pronounced precipitation decline through decreased latent heating, although dynamical trends may also play a role (see Discussion). In winter also, warming trends appear larger over the mountains, especially the High and Middle Atlas, and the Sierra Nevada (Fig. 5-12-a,b). This enhanced warming may be connected to the snow-albedo feedback [203, 192], since these areas all possess extensive snowpacks in the current climate, although this process is not very well resolved at our 12km scale

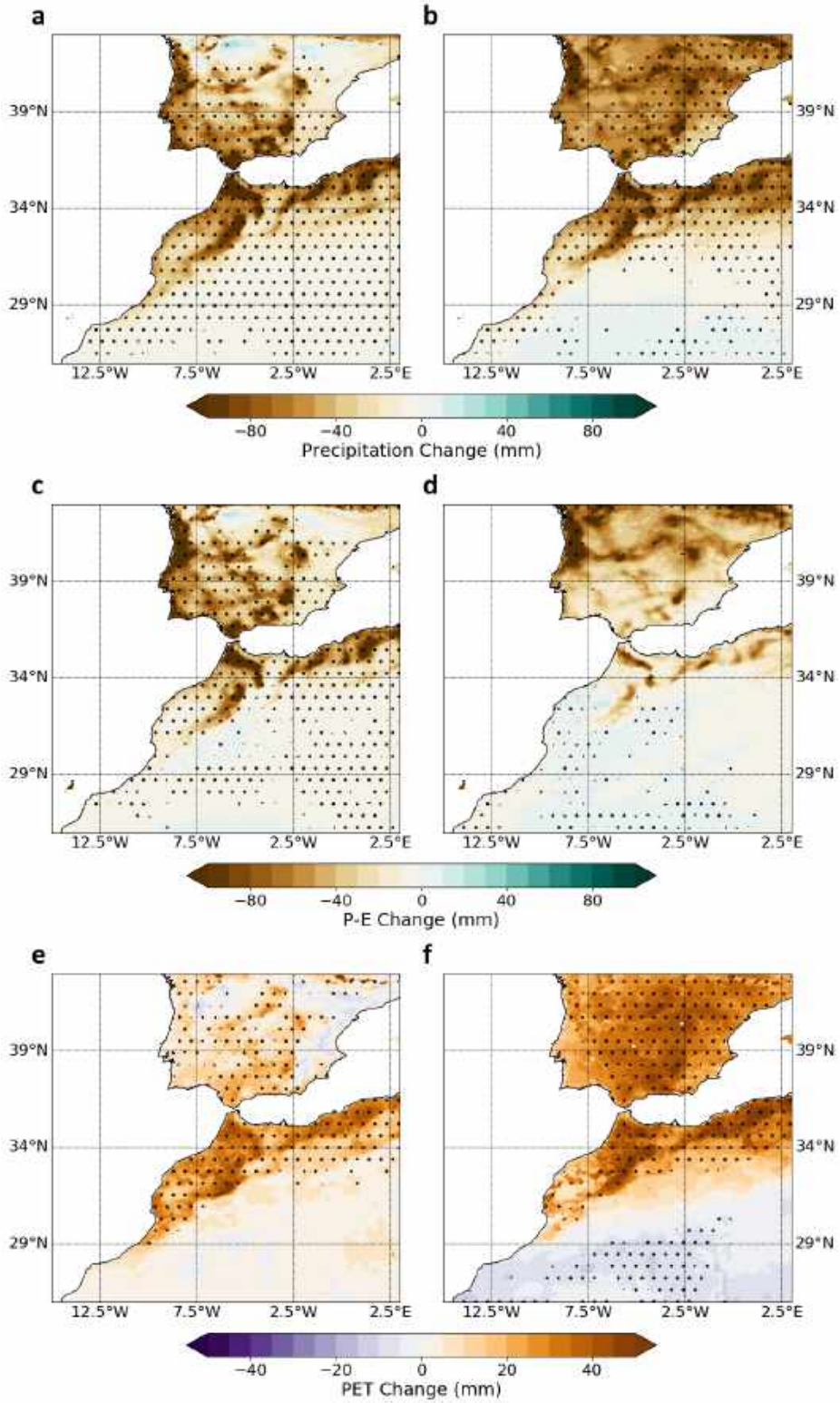

Figure 5-11: MRCM ensemble-mean percentage change in (a,c,e) DJF and (b,d,f) MAM (a,b) precipitation, (c,d) P-E and (e,f) PET under the RCP8.5 scenario, 2071-2100 minus 1976-2005. Dots indicate agreement by three MRCM simulations on the sign of the change.

and deserves a more detailed treatment [259]. Rather, since mountain regions receive higher precipitation amounts during winter, they will experience larger absolute drops in precipitation, and therefore larger reductions in latent heat flux which will impact the temperature change through soil-moisture feedbacks.

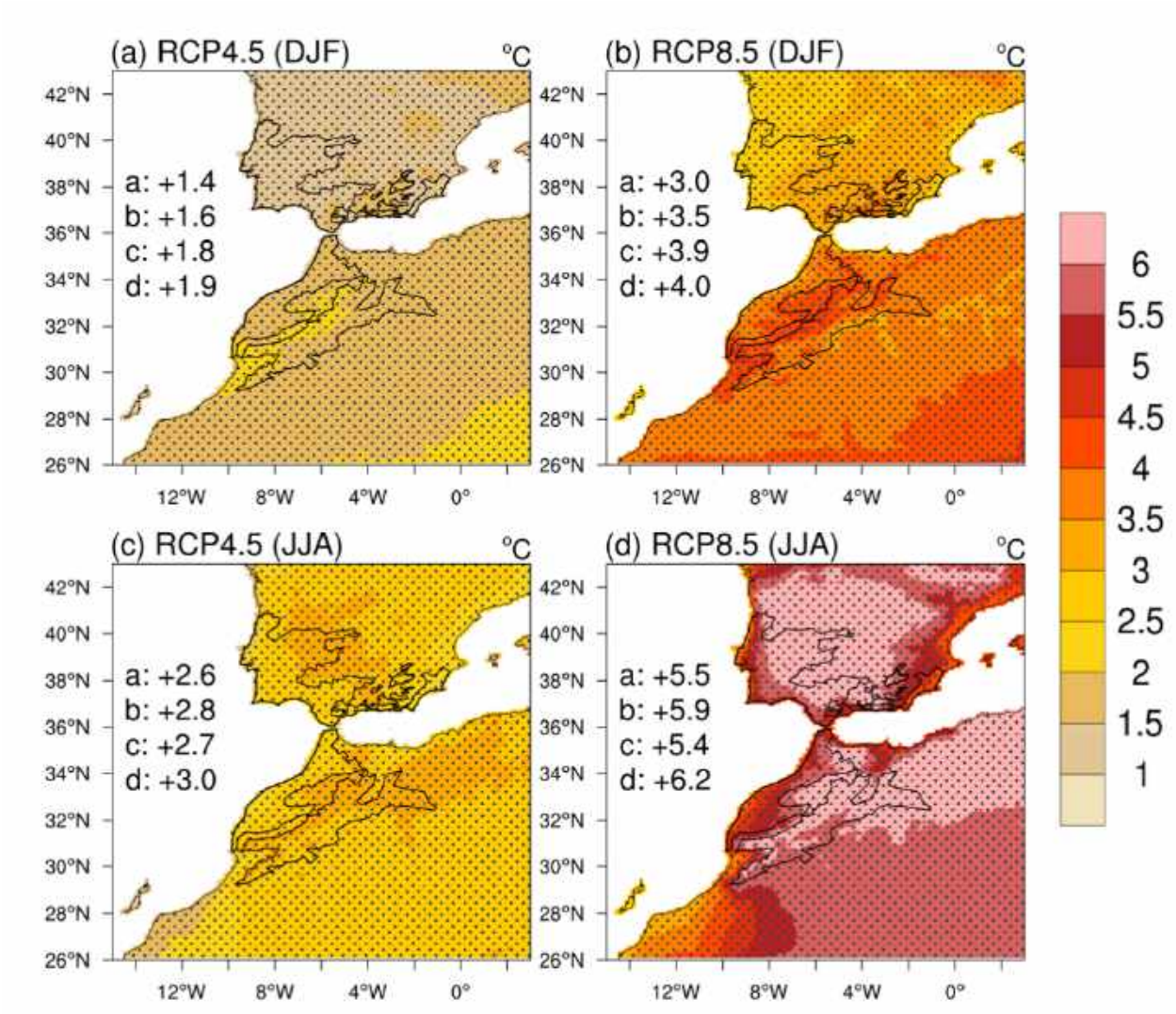

Figure 5-12: MRCM ensemble-mean change in (a,b) DJF and (c,d) JJA surface temperature, under (a,c) RCP4.5 and (b,d) RCP8.5, 2071-2100 minus 1976-2005. Mean values averaged over the four regions on Fig. 5-1-c are shown on the left-hand side of each plot. Dots indicate agreement by three MRCM simulations on the sign of the change.

Summer temperature changes are much higher than in winter (by 1-2°C). They are characterized by a clear coastline/interior contrast, common to all seasons and scenarios, although here again mountain regions seem to exhibit enhanced warming compared to plains, especially

the Atlas and the Pyrénées. As in winter, this may be connected to a reduction in precipitation, here brought by summer convective cells quite common at high elevations in this region [27]. Lapse-rate effects over the Mediterranean are also believed to contribute to the enhanced summertime warming [35]. The reduced warming along the coasts is a classic feature of climate change linked to less pronounced warming of surface air over oceans.

5.5 Discussion: Mechanisms of Regional Climate Change

So far, our downscaling results have been consistent with the existing literature which highlighted a pronounced wet-season precipitation decline and enhanced summer warming [59]. However, the improved representation of the complex regional topography can offer new perspectives on regional climate changes, particularly to understand the physical mechanisms behind the projected decline in precipitation. This regional drying is probably the most critical feature of the climate response to anthropogenic forcing in the Western Mediterranean. Together with enhanced temperatures, it will drive substantial declines in river runoff and water availability and severely threaten the habitability of the region.
The analysis of CMIP5 GCM projections concluded that the regional decrease in winter and spring precipitation followed from enhanced easterly flow under climate change, a feature linked to the development of a strong anticyclone centered on the Mediterranean (Chapter 4). The pronounced anomalous that develops over the Mediterranean Basin (Fig. 4-1-a) is highly robust across models and its magnitude essentially determines that of the regional winter drying. The associated wind changes impact the hydrology of the whole Mediterranean Basin, also causing a decline in winter precipitation over its eastern shores. This strong anomalous high finds its origin in the combination of large-scale shifts in winter planetary waves due to the strengthening of the mid-latitude jet [231] and to the reduced warming of the Mediterranean Sea with respect to the surrounding land, which triggers a circulation response characterized by higher pressure over the region.

Because the Western Mediterranean is characterized by a steep northeast-southwest humidity gradient, between the relatively moist western side of the Atlas Range, which stands

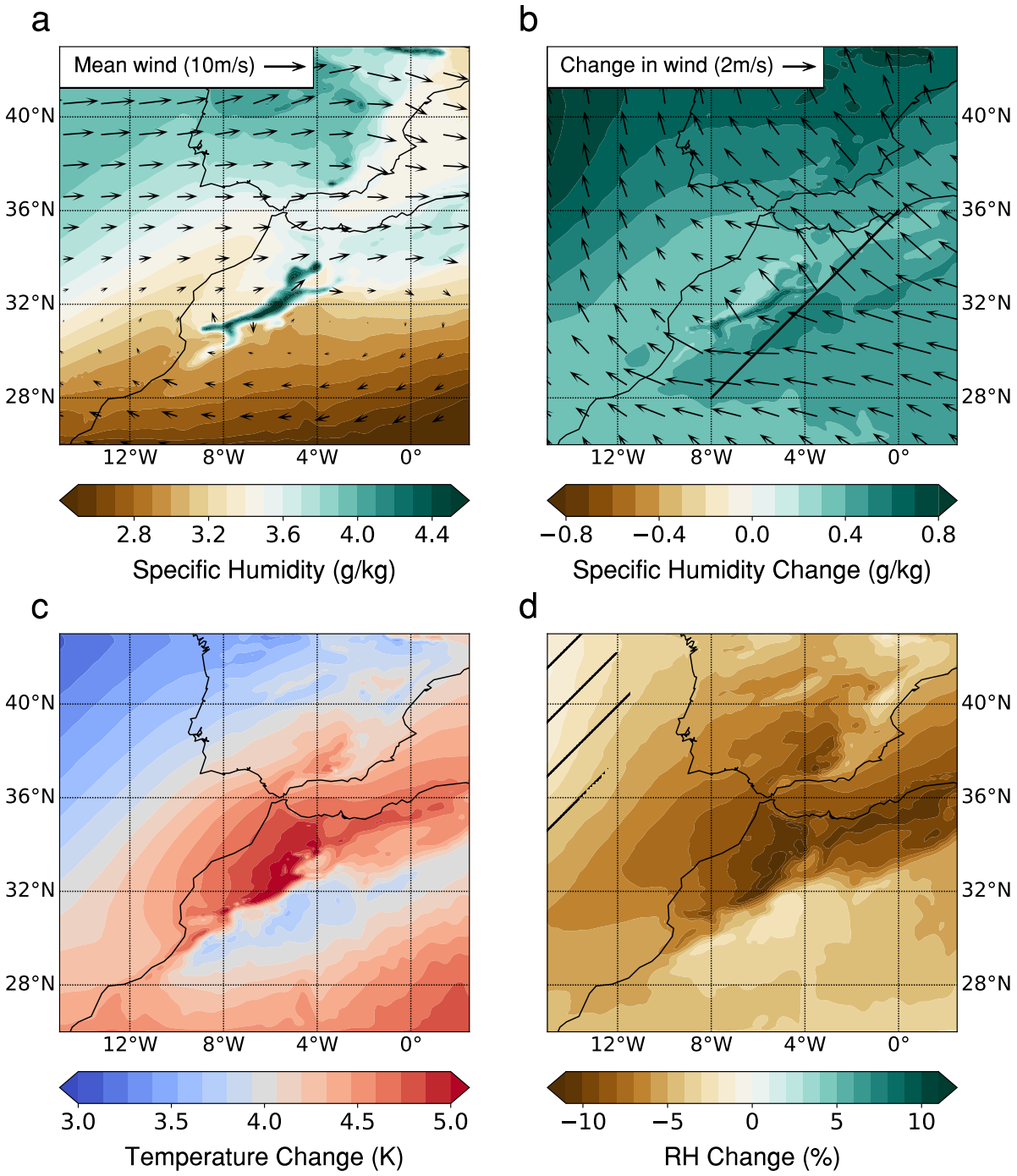

Figure 5-13: (a) DJF MRCM ensemble-mean historical (1976-2005) 850 hPa specific humidity (shaded) and circulation (arrows). (b,c,d) MRCM ensemble-mean change in 850 hPa DJF (b) specific humidity (shaded) and circulation (arrows), (c) temperature and (d) relative humidity, under the RCP8.5 scenario, 2071-2100 minus 1976-2005. Hatching in (d) indicates disagreement by one of the three models on the sign of the change. The solid black line in (b) is used to define a regional wind index (see text).

under oceanic influence, and the dry Sahara Desert to the east (Fig. 5-13-a), changes in average winds, however small, can significantly impact the regional moisture distribution. Looking at the MRCM projections, we find definite trends towards a more easterly kind of circulation in both winter and spring, consistent with the regional picture just mentioned (Fig. 5-13-b). Average changes in just three models are very similar to the much larger CMIP5 multi-model mean, underlining the robustness of regional wind trends under continued anthropogenic forcing. Wind changes over North Africa and southern Spain average about 2m/s at 850 hPa; this must be compared to average westerlies of 1-5 m/s, which is quite weak, even during the wet season when moisture advection from the North Atlantic is largest (Fig. 5-13-a). Storms that hit Morocco and the southern parts of the Iberian Peninsula indeed remain quite rare, even under negative NAO conditions.

The robust shift towards enhanced easterlies, which should lead to enhanced advection of dry air, is consistent with regional projections of atmospheric moisture (Fig. 5-13-b). The northwest African and southern Iberian coastlines are located near areas of local minima in atmospheric humidity increase; the rest of the region, particularly northern Spain and Portugal, exhibit much larger moistening trends. The lowest increase is found over the western foothills of the High Atlas. Two factors probably combine to further limit the increase in humidity over this small region. First, the humidity gradient is particularly steep, with the Atlas acting like a barrier between the very dry Sahara and their much moister western flanks. Second, a future circulation with more frequent easterlies will result in strengthened descent of dry air, its moisture having been "squeezed" out as it passed over the mountains. In other words, this region will become a rain shadow as the prevailing winds change direction. This interpretation is further buttressed by the enhanced local wetting on the southeastern side of the Atlas (e.g., around 4°W-32°N, Fig. 5-13-b), which clearly points to enhanced removal of atmospheric water on what is currently the leeward side of the mountain range.

Therefore, for the region as a whole, the circulation shift acts to both increase dry advection, and to cut off the moisture supply from the Atlantic, consistent with the discussion in Chapter 4 based on CMIP5 projections. Relative humidity, however, is not only dictated by moisture content but also temperature (Fig. 5-13-d). Regional projections show a stark enhancement of lower-tropospheric warming in the regions downwind of future wind anomalies, i.e. on

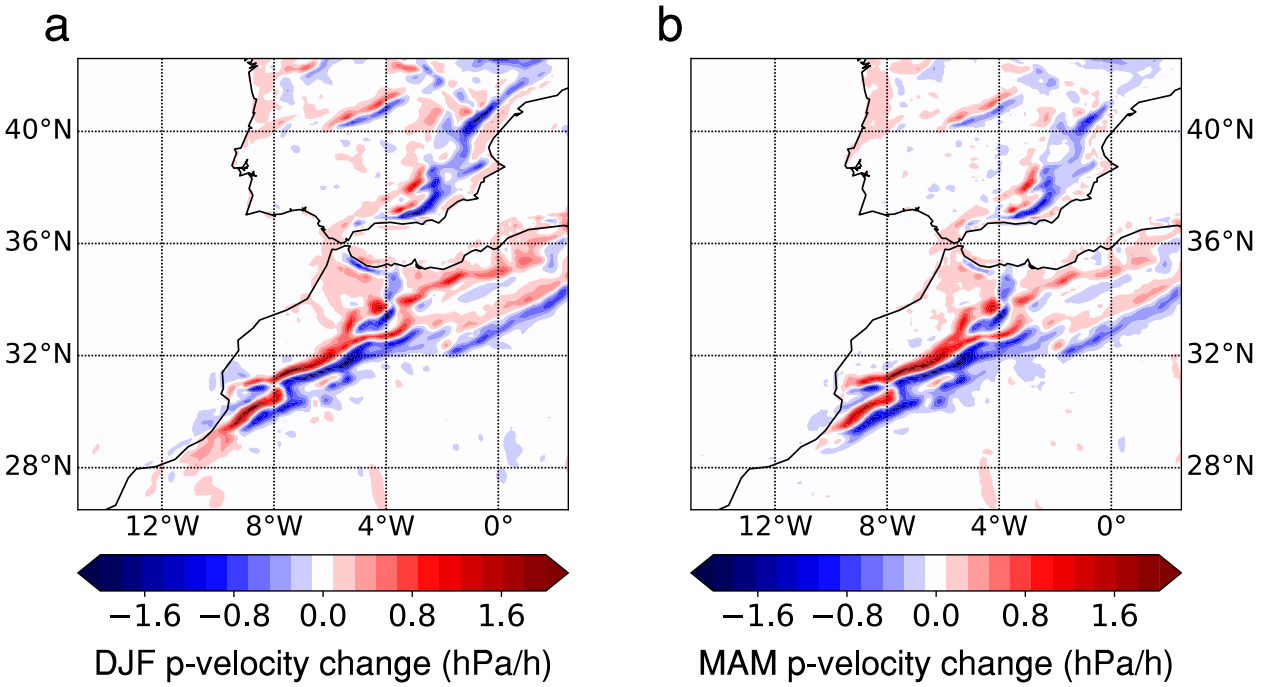

Figure 5-14: MRCM ensemble mean change in 850 hPa pressure-velocity in (a) DJF and (b) MAM under the RCP8.5 scenario, 2071-2100 minus 1976-2005.

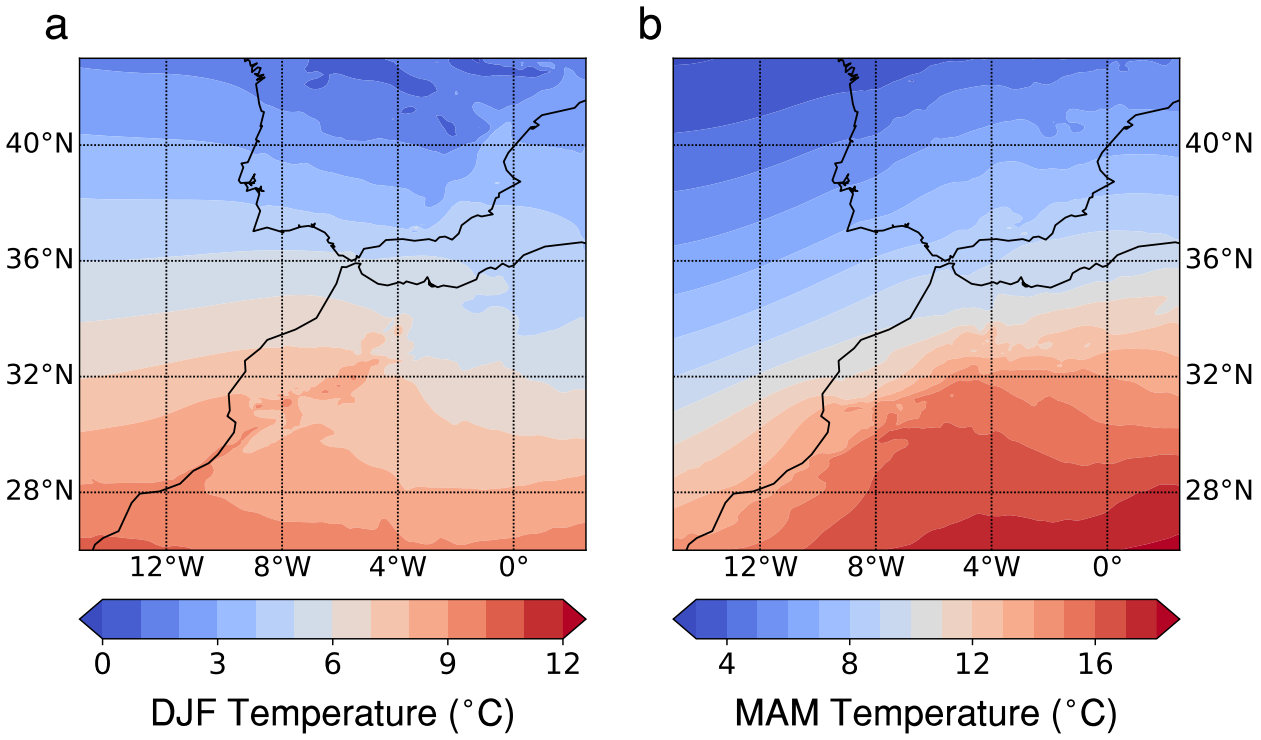

Figure 5-15: ERA/MRCM mean 850 hPa temperature in (a) DJF and (b) MAM.

the northwestern flanks of the Atlas Range and Sierra Nevada (Fig. 5-13-c, S2-c). At the same time, the warming is relatively weaker, by 1-1.5°C, on the upslope slide, especially the Saharan Atlas. The geography of the warming and wind change patterns, common to both winter and spring, suggests that topography-driven anomalous vertical motion is an important driver. Strengthened easterlies lead to uplift southeast of the mountain ranges (i.e., upwind) and subsidence on their northwestern slopes (i.e., downwind), respectively associated with adiabatic cooling and warming. Changes in vertical motion near the boundary layer top are consistent with this perspective (Fig. 5-14). In fact, the more realistic topography in MRCM simulations generates stronger subsidence motion and enhanced warming locally (not shown). While temperature gradients across the Atlas Range are negligible in winter, they strengthen over spring as the Sahara Desert warms up fast (Fig. 5-15); consequently, enhanced easterlies likely also contribute to the substantial warming over northwestern Morocco and the Algerian coastline at that time of year. Other factors, such as the soil moisture feedback or the snow feedback over the high mountain peaks, may also play a role.

We further explore the role of the regional circulation in determining hydroclimate trends by defining, as a proxy for the regional circulation, a wind index along the African coastline (see line in Fig. 5-13-b), where future projections show enhanced easterlies. The value of the index is defined as the direction (in degrees) in which the wind blows; for example, a westerly wind will have an index of 0° and a southerly wind an index of +90°. We focus on the November-April period, the wet season for most of our domain. This index strongly determines to the likelihood of precipitation over Northwestern Morocco and the southern Iberian Peninsula (Fig. 11-a), a relationship that, overall, MRCM simulations succeed in capturing (Fig. 5-16-b, 5-17). Precipitation occurs, as expected, when westerlies prevail (wind index between -45° and 45°). Similarly, easterlies tend to be associated with dry conditions (index higher than 135° or lower than -135°). On the whole, westerlies are more frequent, as would be expected in the midlatitudes during winter. Consistent with regional circulation changes (Fig. 5-13-b), the frequency of northwesterlies decreases across all simulations (by 10-40% across models), while that of southeasterlies goes up significantly. While westerlies are still the most frequent circulation regime, southeasterly winds (index between 90° and 180°) become much more common. Meteorological conditions during southeasterly days are characterized by a

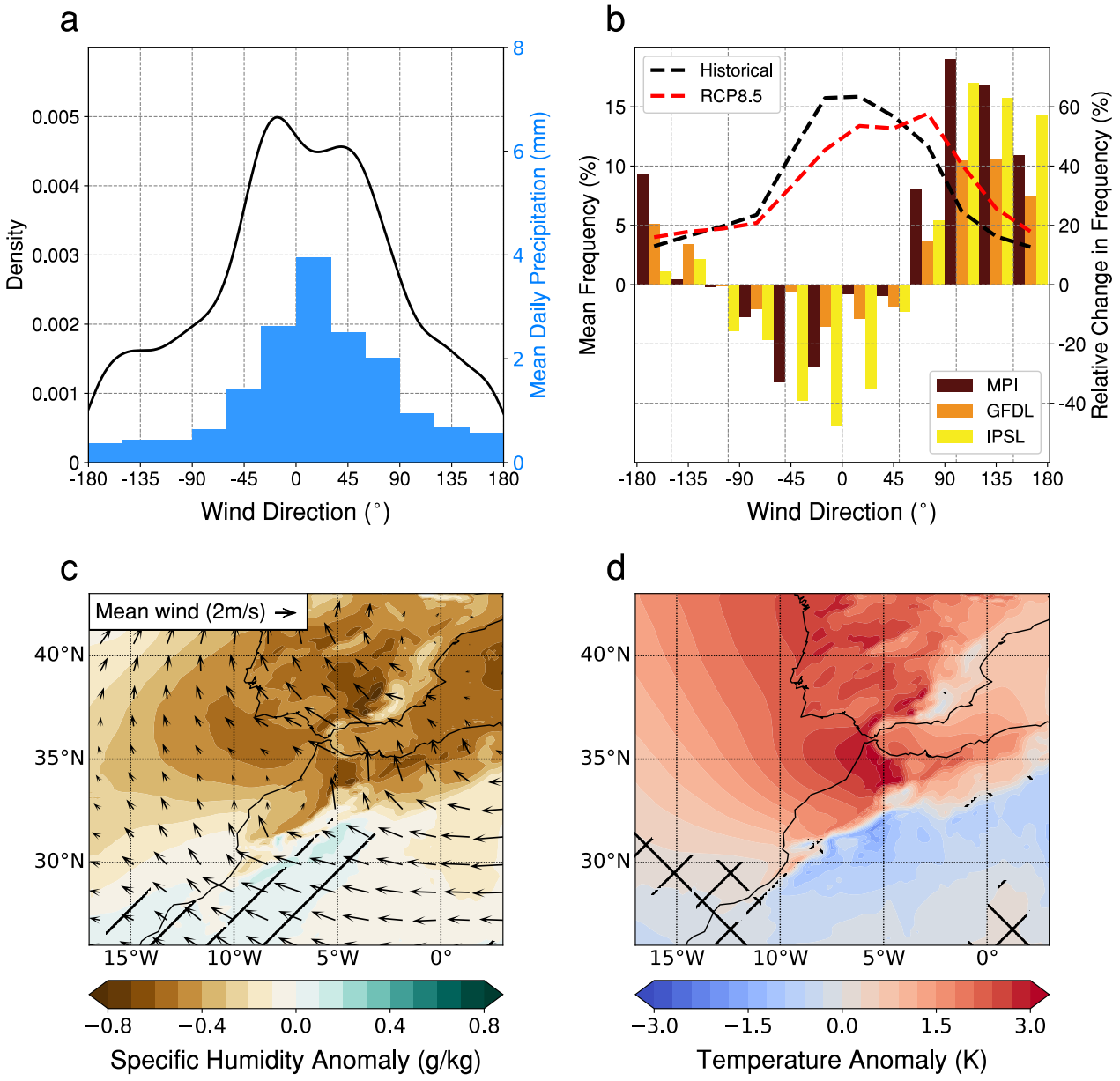

Figure 5-16: (a) Distribution of November-April daily wind index values from ERA-Interim (solid black line) and average daily precipitation from TRMM over northwestern Morocco and the southern Iberian Peninsula (up to 38°N) in each 30-degree wind direction category (blue bars). (b) MRCM ensemble-mean distribution of November-May daily wind index values in the historical (dashed black) and RCP8.5 (dashed red) simulations, and relative change in the frequency of each 30-degree wind index category for the three MRCM runs (colored bars). (c,d) MRCM ensemble-mean average 850 hPa (c) specific humidity anomaly (shaded) and wind values (arrows) and (d) temperature anomaly, during "southeasterly days" (when the wind index is between +90° and +180°) in historical simulation. Hatching in (c,d) indicates disagreement by one of the three models on the sign of the anomaly.

substantial atmospheric moisture deficit over the Iberian Peninsula and along the northwestern African coastline (Fig. 5-16-c), and the wind pattern is very similar to the future projected shift (Fig. 5-13-b). Additionally, southeasterly days exhibit warmer-than-usual temperatures over the same regions with moisture deficit, and cooler-than-usual temperatures on the upwind side of the Atlas and Sierra Nevada, a pattern highly similar to the projected temperature change (Fig. 5-16-d and Fig. 5-13-c). This confirms the hypothesis that the circulation shift is responsible for the increase in moisture deficit and enhanced warming seen in regional projections. The combined effects of those mechanisms result in a large decrease in lower-troposphere relative humidity over Northwestern Morocco and Algeria, southern Spain, and the surrounding ocean (Fig. 5-13-d), from which the precipitation decline follows.

5.6 Analysis of subseasonal extremes

We now move beyond seasonal means to analyze future trends in sub-seasonal climate indices, more specifically extremes. Extremes are particularly relevant for climate change adaption and risk, as they tend to be associated with the largest impacts on human systems (droughts, floods, etc.) Accurate simulations of the distribution of various climate extremes is still challenging for most global and regional climate models. Therefore, robust projections of future risk from such extremes require station data for the validation of historical runs and their bias-correction. However, station data is by definition available only in specific locations that do not cover the whole simulation domain. Point locations are not enough to evaluate risks from sub-seasonal climate extremes. Rather, we would prefer to have access to the corresponding spatial field, which requires moving from a univariate to a multivariate perspective. Recent years have seen substantial developments of spatio-temporal statistical models for weather extremes, e.g. in the case of extreme rainfall [54, 243, 218]. All rely on extreme value statistics, the branch of statistics that applies to extremes of random variables. In particular, max-stable models have emerged as a reliable tool to model extreme fields from pointwise measurements while taking spatial relationships and dependence into account. In the following, we apply max-stable models to infer future risks of droughts over northwestern Morocco. We also analyse extreme warm days during the growing season, for which however station data is not sufficient to fit

spatial models. The selected indices for extremes are relatively simple and are not intended to cover all weather extremes potentially relevant for agriculture. Rather, we analyze them in the spirit of a proof of concept which could be developed further according to specific needs formulated by local stakeholders.

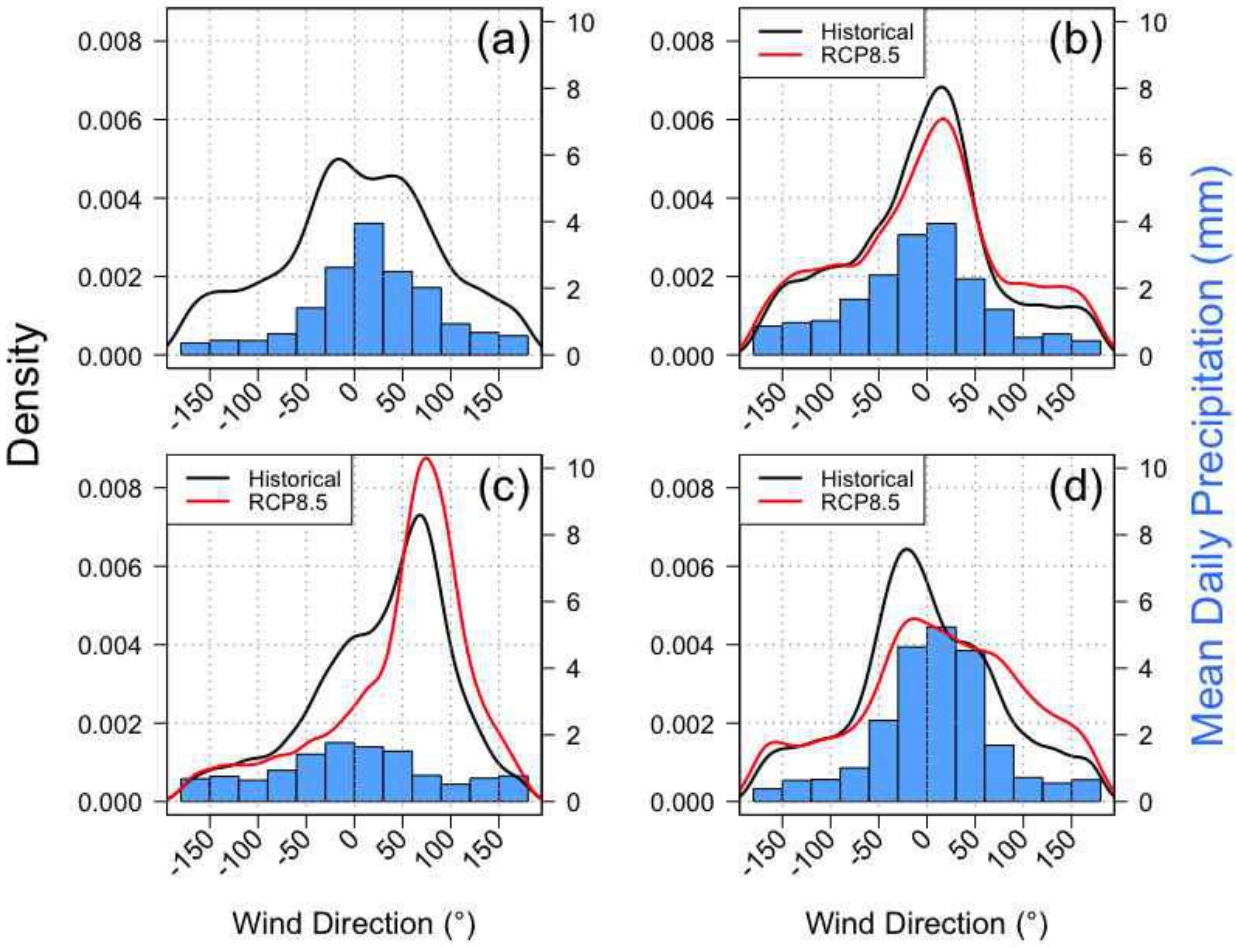

Figure 5-17: (a) Distribution of November-May daily wind index values from ERA-Interim (solid black line) and average daily precipitation from TRMM over northwestern Morocco and the southern Iberian Peninsula (up to 38°N) in each 30-degree wind direction category (blue bars). (b,d) Same as (a) but with data from (b) MPI-ESM-MR, (c) IPSL-CM5A-LR and (d) GFDL-ESM2M, and with the addition of the RCP8.5 wind index distribution (solid red lines).

5.6.1 Extreme values statistics and max-stable models

Univariate extreme value theory is well-developed and an introduction to it can be found for instance in Coles (2001) [47]. What is important to note here is that block maxima M_n of a univariate time series (*i.e.* maxima taken over successive and exclusive time slots, like years), under certain assumptions of convergence, will in the asymptotical limit of large blocks follow a Generalized Value Distribution (GEV) with a cumulative distribution function expressed as:

$$P(M_n \leq y) = \exp\left[-\left\{1 + \xi\left(\frac{y-\mu}{\sigma}\right)^{-1/\xi}\right\}\right] \tag{5.1}$$

for all y such that $1 + \xi\left(\frac{y-\mu}{\sigma}\right) > 0$ and where σ is called the scale parameter, μ the location parameter and ξ the shape parameter. ξ provides information about the tail of the distribution: the $\xi > 0$, $\xi = 0$ and $\xi < 0$ cases are respectively referred to as heavy-, light- and bounded-tailed cases. In environmental sciences, extreme temperatures are an example of a bounded-tail variable, while heavy precipitation is one of a heavy-tailed variable.

Max-stable models (or processes) are a natural extension of univariate extreme values to continous space with dependence between variables. If s is our variable of space (*e.g.* latitude and longitude), a max-stable process $Z(s)$ can be formulated as

$$Z(s) = \max_{i \geq 1} \zeta_i f(s - Y_i) \tag{5.2}$$

where (ζ_i, U_i) are points of a Poisson process on $(0, +\infty) \times \mathbb{R}^d$ (here we take $d = 2$) with intensity measure $\zeta^{-2} d\zeta du$ and f is a probability density function on $\mathbb{R}^2$. Different choices for f yield common models such as the Brown-Resnick or extremal-t models [54]. This representation allows for a rough understanding of the statistical object. The Y_i can be interpreted as centers for the location of different extreme events, whose shape in space is defined by f (think of a Gaussian surface on $\mathbb{R}^2$), and ζ_i characterizes the intensity of that extreme event. A max-stable model then emerges as the maximum value, in each point of space, of the infinite number of values obtained from each extreme event at that particular location. One simple way to understand this is to think of Y_i as "heatwave" centers, f as the heatwave "shape" and ζ_i as

its magnitude: over a given region, the maximum temperature field observed in a season will indeed be the field of maxima obtained from all possible heatwaves over that region. The main advantage of using a max-stable model is that it captures the spatial dependence of extremes. Therefore, it allows to accurately simulate fields of extreme variables based on information at only a few specific locations.

In a max-stable model, marginal densities (at station locations) follow a GEV distribution (5.1). Checking that observations are consistent with this implication is therefore an important step to validate the use of a max-stable model. Spatial covariates, like elevation or latitude, can be incorporated into the model as explanatory covariates for the σ and μ parameters in the GEV marginals (ξ, being more difficult to estimate, is usually taken as constant [54]). We select several potential such covariates (latitude, longitude, elevation, mean annual precipitation and distance to the coast) and select the best model using a stepwise regression framework in which the best covariate is selected at each step until no more improvement to the model is found [250]. "Best" is defined by the Takeuchi Information Criterion [218]. We also test different model classes (Brown-Resnick and extremal-t). The model is fitted by maximizing the corresponding composite likelihood [243], for which we use here the SpatialExtremes R package [207]. The package also allows to simulate from the model once fitted – we simulate here 1000 random extremal fields to calculate median CDD values and probabilities of maximum CDD being above various thresholds.

5.6.2 Future drought risk

We define drought extremes as the maximum number of consecutive dry days (CDD) between November and April, or roughly the growing season in Morocco [14] (see section 5.2), with a threshold of 0.5mm/day of precipitation to separate dry from wet days. We focus on the northwestern part of Morocco only, bounded by the Atlas Range and Rif mountains (see inset in Fig. 5-19-a), where almost all of the country's agriculture is concentrated and which include 88 of the 90 available precipitation stations. The statistics of the corresponding dry CDD series all closely follow GEV distributions (Fig. 5-18-a), which justifies the use of max-stable processes to model their dependence in space.

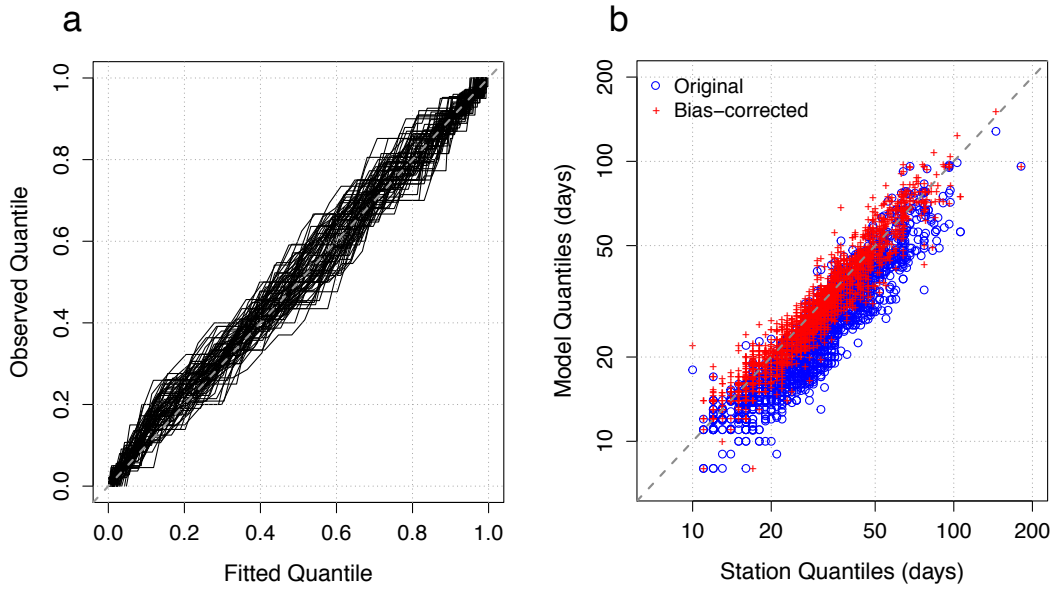

Figure 5-18: (a) Observed maximum CDD quantiles against quantiles estimated from a fitted GEV distribution for each of the 88 stations. (b) ERA/MRCM maximum CDD quantiles (original: blue; after bias-correction: red) against station quantiles, for all 88 stations.

Compared to station data, ERA/MRCM suffers from a wet bias which leads to shorter dry periods, but which is substantially reduced after bias-correction (Fig. 5-18-b). Model fitting indicates that an extremal-t process with $\mu = \mu_0 + \mu_1 \times \text{latitude} + \mu_2 \times \text{longitude} + \mu_3 \times \text{elevation}$ and $\sigma = \sigma_0 + \sigma_1 \times \text{latitude}$ yields the best fit. For the extremal-t process, the f function of equation 5.2 is defined as $f(x) = c_\nu \max(0, W(x))$ where $W(x)$ is a stationary Gaussian process and $c_{nu} = \sqrt{\pi} 2^{-(\nu-2)/2} \Gamma\left(\frac{\nu+1}{2}\right)^{-1}$ where *Gamma* is the Gamma function [218].
The max-stable model succeeds in capturing the dependence between stations (Fig. 5-19-b). Simulated fields of maximum CDD highlight the wet north/dry south pattern also clear in station data (Fig. 5-19-a). Median maximum dry periods in the northern tip of Morocco are typically around 25-30 days, but 35-40 days south of 32°N. Individual stations deviate from the mean pattern, which also exhibits less small-scale variability than station values, which is unsurprising since local effects that matter at the station scale (rain shadows, exposure, inter-annual variability) are not taken into account in the model.

We now apply the same procedure to bias-corrected MPI and GFDL MRCM runs: max-stable models are fitted to each of the six runs (two models and three scenarios). As expected from the overall drying tendency projected for the whole region (Fig. 5-10), median maximum

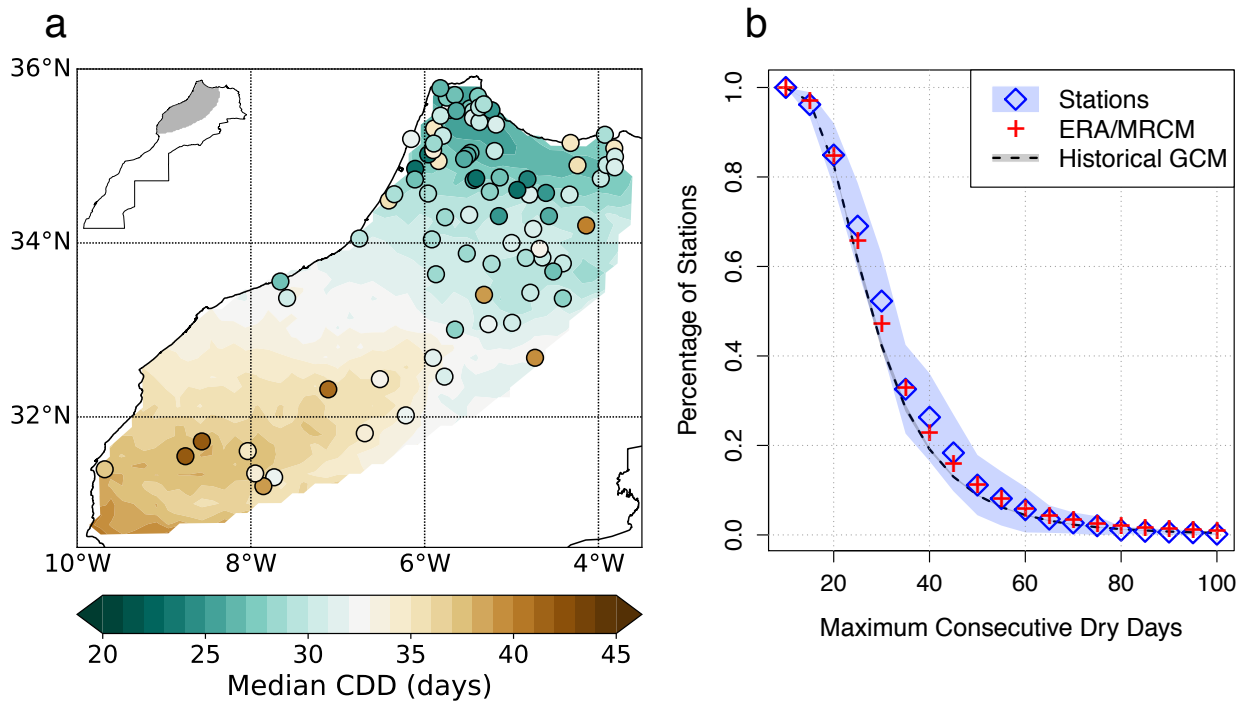

Figure 5-19: (a) Median of maximum November-April CDD length over northwestern Morocco, as estimated by a max-stable model fitted to ERA/MRCM bias-corrected data at station locations (shaded contours) and in observed station data (filled circles). The topleft inset shows the location of the analysis region within Morocco. (b) Percentage of stations experiencing a maximum CDD length longer than N days as a function of N, in station data (median: blue diamonds; 95% confidence interval: shaded light blue), bias-corrected ERA/MRCM (red +) and historical bias-corrected MRCM runs (MPI+GFDL; median: dashed black; range: shaded gray).

CDD values will increase over the domain (Fig. 5-20). The increase is quite uniform under RCP4.5 (Fig. 5-20-a), at about +6 days, but displays a clear north/south gradient under RCP8.5 with drying decreasing with latitude. Changes in this second scenario range from +8/12 days to the north to +14/18 days to the south.

Median values are informative, but say nothing about the tail of the distribution, in this case particularly dry years that have the potential to annihilate rainfed crops. In the current climate, the likelihood of experiencing at least one full dry month during the growing season is about 60% to the south of the region, and only 30% to the north (Fig. 5-21-a,b,c). Despite its weak changes in median CDD values, the RCP4.5 scenario would increase that probabil-

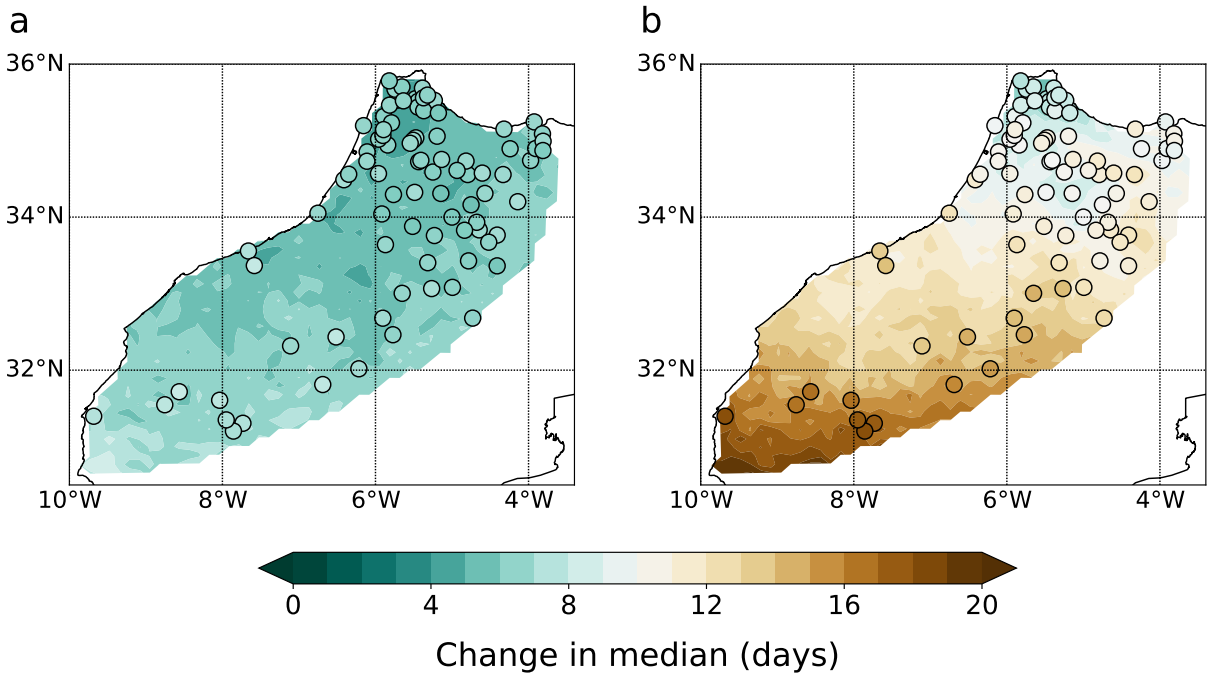

Figure 5-20: Change in median maximum November-April CDD length over northwestern Morocco, as estimated by a max-stable model fitted to bias-corrected MPI and GFDL MRCM data at station locations (MPI+GFDL average, shaded contours) and in bias-corrected MPI/GFDL data at station locations (filled circles), under (a) RCP4.5 and (b) RCP8.5.

ity to above 50% of the whole region. RCP8.5 would make it a quasi-certainty everywhere south of 33°N. The occurence of two consecutive dry months is extremely rare in the present climate, but would increase significantly to preoccupying levels under RCP8.5, becoming a twice-in-a-decade event over three quarters of the region (Figs. 5-21-d,e,f and 5-22). The two simulations (MPI and GFDL) show reasonable agreement regarding their projections, less so for the RCP4.5 scenario (Fig. 5-22). Both highlight the large projected increase in the risk of very long droughts, even under the mitigation scenario.

These projections have important implications for the region's agriculture. In the current climate, crop failures are already common in the dry plains near Marrakech (31-32°N) – as evidenced by the dry 2018-2019 and 2019-2020 seasons and the corresponding severe drops in crop yields. Importantly, our results suggest that conditions prevailing there today will become the normal for the north as well, which may therefore enter a state of quasi-permanent water shortages. Rainfed agriculture, already marginally productive in the south, will become all but impossible – at least for important rainfed crops like cereals – while yields to the north

may decline as droughts become more frequent and severe. Morocco's planned $8bn "Water Highway" project will also undoubtably be severely impacted with water surpluses in the north becoming scarcer and smaller [73]. Significant adaptation measures will be required, such as the transition to drought-tolerant crops, the development of tree crops like olives and improved management of water for irrigation.

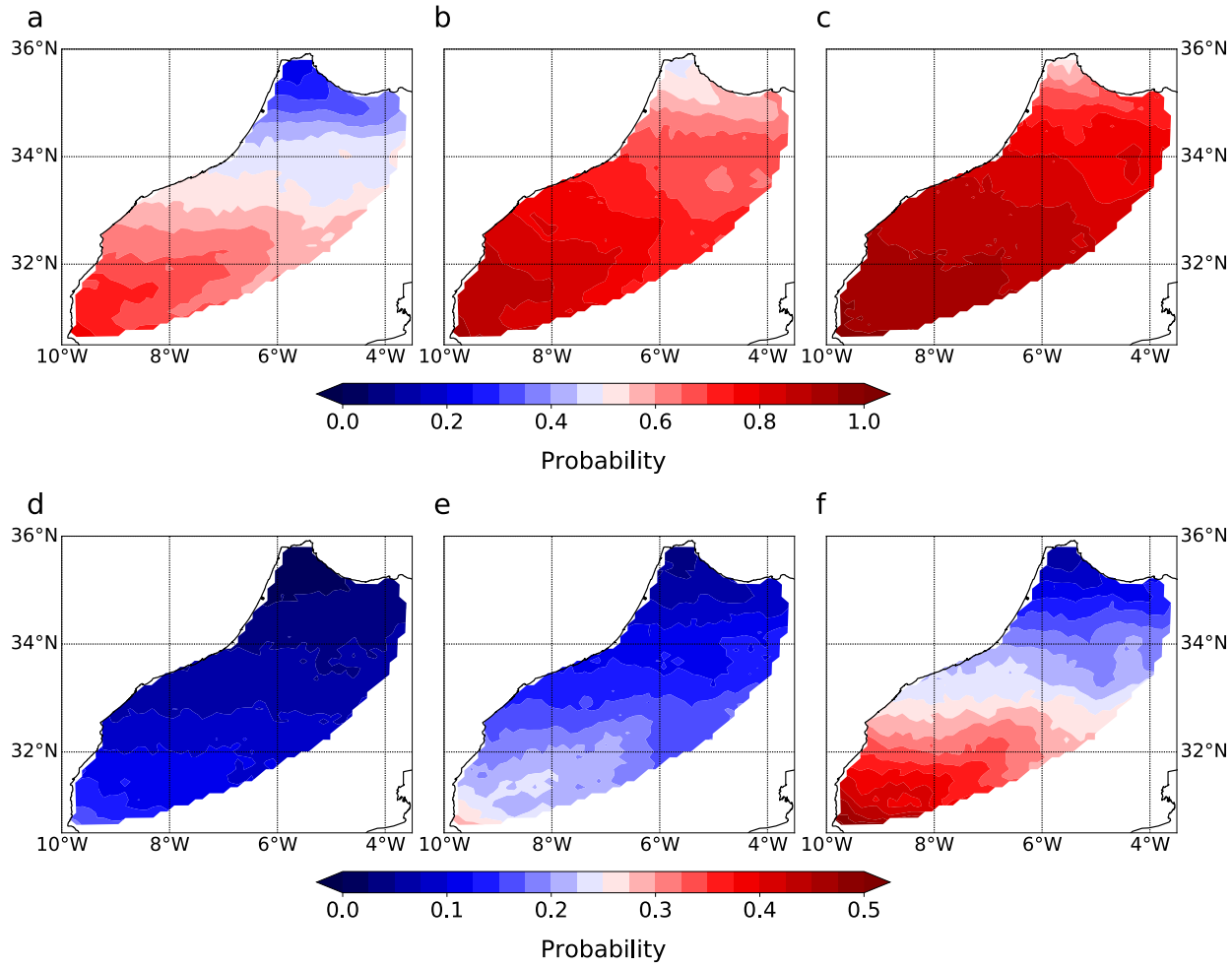

Figure 5-21: (a-c) Probability of a > 30-day long maximum CDD length between November and April in the (a) historical, (b) RCP4.5 and (c) RCP8.5 scenarios, as inferred from the fitted max-stable models (MPI+GFDL average). (d-f) As (a-c), but for a 60-day threshold.

5.6.3 Extreme temperatures in future climate projections

We now turn our attention to April-May daily temperature extremes in Morocco and their future distribution under climate change. These extremes are of particular relevance for agri-

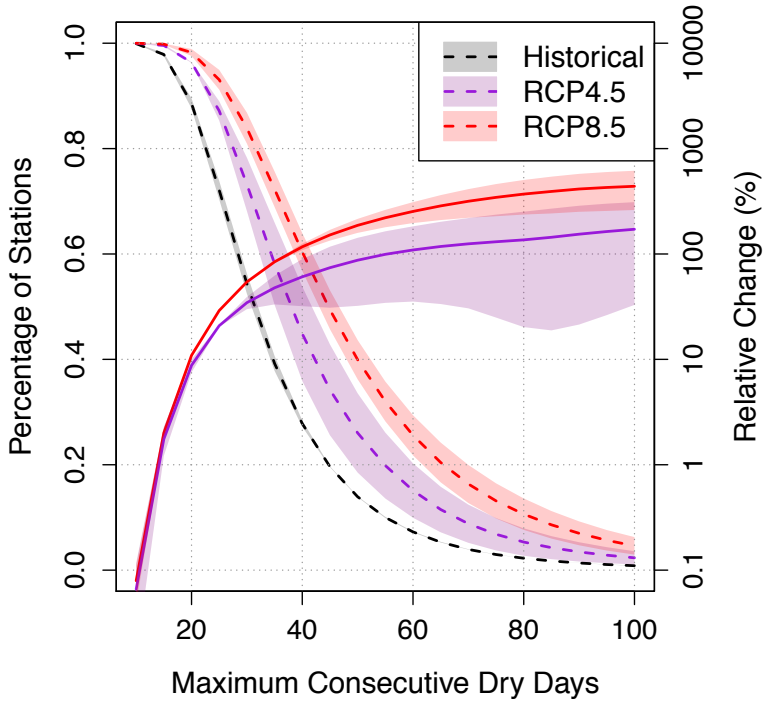

Figure 5-22: Left axis: Fraction of area (see Fig. 5-19-a) experiencing a maximum CDD length larger than N days as a function of N (dashed lines; black: historical; purple: RCP4.5; red: RCP8.5). Right axis: Relative change in that same fraction, as a function of N (solid lines; purple: RCP4.5; red: RCP8.5). For both axes shading represents MPI-GFDL inter-model range.

culture, since they occur at critical periods of crop growth (grain filling for cereals, which account for 55% of all Moroccan arable land, for instance) and can therefore have particularly negative impacts on yields [102]. Unfortunately, the 11 temperature stations available are not enough to fit realistic max-stable models and capture the spatial dependence of temperature extremes. ERA/MRCM accurately simulates the distribution of daily temperatures and much of its variability (Fig. 5-8), but tends to overestimate temperature extremes by several degrees (Fig. 5-23-a). Thus, relying on uncorrected ERA/MRCM daily temperature values may be justified when analyzing the distribution as a whole, but not when considering extreme values for which bias-correction remains necessary. Therefore, we limit our analysis to station locations only.

In the current climate, almost all April-May maxima fall in the 19-30°C range (Fig. 5-24). On average, in a given year, less than 5% of stations experience at least one day with an average of more than 30°C. This is projected to change significantly under future scenarios.

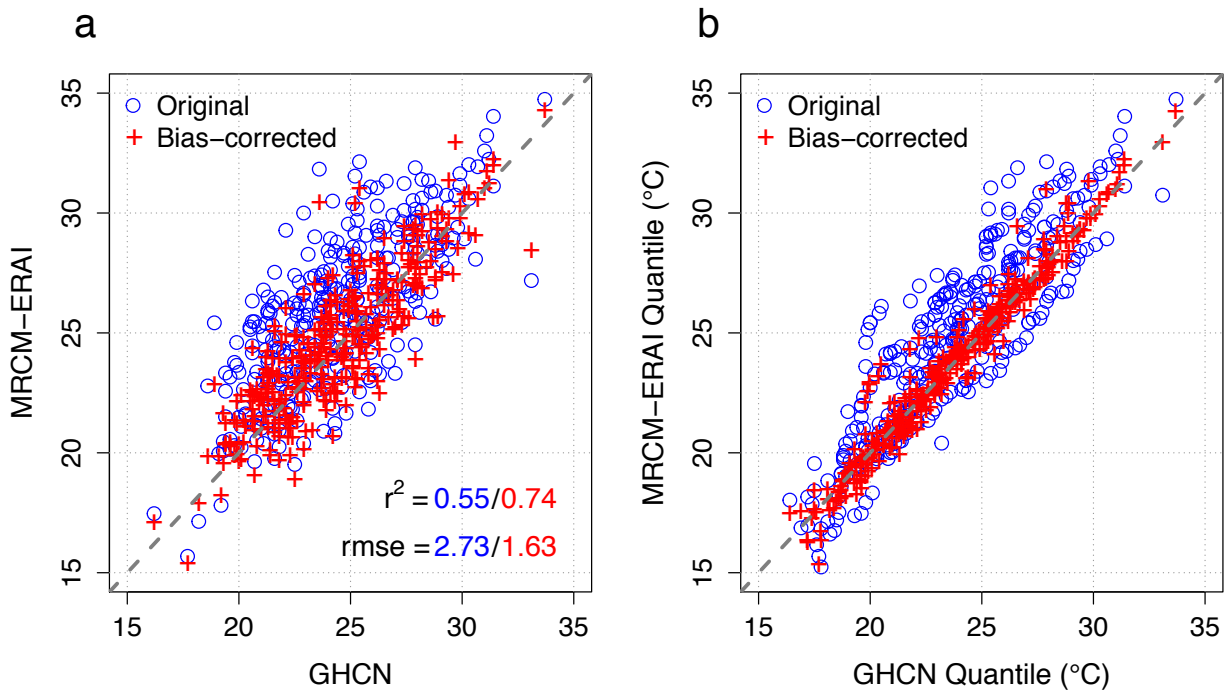

Figure 5-23: (a) April-May daily average temperature maxima at GHCN stations and corresponding maxima in the ERA/MRCM simulation, before (blue) and after (red) bias-correction. (b) Same as (a), but for the quantiles of the two distributions.

In RCP4.5, as average April-May temperatures at all stations increase by about 2.3°C, the median for extremes increases by +3°C and above-30°C extremes now impact 20% of all stations, a four-fold increase relative to historical levels (Fig. 5-24). For RCP8.5, an eight-fold increase is projected. More worryingly, above-25°C extremes will become almost inevitable under RCP8.5, and extremes of 35°C or more, never observed yet in the historical climate would become a once-in-a-decade event. Daily averages of 35°C are very high for that time of the year and, as stated in section 5.2, approach the upper tolerance threshold for crops like wheat. In addition, as precipitation becomes scarcer and droughts more frequent, soil moisture feedbacks may even enhance these extremes beyond the projections.

It is important to note that we do not model the dependence structure of the temperature extremes across the stations, and therefore we make the implicit assumption that MRCM is able to correctly simulate that dependence compared to observations. This is not a given and a more advanced analysis of temperature extremes for the region would require testing that hypothesis, possibly with spatial GEV models. With so few stations, however, only a crude

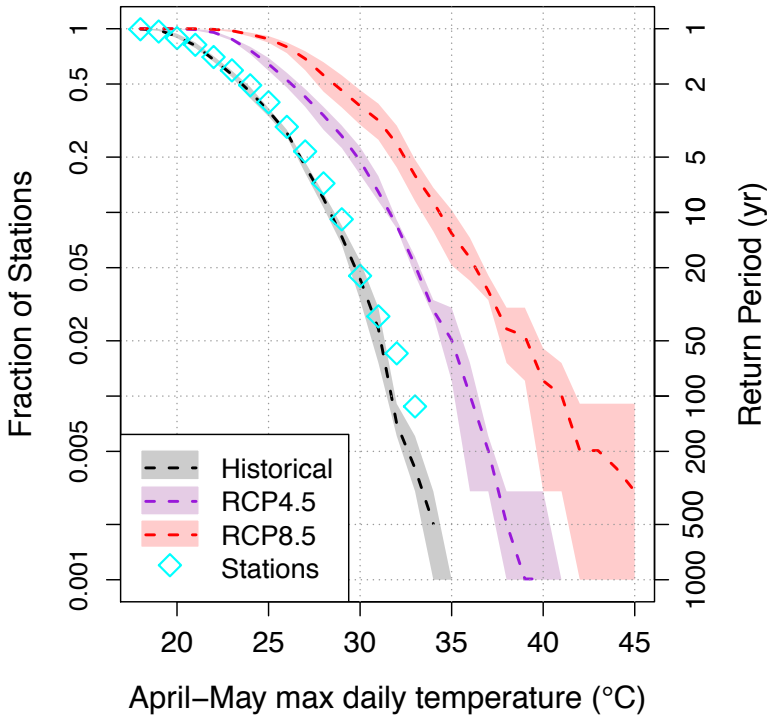

Figure 5-24: Fraction of stations experiencing a maximum April-May daily average temperature higher than x as a function of x, in observations (diamonds), and the historical (black), RCP4.5 (purple) and RCP8.5 (red) simulations. For the MRCM simulations, dashed lines represent three-model (MPI, GFDL, IPSL) medians and shading the three-model range.

modeling of that dependence would be possible, and efforts should rather be put in collecting more station data with the relevant Moroccan organizations.

5.7 Summary and conclusions

The results of this chapter underline the high vulnerability of the Western Mediterranean to climate change, and Morocco in particular. Future projections obtained by downscaling coarse-resolution output from carefully selected GCMs show a severe precipitation decline over much of the region during the wet season, and strong warming during summer, especially in continental interiors. In particular, we find that even under a substantial mitigation of emissions, 20-30% of wet season precipitation could be lost by the end of the century, a severe impact on the potential for agriculture in the region. We can expect that the future changes in net precipitation (accounting for evaporation) will follow those of precipitation [246], since evap-

oration in the NWAIP tends to be more constrained by water availability than by incoming energy. Further analysis using either hydrological models or simple runoff coefficient estimates could provide more detailed estimates of the decline in river flow for the region.

In addition, the analysis of monthly temperature projections shows widespread, severe warming throughout the year, reaching dangerous levels in the summer. For the coast, where most of Morocco's largest cities are located, mean monthly temperatures may reach extremes of 37°C under the RCP8.5 scenario, a 7°C increase compared to the present-day distribution. Inland cities currently regularly experience mean temperatures well above that threshold, but the relative humidity is much lower there than on the coast, where it remains high even at the peak of summer. This means that summer days may become significantly more uncomfortable in cities like Rabat or Casablanca. This large temperature increase, even under a mitigation scenario, could have significant impacts on Morocco's economy, notably its tourism and agriculture. Enhanced drought and temperature extremes during the growing season and near harvest threaten to impact cereal yields. Our downscaling of climate change over Morocco may help refine assessments of impacts on agriculture and help develop informed adaptation strategies in future research.

These trends are consistent with GCM projections of future Mediterranean winter drying and enhanced summertime warming, though GCM deficiencies may cause the latter to be overestimated [23]. Still, the high resolution of our projections allows us to shed light on the physical mechanisms responsible for the remarkably robust projected decline in wet-season precipitation over the Western Mediterranean. The vulnerability of the region is due to its geographical location. Large-scale circulation trends put it downwind of a large and very dry desert, and of high mountain ranges, causing enhanced advection of dry air and adiabatic warming which result in substantial drops in relative humidity and precipitation. The substantial role played by fine-scale topography and its interaction with regional circulation change make a strong case for the use of high-resolution models in the region. While the selection of GCMs for downscaling could be improved upon, the identified physical mechanisms behind the drying appear robust enough to be found in all regional simulations. Their better understanding that follows from our results may help further constrain the spread of Western Mediterranean future projections.

Chapter 6

Dynamics of seasonal snowpack over the High Atlas in the present climate

6.1 Introduction

While average annual precipitation hardly reaches at best 500mm over Morocco's agricultural plains, the Atlas Mountains, which rise up to 4000m high, usually receive up to twice that amount, most often in the form of snow between November and March [32]. Consequently, mountain precipitation is a major source of freshwater for the country, especially its agriculture, which accounts for 90% of all water use. The melting of the winter snowpack during spring substantially contributes to river discharge — up to 50% in some local catchments [32], filling dams beyond the wet season and allowing for continued water use and irrigation until the end of the growing season in May. Infiltration of mountain runoff also accounts for much of the aquifer recharge, on which agricultural activities in the fertile plains at the foot of the Atlas critically depend [41]. Yet, although the importance of the mountain snowpack for water resources is well-established, much remains unknown about its characteristics and

[1]This chapter is an edited reproduction of Tuel et al. (2020d) [249].

spatio-temporal dynamics.

Accurate estimates of Snow Water Equivalent (SWE) fields in the High Atlas are necessary to improve our understanding of the regional hydrology and thus water resources management. In addition, assessing the sensitivity of the regional snowpack to meteorological and climate variables is critical in order to project its response to climate change, which is expected to bring warmer and much drier conditions over Morocco. The scarcity of ground measurements, combined with the complex regional topography and the large spatio-temporal variability in hydroclimate [77, 251], create significant challenges to snowpack monitoring, modeling and estimation at the basin scale. Satellite-based snow cover maps can provide a good first estimate of the extent and temporal evolution of the snowpack, as was shown for the Atlas Mountains [165]. Where enough station data are available, complex physically-based snow models that resolve the energy balance at the surface, and may even include several snow layers [155, 115, 29], are usually preferred. Recently, Baba et al. (2019) applied SnowModel, a physical snowpack evolution model based on the snow energy balance, to simulate snowpack dynamics in the Rheyara catchment of the High Atlas, outside our study zone, down to a resolution of 8m [13]. Their approach was made possible by the small size (220km^2) of the catchment and its relatively high density of weather stations. The large data requirements of such models, however, make them less applicable over large areas, where even basic data like temperature are often missing. Therefore, essential questions remain unanswered for the High Atlas: most importantly, how much water is stored in the snowpack? And how does this amount vary in space and time?

At the catchment scale, conceptual, distributed snow models, typically based on simple parametrizations of melt as a function of temperature, and forced with remotely-sensed data, spatially interpolated station data or analytical mesoscale model output, can yield useful results [169, 43, 201]. When ground data are particularly scarce or unavailable, one possibility is to resort to remotely-sensed snow cover maps and reconstruct SWE backwards in time using the observed snow fraction time series at each grid point as constraints [179, 202]. An advantage of this approach is that it only requires temperature as input if no new snowfall accumulates after peak SWE; on the downside, it can only reconstruct SWE during the melt phase, is not useful to make SWE projections and is also very sensitive to biases in snow cover data [180].

Often, forward configurations in which precipitation is partitioned between rain and snow and accumulated snowfall stored as SWE are preferred [202]. In their simplest form, empirical snow models only require temperature and precipitation, although more complex formulations involving radiative fluxes are also available [117, 83]. Several previous studies that relied on station measurements have shown that they were able to satisfactorily estimate snow accumulation and melting in various climate zones, including the High Atlas [83, 29, 28]. Such models have also been successfully applied to reconstruct SWE fields in various Mediterranean-climate regions [229, 103, 75, 77]. However, station data are often missing, which has led to increased interest in the applicability of gridded climatological datasets, like climatological reanalyses (e.g., ERA-Interim [55]), station-based interpolated datasets or satellite-based products, to be used as input to snow models [181, 230]. However, questions still remain as to their accuracy to represent fine-scale conditions in complex topography, especially precipitation maxima near mountain peaks [181]. To circumvent that problem, reanalysis data can be downscaled to finer resolution with regional climate models [273], an approach that has proved successful over several mountainous regions (Alonso-González et al. 2018 [8] and reference therein). The forcing datasets can suffer from numerous biases, however, especially precipitation, which in complex terrain typically exhibits strong spatio-temporal variability that is hard to capture. Regional models can be unreliable since precipitation relies on parametrizations that require observations as input, and gridded satellite-based precipitation products, like TRMM [126], CHIRPS [87] or GPM [125], are often the only estimates available. Such products usually tend to underestimate snowfall and wet season precipitation in mountain regions [56, 109], which may bias the results, particularly since parameter fitting of empirical snow models is typically highly sensitive to input uncertainty [85, 110]. Few studies seem to rely on satellite-based precipitation, preferring model-simulated precipitation [273, 8] or global station-based products [181], when direct interpolation from local stations is not possible. In addition, one downside of previous such studies is the absence of explicit sublimation fluxes. Yet, because the High Atlas has a particularly arid climate, latent heat fluxes are significant: locally, 25-45% of accumulated snow has been found to be lost to sublimation [224, 157]. Sublimation is known to vary significantly in space, especially in complex mountain regions [238]. Any snow model applied at the basin scale in this area should therefore include latent heat fluxes, which

requires additional meteorological information, notably atmospheric humidity.

In this chapter, we aim to estimate the spatial and temporal distributions of snowpack water content and sublimation in a large area of about 13,000 square kilometers in the High Atlas, using a distributed physically-based snow model constrained by a combination of topographical data, remotely-sensed data, and meteorological data dynamically-downscaled down to 12 kilometers. In addition, we model sublimation explicitly to provide the first estimate of the spatial distribution of latent heat fluxes in the High Atlas. Our focus is the Oum-Er-Rbia watershed (Fig. 2-1), one of Morocco's major agricultural regions and an important producer of hydropower, which receives the most snowfall among all the country's main watersheds [165] and depends almost exclusively on mountain precipitation. Satellite-based snow cover is used as a constraint in order to estimate snow model parameters. While previous studies have suggested that the strong spatial variability of Atlas snow cover warranted <500m resolution [13], we select a resolution of 1km for our model, based on data availability and computing power. Despite this limitation, snow modeling at such a resolution and spatial scale has never been attempted for the Moroccan Atlas. Our aim is to capture the main features of variability in snow cover and provide a first order characterization of the snow water balance of the basin. We demonstrate how the scarcity of ground data, which has been a major obstacle to investigating snow processes in the High Atlas, can be partly overcome by using remotely-sensed meteorological variables and downscaled climate reanalysis data to gain important insights into snow water balance in a semi-arid region.

6.2 Study Area

The Oum-Er-Rbia, with its 550km length and 3 km^3 annual discharge, is one of Morocco's major rivers (Fig. 2-1). Its water supports 30% of the country's irrigated land, 50% of its hydropower capacity, and provides for the daily needs of seven million people, including two major cities, Casablanca and Marrakech. It flows northwestward from the northern slopes of the High Atlas, Morocco's largest mountain range. Our 13104 km^2 study area covers the drainage basins of four main dams, corresponding to the major tributaries of the Oum-Er-

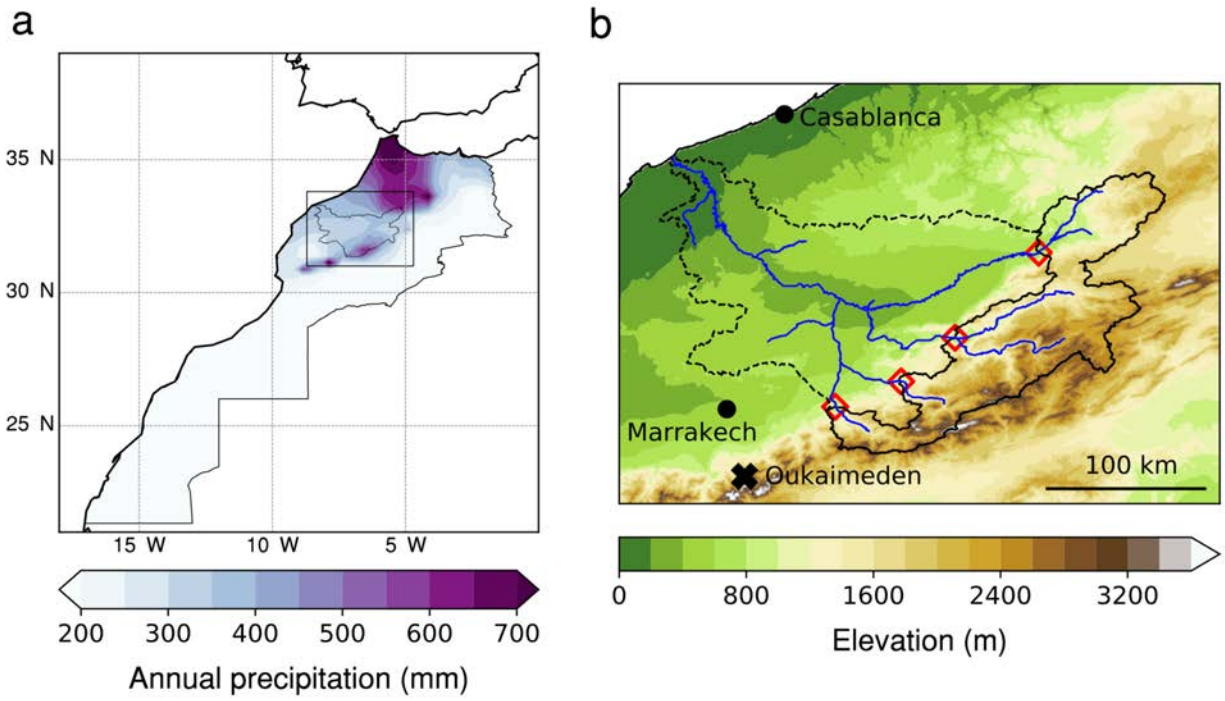

Figure 6-1: (a) Annual precipitation over Morocco (TRMM 3B43 V7) and Oum-Er-Rbia watershed. (b) Study area (solid black line) within the Oum-Er-Rbia watershed (dashed line), with elevation in shaded contours, main cities (dots), river network and snow station (cross). The four main dams whose catchments define our study area are shown by red diamonds; from north to south and east to west: El Hansali, bin-El-Ouidane, Moulay Hassan 1 and Moulay Youssef.

Rbia, all located at the foothills of the High Atlas (Fig. 6-1). Elevation in the area ranges from 621m to 3890m, for a mean of 1882m. Vegetation is sparse, consisting mostly of bare soil and grass and rare shrubs in areas where snow is present [13], with forest cover essentially limited to the valleys. The area is under a rather continental climate, characterized by a large amplitude of annual temperature cycles [147]. Temperatures are minimum in January, when they range from mild (≈12 °C) below 1000m to cold (-5 °C) above 3000m. Even at that time, the foothills seldom go below freezing. By contrast, peak summer temperatures, occurring in July, are very high (35 °C) at the lowest elevations, and still quite warm above 3000m (10-15 °C) [185]. Conditions are overall quite dry, even at high elevations, where annual precipitation reaches 800-1000mm, against lows of 250mm in the plains to the west (Fig. 6-1-a). About 80% of annual precipitation occurs during the wet season, from October to April, when the region is under the influence of North Atlantic westerlies which bring the occasional storm systems responsible for most of the precipitation [147, 251]. Above 1500m, snowfall is

common during the winter months. Persistent snow cover is frequent above 2500m, typically extends from December to April, and rapidly disappears by the end of May [31], though inter-annual variability is substantial [165] (Fig. 6-2). Our study area is defined as the combined catchments of the four main dams within the Oum-Er-Rbia watershed: El Hansali, Bin-El-Ouidane, Moulay Hassan 1 and Moulay Youssef (Fig. 6-1-b). It encompasses most of the zones in the Oum-Er-Rbia watershed that receive at least modest snow amounts on average during the winter.

High Atlas snow cover is characterized by substantial variability in both space and time, a key feature in arid environments [31]. At the annual time scale, wet season precipitation exhibits a large inter-annual variability [147], with a coefficient of variation of about 0.3 [251], a variability that is reflected in seasonal snow extent [164]. Within a season, precipitation also tends to occur in short and irregular storm events; warm temperatures over a few dry weeks can lead to complete disappearance of the snowpack even in mid-winter at high elevations [224]. Because net radiation dominates the snow energy balance [157], snow cover is also highly dependent on terrain slope and aspect, with bare ground not uncommon even at high altitude [165].

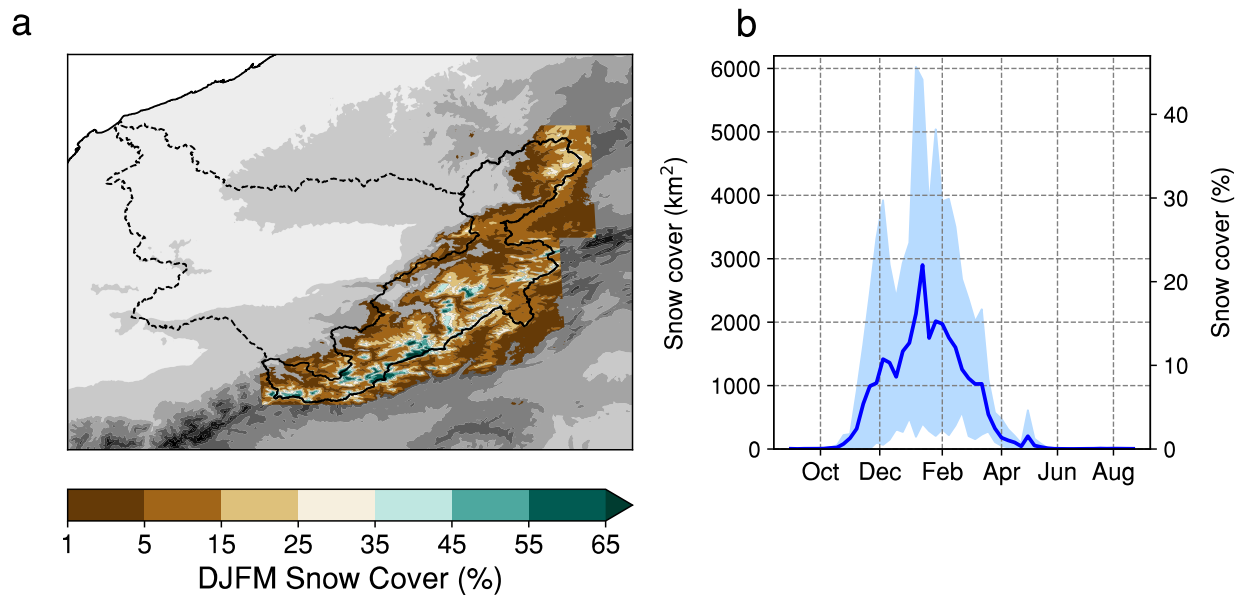

Figure 6-2: (a) December-March average snow cover in the Oum-Er-Rbia basin (outlined in dashed black), from MOD10A1 v6 (2001-2011). Data outside the direct neighborhood of the basin is not shown. The study area (see below) is shown by the thick solid black contour. (b) Annual cycle of snow cover extent in the study area (mean: solid blue line, 90% range: blue shading).

6.2.1 Station data

Quality checked snow and weather data are available at the Oukaimeden automatic weather station, located at 3200m altitude near the Oukaimeden ski resort, about 75km away from the border of our study region (Fig. 6-1-a) in a similar physio-geographical setting. Daily snow depth is available for 6 seasons (2003-2006 and 2007-2010), and daily air temperature, relative humidity and 2-meter wind speed are available from 2003 to 2016, with occasional gaps (5-14% of the data depending on the variable). 30-minute air temperature was also measured from 2010 to 2018. Daily precipitation data are not available at the station, but only at the nearby CAF (Club Alpin Français) station located 600m downslope, for the 1989-2010 period.

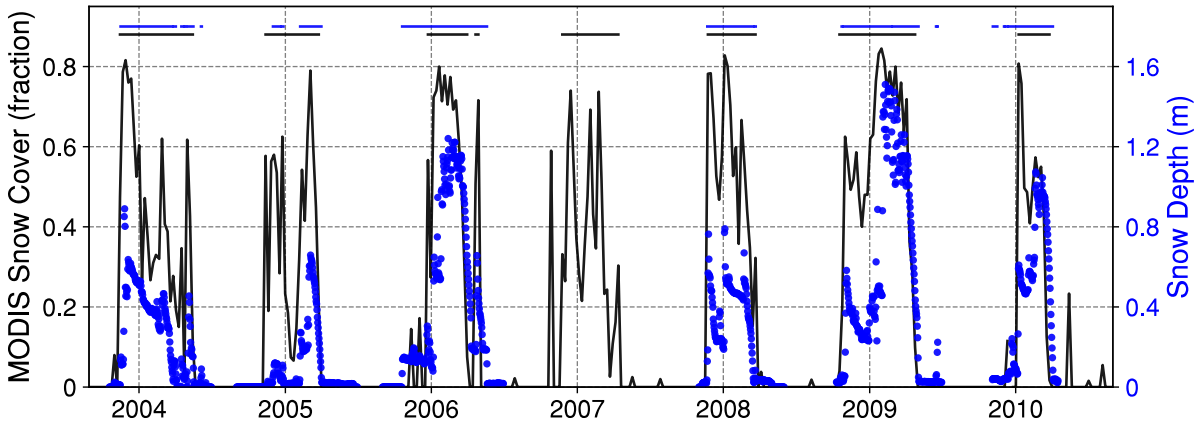

Figure 6-3: Time series of weekly mean snow depth measured at Oukaimeden station (blue dots) and fractional snow cover for the corresponding 500x500m MOD10A1 grid cell (black line). Horizontal bars at the top highlight periods with more than 5% snow cover or 5cm snow depth.

6.3 Modeling of observed snowpack

6.3.1 Snow model

In Mediterranean mountains, the snow energy balance is largely dominated by radiative fluxes [29, 157]. Therefore, we select the radiation-derived temperature index (RTI) melt formulation [83, 84], within the framework of the SNOW-17 model [10]. SNOW-17 simulates snow accu-

mulation and loss empirically, using meteorological variables to account for the various energy balance equation terms. The main difference here with the Follum et al. (2015) study is that we add a sublimation module, based on a bulk-aerodynamic flux formulation. We give here a brief summary of model structure (Fig. 6-4) and equations; readers are referred to Anderson (2006) and Follum et al. (2015) for more details [10, 83].

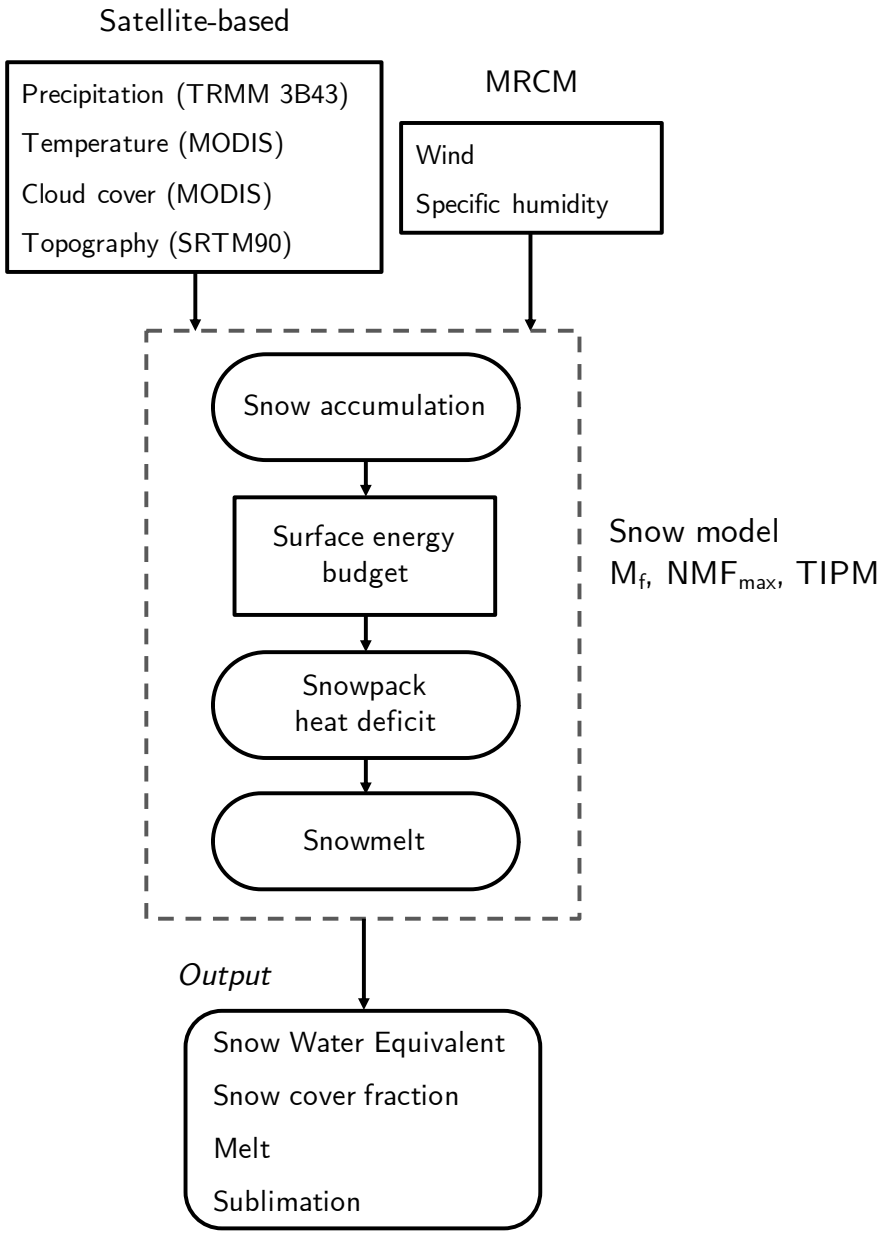

Figure 6-4: Schematic of the methodology: Input data, snow model and output.

RTI uses a proxy temperature T_{rad} calculated from the surface radiation balance, instead

of actual air temperature, to estimate snow melt. It therefore includes spatial variability in potential melt due to variability in incoming shortwave and longwave radiation, at the resolution of the topographic data. T_{rad} is given by the following:

$$T_{rad} = \left(\frac{LW_{\downarrow} + (1-\alpha)SW_{\downarrow} - LE}{\epsilon_s \sigma} \right)^{1/4} \tag{6.1}$$

where $LW_{\downarrow}$ is the downward longwave radiation, $SW_{\downarrow}$ downward shortwave, α snow albedo, LE the latent heat flux (see below), ϵ_s the snow surface emissivity (taken to be 1) and σ the Stefan-Boltzmann constant. Although equation 6.1 neglects many terms of the energy balance (e.g., ground heat flux, sensible heat flux), at first order, T_{rad} represents the snow surface temperature that balances net surface radiation and can be interpreted as a measure of the amount of energy available to heat/melt the snowpack. In particular, T_{rad} can be above 0 °C. To calculate downward longwave and shortwave, we adopt the formulations of Follum et al. (2015) used in the GHSSA model [62], with the exception that we assume no vegetation cover, an approximation we make due to the High Atlas' sparse vegetation. Tree cover is present at lower elevations (below 1500m), where snow cover is short-lived (a few days at most) due to relatively high temperatures.

$$\begin{cases} SW_{\downarrow} = S_0 K_r K_{atm} K_c K_s K_t \\ LW_{\downarrow} = \sigma \cdot \epsilon_a \cdot (T_a + 273.15)^4 \cdot (1 + 0.17N^2) \end{cases} \tag{6.2}$$

where S_0=1366 W/m^2 is the solar constant, ϵ_a is air emissivity (taken to be 0.757 when snow is present), T_a is air temperature, N is fractional cloud cover and the K factors are coefficients of reduction of incoming solar radiation due to Earth-Sun distance (K_r), atmospheric scattering (K_{atm}), cloud absorption (K_c), terrain slope and aspect (K_s) and topographic shading (K_t). The daily cycle of solar radiation is included in K_s. In particular, $K_c = 1 - 0.65N^2$.

Snow albedo is parametrized according to the formula proposed by Brock et al. (2000) [34]

and calibrated for the High Atlas by Boudhar et al. (2016) [29]:

$$\alpha = 0.8 - 0.21 \log_{10}(t_d) \tag{6.3}$$

where t_d is the number of days since last snowfall. The albedo of new snow (less than 1 day old) albedo is set at 0.8; this is a low value but which best fits observations in the High Atlas, likely connected to the high concentration of mineral dust due to the proximity of the Sahara Desert [274].

Air temperature T_a is used to determine the phase of precipitation: we assume it will fall as snow if T_a is below 0 °C. Snowpack is characterized by its snow water equivalent SWE (in mm) and its heat deficit D_t, a measure of the energy needed to bring the snowpack to its melting temperature (0 °C). The heat deficit is expressed in mm of snow water equivalent (Anderson 2006). At each time step, the heat deficit is updated as new snow falls, as snow sublimates or as energy is transferred from the atmosphere to the snowpack. The change in heat deficit due to differences between snowpack and air temperatures is expressed as:

$$\Delta D_t = NMF \cdot (ATI - T_{\text{snow}}) \tag{6.4}$$

where ATI is the antecedent temperature index (in °C), T_{snow} is the snow surface temperature, and

$$NMF = NMF_{\max} \cdot \frac{SW_{12h}}{\max(SW_{12h})} \cdot dt \tag{6.5}$$

where $NMF_{\max}$ is the maximum negative melt factor (in mm/ °C/hr), SW_{12h} is the incoming shortwave radiation at noon on a flat surface on the current day and $\max(SW_{12h})$ its maximum value across the whole year. dt is the time step (in hours), here chosen to be 6. Snow surface temperature is parametrized as in Boudhar et al. (2016) [29]: $T_{\text{snow}} = \min(0, 0.72 \cdot T_a - 2.47)$; an expression based on a linear fit of observed data at the Oukaimeden station. The calculation of ATI in equation6.4 also involves an empirical parameter, $TIPM$ [10]. In the case of a

positive latent heat flux LE, the heat deficit is reduced proportionally to the amount of snow lost by sublimation during the time step:

$$\Delta D_t = -\frac{3600\frac{LE}{L_s}dt}{SWE_t} \cdot D_{t-1} \tag{6.6}$$

where L_s is the latent heat of sublimation (2.834 MJ/kg).
Melt can occur once the heat deficit reaches 0. If less than 1.5mm of rain occurred during the previous 6 hours, melt is calculated by

$$M = dt \cdot M_f \cdot T_{rad} + 0.0125 \cdot p \cdot f_r \cdot T_r \tag{6.7}$$

with M_f the melt factor, p precipitation (mm), f_r equal to 1 if T_a is larger than 0 °C, 0 otherwise, and T_r is the precipitation temperature (maximum of 0 °C and T_a). Otherwise, melt is given by

$$\begin{aligned} M = dt \cdot \sigma \left\{ (T_{rad} + 273.15)^4 - 273.15^4 \right\} + 0.0125 \cdot p \cdot f_r \cdot T_r + \\ 8.5 \cdot f_u \cdot \frac{dt}{6} \left((rh \cdot e_{sat} - 6.11) + 0.00057 \cdot P_a \cdot T_a \right) \end{aligned} \tag{6.8}$$

where $f_u = 0.5$ mm/mbar/6hr, rh is the relative humidity, e_{sat} the saturation vapor pressure (mb), and P_a the air pressure (in mb). e_{sat}, taken over water for $T_a \geq 0$ and ice otherwise, is calculated as in Alduchov and Eskridge (1996) [6]; P_a is assumed to vary with elevation H only, given by $P_a = 1013.25 \cdot \left(1 - 2.25577 \cdot 10^{(} - 5)H\right)^{5.25588}$ (in hPa).

Equations (6.4)-(6.7) involve three parameters: M_f, $NMF_{\max}$ and $TIPM$ (used to calculate ATI, see [10]) which must be calibrated. The RTI originally also includes another parameter, PLWHC, the maximum fraction by volume of liquid water that can be held in the snowpack, which we take to be fixed at 0.05.
We parametrize sublimation based on the bulk-aerodynamic method, which assumes the latent heat flux (LE, in W/m^2) to be proportional to wind speed and water vapor gradient between

the surface and a given level z:

$$LE = FSC \cdot \frac{f \cdot L_s \cdot \rho \cdot \kappa \cdot U(z) \cdot (q(z) - q_s)}{\log\left(z/z_0\right)^2} \tag{6.9}$$

where FSC is the grid cell fractional snow cover, ρ is air density (kg/m^3), κ is the von Karman constant, $U(z)$ and $q(z)$ are respectively the wind speed (m/s) and specific humidity (kg/kg) at height z, q_s is the surface specific humidity (kg/kg), z_0 is the surface roughness length (set to 0.001 following Boudhar et al. 2016 [29]), and f is a non-dimensional stability factor based on the bulk Richardson number $Ri = 9.81\frac{(T_a - T_{\text{snow}})\cdot(z-z_0)}{(T_a+273.15)\cdot U(z)^2}$ [9, 37]:

$$f = \begin{cases} 1 & \text{if } Ri = 0 \\ (1 - 5Ri)^2 & \text{if } Ri < 0 \text{ (unstable)} \\ (1 - 16Ri)^{0.75} & \text{if } Ri > 0 \text{ (stable} \end{cases} \tag{6.10}$$

q_s is calculated assuming surface saturation at T_{snow}.

The model estimates SWE at each grid cell; we translate it to snow cover using the following formula:

$$SC = 0.85 \cdot \tanh\left(k \cdot SWE\right) \tag{6.11}$$

with $k = 100\text{m}^{-1}$ [30] and SWE in meters. 0.85 is selected as maximum allowable snow cover due the quasi-absence of grid-scale (500m) snow fractions larger than 85% in satellite observations. This likely reflects the strong small-scale variability of snow cover in the High Atlas at high altitudes, a feature linked to the rockiness of the terrain leading to high variability in radiative balance [13]. In theory, fractional snow cover is more directly connected to snow depth rather than SWE. Therefore, a strong assumption of constant snow density is made by using equation 6.11. We discuss this point further in section 6.4.6.

Due to the large number of grid cells (≈13000) and associated computing time, the three parameters (melt factor M_f, maximum negative melt factor $NMF_{\max}$ and antecedent tem-

perature index coefficient $TIPM$) are fitted by maximizing the Nash-Sutcliffe coefficient [182] between the observed and simulated snow cover at 250 randomly selected grid points, at altitudes representative of the distribution of altitudes across the whole basin. Each parameter is calibrated independently across a ranges of values (allowable range, see Table 6.1). To test the applicability of the RTI-SNOW17 model, and compare our results with [29, 157], we also fit the parameters to the observed snow depth series at Oukaimeden, using the TRMM precipitation estimate for the corresponding grid cell. SWE in the model is converted to snow depth (SD) (to compare with Oukaimeden measurements only) with the formulation used in Bouamri et al. (2018) [28]:

$$SD(t) = SWE(t) \times \frac{\rho_w}{\bar{\rho_s}(t)} \tag{6.12}$$

with ρ_w=1000kg/m^3 (density of liquid water) and $\bar{\rho_s}$ is snowpack density, calculated at each time step t as the average between the density of the previous snowpack (at time $t - dt$):

$$\rho_s(t) = (\rho_s(t - dt) - \rho_{max}) \times \exp\left\{\frac{\tau_f}{\tau} \cdot dt\right\} + \rho_{max} \tag{6.13}$$

and that of fresh snow $\rho_{new} = 67.9 + 51.3 \times \exp\left(\frac{T_a}{2.6}\right)$ (in kg/m^3)[111]. $\tau_f/\tau = 0.24/4800$ s^{-1} is a characteristic time of density evolution and ρ_{max} a maximum snow density, equal to 350 kg/m^3 [28]. Therefore, the snow compaction ratio will typically evolve between 12:1 for fresh snow and 1:3 for old snow.

6.3.2 Input data

MODIS snow cover

For snow cover data, we use the MODIS Terra snow cover daily L3 product (MOD10A1) at 500m resolution [105]. The data are available from late February 2000 to present. Snow cover is detected based on the Normalized-Difference Snow Index (NDSI), calculated from reflectances in the visible/near infrared and middle infrared. Snow cover fraction is then estimated from

the NDSI using an empirical relationship fitted to high-resolution LANDSAT images from various regions of the world (Fig. 6-2). Because of frequent cloud (≈30%) cover in the High Atlas during the wet season, many data are missing or potentially misclassified. We apply the filtering algorithm introduced by Marchane et al. (2015) to filter missing data at the daily timescale, and then average snow cover at a weekly timescale. By comparing to station data and high-resolution (8m) FORMOSAT-2 images, Marchane et al. (2015) found that, using this filtering process, the MOD10A1 product was able to accurately reproduce snow cover area in Morocco's mountains, including the timing of onset and melt. Figure 6-3 shows the correspondence between observed snow depth and MODIS fractional snow cover for the Oukaimeden station.

Topography

Elevation data are derived from the Shuttle Radar Topography Mission 90-meter resolution dataset version 4.1 (STRM90) [135], and resampled by bilinear interpolation to the MODIS land surface temperature resolution of about 1km.

Surface temperature

Spatially distributed air temperature is derived from the global MODIS Land Surface Temperature (LST) product MOD11A1 L3 version 6 at 1km resolution [261]. MOD11A1, available from February 2000 to present, provides an estimate of land surface temperature based on clear-sky thermal infrared brightness temperatures, twice every 24 hours (daytime measure at 10:30 and nighttime measure at 22:30 local solar time). The underlying algorithms rely on additional MODIS data for local corrections, including snow and cloud cover, emissivity, or water vapor. Details of the algorithm can be found in Wan (2008) [260]. The MODIS LST data were shown to be accurate within 1 °C in clear-sky conditions for snow-covered areas at temperatures above -15 °C [104], below which air temperature seldom goes in the High Atlas. The strong correlation between LST and air temperature T_a has been documented in a number of studies, notably over snow cover [42, 265], with root-mean square errors of up

to 4-5 °C in cold mountain environments [268]. MODIS LST has been used for distributed snow modeling with SNOW-17 by Shamir and Georgakakos (2014) [230] in the mountains of Turkey, who found that LST-derived air temperature was highly correlated to station temperature ($r = 0.93$) and performed well in estimating snow mass and maximum SWE.

There are three main challenges associated with the use of LST for snow modeling. First, thermal satellite LST data collection is impossible under cloud cover, since cloud-top temperatures are measured instead [2]. Many LST data are therefore missing and need to be filled. Second, although highly correlated, LST and air temperature are not the same, and a correction needs to be applied. Third, LST is measured only twice a day, and we need to infer its daily cycle in order to run a snow model at 6-hour time steps.

Filling of missing LST values

We fill missing LST values for daytime and nighttime series separately, by first calculating the daily deviation to an estimated annual LST cycle, and then interpolating missing values in both space and time. Since fewer than 20 years of data are available for any single day of the year (and even less for some grid cells due to cloud cover), and since LST can vary wildly on any given day, we estimate an annual cycle for LST at each grid point by averaging LST data for each week of the year. Then, we interpolate anomalies relative to that annual cycle as follows: for each 50km-square in our domain, if less than 75% of data is missing, interpolation is performed spatially using 2D-kriging with an exponential semivariogram, fitted over the full area for all days and years available in the week of interest. If not, then interpolation is performed temporally using an autoregressive model of order 1 fitted to the time series of LST anomalies at each grid point.

Derivation of air temperature from MODIS LST

In general, the difference between LST and T_a is positive during the day, as solar radiation warms up the land surface, and negative at night, because the land surface cools faster than the air (Fig. 6-5-a). The LST-T_a relationship has been extensively studied, both theoretically and empirically. The general conclusion is that it depends on local variables, such as land cover, terrain aspect, the presence of snow, or soil moisture (e.g., [175]). Here, we apply a simple linear correction $T_a = a \times LST + b$ inferred from the 30-minute air temperature data

measured at Oukaimeden station. We select the closest station measurement for each LST value in the Oukaimeden grid cell, and estimate regression coefficients a, b for each three-month period October-December, January-March, April-June and July-September, and for day- and nighttime measures separately. The resulting RMSE is found to be 3 °C. The same correction is assumed valid for the whole basin, admittedly a very broad assumption, justified here however by our lack of additional station temperature data.

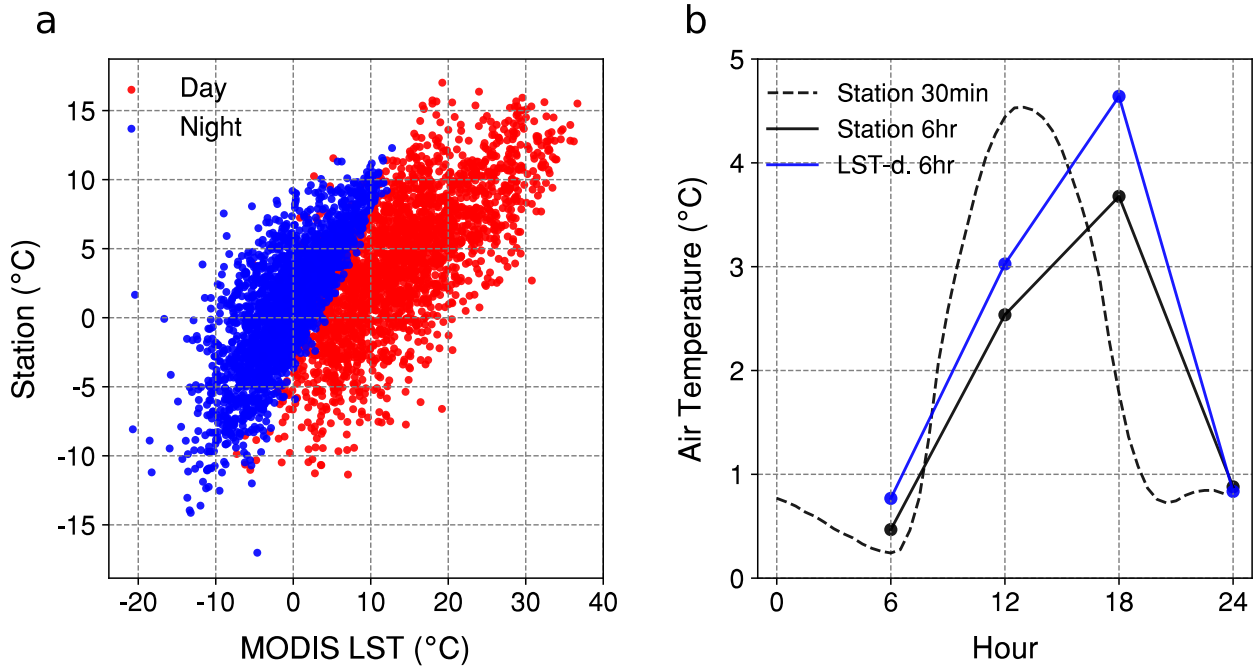

Figure 6-5: (a) Air temperature measure at Oukaimeden station against the corresponding MODIS LST value, for daytime (red) and nighttime (blue) measurements. (b) Daily cycle of air temperature at the Oukaimeden station (dashed black line: 30-minute time step; solid black: 6-hourly) and 6-hourly cycle of MODIS LST-derived air temperature (blue).

Daily cycle

To interpolate the daily temperature cycle to 6-hour time steps (0, 6, 12 and 18 hour local time), a common approach is to rely on harmonic functions (e.g., [230]). However, daily cycles of LST and air temperature do not match sine waves (Fig. 6-5-b), as expected from the nature of sloar forcing over its 24-hour cycle, so we opt for a different formula. At each grid point, the hour of sunset and sunrise are calculated based on day, slope and aspect [66]. The nighttime LST-derived T_a is assumed representative for the whole night, from two hours after sunset till sunrise. This assumption neglects the potential for radiative cooling overnight, but in the

absence of sufficient ground data it is difficult to quantify. Observed data at Oukaimeden indicate however that the temperature decline during the night is of small amplitude (Fig. 6-5-b).. Between sunrise and the daytime LST measure, LST-derived T_a is linearly interpolated. Between the daytime measure and two hours after sunset, it is interpolated using a second-degree polynomial with a maximum forced at two hours after solar noon. At the Oukaimeden station, the resulting LST-derived daily cycle of air temperature is on average within 0.5 °C of the observations (Fig. 6-5-b).

Precipitation

In complex, mountainous terrain with little to no station data, as is the case of the High Atlas, precipitation data from high-resolution satellite-based products is often the only option available. A number of such products are available at sub-daily and high spatial resolutions over the High Atlas: TRMM TMPA (TRMM Multi-Satellite Precipitation Analysis, 3-hourly at 0.25° resolution) [126], CHIRPS (Climate Hazards Group InfraRed Precipitation with Station data, 30-minute at 0.05° resolution) [88] and GPM (Global Precipitation Measurement, 30-minute at 0.1° resolution) [125]. All three products involve a combination of remotely-sensed data (both TRMM and GPM include radar and infrared data while CHIRPS includes radar data only) corrected with ground data, usually at the monthly timescale. TRMM performs reasonably well in our region of focus (Figs. 6-6-a, 6-7-a), though it exhibits a dry bias in mountainous areas, consistent with the findings of Ouatiki et al. (2017) [185]. CHIRPS is available starting from 1981, which makes it attractive for our study; however, the comparison of the three available products with stations in and near our study area suggests that CHIRPS suffers from a significant wet bias (Fig. 6-6-b). In addition, the mean precipitation pattern in CHIRPS exhibits complex features somewhat inconsistent with elevation (a few local maxima at low elevations). Monthly correlation with station data is also less good than TRMM (Fig. 6-7-b). As to GPM, its dry bias is obvious (Fig. 6-6-c); however, its spatial structure is similar to TRMM, with higher resolution, and could potentially be used to disaggregate TRMM data as a future step.

Therefore, for this analysis, we choose to use 6-hourly precipitation from the TRMM 3B42

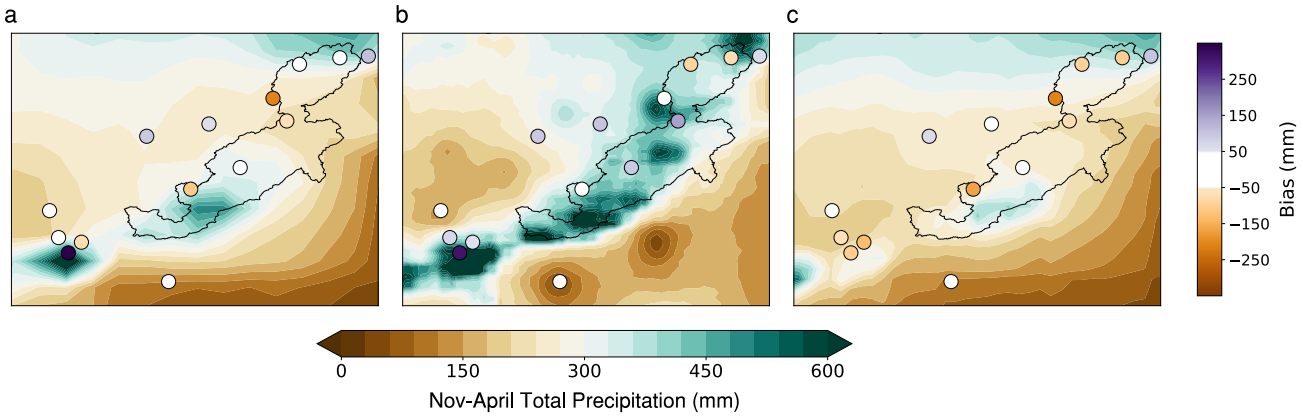

Figure 6-6: November-April mean total precipitation (2000-2010) in (a) TRMM, (b) CHIRPS and (c) GPM (shaded contours), along with mean relative biases with respect to all available stations in and near the study domain (filled dots).

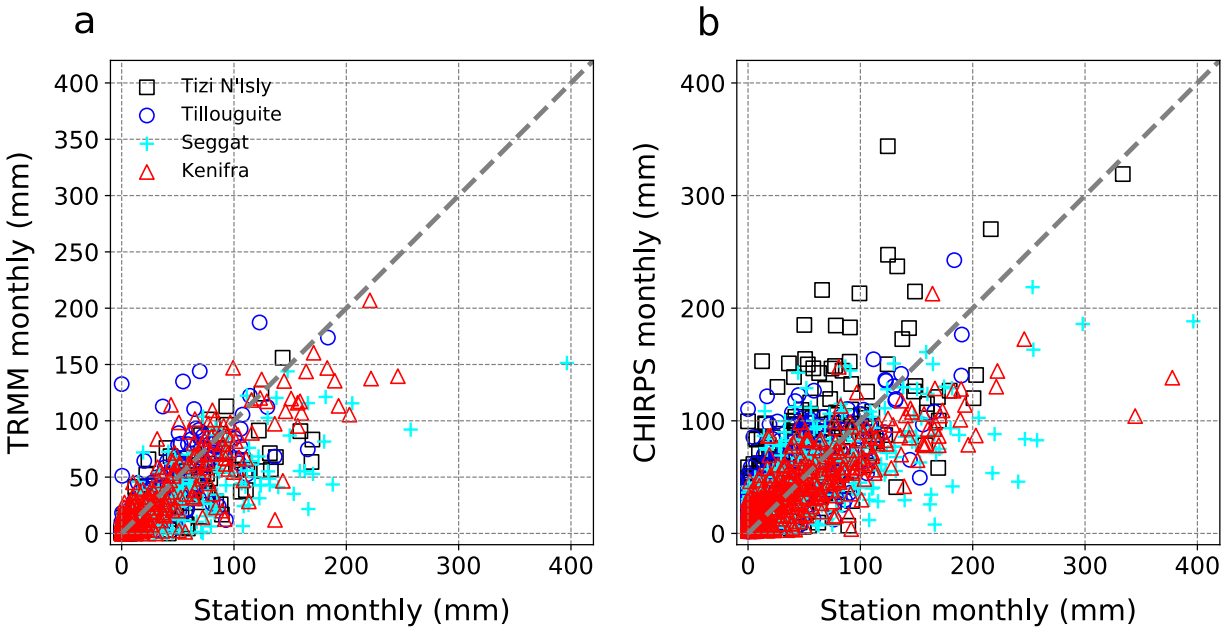

Figure 6-7: Monthly precipitation at the four available stations above 1000m altitude, compared to the corresponding (a) TRMM and (b) CHIRPS data.

version 7 dataset [126]. The data covers the period 1998 to present. As just discussed, TRMM suffers from numerous biases, particularly at high elevations. First, accurately capturing snowfall remains challenging, particularly over snow surfaces. Second, in regions with few stations, gauge correction is uncertain, and made difficult by the topography (e.g., rain shadows). Third, TRMM generally tends to underestimate wet season precipitation, a particular concern in the

present case [176, 56, 109, 185]. Station data themselves can also be unreliable, suffering especially from a tendency to underestimate snowfall because of wind transport (it is unclear whether the available data for the region were corrected for this, if they even were). The accuracy of the TRMM 3B42 V7 dataset was evaluated over the Oum-Er-Rbia watershed by Ouatiki et al. (2017) [185]. While TRMM precipitation is unreliable at the daily timescale, its quality improves when averaged in space and time; at the annual time scale, they found RMSE values of 150-250mm for stations at 1600-1800m altitude. A large part of the bias occurs during summer, when local (small-scale) convective events are badly captured, but underestimation of winter precipitation is also important in mountain stations. Their results are consistent with those of Milewski et al. (2015) who analyzed TRMM V7 data over northern Morocco, including the Oum-Er-Rbia [176]. At the location of the only currently available high-altitude station (CAF station), TRMM indicates an average of 725mm of precipitation from November to April, against 350mm measured at the station. Still, topography varies substantially within the 25x25km TRMM grid cell, ranging from 1000m in the valleys to 4167m at the Jbel Toubkal, Morocco's highest peak. Despite its deficiencies, TRMM remains our best baseline to estimate precipitation in this rugged and ungauged terrain.

Cloud cover

We estimate fractional cloud cover N (equation(6.2)) from the Terra MODIS MOD06_L2 version 6 cloud cover dataset [196], available at 5km-resolution from late February 2000 to present. The data are first linearly interpolated to extract 6-hourly time series. Over the whole available period, 9 sequences of more than two consecutive days are missing, during which MODIS LST data are also unavailable. In these cases, we randomly sample cloud cover values at each grid cell among non-missing values in the same cell and during the same month. Finally, the data are resampled at the MOD10A1 1km resolution selected to run the model.

High-resolution dynamical downscaling of ERA-Interim

For humidity and wind data, we rely on the regional MRCM dynamical downscaling of ERA-Interim (Chapter 5). We extract 6-hourly 2-meter wind speed u, specific humidity q and air temperature T_a over our domain. Air temperature is used only to compare to the MODIS LST-derived estimates. Since the 12km resolution is too coarse to account for all the sharp elevation gradients, we downscale specific humidity and temperature using 1km elevation and altitude lapse rates estimated at each time step. Wind speed is left unchanged. Within a 12-km MRCM cell with temperature T_{12}, humidity q_{12} and elevation z_{12}, the downscaling to the 1km grid cell with elevation z is given by:

$$\begin{cases} T_a = T_{12} + \lambda\,(z - z_{12}) \\ \log(q) = \log(q_{12}) + \mu\,(z - z_{12}) \end{cases} \tag{6.14}$$

where λ, μ are elevation lapse-rates, estimated from the MRCM output at each time step.

6.3.3 Model configuration and experiments

We run the snow model at a 6-hourly time step over the 2001-2011 period (10 hydrological years), during which all the forcing data are available, at the native MODIS LST (MOD11A1) resolution, of about 1000m. While that resolution was suggested to be too coarse to account for the small-scale variability in snow cover characteristic of the High Atlas [13], we select it here as a compromise between resolution and computation time. For comparison, 1000m is the resolution at which SNOW17 is run over the coterminous United States within the Snow Data Assimilation program [40]. To check our results, we also ran the model at a 500m resolution over the whole basin, and found no significant difference with the 1km experiment.

To test the sensitivity of the results to uncertainties in the forcing data, specifically temperature and precipitation, we fit the snow model under several configurations. First, three experiments in which an offset of respectively -3, 0 and 3 °C is applied to the LST-derived air temperature, with precipitation kept constant. We refer hereafter to these experiments

as "LST-3", "LST+0" and "LST+3". The "LST+0" experiment is also considered to be the control experiment. Second, in the fourth experiment ("TRMM+33%") TRMM precipitation is amplified by 33%, under unchanged LST-derived air temperature, to compensate for a potential negative bias in TRMM data. Finally, we also assess the influence of the choice of SWE-snow cover relationship by fitting the snow model to a more conservative version of (6.11): $SC = 0.8 \cdot \tanh(k \cdot SWE)$ with $k = 40$ (the two relationships can be compared on Fig. 6-10-b.). We refer to this experiment as "SC40". Optimized model parameters are determined for each experiment as described at the end of section 6.3.1.

6.4 Results and discussion

6.4.1 MRCM performance

Figure 6-8 shows the December-March mean daily LST-derived air temperature and the corresponding MRCM field. Overall, there is relatively good agreement between the two, with MRCM colder by 0.92 °C on average. While MRCM temperatures undoubtedly suffer from bias as well, this suggests that the LST correction calculated at the Oukaimeden station and applied to the whole area reasonably succeeds in capturing the overall magnitude of surface air temperature during the wet season. For the most part, the two datasets are within 3 °C of each other, but the difference is largely elevation-dependent. MRCM is colder in the valleys by 1-2 °C, and warmer at high elevations, especially where snow cover is present, by 3-4 °C (Figure 6-8-a,b). This is likely due to the lack of snow cover in MRCM (largely absent at 12km resolution) which leads to a warm bias due to snow-albedo feedback, and potentially to an uncorrected cold bias in the MODIS data due to the presence of snow at high elevation [230]. Above-zero air temperatures are frequent at high elevations during winter ($T_a \geq 0$°C 47% of the time between December and March at the Oukaimeden station); in such cases, if snow is on the ground, LST will be colder than the air temperature since the snow surface temperature will not exceed 0 °C. MRCM also fails to capture much of the contrast between north- and south-facing slopes: these are small scale (<10km) effects unresolved at the chosen

resolution. Our imposed ±3°C range around the LST-derived air temperature in the sensitivity data should therefore be enough to capture the "true" air temperature values.

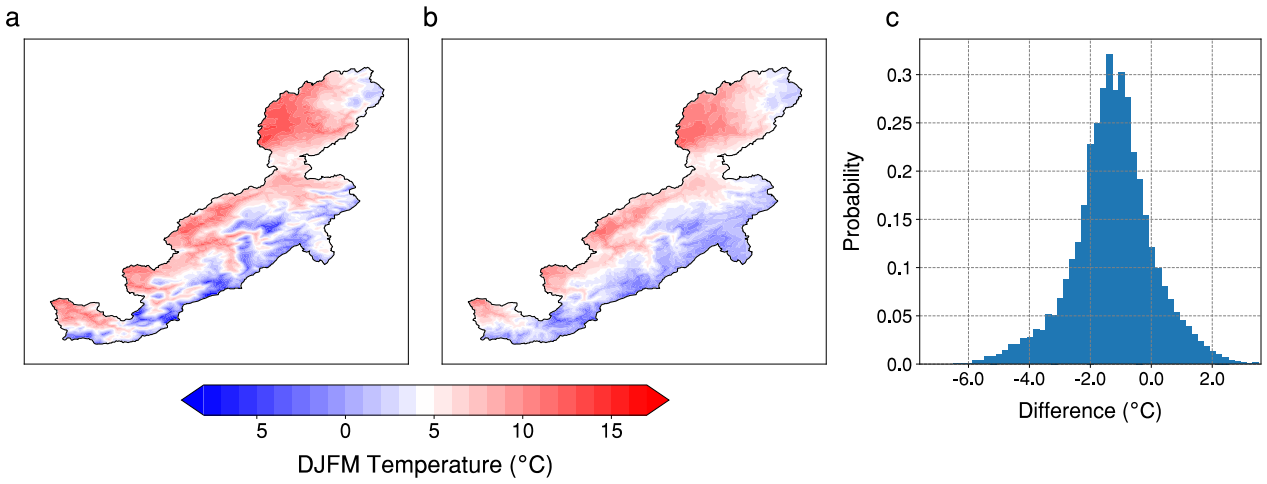

Figure 6-8: December-March average surface air temperature in our study area: (a) MODIS LST-derived, (b) MRCM interpolated to 1km resolution with elevation lapse-rates, and (c) histogram of the difference ((a) minus (b)).

At the Oukaimeden station, the annual cycles of both MRCM and MODIS LST-derived air temperature are in good agreement, with a slight warm bias for MRCM (+0.5 °C) and insignificant bias for MODIS (+0.12 °C), unsurprising here since observations are used to define the linear correction (Fig. 6-9-a). The spread of daily deviations to each series' annual cycle is also well-captured, although here MRCM performs better (RMSE of 1.8 °C against 3 °C for MODIS) (Fig. 6-9-b).

MRCM also performs well for daily surface wind and humidity. The correlation of daily 2-meter wind speed with station data is quite low ($r = 0.18$), but is higher at the monthly time scale ($r = 0.59$). The distribution of daily wind values also closely follows that of the observations (Fig. 6-9-c). In addition, daily variability of specific humidity is reasonably captured (correlation of 0.66, bias of 0.1 g/kg and RMSE of 0.8 g/kg, or 33% of the mean), which highlights the performance of MRCM and the satisfactory accuracy of the statistical downscaling.

6.4.2 Oukaimeden station

The snow model, forced with MODIS LST-derived air temperature, TRMM precipitation, empirical estimates of incoming radiation and MRCM surface wind and humidity, is fitted to the observed snow depth value at the Oukaimeden station. With M_f=0.05, $NMF_{\max}$=2.5 and $TIPM$=0.15 (Table 6.1), there is a very good fit between the annual cycles of observed and modeled snow depth (Fig. 6-10-a). The rapid melt starting in early March is nevertheless faster in the simulation compared to observations. While inter-annual variability is not correctly captured, likely due to TRMM biases, weekly fractional snow cover is not far off from the MODIS estimates (Fig. 6-10-b), even though MODIS represents a larger 500x500m area. Unsurprisingly, given the characteristic patchiness of snow cover within a grid cell [13], MODIS snow cover is often smaller than the fractional coverage inferred from the modeled SWE series (which is itself not perfect). Peak SWE occurs around March 1$^{\text{st}}$, and averages 240 mm in the simulation, against an observed value of 300 mm [28], a negative bias consistent with that of TRMM precipitation at high elevations. Sublimation losses average 90mm of water equivalent, or 21.4 $\pm$ 4.6% of snowfall, in good agreement with the 25% estimate of Lopez-Moreno et al. (2017) obtained for the same station [157].

6.4.3 Snow cover area

The allowable range and calibrated values of the three model parameters for all basin-wide experiments and the Oukaimeden experiment are given in Table 6.1. Like Follum et al. (2015), we find that M_f is the most sensitive for the calibration, but that $NMF_{\max}$ is slightly more sensitive than $TIPM$. Near the optimal M_f, two or three combinations of $NMF_{\max}$ and $TIPM$ often yield Nash-Sutcliffe coefficient values not far from the maximum. Thus, while the calibration of M_f is probably more reliable (it is constrained by the observed disappearance of the snowpack once the heat deficit has reached 0), that of the other two parameters should be seen with some caution. In addition, while fitted parameter values for the station experiment may seem similar to those for the LST-3 experiment, they are obtained by optimizing with respect to pointwise observed snow depth, and not MODIS snow cover as in other experiments,

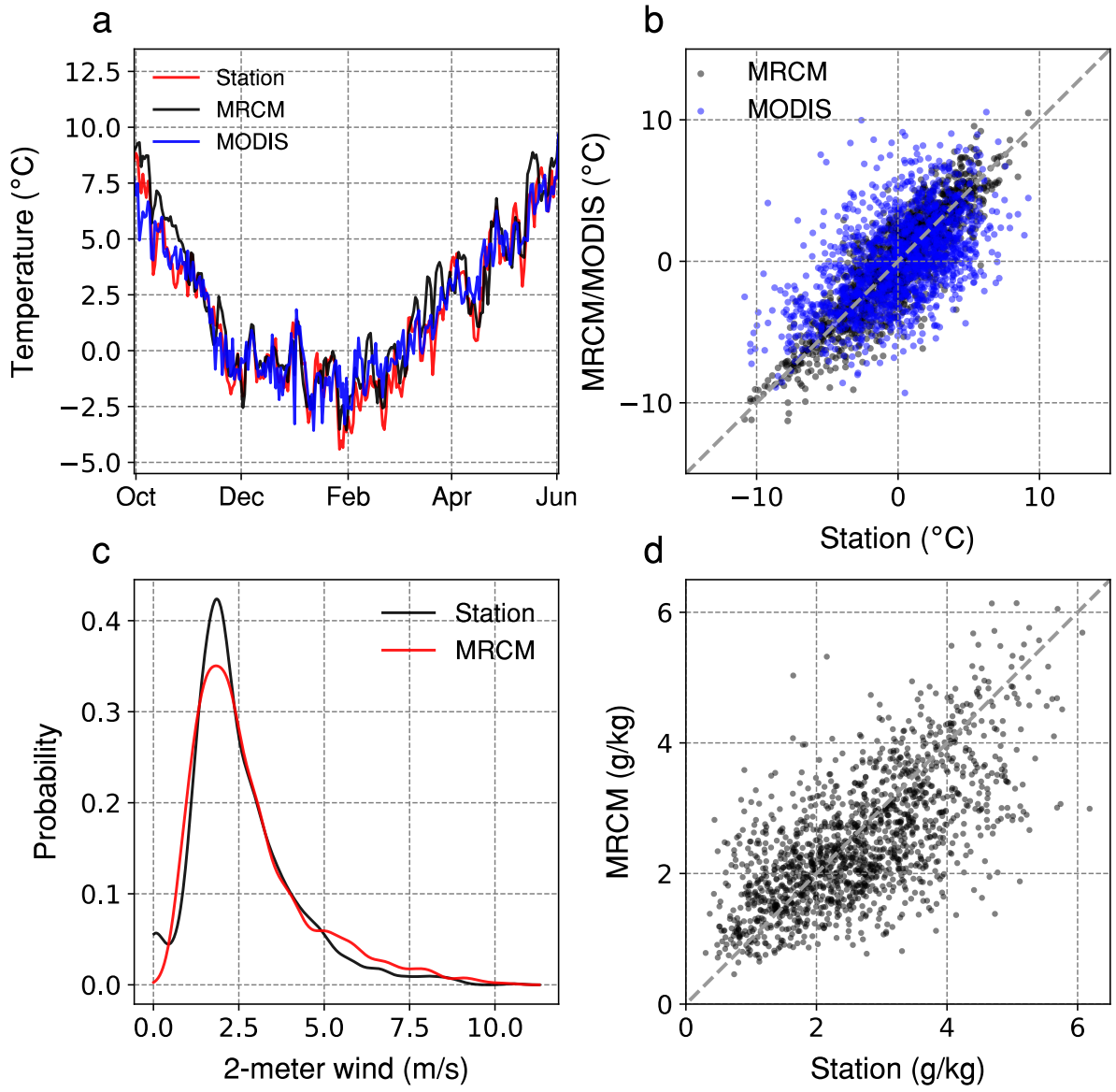

Figure 6-9: (a) Average daily temperature during the snowy season (October 1st–June 1st) at the Oukaimeden station: observations (red), MRCM (black) and MODIS LST-derived (blue). (b) Daily air temperature deviations to averages shown in (a): MRCM (black) and MODIS (blue) against observations. (c) Density of October-May daily wind speed at the Oukaimeden station in observations (black) and the MRCM simulation (red). (d) October-May daily specific humidity at the Oukaimeden station: observations against MRCM simulation.

and precipitation at the exact station location is not available either. Snow depth at the station may also not be representative of conditions prevailing for the 1km grid cell.

At the basin scale, the fitted model reproduces much of the characteristics of the snow cover distribution as inferred from the MODIS data. The magnitude and variability of snow cover

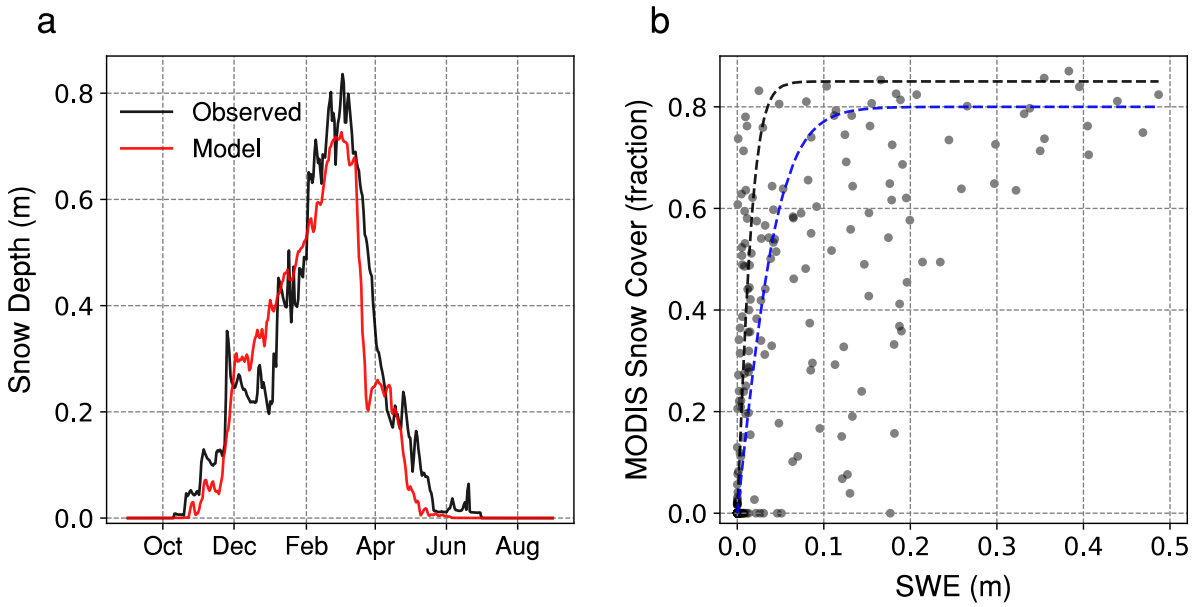

Figure 6-10: Results of snow model at Oukaimeden station. (a) Average annual cycle of snow depth (black: observed; red: calibrated model output). (b) Weekly modeled SWE against MODIS fractional snow cover for the corresponding grid cell. The dashed black (respectively blue) line shows the two SWE-snow cover relationships (see (6.11)): $SC = 0.85 \cdot \tanh(100 \cdot SWE)$ (dashed, black) and $SC = 0.80 \cdot \tanh(40 \cdot SWE)$ (dashed, blue).

Par.	**Name**	**Unit**	**Range**	**Value**				
				Station	LST+0	LST-3	LST+3	TRMM +33%
M_f	Melt factor	mm/°C/hr	0.001-0.6	0.05	0.06	0.205	0.035	0.08
$NMF_{\max}$	Maximum negative melt factor	mm/°C/hr	0.1-3	2.5	1.2	0.15	2.5	0.3
$TIPM$	Antecedent temperature index par.	fraction	0.001-1.0	0.15	0.3	0.91	0.2	0.8

Table 6.1: Model parameters: Allowable range and calibrated values for the RTI-SNOW17 model parameters.

are well approximated, both at the daily and seasonal timescale (Fig. 6-11). Some short-term peaks in snow cover are underestimated, as in January 2007 (Fig. 6-11-b), or overestimated, as in March 2009 (Fig. 6-11-c). This is not unexpected given the uncertainty in the forcing data; many snowfall episodes in the High Atlas, particularly at lower elevations, also occur

near the freezing point. A small error of even just 1°C could therefore lead to largely underestimate snow cover after a specific storm. One should also remember that MODIS snow cover is itself an imperfect measure of snowpack extent, even when averaged at the weekly timescale. Non-missing data is not free of errors and the filtering algorithm implemented here may fail in certain circumstances (e.g., particularly persistent cloud cover) [13].

Looking at different elevation ranges, we find that mean snow cover and its inter-annual variability are also well reproduced (Figs. 6-11-d and 6-12), particularly the timing and speed of snowpack build-up and melt. Still, the model tends to overestimate snow cover at high elevations ($\geq$2500m) and underestimate it at low elevations. The latter is not particularly critical since snow cover below 1500m is mostly scarce and short-lived, and stores little to no water over the winter season. The former, however, suggests an overestimation of the snow water content, or an inadequacy of our SWE-fractional snow cover relationship. For a given SWE, we may be underestimating the variability of snow cover below 1km, and therefore falsely inflating the corresponding fractional snow cover.

6.4.4 SWE distribution and basin-wide SWE volume

Although no basin-wide SWE observations are available, it is useful to estimate the total snowpack water content inferred by the model constrained by the observed snow cover, as well as its altitudinal distribution. The distribution of winter temperatures indicates that only areas above 2500m experience below-freezing average temperatures (Table 6.2). Based on the MODIS LST-derived air temperature, the fraction of snowfall to annual precipitation ranges from 2-3% at the lowest elevations ($\approx$800m) to more than 60% near the highest peaks (Fig. 6-13-a, Table 6.2). Areas above 2500m, which account for most of the snowpack, receive about 52% (respectively 75%) of their annual (respectively November-April) precipitation as snow. Therefore, SWE is essentially concentrated above 2500m (Fig. 6-13-c), an area which covers about 15% of the whole basin (Fig. 6-14-a).

The average annual cycle of basin-wide SWE is shown on Figure 6-14-b. The build-up of the snowpack is gradual, starting in early November; a peak is reached around February 1st followed by melting ending in mid-May. At its peak, basin-wide SWE reaches 150 million cubic

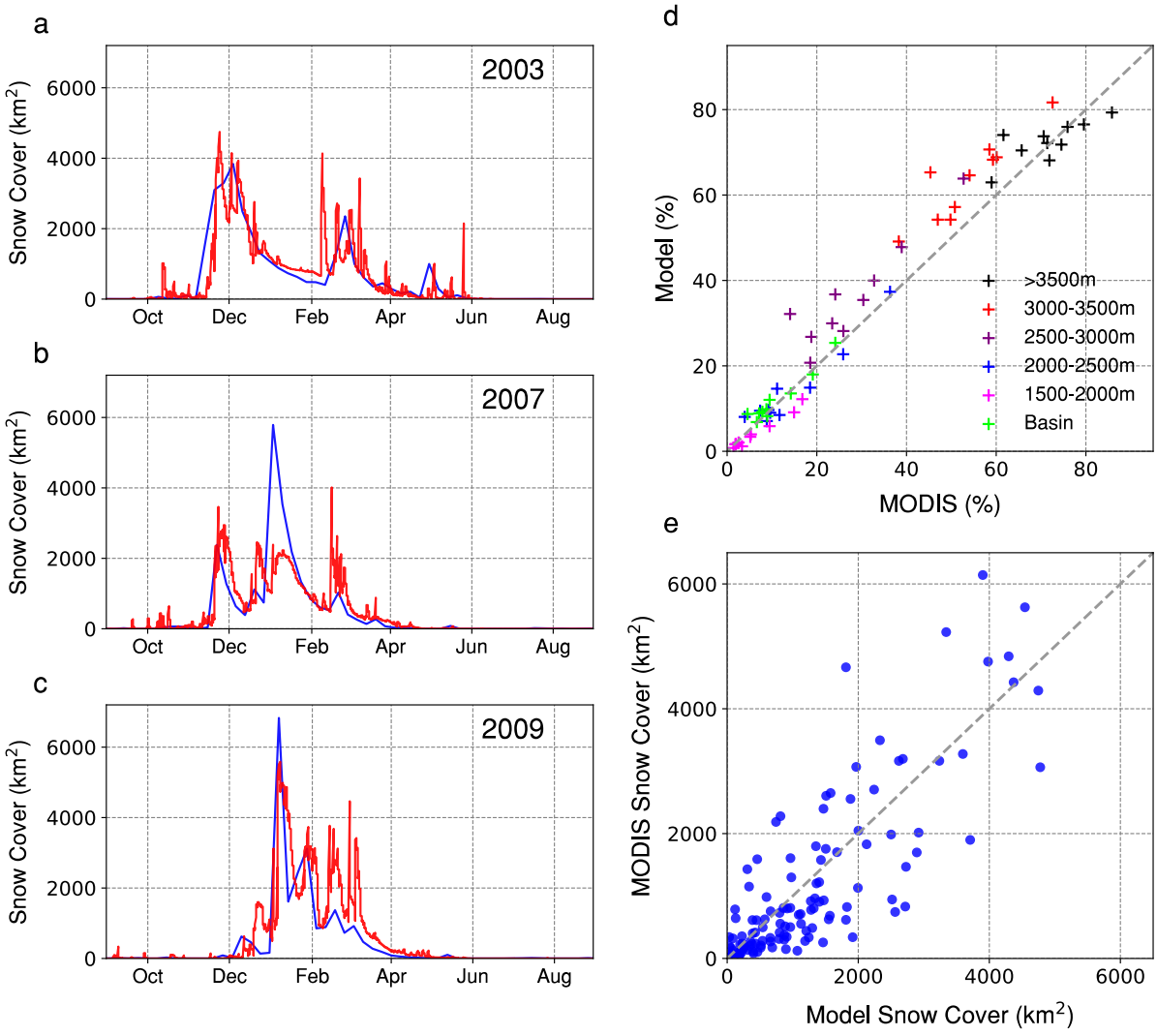

Figure 6-11: Snow model results for the control (LST+0) experiment. (a-c) Daily snow cover extent from model simulations (red) and weekly extent from the MOD10A1 dataset (blue) for three hydrological years (shown topright): (a) 2003-04, (b) 2007-08 and (c) 2009-10. (d) December-March average snow cover (in %) in model simulations and MOD10A1 data, for all 10 hydrological years of the simulations, at various elevation ranges. (e) Weekly modeled snow cover extent against MOD10A1 estimates (2001-2011).

meters (MCM), or 0.15 km^3 (Fig. 6-14-a). This is a small fraction of cumulative snowfall for the area, which amounts to roughly 1 km^3. Due to the high inter-annual variability of precipitation, the SWE peak can range anywhere from 50 to 450 MCM, a much larger variability than that of precipitation. Peak SWE is reached at different times depending on the elevation, however. Above 3000m, where temperature remain longer below freezing, peak SWE occurs in late March, right before the onset of melt (Fig. 6-15-a,b). SWE above 3000m represents only

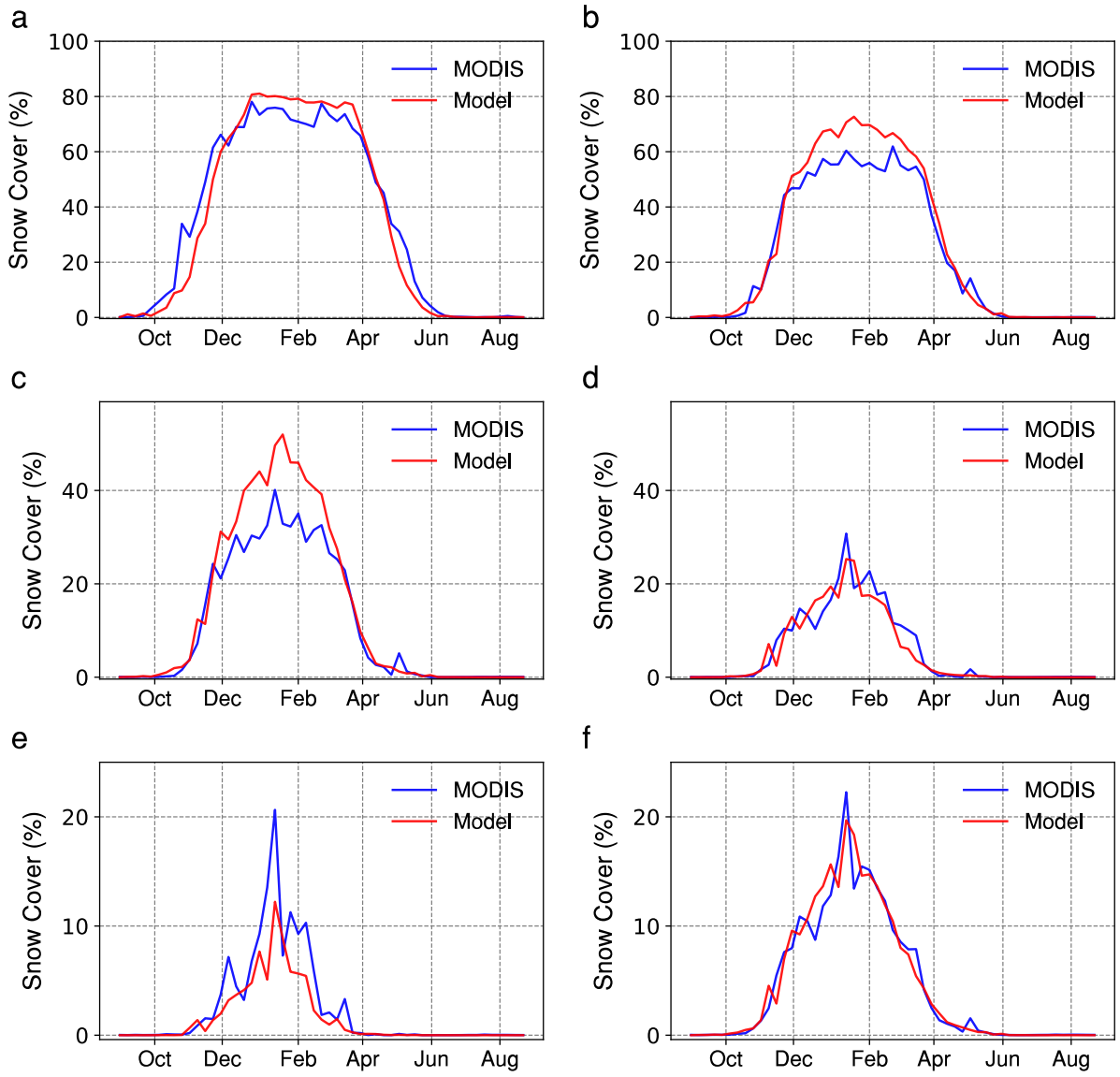

Figure 6-12: Average annual cycle of snow cover (in %) in the control (LST+0) experiment at various elevations ranges within our study area: (a) > 3500m, (b) 3000-3500m, (c) 2500-3000m, (d) 2000-2500m, (e) 1500-2000m and (f) whole area.

20% of total SWE, whereas about half of the basin's SWE is concentrated between 2500 and 3000m. At lower elevations, snowpack is much less persistent and peaks in January, when temperatures allow for short-term snow cover.

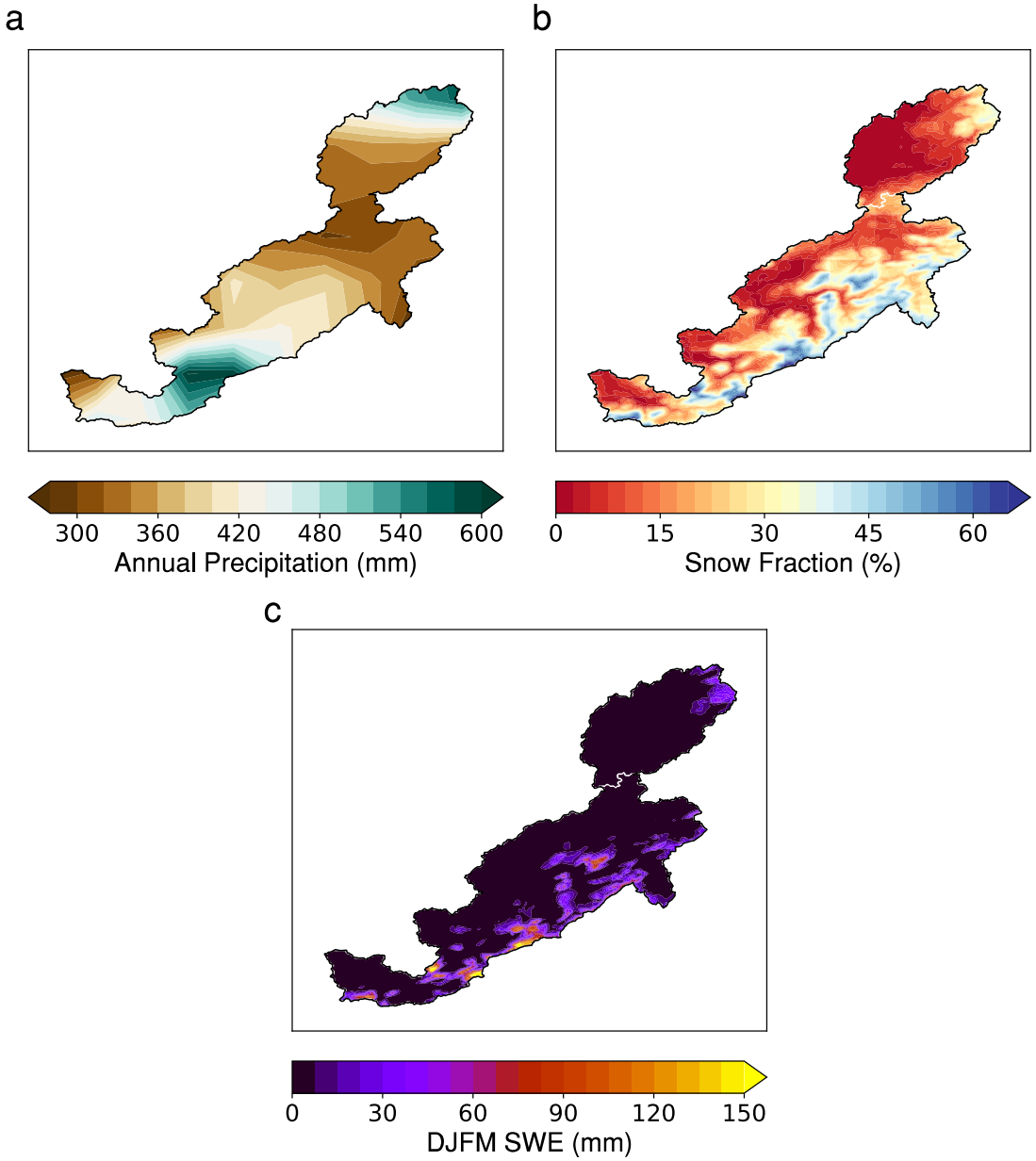

Figure 6-13: (a) Annual precipitation over the study area (TRMM 3B43 V7). (b) Fraction of annual precipitation falling as snow. (c) Mean December-to-March (DJFM) modeled SWE (in mm).

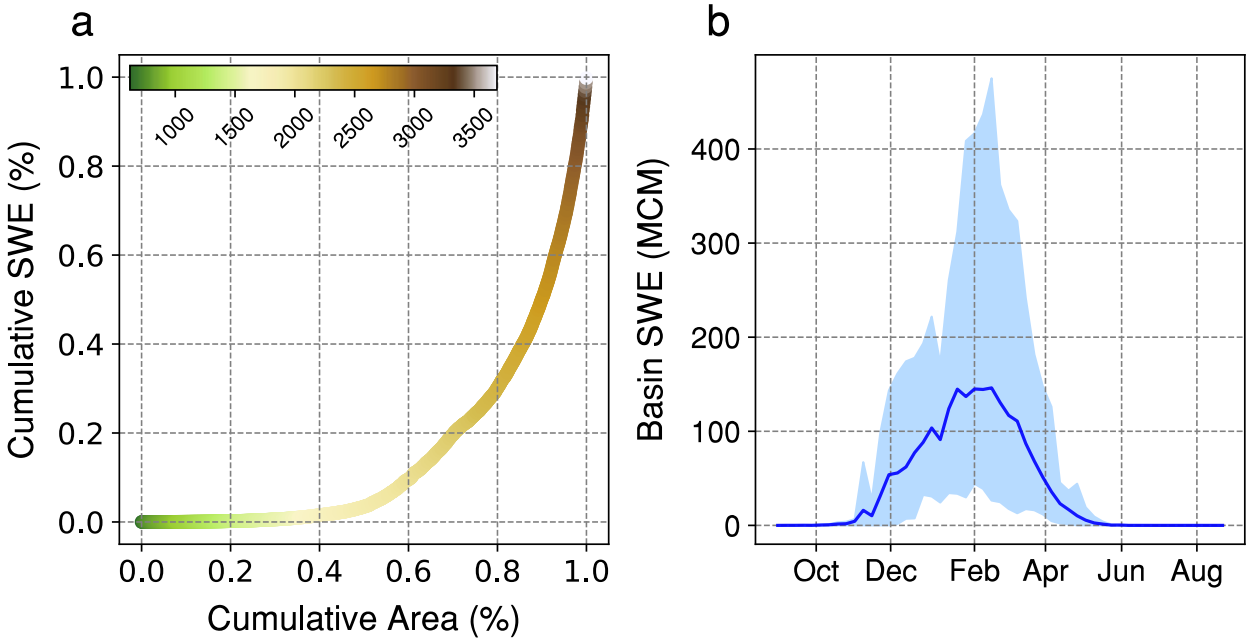

Figure 6-14: (a) Cumulative distribution function of basin area (x-axis) and peak SWE (y-axis) as a function of elevation (shading). Basin area and peak SWE were both renormalized by their maxima to make the two axes equal. (b) Annual cycle of basin-wide SWE in the control experiment: mean (solid blue) and 90% range (blue shading).

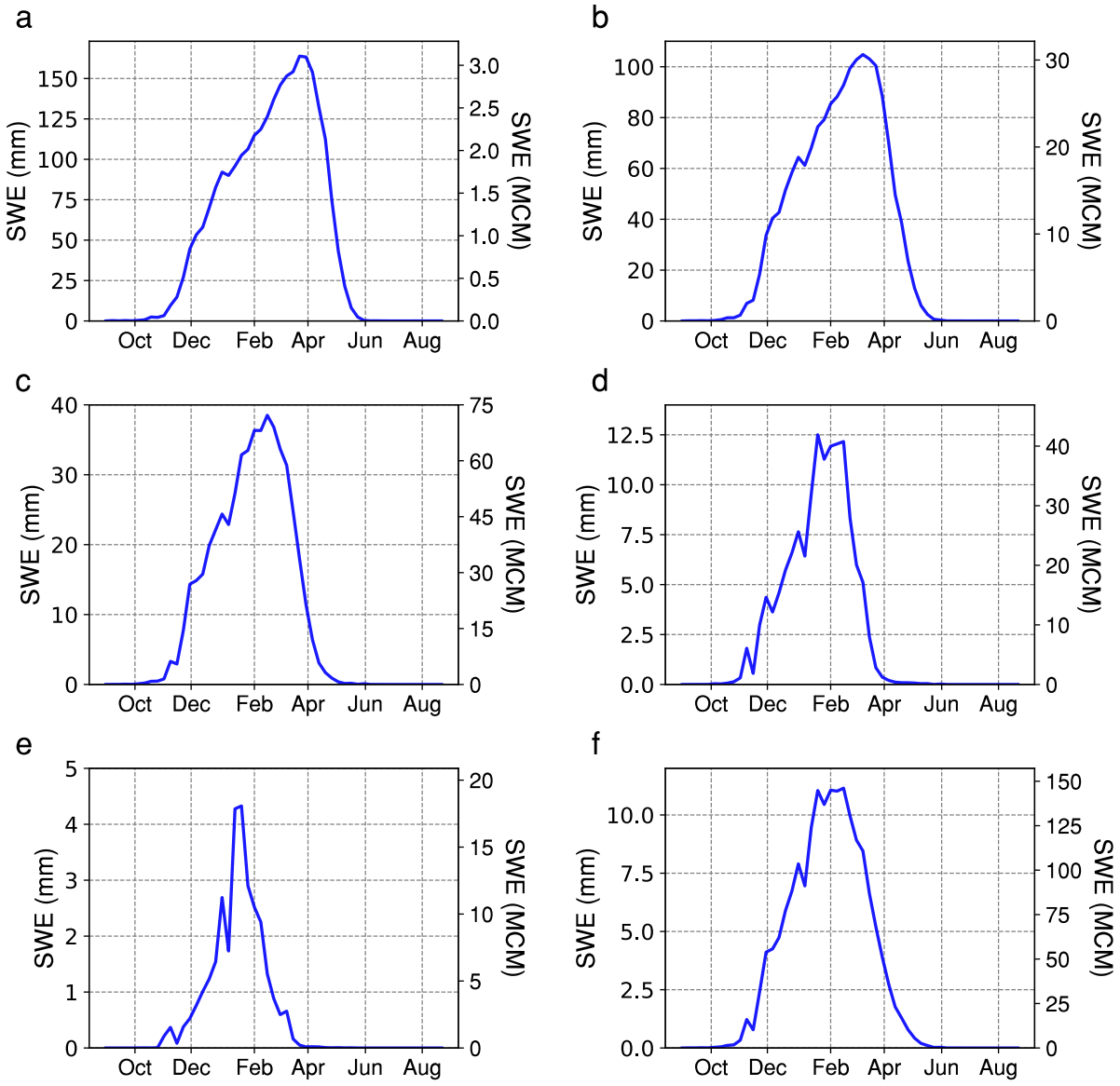

Figure 6-15: Average annual cycle of SWE in mm (left axis) and MCM (right axis) in the control (LST+0) experiment at various elevations ranges within our study area: (a) $>$ 3500m, (b) 3000-3500m, (c) 2500-3000m, (d) 2000-2500m, (e) 1500-2000m and (f) whole area.

Elevation	Ann. prec. (mm)[1]	DJFM prec. (mm)[2]	Ann. snow (mm)[3]	DJFM snow (mm)[4]	Snow frac. (%)[5]	Melt (mm)[6]	DJFM Temp. (°C)[7]	DJFM wind (m/s)[8]	DJFM RH (%)[9]	DJFM SCr (%)[10]	DJFM SWE (mm)[11]	Frac. Area (%)[12]	Sublim. (mm)[13]
All	192	426	59	81	19	74	5.4	2.6	56	11	7.3	35	7
	111/346	312/549	32/108	43/135	12/27	38/124	3/6.9	2.2/3.1	48/71	5/22	2/22	22/55	5/12
≥3500m	264	563	213	347	61	247	-6.4	3.1	60	74	103	100	99
	166/530	434/740	130/453	223/533	48/72	148/433	-8.8/-5.2	2.7/3.9	54/79	59/82	24/194	–	75/118
3000-3500m	261	558	188	300	53	244	-4.2	2.9	61	60	71	99	56
	160/482	422/704	119/388	186/432	44/62	142/382	-7/-2.9	2.6/3.6	52/76	42/80	18/179	97/100	44/68
2500-3000m	206	452	121	183	40	158	-0.3	2.9	59	32	24	87	25
	100/348	338/558	66/241	97/274	29/49	80/240	-3.4/1.1	1.6/3.6	51/75	17/61	6/67	66/99	16/37
2000-2500m	201	443	84	118	26	111	3.2	2.7	57	11	6.3	55	7
	108/332	334/552	46/153	56/198	16/36	51/186	0.1/4.7	2.4/3.4	49/74	5/31	1.6/25	19/87	4/13
1500-2000m	186	416	42	50	12	48	6.6	2.5	55	3	1.4	17	2
	100/334	291/546	18/91	28/94	8/19	27/92	4.5/8.2	2/2.3	47/69	0.1/9	0.2/5.3	1/49	0/5

Table 6.2: Snow model results and input data, averaged for the whole study area and various altitudinal bands: (1) Annual precipitation; (2) December-to-Mach (DJFM) precipitation; (3) Annual snowfall; (4) DJFM snowfall; (5) Fraction of solid precipitation; (6) Total snowmelt; (7) DJFM air temperature; (8) DJFM wind speed; (9) DJFM relative humidity; (10) DJFM average snow cover; (11) DJFM mean snow water equivalent; (12) Fraction of area with ≥5% snow cover in DJFM; (13) Total sublimation. For each elevation range, the top line indicates the 2001-2011 average and the bottom line shows the full range of values.

As can be deduced from Fig. 6-15, melt is extremely rapid, essentially occurring between February and May (Fig. 6-16), when temperatures quickly rise above freezing at all altitudes. However, even during winter, positive temperatures are frequent below 2500m and this is reflected in non-negligible melt rates throughout the snowy season.

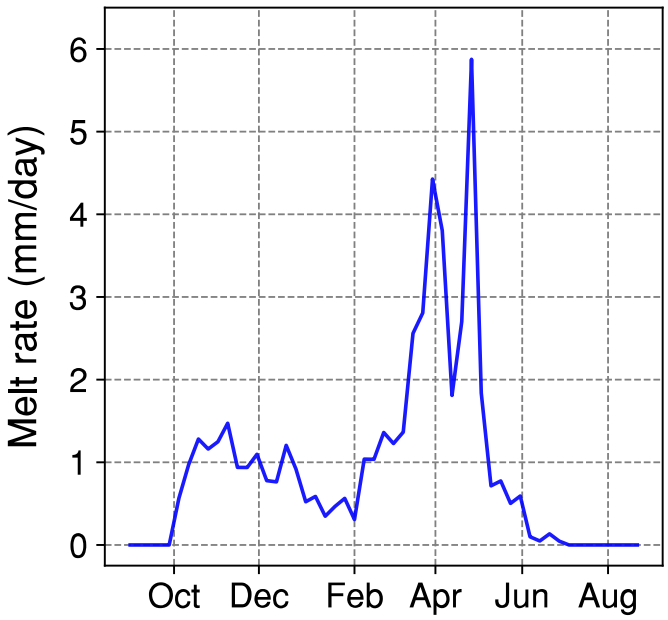

Figure 6-16: Annual cycle of average daily melt rate for all areas with positive (>5%) snow cover, regardless of elevation.

6.4.5 Latent heat fluxes

The High Atlas is characterized by rather dry conditions, even at high altitudes during winter: for instance, the average relative humidity between December and March at the Oukaimeden station (3200m asl) is only 46%. Together with persistent snow cover above 2500m and occasional strong winds (Fig. 6-9-c), conditions are met for large latent heat fluxes. In the control (LST+0) simulation, we find for the basin as a whole that snowpack losses by sublimation amount to 0.095 km^3 on average, which is small compared to total precipitation (1.9% of annual precipitation, 2.8% of November-April precipitation) and to the total snowfall (≈9%). Relative losses increase rapidly with elevation, from only 5% at 2000m to about 30% above 3500m (Fig. 6-17-c). Near 3200m altitude, sublimation removes 20% of the snowpack, not far from the 25% found by López-Moreno et al. (2017) at Oukaimeden [157]. This difference is still

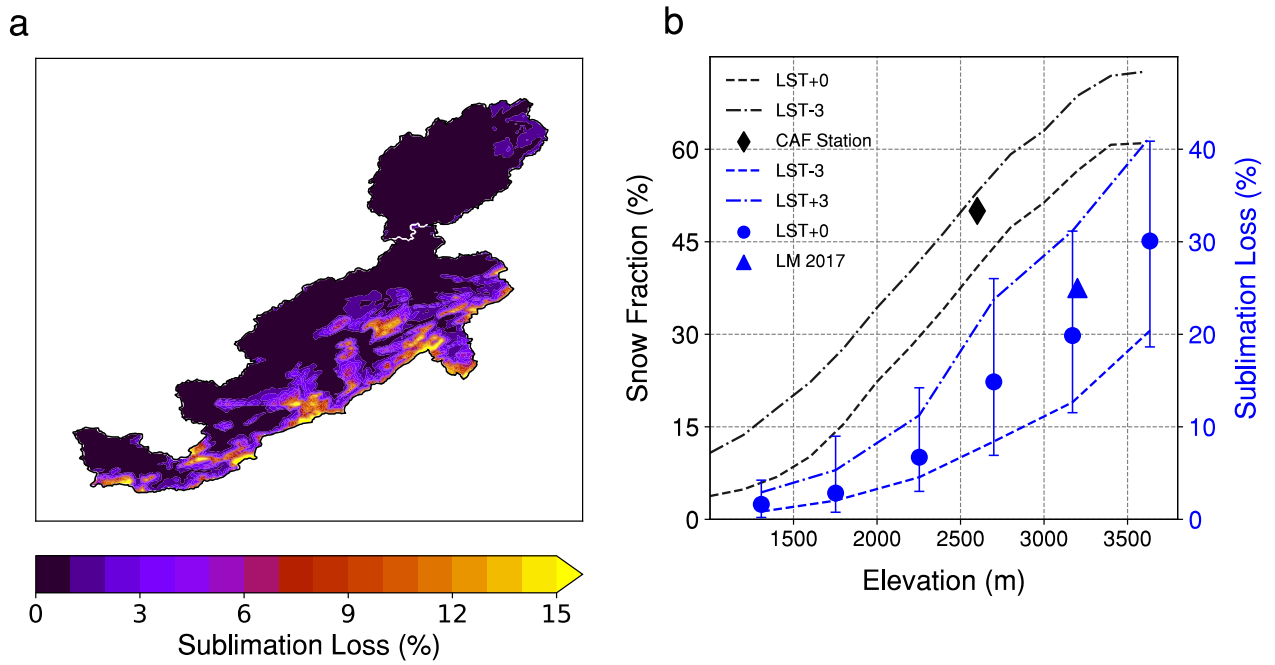

Figure 6-17: (a) Fraction of annual precipitation lost by sublimation in the control (LST+0) experiment. (b) Fraction of annual precipitation falling as snow (black, left axis) and fraction of snowfall lost to sublimation (blue, right axis) as a function of elevation. Estimated values for the CAF station and Oukaimeden experimental site are also shown.

large, but given all the uncertainties involved in our analysis may not be significant. Part of it may be due to the fact that the latitude of our domain is slightly higher and relative humidity is consequently larger (46% at Oukaimeden vs. 54% at similar locations in our domain). At 12km, the resolution of our downscaled regional climate simulations remains coarse for snowpack modeling and therefore wind speed at high elevations may also be underestimated, a possibility that would require additional wind measurements to verify. Inter-annual variability in sublimation losses is also substantial: they vary between 18% and 42% above 3500m, and, even below 2000m, range from 1-5%.

These estimates are naturally very dependent on the wind, humidity and temperature data used as forcing. They are about a third lower in the LST-3 simulation compared to LST+0, and half again as much in LST+3, but display the same strong dependence to elevation (Fig. 6-17-d). For instance, above 3000m, 21% of the snowpack is lost to sublimation on average in LST+0, 14% in LST-3 and 32% in LST+3. The comparison with the CAF station figures (snowfall is 50% of annual and 68% of November-April precipitation, Fig. 6-17-b) also suggests

that the MODIS LST-derived air temperature may still be positively biased with respect to real-world T_a (see Fig. 6-5-b). The higher snow fractions in the LST-3 run are indeed closer to observed values. Another possibility is that precipitation is preferentially underestimated when it is solid, a common problem with satellite-based estimates [56, 77], thus automatically decreasing the fraction of snow to annual precipitation.

6.4.6 Sensitivity to inputs

Finally, we turn to the sensitivity analysis of basin-wide SWE to uncertainties in the forcing data and to the SWE-snow cover relationship. Optimal parameters are found for each experiment so that they all reproduce basin-wide and elevation-specific snow cover series, though most (except LST+3 and the SC40 experiments) tend to overestimate snow cover area between 2500 and 3000m (as in Fig. 6-12). The build-up of the snowpack is also too slow in the SC40 run, no doubt due to the larger SWE required to reach maximum snow cover (section 6.3.3). However, constrained as they are by the observed snow cover series, the various experiments all show somewhat similar basin-wide SWE value, between 120 and 210 MCM at their peaks (Fig. 6-18-c). The potential underestimation of precipitation does not seem to impact the SWE estimates very much: they are only about 10% higher in the TRMM+33% experiment than in the control run. However, a 33% correction may not be enough to compensate for underestimated or even missing snowfall episodes in the TRMM data; for an improved correction of TRMM biases in this region, additional station data is vital. The maximum peak SWE is unsurprisingly attained in the SC40 experiment, since it requires a higher SWE to attain the same fractional snow cover. Even then, we remain within

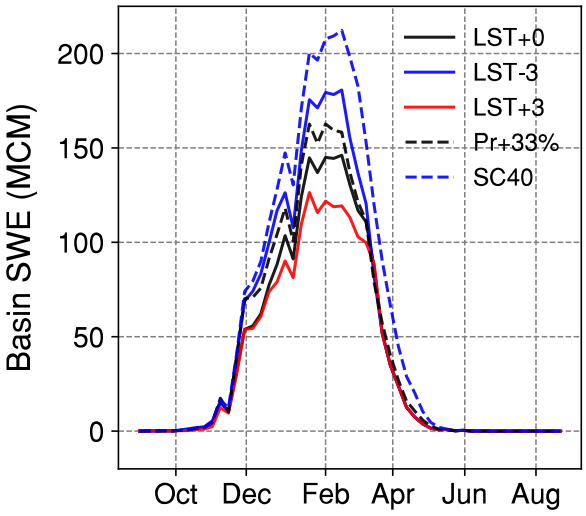

Figure 6-18: Annual cycles of basin-wide SWE in the various sensitivity experiments.

the same range of estimates, and it seems fair to say that snowpack in our catchment holds about 150-175 MCM at its peak.

This still amounts to a significant uncertainty, which is difficult to resolve. An empirical backward SWE reconstruction constrained by the evolution of the snow cover [77] may be useful as a future step to test the validity of our SWE results, for instance using higher-resolution (<60m) Sentinel-2 data [91]. Additional station data, even at low elevations, would be helpful to improve temperature estimates. Precipitation biases, however, are more challenging to tackle with no high-altitude data at hand. Statistical models to correct and distribute precipitation within a TRMM grid cell based on fine-scale topography may help resolve some of the biases due to the complexity of the terrain at small scales. Another possibility would be to calibrate additional parameters in SNOW17 which we assumed as constant here, as for instance the temperature threshold to define snowfall (0°C in this analysis) and a precipitation under-catch adjustment factor [83]. Still, the potential underestimation of precipitation does not seem to impact the SWE estimates very much: they are only about 10% higher in the TRMM+33% experiment than in the control run. In the absence of station data, it is difficult to determine whether this correction is enough to compensate for underestimated or even missing snowfall episodes in the TRMM data; results by Hashemi et al. (2017) over the United States suggest that winter precipitation above 3000m altitude may be underestimated by as much as 50% [109]. For a fixed SWE-snow cover relationship, the impact of precipitation uncertainty on peak SWE seems small (Figure 6-18-c), though it would matter for melting rates: too much precipitation at fixed snow cover may lead to overestimation of melt during the cold season.

As discussed previously, sublimation rates are also uncertain, mainly because of biases in air temperature and surface wind speed. At the highest elevations, we find a rate of 0.65-1mm/day (Table 6.2), comparable to that measured on Kilimanjaro (0.92 mm/day), where incoming shortwave and latent heat fluxes dominate the snow energy balance [178]. The low rates found in the LST-3 experiment seem unlikely based on what is known in such environments [157], and our 20% estimate above 3000m is probably at the low end of the range. Rates of 45% were measured on the southward, much drier side of the Atlas, thus setting an upper bound to what can reasonably be expected in our region. Overall, a 20-35% range is realistic.

Because our approach uses snow cover to fit the snow model, the SWE-snow cover relationship is a major source of variability in the results, as we see in the case of the SC40 experiment. In the control formulation, maximum cell snow cover is reached for 5mm SWE, roughly 15-40cm of snow depth. Increasing that threshold to 10mm as in SC40 increases peak basin-wide SWE by 60MCM, and therefore the extreme case of a 20mm threshold could potentially bring the result up to 300MCM, or double what we found in the control experiment. The analysis of spring runoff volumes could help put an upper bound on that figure.

In addition, as mentioned previously, our assumption of a one-to-one relationship between snow cover and SWE for an individual grid cell is questionable. Fresh and old snow have very different compaction ratios (respectively of the order of 1:10 and 1:3), meaning that the same SWE at different times in the life of the snowpack will be associated with very different snow depths and likely different fractional snow covers. Initial compaction ratios can also vary significantly depending on the type of solid precipitation (graupel, sleet, powder snow, etc.), a detail we do not take into account in this analysis. It is difficult to estimate a priori the respective frequencies of each type of solid precipitation, especially due to the scarcity of ground measurements in the High Atlas. The difference between snow and graupel could potentially be resolved by considering the spatial scale of the storm, since graupel is typically associated with small-scale convective systems and higher radar reflectivity compared to snow. Graupel also occurs in conjunction with faster upward velocities than for snow (3m/s against 1-2m/s). Lightning activity in the Atlas is high in May and in October[2], which suggests that small-scale convective activity and therefore the likelihood of graupel would be higher in these months.

Still, even if we assume equations 6.12-6.13 to be valid at all times, our results could be improved by using modeled snow depth from equation 6.12, instead of SWE, to infer fractional snow cover at the grid cell scale. Such a relationship has not been described for the High Atlas, but analyses in similar mountain environments could be used as first step. One advantage of using snow depth as the output variable is that satellite-based snow depth products, based on Synthetic Aperture Radar (SAR) data, are becoming increasingly available (e.g. as part of the Sentinel project [154]), and could therefore be used as input for the data assimilation as well.

[2]See for instance https://ghrc.nsstc.nasa.gov/lightning/data/data_lis_vhr-climatology.html

6.5 Conclusion

We developed in this chapter the first implementation of a distributed, physically-based empirical snow model at large scale in the High Atlas of Morocco. This region is characterized by a very sparse station network, and therefore we relied on satellite-based and dynamically-downscaled meteorological data as forcing for the SNOW-17 model, and compared the model-simulated snow cover to remotely-sensed snow cover estimates from MODIS. The model accurately captures the distribution of snow cover at various elevation bands as well as its temporal dynamics. When applied at the Oukaimeden station, results were also consistent. While our coarse resolution and the numerous uncertainties associated with the forcing data bring important limitations to our results, we find reasonable confidence in a peak basin-wide SWE estimate of 0.15-0.175 km^3, almost exclusively concentrated above the 2500m altitude line. We also find that sublimation losses are substantial, ranging from 0.06-0.14 km^3 for the whole basin and amounting on average to 20% of total snowfall above 3000m, in keeping with previous results [157]. Our results thus offer a first-order estimate of sublimation in the High Atlas, in absence of even a sparse network of direct sublimation observations. In addition, the model offers the potential for assessing the sensitivity of High Atlas snowpack to climate change, of critical importance for the region. Many improvements to our approach are possible, whether regarding the selection and correction of data or the modeling itself, and the advent of higher-resolution snow cover estimates with Sentinel-2 [91] will certainly help in this direction [13]. However, as long as station observations remain so scarce, any estimate of snow dynamics in the High Atlas will remain quite uncertain. In particular, more direct measurements of latent heat fluxes are necessary to validate sublimation parametrizations and modeled fluxes in this region.

Chapter 7

Projections of High Atlas snowpack and runoff in future climates

7.1 Introduction

The High Atlas is the major source of freshwater for the semi-arid plains of central Morocco. Much of the discharge of the Oum-Er-Rbia and Tensift, the two main rivers of central Morocco, comes from the mountainous terrain where they begin their course. In this region, precipitation essentially falls at elevations above 1000m [32]; below that, it is scarce and evaporation is extremely high, leading to minimal runoff. Though located in a rather warm region, the High Atlas rises up to more than 4000m and often experiences below-freezing conditions between November and March [32]. Consequently, snow is a major component of the regional water cycle [165, 253]. It accounts for a substantial fraction of annual runoff, up to 50% in some mountain catchments [32], and for most of the runoff during spring, as the wet season comes to an end.

Still, climate projections over Morocco happen to agree on robust warming and drying trends under greenhouse gas forcing. By the end of this century, average winter temperatures in the High Atlas could be 2-4°C higher, and precipitation 25-45% lower, depending on the emissions scenario (Chapter 5). Being already close to the 0°C isotherm, the High Atlas stands out as

particularly vulnerable to snow cover loss. However, few studies have analyzed climate change impacts on the local snowpack and regional water availability. Applying a complex physically-based snow model to one station snow data series from the Moroccan High Atlas, Lopez-Moreno et al. (2017) found that Atlas snowpack was somewhat less sensitive to warming and drying than that in other Mediterranean-climate regions, because of colder snowpack temperatures associated with high latent heat losses [157]. Still, their results pointed to a decrease in average snow duration of 25-30% and mean Snow Water Equivalent (SWE) of 30-55% by 2050. By contrast, the analysis of 12 years (2000-2013) of remotely-sensed snow cover area from the MODIS satellites yielded few significant trends in snow cover duration across the region [165]. At these relatively short timescales, however, the variability in Atlas snow cover is primarily determined by the inter-annual variability in wet-season precipitation, itself largely dependent on the North Atlantic Oscillation [147, 31]. Because precipitation exhibits a large coefficient of annual variation (0.25), potential long-term climate trends will be difficult to identify in such short-term series. Only one study tried to quantify the impact of climate change on High Atlas runoff by taking snow dynamics into account: Marchane et al. (2017) developed runoff projections for the Rheyara catchment, south of Marrakech and part of the Tensift watershed, by running conceptual monthly water-balance models incorporating a simple parametric snow module [166]. They projected a 19 to 63% decline in surface runoff by the middle of the century, dependent on model and scenario. Therefore, while it is clear that the region is headed towards a pronounced decline in snowpack and runoff, much remains to be done to quantify that decline at the catchment level and reduce uncertainties.

In the previous chapter, we described the High Atlas snow water balance by assimilating remotely-sensed and dynamically-downscaled data into a simple distributed snow model to reconstruct snowpack within the Oum-Er-Rbia watershed. In this chapter, we build on this methodology by applying the same snow modeling framework to the regional climate projections developed in Chapter 5 to assess the future of High Atlas snowpack under anthropogenic warming. In addition, we quantify the sensitivity of runoff in seven mountain catchments within the Oum-Er-Rbia watershed to large-scale meteorological conditions, and use the results to assess the impact of warming, drying and snowpack disappearance on runoff. We first describe our study area, the data and climate model output used in this study, before

detailing the runoff modeling framework. Snowpack and runoff projections are then presented and discussed, before concluding with major results and implications.

7.2 Data and study area

As in Chapter 6, our focus is on the Oum-Er-Rbia catchment, Morocco's second largest watershed and a major agricultural center. The Oum-Er-Rbia flows northwestward from the northern slopes of the High Atlas. Much of its discharge originates from the High and Middle Atlas, where average precipitation is typically three to four times that over the plains. Snowfall also regularly occurs above 1000m, and builds a persistent snowpack above 2500m.

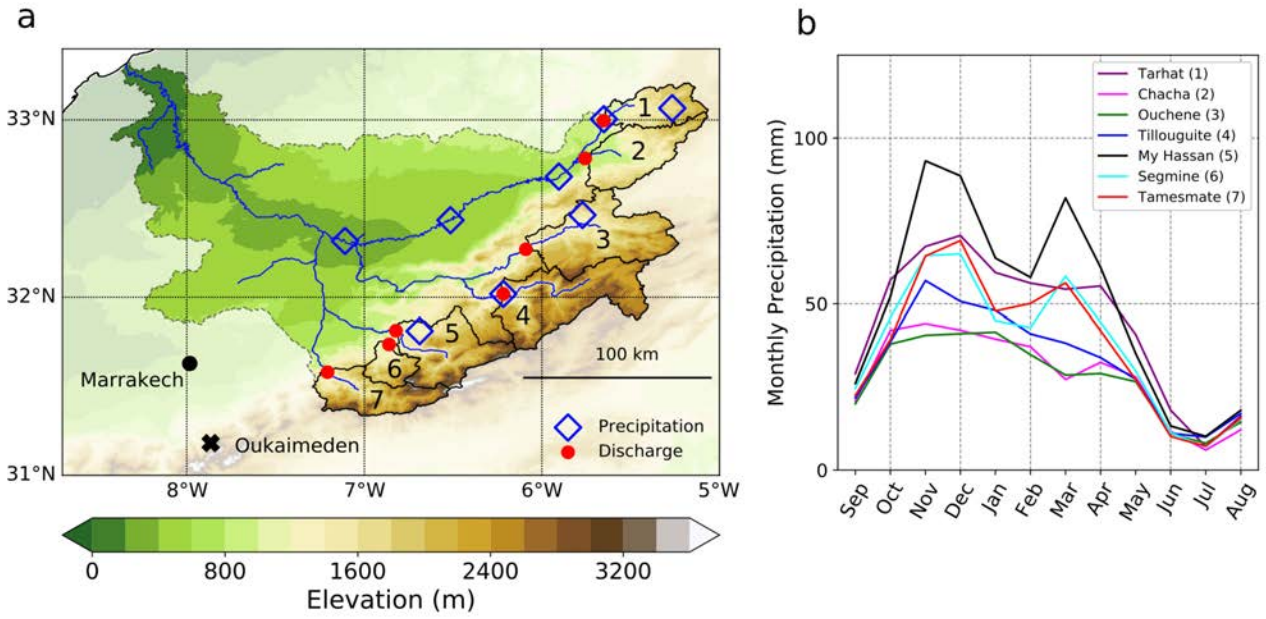

Figure 7-1: (a) Map of study area, the Oum-Er-Rbia watershed, with elevation shown in filled contours. The main waterways are indicated by solid blue lines. Blue diamonds and red circles indicate the location of precipitation and river discharge stations, respectively. The seven catchments defined by the discharge stations are indicated by numbers: (1) Tarhat, (2) Chacha, (3) Ouchene, (4) Tillouguite, (5) Moulay Hassan, (6) Segmine and (7) Tamesmate. The location of the Oukaimeden snow station, outside our study area, is shown by a black cross. (b) Annual cycles of precipitation for the seven catchments, based on TRMM data (1998-2015).

7.2.1 Hydroclimatological data

Daily discharge measurements are available at seven locations between 1978 and 2015 (Fig.7-1-a). Each has at most 0.5% of missing data. These locations define the seven sub-catchments for which runoff will be modeled, from north to south: Tarhat, Chacha, Ouchene, Tillouguite, Moulay Hassan, Segmine and Tamesmate. These catchments cover most of the area we focused on in Chapter 6, *i.e.* most of the area within the Oum-Er-Rbia watershed that receives significant snowfall. Their average elevation varies from 1460 to 2360m. We remove the contribution from base flow by subtracting the minimum monthly discharge value for each catchment and for each hydrological year (September-August). This correction is minor for all catchments except Tarhat, the northernmost one. It includes the headwaters of the Oum-Er-Rbia river, and receives a substantial contribution of base flow to its annual discharge. In particular, the flow at Tarhat remains high during summer (≈35% of its wet-season peak), likely due to groundwater discharge from deep mountain aquifers. Annual cycles of corrected monthly discharge are shown on Fig. 7-2-a.

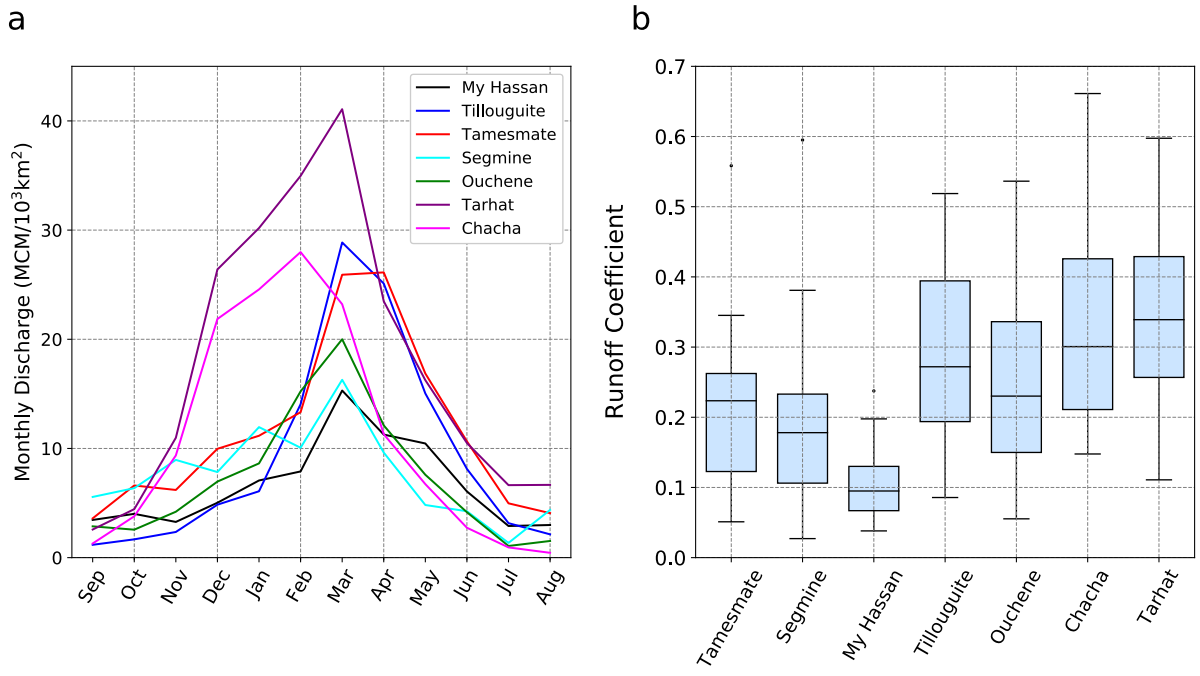

Figure 7-2: (a) Annual cycles of monthly runoff at the seven runoff gauges, after base flow removal and normalization by catchment area (km^2). (b) Boxplot of annual runoff coefficients for the seven catchments (1982-2011), using ERA/MRCM precipitation bias-corrected with TRMM data.

As in the previous chapter, we use the TRMM TMPA (TRMM Multi-Satellite Precipitation Analysis) 3B42 version 7 dataset [126] as the reference precipitation dataset for the region. The data cover the period 1998 to present. Milewski et al. (2015) and Ouatiki et al. (2017) assessed the accuracy of the TRMM 3B42 V7 dataset in the Oum-Er-Rbia and found that, although unreliable at the daily timescale, it offered satisfactory estimates of precipitation if averaged in space or time [176, 185]. Annual cycles of TRMM precipitation for the seven catchments are shown on Fig.7-1-b.

Reference surface air temperature is derived from MODIS Land Surface Temperature (LST) product MOD11A1 L3 version 6 at 1km resolution [261], as described in Chapter 6. Observed snow cover area for the region is extracted from the MODIS Terra snow cover daily L3 product (MOD10A1) at 500m resolution [105]. All MODIS data are available from February 2000 to present. Elevation data are taken from the Shuttle Radar Topography Mission 90-meter resolution dataset version 4.1 (STRM90) [135], and interpolated to the approximately 1km resolution of the MODIS land surface temperature data.

7.2.2 Regional climate simulations

We consider the regional climate downscaling projections obtained in Chapter 5. We remind the reader that the corresponding simulations were run at a 12km resolution using the MIT Regional Climate Model (MRCM). MRCM is based on the Abdus Salam International Centre for Theoretical Physics Regional Climate Model Version 3 (RegCM3), but with significant enhancements of model physics, and notably a coupling with the Integrated BIosphere Simulator land surface scheme (IBIS). Dynamical downscaling was performed for ERA-Interim (1982-2011) [55] (ERA/MRCM simulation) as well as three carefully-selected GCMs from the Coupled Model Inter-comparison Project Phase 5 (CMIP5) [241]: MPI-ESM-MR, GFDL-ESM2M and IPSL-CM5A-LR, for the historical (1976-2005) and RCP4.5 and 8.5 (2071-2100) scenarios.

6-hourly wind speed, specific humidity, air temperature, precipitation, and downward longwave and shortwave are extracted from the MRCM output over our domain. For all three GCM-driven simulations, as well as the ERA/MRCM run, air temperature and precipitation

data are statistically downscaled and bias-corrected at the 6-hourly timescale using MODIS LST-derived air temperature and TRMM precipitation at their native resolutions as respective targets, via the CDF-transform method [174]. Bias-corrected of precipitation conducted as described in section 5.3.4 in Chapter 5. The main difference is that since we consider here the IPSL-CM5A-LR model, we correct its dry bias at each grid cell by randomly generating wet days of magnitude drawn from the corresponding distribution of wet-day precipitation in the TRMM dataset. Reference periods for "perfect" observations are 1998-2011 for TRMM and 2000-2011 for MODIS. The corresponding periods in the simulations are the same for the ERA/MRCM, and the 1992-2005 and 1994-2005 periods, respectively, for each of the three GCM-driven simulations. All bias corrections are performed for the cold (November-April) and warm (May-October) seasons separately.

Additionally, we use wind speed, downward long- and shortwave radiation and specific humidity from the ERA/MRCM simulation as reference, like in Chapter 6. The corresponding variables in each GCM-driven simulation are therefore bias-corrected using the ERA/MRCM data as reference. Specific humidity is further downscaled to the 1km MODIS LST resolution based on an empirical lapse-rate μ estimated at each time step:

$$\log(q) = \log(q_{12}) + \mu \cdot (z - z_{12}) \tag{7.1}$$

where q_{12} is the specific humidity in a given 12-km resolution grid cell of elevation z_{12}, and q the downscaled value at elevation z.

7.3 Methods

The methodological framework adopted for this analysis is summarized in Figure 7-3. We start from GCM simulations from the CMIP5 archive, dynamically-downscaled with MRCM. We apply bias-correction to the MRCM output, which we then feed into a 1km-resolution snow model over our study region to reconstruct snowpack under the various emissions scenarios. Finally, a statistical model is developed for catchment runoff coefficients (RCs), in order to

make projections of runoff under future climate conditions.

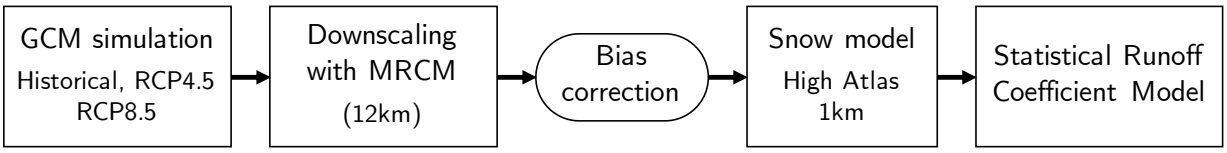

Figure 7-3: Summary of methodology to assess climate change impacts on snowfall, snowpack and runoff in the Oum-Er-Rbia watershed.

7.3.1 Snowpack modeling

We refer the reader to Chapter 6 for the detailed description of the snow modeling approach. The three required snow model parameters are optimized for each historical GCM-driven run and the ERA/MRCM simulation separately. We look for parameters that maximize the Nash-Sutcliffe coefficient [182] between the annual cycles of observed (MODIS) and simulated snow cover at 250 randomly selected grid points within the snow domain with elevations representative of that of the whole domain. The annual cycles are computed for the 1995-2005 period in the GCM-driven simulations, 2000-2011 period in the ERA-Interim simulation and 2000-2011 period in the MODIS observations. We could also adopt the approach of section 6.3.1 to optimize snow model parameters for ERA/MRCM, since this run represents the "observed" climate, but we choose to optimize with annual cycles rather to be more conservative and consistent with the GCM-driven runs. For the future GCM-driven simulations, parameter values are kept constant, equal to their calibrated values in the corresponding historical run.

7.3.2 Statistical modeling of Runoff Coefficients

While we rely on TRMM as the best gridded daily precipitation dataset available for our area, its main drawback is that it covers only the post-1998 period. Using TRMM directly would limit our analysis to a mere 18 years (1998-2015), likely insufficient given the region's

high inter-annual variability in precipitation. Therefore, we use the ERA/MRCM precipitation data, bias-corrected with TRMM, to estimate catchment-scale precipitation for the longer 1982-2011 period, during which runoff data are available for all catchments. This allows us to calculate catchment runoff coefficients (RCs), defined as observed total October-June discharge divided by estimated total October-June precipitation. To assess the robustness of the results, we also calculate RCs based on CHIRPS precipitation (available from 1981-present). RCs are modeled across time and space as functions of large-scale hydrological variables by adopting a panel regression framework. Panel regression allows to enhance the effective size of a dataset and to obtain more robust estimates of the response to selected covariates compared to more traditional regression approaches [235, 52]. It also allows to account for static (space-dependent) and time-varying (time-dependent) factors, although here, with only seven catchments, we do not have enough data to make robust statements about static factors responsible for the disparity in average runoff coefficient (Fig. 7-2-b). Therefore, we focus on time-varying covariates, and consider a fixed-effects formulation:

$$\log\left(RC_{j,t}\right) = \log\left(\overline{RC}_j\right) + \sum_i \beta_i X^i_{j,t} + \epsilon_{j,t} \tag{7.2}$$

where RC_j represents time-invariant, watershed-specific fixed effects (drainage area, land cover, mean climate), covariates $X(i)_{j,t}$ are covariates indexed by i, β_i are regression coefficients and $\epsilon_{j,t}$ random noise. For covariates, we consider variables that can reasonably be thought to impact runoff at the regional scale: catchment-averaged October-May precipitation (P), relative humidity (RH), temperature (T), snow water equivalent (SWE) and snow fraction of precipitation (SF). Enhanced precipitation or relative humidity lead to wetter soils and can be expected to be associated with higher RC values. Similarly, higher temperatures increase evapotranspiration and tend to decrease runoff. Finally, increased snow cover favors losses by sublimation and shifts the distribution of runoff regimes towards slower ("trickle") runoff as opposed to rapid overland flow following rain storms. However, larger snow cover may also increase the risk of rain-over-ice events, which tend to have very high runoff coefficients [52]. Environmental model covariates are calculated using the ERA/MRCM run and associated snow model output, with temperature and precipitation bias-corrected as described previously.

Feature selection is performed by stepwise regression: starting from a model with no covariates, covariates are added one at a time in the order of highest improvement to model skill, as determined by its Akaike Information Criterion (AIC). At each step, we also test whether removing any of the currently selected variables and replacing it by one of the remaining, non-selected ones, brings any improvement. To estimate the sensitivity of runoff coefficients to changes in climate conditions, we modify covariate values in the 1982-2011 ERA-Interim downscaled simulation by adding projected long-term changes in the GCM-driven simulations:

$$\log\left(\widehat{RC}^{m}_{j,t}\right) = \log\left(\overline{RC}_{j}\right) + \sum_{i\in\mathcal{I}} \beta_i \left(X^{i}_{j,t} + \overline{X}^{i}_{m}\right) \tag{7.3}$$

where m $\in \{1, 2, 3\}$ is model index, $\mathcal{I}$ is the set of optimal covariates, $X^{i}_{j,t}$ are ERA-Interim downscaled covariate values and $\bar{X}^{i}_{m}$ represent long-term covariate changes drawn at random according to:

$$\overline{X}^{i}_{m} \sim N\left(\mu^{i}_{m,\text{rcp}} - \mu^{i}_{m,\text{hist}}, \sqrt{\sigma^{i}_{m,\text{rcp}} + \sigma^{i}_{m,\text{hist}}}\right) \tag{7.4}$$

where $\mu^{i}_{m,s}$ (respectively $\sigma^{i}_{m,s}$) is the average (respectively standard deviation) of covariate i in model m and scenario s. Results for the three models are then pooled together to yield a future distribution for $RC_{j,t}$.

7.4 Results and discussion

7.4.1 Snowpack projections

Annual cycles of reconstructed snow cover as a function of elevation are shown on Figure 7-4. Overall, all models succeed in accurately reproducing snow cover dynamics in the region, although the ERA-Interim simulation tends to have a positive bias at high elevations (Fig. 7-4-b) and all simulations have a negative bias at low elevations (Figs. 7-4-d,e and 7-5-a,b). Despite the statistical downscaling of the MRCM output to 1km, elevation-driven gradients in

snow cover are also less sharp in the MRCM experiments compared to observations (Fig. 7-5-a,b). Additionally, compared to ERA-Interim, the GCM-driven experiments generally show too little snow cover, and a later snowpack build-up (Fig. 7-4-f). All results remain however in a narrow band around the MODIS values and, excepted for elevations below 2000m, inter-model spread generally covers observed snow cover values. Inter-annual variability in basin-wide snow cover is a lower in the simulations compared to MODIS (standard deviation of 220-440 km^2 compared to 480 km^2 in MODIS) but the discrepancy is mainly due to the negative bias at low elevations, where snow plays a much more limited role in the overall water balance.

Unsurprisingly, future projections show a stark decline in snow cover across all the region (Figs. 7-5, 7-6). The greatest relative decline is at low elevations, as expected since they are already seldom above the 0 °C isotherm [29]. Above 2500m, projections still exhibit a 30-40% decrease in snow cover area under RCP4.5 and 50-60% decrease under RCP8.5. The outlook is even worse in terms of snowpack water content (Fig. 7-7): it is reduced on average by 60% under RCP4.5 and 80-85% under RCP8.5, bringing its peak value from about 125 million m^3 (MCM) down to 20 MCM (Figs. 7-7-f, 7-8). As discussed in Chapter 5, the projected decrease in wet-season precipitation is about 25% under RCP4.5 and 40-45% under RCP8.5. Because most areas in the High Atlas are very close to the zero-degree line, even at high elevations, warming trends largely amplify the precipitation signal and result in such SWE declines. Warming causes the percentage of solid precipitation to decrease, particularly at mid-elevations (2000-2500m) (Fig. 7-9) and also favors melt during winter, thus preventing the build-up of the snowpack. Detailed input data and snow model projections for the area and various elevation bands are given in Appendix A.

As discussed previously, the historical SWE peak of 125 MCM is subject to caution; experiments with enhanced precipitation or reduced temperatures suggest it may in fact be as high as 200 MCM. Still, while inter-model spread is large in the historical experiments (≈60MCM) and still large (≈40MCM) in the RCP4.5 experiment, it is reduced to almost zero under RCP8.5. Whatever the historical disparity in temperatures or precipitation are between models, they all agree on the large reduction in snowpack under business-as-usual. This is consistent with observations that in mountain regions, above-freezing temperatures are common, even at high

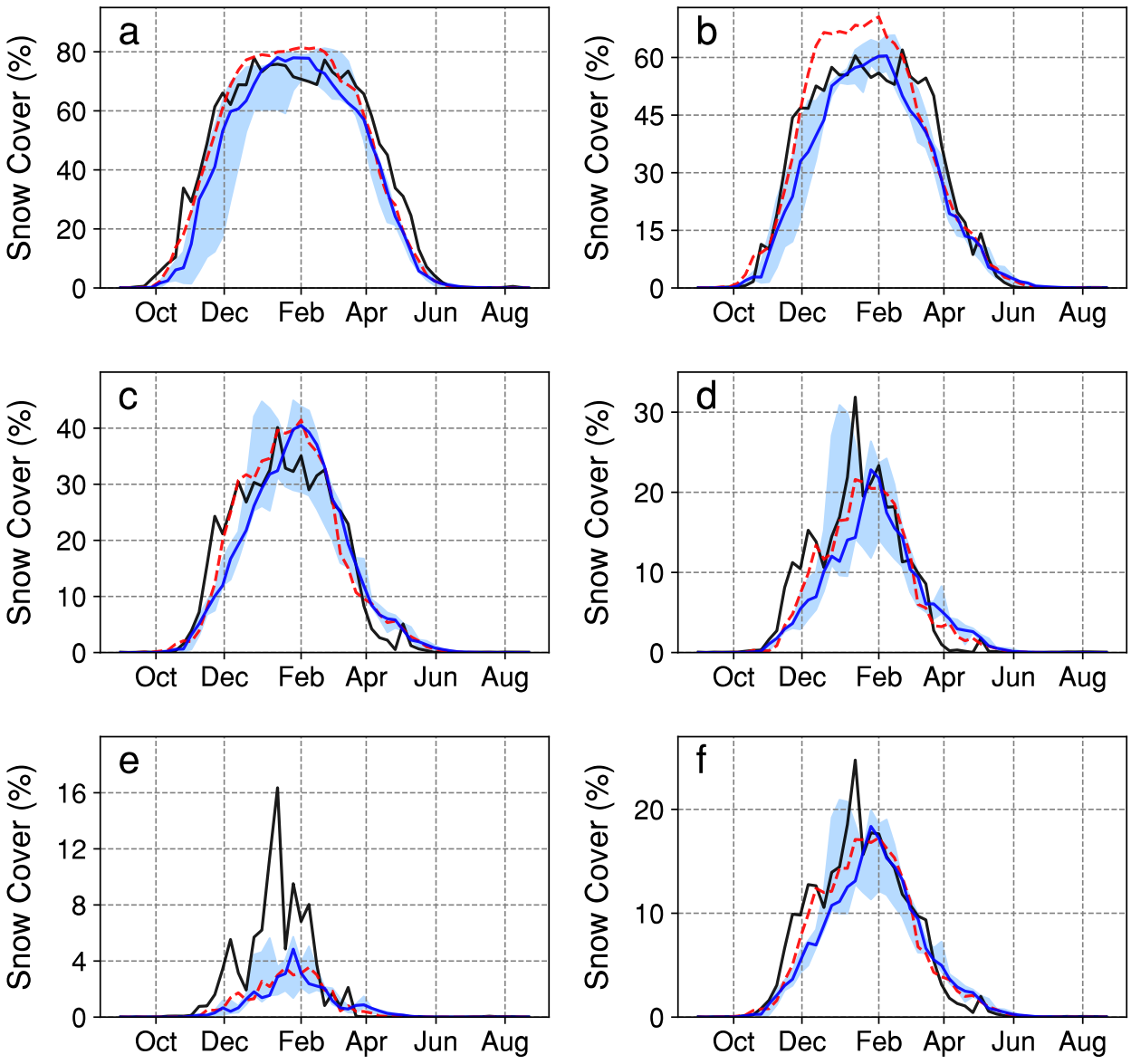

Figure 7-4: Annual cycles of snow cover (in %) in the MODIS observations (black), ERA-Interim simulation (dashed red) and three GCM-driven historical simulations (solid blue: median; blue shading: 3-model range), at various elevations ranges within our study area: (a) > 3500m, (b) 3000-3500m, (c) 2500-3000m, (d) 2000-2500m, (e) 1500-2000m and (f) whole area.

altitudes, where average winter temperatures are not far from freezing [157]. Therefore, under the RCP8.5 scenario, the projected 4 °C warming (Chapter 5) would bring all but the very highest peaks clearly above freezing, and prevent seasonal snowpack accumulation.

Due to the particularly arid climate of the High Atlas, sublimation losses are quite significant in our study area: about 9% of all snowfall on average, and up to 30% above 3500m

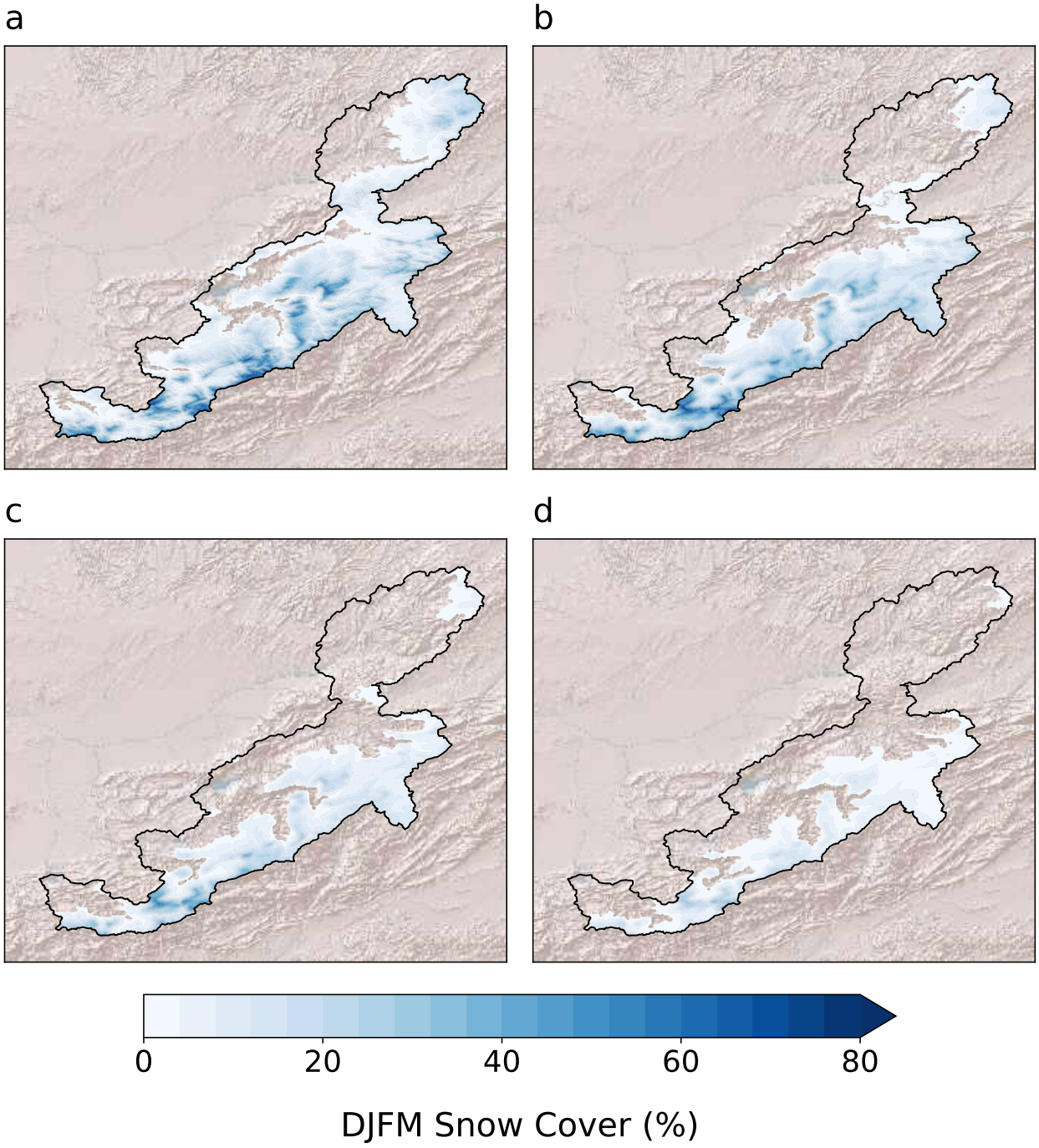

Figure 7-5: Mean December-to-March (DJFM) fractional snow cover (%) over the basin in (a) MODIS (2000-2010) data, and (b-d) three-GCM average under the (b) historical (1976-2005), (c) RCP4.5 (2071-2100) and (d) RCP8.5 (2071-2100) experiments.

[224, 157]. Annual relative sublimation losses are strongly associated with annual-mean precipitation (Fig. 7-10-a). Losses from latent heat fluxes are much smaller during wet years as compared to dry years, a relationship robust across all experiments. Wet years indeed bring

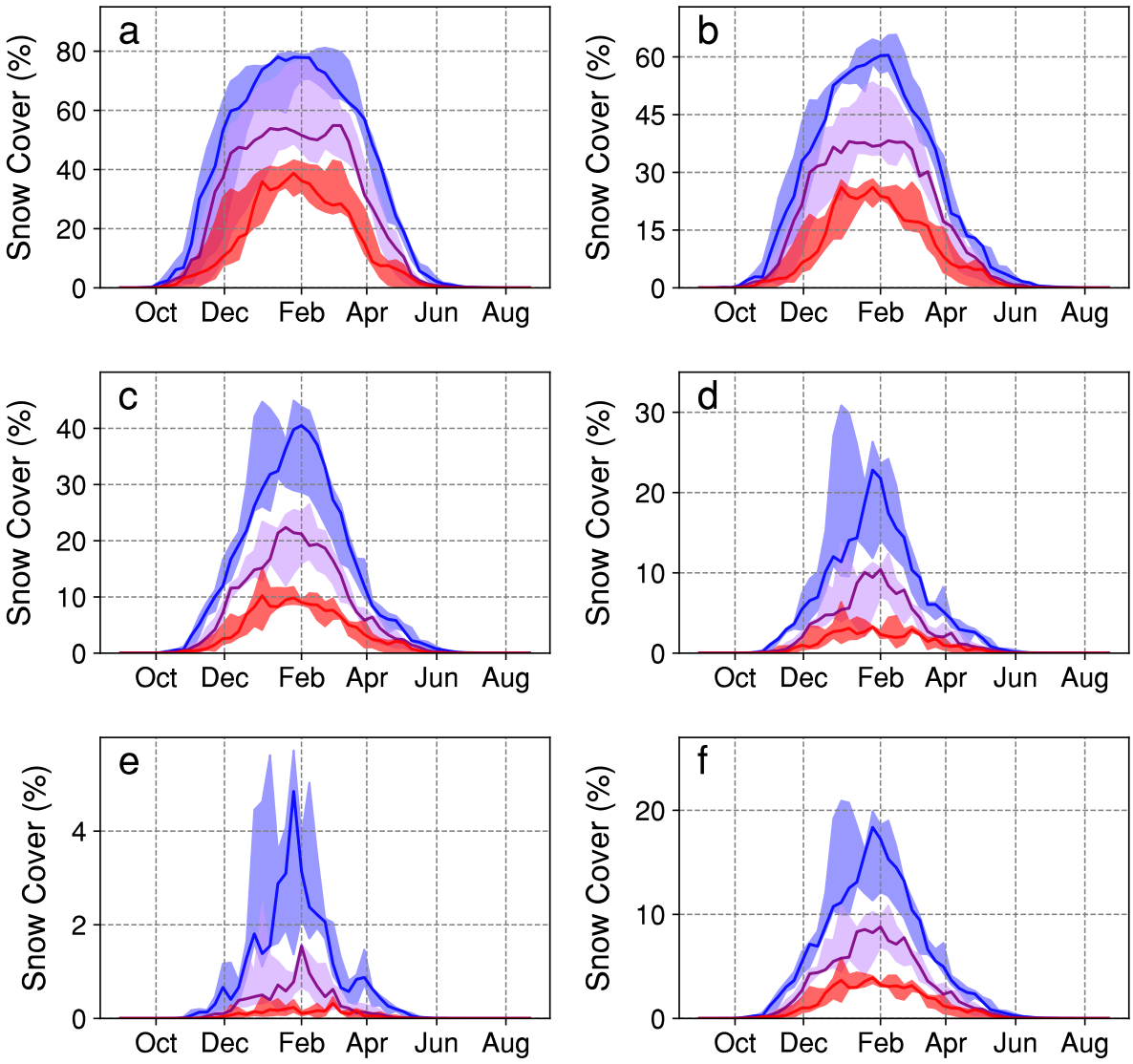

Figure 7-6: Annual cycles of snow cover (in %) in the three GCM-driven experiments under the historical (blue, 1976-2005), RCP4.5 (purple, 2071-2100) and RCP8.5 (red, 2071-2100) scenarios, at various elevations ranges within our study area: (a) > 3500m, (b) 3000-3500m, (c) 2500-3000m, (d) 2000-2500m, (e) 1500-2000m and (f) whole area. Solid lines represent the three-model medians and the shading corresponds to the three-model spreads.

higher RH over the region, due to enhanced moisture advection from the Atlantic which more than compensates for the larger heat advection and increased air temperatures that also occur in parallel [147]. In addition to the influence of higher RH, warmer temperatures in wetter years also tend to decrease the snow-to-precipitation ratio, thus leading to reduced relative sublimation losses. This makes the case for higher RC values during wet years. Under future climate conditions, average relative humidity will decline by 3-6% (Chapter 5), and thus subli-

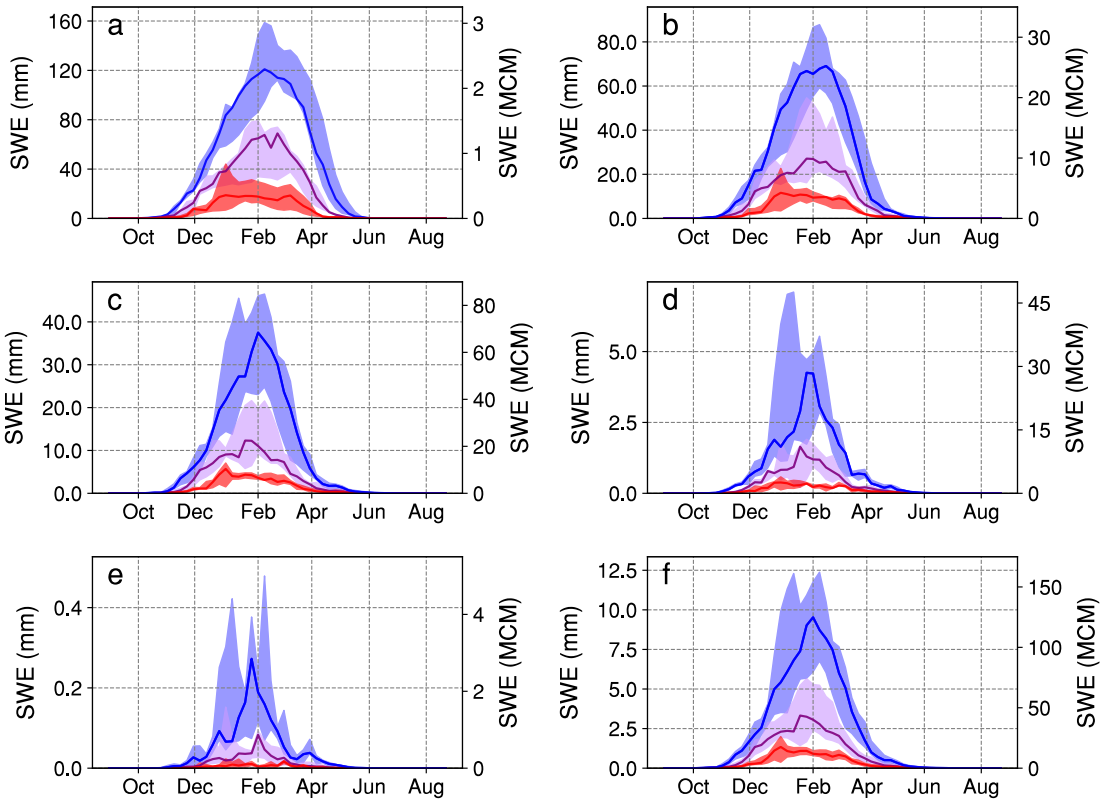

Figure 7-7: Same as Fig. 7-6, but for total snow water equivalent (in million m^3).

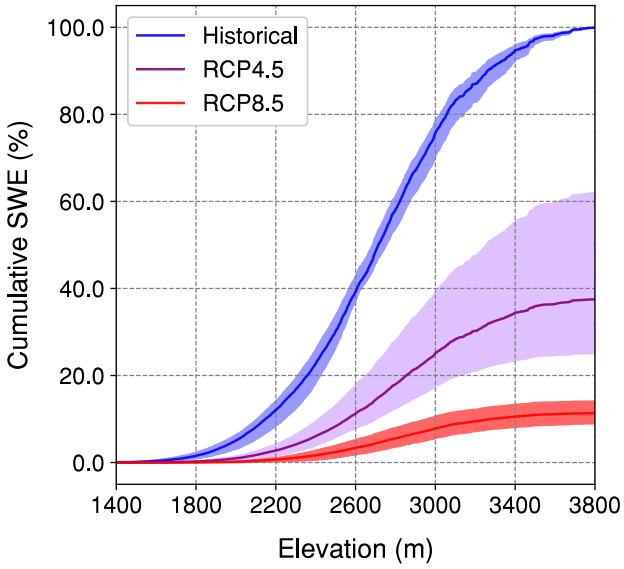

Figure 7-8: Distribution of cumulative basin-wide SWE with elevation in the GCM-driven experiments, under the historical (black), RCP4.5 (purple) and RCP8.5 (red) scenarios. SWE is normalized in each model by that model's historical total basin-wide SWE.

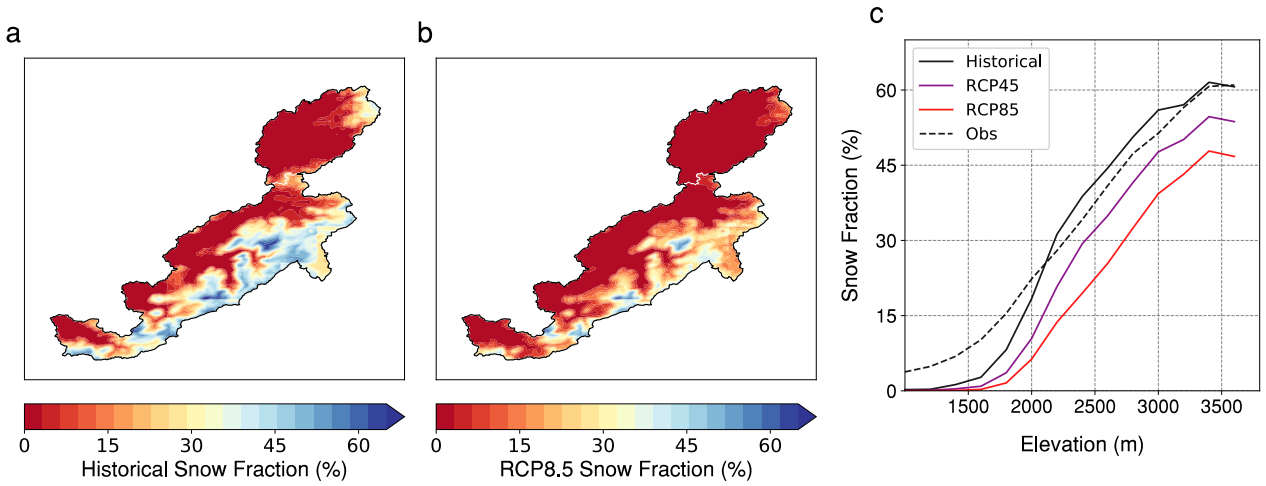

Figure 7-9: (a-b) Snow fraction of annual precipitation in the (a) historical and (b) RCP8.5 scenario (average between all three GCM-driven simulations). (c) Snow fraction of annual precipitation as a function of elevation, in each scenario (historical, RCP4.5 and RCP8.5; three-model average) and in the assimilated control simulation of Chapter 6 ("Obs").

mation rates will be higher when snow is present. However, because the snow-to-precipitation ratio will also sharply decline due to rising temperatures, the overall loss of annual precipitation by sublimation will tend to decrease by about a third (Fig. 7-10-b).

For the areas as a whole, decasing precipitation and warmer temperatures are the primary causes of the projected decline in snowpack. In addition, drier soils together with enhanced absorption of solar energy where snowpack disappears will also lead to enhanced warming locally, driving yet further snowpack melt. We do not explicitly take this into account in our model. In particular, the snow albedo effect is largely absent from the MRCM simulations due to their 12km resolution, which is still too coarse to represent the complex topography. For areas at the highest elevations (near 4000m) which may still remain largely below freezing in future winters, melt may not increase very significantly in the middle of winter; however, a drier atmosphere will still be associated with reduced precipitation and increased sublimation losses, which will play a critical role in reducing the snowpack. A similar phenomenon has been occuring at the top of Mount Kilimanjaro (5149m), whose glaciers have been retreating fast over the last century primarily due to increasing atmospheric dryness that led to higher sublimation losses [140].

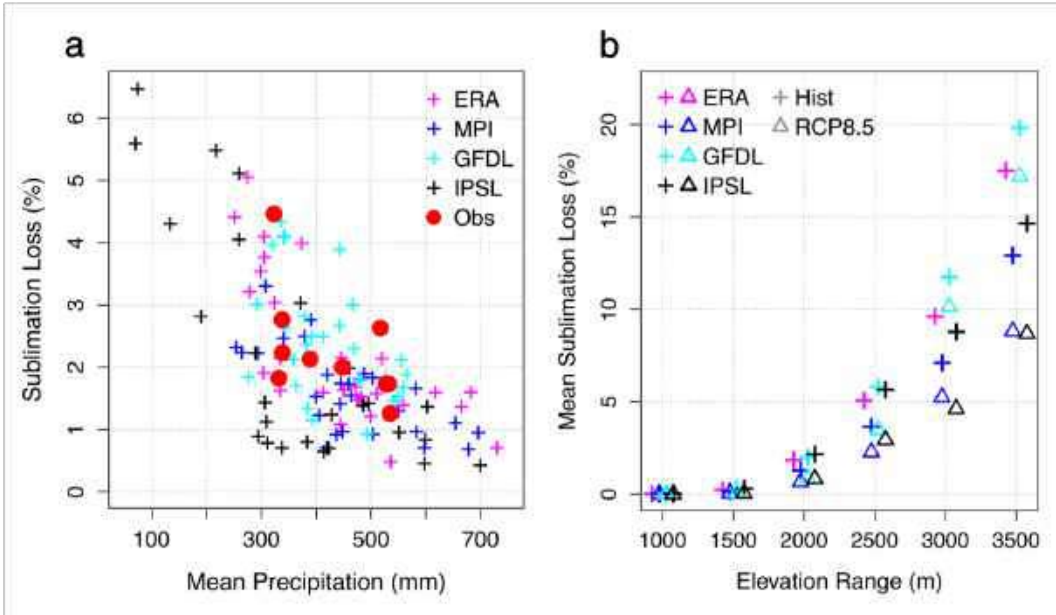

Figure 7-10: (a) Fraction of annual precipitation lost by sublimation against total annual precipitation in the MRCM downscaled experiments forced with ERA-Interim (1982-2011, magenta), the three GCMs (historical, 1976-2005): MPI-ESM-MR (blue), GFDL-ESM2M (cyan) and IPSL-CM5A-LR (black), and the snow run forced with "observed" MODIS and TRMM data only. (b) Fraction of annual precipitation lost by sublimation as a function of altitude range in our study area, for the various downscaled experiments, and in historical (1976-2005, "+") and RCP8.5 (2071-2100, "Δ") scenarios.

7.4.2 Runoff modeling and projections

The panel regression and model selection framework are applied to runoff coefficients and selected covariates over the 1982-2011 period. Stepwise regression yields as optimal covariates relative humidity and snow fraction. The adjusted r^2 is equal to 0.29, meaning that these two covariates explain a small third of inter-annual variability in RC. Fitted RCs against observations are shown on Figure 7-11. Consistent with the model r^2, fitted values have a much smaller variance. Still, for all the catchments, except Segmine, we observe a significant positive relationship between fitted and observed values. The coefficients for RH and snow fraction are both significant, with $\beta_{RH} > 0$ and $\beta_{SF} < 0$ (Table 7.1). All else being equal, a larger RH yields more runoff, and more of the precipitation falling as snow yields less runoff. The effect of RH on runoff coefficient, as measured by the regression coefficients β in 7.2, is 4-5 times that of snow, however. As discussed above, we can understand the influence of snow fraction by noting that a higher snow fraction means more opportunity for sublimation, particularly

large at high elevations, and evaporation of melted snow, consistent with our analysis of sublimation losses (Fig. 7-10). Precipitation in the area tend to occur in short and intense storms, and quickly saturate the dry soil, leading to rapid overland flow with limited opportunity for evaporation [72]. By comparison, snowmelt is slow and leads to a more gradual surface flow with the potential for higher evaporative losses in this climate where evaporation tends to be water-limited. More winter snow also leads to a higher likelihood of rain-on-snow episodes in spring, known to cause rapid flooding due to high runoff efficiencies [52]. More snow may also mean more opportunity for infiltration and aquifer recharge [123]; however, in six out of seven catchments considered here, base flow is negligible. Still, aquifer discharge may occur naturally further down the mountains, or artificially via direct groundwater pumping in the agricultural plains. Compared to surface runoff, groundwater remains a small fraction of water use in the Oum-Er-Rbia basin (<15%), and even less of available renewable water since aquifers are largely overdrawn [123] (Chapter 2, Fig. 2-13). Groundwater data are quite scarce in this region; we make the choice of purely focusing on surface runoff, keeping in mind that a more complete picture of basin-wide water availability would also require taking aquifer fluxes into account.

	MRCM-BC		**CHIRPS**	
r^2	0.30		0.36	
SF	-1.84	4E-03	-1.47	2E-02
RH	5.71	2E-05	8.71	1E-09
Pr	–	–	2.04E-03	1E-06

Table 7.1: Runoff coefficient model results. The bottom three lines show coefficient values (left-hand column) and their statistical significance (p-value, right-hand column).

Future runoff projections are characterized by consistent, steep declines in runoff coefficients of 5-17% under RCP4.5 and 15-30% under RCP8.5 (Fig. 7-12-a). The impact of decreasing RH largely dominates over that of declining snow fraction. This is consistent with the projection that relative decline in RC is largest in the Tarhat and Chacha catchments, that both already receive almost no snow in the historical simulations and where therefore

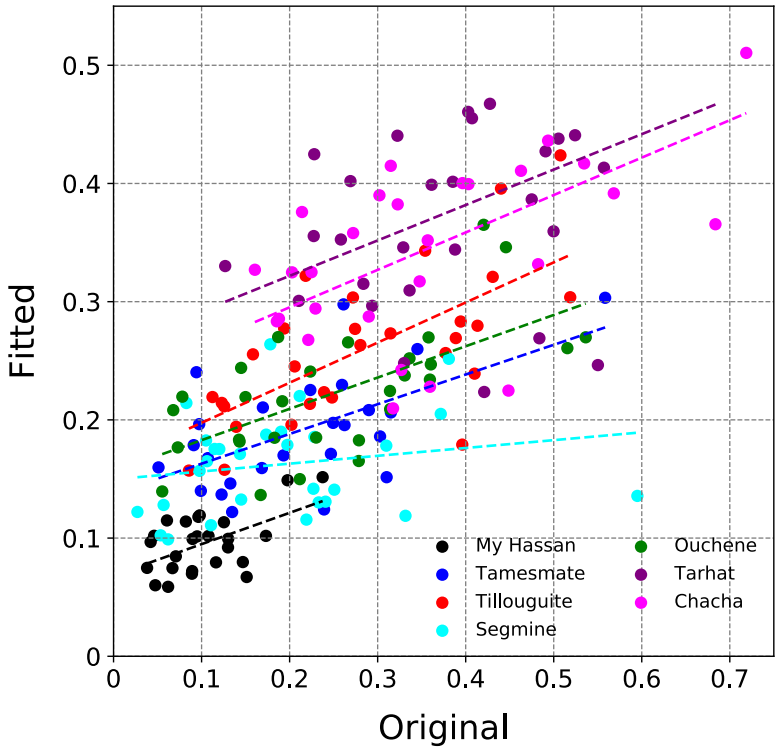

Figure 7-11: Fitted runoff coefficient values against observed values (defined with TRMM precipitation), for the seven catchments in our study area. Best-fit linear regression lines are shown by dashed lines.

declining snow fraction will not matter much. Combining now precipitation and runoff coefficient estimates, we find a 20-40% decrease in runoff in the RCP4.5 experiments, compared to a 50-65% decline under RCP8.5 (Fig. 7-12-b, Table 7.2). Decreases in precipitation drive most of the runoff trends, especially in the RCP8.5 scenario. These results are robust to the choice of the precipitation dataset. Using CHIRPS to define runoff coefficients, average RCs are generally lower, due to CHIRPS's wet bias compared to TRMM. The optimal RC model includes RH and SF as well, but also precipitation as a third variable (Table 7.1). Projected RC declines are about the same, although tend to be slightly higher (by 3-6% on average). Our projected runoff trends are consistent with those of El Moçayd et al. (2020) who focused on other catchments within the Sebou watershed, where snow plays a much smaller role than in our region [73]. This is not surprising given the weak impact of the declining snow fraction on runoff coefficients, compared to that of the relative humidity decline.

As a final note, one can ask whether observed runoff trends are consistent with these pro-

jections. At the country scale, government data indicates that river discharge has indeed significantly declined over the last 60 to 70 years, at a rate of about 5% per decade (Fig. 2-10). The wet years of the 1960s tend however to bias the result towards a steeper decline than expected. In this case, natural decadal variability linked to the NAO acted in the same direction as the expected climate change response. Runoff data from the seven sub-catchments studied in this chapter are less clear. They cover shorter time periods (by about 25 years) and, more importantly, begin in the late 1970s, just when the climate was about turner much drier in Morocco (drier-than-average conditions prevailed from 1980 to the mid-1990s, see Figs. 2-3 and 2-10). Thus, runoff trends tend to be slightly positive (about +1%/yr), though none are significant, even at the 10% level.

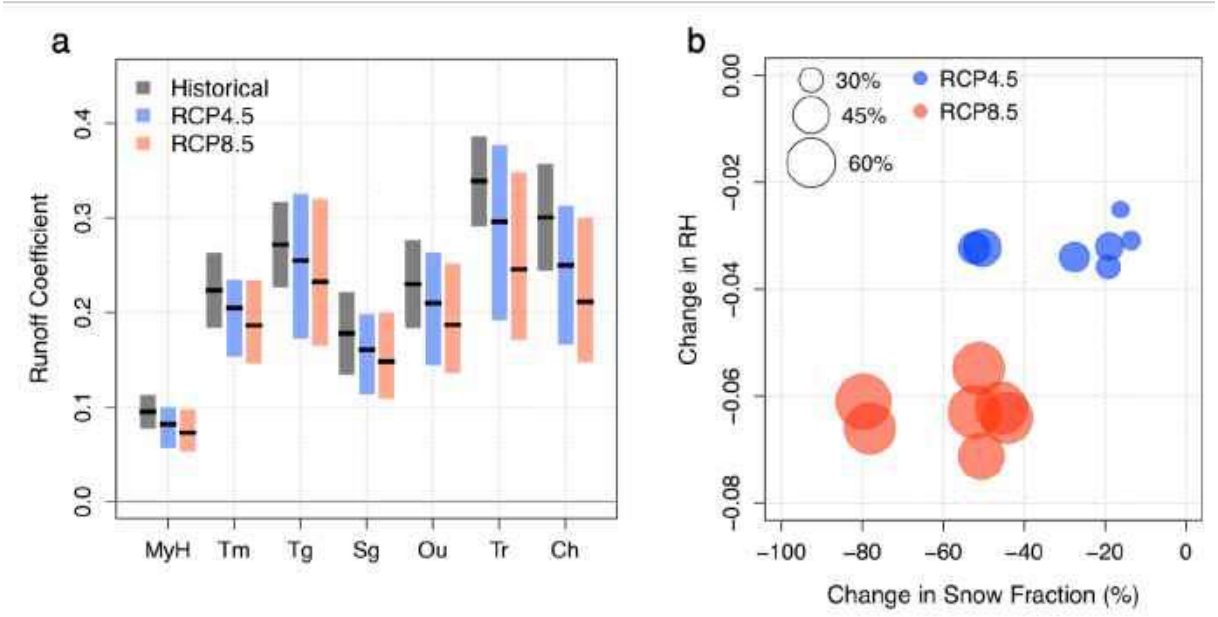

Figure 7-12: (a) Average runoff coefficients for the seven catchments in the observations (black), and projected average values in the RCP4.5 (blue) and RCP8.5 (red) scenarios. Boxes represent 90% confidence intervals. (b) Projected relative changes in runoff across the seven catchments against relative change in snow fraction (x-axis) and change in catchment-wide relative humidity (y-axis), for the RCP4.5 (blue) and RCP8.5 (red) scenarios.

Catchment	M. Hassan		Tamesmate		Tillouguite		Segmine		Ouchene		Tarhat		Chacha	
	RCP4.5	RCP8.5	RCP4.5	RCP8.5	RCP4.5	RCP8.5	RCP4.5	RCP8.5	RCP4.5	RCP8.5	RCP4.5	RCP8.5	RCP4.5	RCP8.5
$\Delta T(°C)$	2.3	4.6	2.2	4.4	2.2	4.5	2.3	4.6	2.3	4.6	2.3	4.8	2.3	4.7
ΔPr (%)	-11	-53	-14	-57	-30	-57	-22	-48	-31	-57	-31	-50	-31	-55
ΔRH (%)	-3.1	-6.2	-2.5	-5.5	-3.2	-6.4	-3.6	-7.1	-3.4	-6.3	-3.2	-6.6	-3.2	-6.1
ΔSnow (%)	-3.3	-11.3	-3.9	-12.3	-6.7	-15.7	-5.7	-14.9	-6	-11.3	-5	-7.5	-2	-3.2
ΔSF (%)	-14	-46	-16	-51	-19	-44	-19	-51	-28	-52	-52	-78	-50	-80
ΔRC (%)	-14	-23	-8	-17	-6	-14	-10	-17	-9	-19	-13	-27	-15	-30
ΔRunoff (%)	-23	-64	-21	-64	-34	-63	-29	-57	-37	-65	-39	-63	-41	-68

Table 7.2: Long-term (2071-2100 minus 1976-2005) projections for the seven catchments: October-May temperature (°C), precipitation (%), relative humidity (%), absolute and relative snow fraction (%), runoff coefficient (%) and runoff (%), under RCP4.5 and RCP8.5.

7.5 Conclusion

Based on the robust understanding of its snow water balance in the current climate, we quantified in this final chapter the response of the High Atlas snowpack to climate change using high-resolution downscaled climate projections. Unsurprisingly, given the warming and drying trends projected by climate models for this region, we find that the High Atlas snowpack will significantly decline, even with substantial mitigation of emissions. By the end of the century, snow may become a rarity below 2000m, and even near the highest peaks, snowpack water equivalent could decline by 80%. Precipitation decreases of 40-60% are responsible for much of these trends, with background warming accounting for the rest.

The analysis of runoff coefficients for seven mountain catchments showed that a third of their inter-annual variability could be explained by large-scale meteorological factors like snow fraction of precipitation and relative humidity. Interestingly, in this region, a larger snow fraction leads to less runoff. While the reverse is believed to be true at higher latitudes [19], this finding is consistent with other analyses in warm, semi-arid regions that receive substantial amounts of snow during winter [52]. Warmer conditions tend to enhance runoff efficiencies by reducing snowpack – thus limiting sublimation losses and the slow melting of snow, propitious to evaporation – and by increasing the likelihood of rain-on-snow events that tend to cause high runoff efficiencies. While decreasing snowfall will partly compensate for the projected atmospheric drying over the region, runoff coefficients will tend to decline by 5-30% depending on catchment and scenario. Combined with precipitation trends, basin-wide runoff could be reduced by 60% in the worst case. In addition, earlier snowmelt will likely lead to lower soil moisture levels during spring, further enhancing the temperature rise and increasing the risk of late-season droughts.

The robust physical understanding behind large-scale projections for the region (Chapter 4) increases the likelihood that the dire projections detailed above will be realized provided greenhouse gas emissions are not brought under control. This would deal a severe blow to the region, jeopardizing its agriculture-based economy and the livelihood of millions of smallholder farmers. Agriculture, which accounts for 90% of current water use, will have no choice but to adapt. 40-60% declines in precipitation will make rainfed agriculture, already at the limit of

viability, entirely impossible. At the same time, availability of water for irrigation will also decline sharply. A change of cropping patterns, like a transition to tree crops with less water demand and higher economic value like olives, will likely be unavoidable for Morocco to adapt to this future reality.

Chapter 8

Conclusion

This thesis brings improvement to our current understanding of precipitation variability and change in Morocco and the Mediterranean.

In Chapter 3, we investigated the forecast potential of seasonal precipitation in Morocco using an empirical approach based on sea-surface temperatures as predictors of atmospheric circulation. Using the CRU TS4 station-based precipitation dataset and gridded ocean temperatures from HadISST, it was shown that 30-40% of the variability in December-to-February and February-to-April precipitation could be predicted with lead times of at least one month. Real-time forecasts were also developed, as the first step towards an operational implementation.

Chapter 4 then assessed wintertime climate projections for the Mediterranean Basin. Based on theoretical considerations, global climate model projections from the CMIP5 archive and regional climate simulations, we proposed for the first time a comprehensive physical explanation for the severe drying projected in this region during winter by the end of the 21st century. This drying directly results from the development of an anomalous anticyclone over the Mediterranean, itself a response to shifts in the large-scale circulation of the Northern Hemisphere, and to the relative cooling of Mediterranean Sea temperatures compared to the surrounding land. We then explained why the western and eastern ends of the basin would experience the most severe precipitation declines. To the west, over Morocco and the southern

Iberian Peninsula, the pressure high results in anomalous dry winds from the Sahara which prevent a rise in atmospheric humidity that would compensate for warming temperatures, thus leading to a pronounced decrease in relative humidity. To the east, over southern Turkey and the Levant, the anticyclone triggers anomalous northerlies that cause subsidence and drive precipitation down as well. Additionally, inter-model spread in circulation and precipitation projections was connected to uncertainties in the response of the large-scale circulation.

Chapter 5 presented high-resolution simulations of the current and late-21st century climate of the southwestern Mediterranean developed with the MIT Regional Climate Model. These projections confirmed the severe wintertime drying simulated by global models, with a 20-30% decline in precipitation between December and May under a mitigation scenario (RCP4.5), and 35-45% under business-as-usual (RCP8.5). In addition, the simulations helped validate the role of dry, anomalous winds from the Sahara in driving the regional precipitation decline. Finally, we used them to analyze trends in future weather extremes, namely spring heatwaves and wet-season droughts. Our results imply severe impacts on the region's agriculture, particularly rainfed, in the coming decades.

Chapter **??** investigated the High Atlas snowpack and snow water balance in the present climate. Snow is a major component of the hydrological cycle in Morocco, and yet very little is known about it, mainly due to a lack of observational data. We demonstrated the potential of remotely-sensed and dynamically-downscaled data assimilated into a simple physically-based snow model to accurately reproduce the main features of High Atlas snow cover. In addition to data at the single high-altitude station available, we used satellite-based precipitation, cloud cover, elevation and temperature data in conjunction with dynamically-downscaled wind and humidity fields to reconstruct the dynamics of Morocco's Oum-Er-Rbia catchment snowpack. We estimated that the snowpack was essentially concentrated above 2500m altitude and held 0.05-0.4km^3 at its peak in early February. Sublimation losses were estimated to amount to 0.06-0.14km^3, about 10% of all snowfall.

Chapter 7 finally assessed future trends in snowpack and runoff within the Oum-Er-Rbia watershed. Dynamically-downscaled projections from Chapter 5 were used as input to the snow model previously implemented. This approch resulted in snowpack water content reduction of

60 to 80% depending on the emissions scenario, with areas below 2500m of altitude projected to receive hardly any snow at all in the future. In parallel, the statistical analysis of annual runoff across seven small mountain catchments within the Oum-Er-Rbia watershed showed that snow fraction and relative humidity in each catchment jointly account for 30% of inter-annual variability in runoff coefficients in this region. Unlike mid- to high-latitude watersheds, increases in snow fraction in the Atlas lead to reduced runoff efficiency, likely because of enhanced sublimation and evaporation losses. Applying this framework to future climate and snowpack projections, we estimated that runoff could decline by 20-40% under RCP4.5 and 50-65% under RCP8.5.

In addition to their scientific interest, our results have serious implications for water management and climate change adaptation in Morocco and the Mediterranean. Our analysis of projected winter precipitation trends for this region increased our confidence that the regional drying will occur, which means that countries like Morocco must now prepare for the worst and begin re-thinking their water use to adapt to a drier future. In that regard, Morocco's recently announced 2020-2050 National Water Plan is a step in the right direction. The operational implementation of seasonal forecasts, as well as the guidance of high-resolution projections, should be promoted to improve water management and efficiency in this very water-stressed country.

Still, there remains a number of possibilities for improvement and future research. The benefits of our forecasts could be quantified by modeling the water allocation decision framework described in Chapter 2 to provide incentives for and potentially limits to their implementation. As to climate projections, inter-model uncertainty in Mediterranean winter precipitation trends remains high due to spread in the large-scale circulation response, which should be investigated actively. There also remain some gaps in our understanding of Mediterranean winter dynamical trends, particularly whether mechanisms other than surface relative cooling and planetary wave shifts may contribute to them. An improved quantification of the responses to each of our two proposed mechanisms within a single, coherent modeling framework, could help resolve that question. Finally, our analysis of regional-scale climate change impacts on snowpack, river discharge and weather extremes remains limited in scope and should be pursued, especially if more ground data can be accessed to help constrain projections. In particular, agriculture will

inevitably be severely impacted, and an in-depth analysis of cropping patterns under future scenarios is a promising lead. Overall, more work is needed to translate our results into information that can be used by local stakeholders to help them cope with short-term uncertainty and plan ahead for the future.

Appendix A

High Atlas snowpack: Results of historical and future simulations

Elevation	**Ann. prec. (mm)**[1]	**DJFM prec. (mm)**[2]	**Ann. snow (mm)**[3]	**DJFM snow (mm)**[4]	**Snow frac. (%)**[5]	**Melt (mm)**[6]	**DJFM Temp. (°C)**[7]	**DJFM wind (m/s)**[8]	**DJFM RH (%)**[9]	**DJFM SCr (%)**[10]	**DJFM SWE (mm)**[11]	**Frac. Area (%)**[12]	**Sublim. (mm)**[13]
All	217	433	63	84	19	80	4.4	2.6	56	10	6	32	5
	205/232	406/460	50/74	48/140	11/33	53/132	3.9/4.8	2.5/2.6	55/59	8/11	3/8	29/37	4/5
≥3500m	295	634	230	349	62	274	-5.9	3.1	62	70	100	98	75
	244/352	566/680	199/265	271/467	40/92	242/501	-6.4/-5.8	3/3.2	61/63	64/76	64/155	93/100	55/86
3000-3500m	293	626	213	345	58	303	-3.8	2.9	64	51	59	97	42
	256/326	564/670	185/245	226/510	36/90	220/437	-4.5/-3.3	1.8/2.9	62/66	46/57	33/92	94/100	31/47
2500-3000m	227	476	130	217	48	201	-0.5	2.9	61	25	16	90	17
	205/240	426/514	107/146	127/358	28/82	130/330	-1.2/0	2.8/2.9	59/63	20/31	8/30	88/91	14/18
2000-2500m	221	453	81	137	31	132	2.9	2.7	57	10	4	57	5
	207/235	414/487	62/101	77/239	17/53	77/228	2.3/3.4	–	56/60	8/12	2/7	49/71	5/6
1500-2000m	206	415	19	33	8	32	6.9	2.4	53	1	0	8	1
	193/225	394/440	13/23	17/52	4/12	17/52	6.5/7.2	2.4/2.5	52/56	1/2	0/1	5/11	0/2

Table A.1: Snow model results and input data, averaged for the whole study area and various altitudinal bands, under the historical scenario: (1) Annual precipitation; (2) December-to-Mach (DJFM) precipitation; (3) Annual snowfall; (4) DJFM snowfall; (5) Fraction of solid precipitation; (6) Total snowmelt; (7) DJFM air temperature; (8) DJFM wind speed; (9) DJFM relative humidity; (10) DJFM average snow cover; (11) DJFM mean snow water equivalent; (12) Fraction of area with ≥5% snow cover in DJFM; (13) Total sublimation. For each elevation range, the top line indicates the 3-model average and the bottom line shows the 3-model range.

Elevation	**Ann. prec. (mm)**[1]	**DJFM prec. (mm)**[2]	**Ann. snow (mm)**[3]	**DJFM snow (mm)**[4]	**Snow frac. (%)**[5]	**Melt (mm)**[6]	**DJFM Temp. (°C)**[7]	**DJFM wind (m/s)**[8]	**DJFM RH (%)**[9]	**DJFM SCr (%)**[10]	**DJFM SWE (mm)**[11]	**Frac. Area (%)**[12]	**Sublim. (mm)**[13]
All	166	309	52	45	15	41	6.4	2.6	53	7	3	32	4
	117/193	247/391	26/72	25/55	9/23	21/51	6.1/6.5	2.5/2.7	48/55	6/8	2/4	29/37	3/4
≥3500m	250	486	224	303	59	244	-4	3	59	44	46	98	60
	162/332	349/657	120/326	170/405	38/86	109/335	-4.1/-3.8	1.9/3.2	56/62	35/56	22/68	93/100	45/74
3000-3500m	245	432	206	245	55	213	-1.9	2.9	60	27	19	97	33
	165/317	328/587	113/303	134/305	32/81	98/273	-2/-1.6	2.8/3	56/63	24/32	12/23	94/100	28/36
2500-3000m	176	341	97	134	42	123	1.5	2.8	57	11	5	90	13
	117/215	250/461	57/133	69/177	22/70	57/163	1.3/1.8	1.7/3	53/60	10/12	3/7	88/91	12/14
2000-2500m	167	320	50	66	21	63	4.9	2.7	54	4	1	57	3
	114/194	244/420	21/63	38/80	12/33	35/77	4.7/5.2	2.6/2.8	50/56	3/4	1/1	49/71	3/4
1500-2000m	156	297	9	11	3	9	9	2.5	50	0	0	8	0
	114/187	244/365	7/14	6/17	2/4	7/14	8.6/9.3	2.4/2.6	46/53	0/1	–	5/11	–

Table A.2: Same as A.1, for the RCP4.5 scenario.

Elevation	**Ann. prec. (mm)**[1]	**DJFM prec. (mm)**[2]	**Ann. snow (mm)**[3]	**DJFM snow (mm)**[4]	**Snow frac. (%)**[5]	**Melt (mm)**[6]	**DJFM Temp. (°C)**[7]	**DJFM wind (m/s)**[8]	**DJFM RH (%)**[9]	**DJFM SCr (%)**[10]	**DJFM SWE (mm)**[11]	**Frac. Area (%)**[12]	**Sublim. (mm)**[13]
All	108	208	25	18	6	16	8.5	2.7	48	4	1	10	2
	97/118	137/256	14/32	13/24	10/17	10/22	8.1/9.2	2.5/2.9	46/49	3/5	1/2	7/12	–
≥3500m	155	311	127	131	49	97	-2.1	3	56	33	18	85	39
	135/187	199/396	90/173	91/180	23/82	72/145	-2.2/-1.8	1.9/3.1	52/60	28/39	6/34	65/99	30/51
3000-3500m	152	281	110	104	44	86	0.1	2.9	56	17	7	74	21
	133/175	181/374	73/152	81/147	22/75	59/128	-0.1/0.4	2.8/3.2	53/60	14/21	3/13	59/83	16/27
2500-3000m	206	452	121	183	40	158	-0.3	2.9	59	32	24	87	25
	99/120	138/298	33/79	39/79	16/56	32/73	3.3/3.8	2.7/3.1	50/56	4/6	1/3	31/34	5/8
2000-2500m	107	213	29	25	14	24	7	2.8	49	1	0	5	1
	97/116	134/275	14/37	17/33	8/24	16/32	6.7/7.5	2.6/3	47/51	0/1	–	4/7	1-2
1500-2000m	102	201	4	3	1	3	11.1	2.6	45	0	0	0	0
	93/115	133/243	2/6	2/4	1/2	2/4	10.6/12.1	2.4/2.9	43/47	–	–	–	–

Table A.3: Same as A.1, for the RCP8.5 scenario.

Bibliography

[1] J. T. Abatzoglou, S. Z. Dobrowski, S. A. Parks, and K. C. Hegewisch. TerraClimate, a high-resolution global dataset of monthly climate and climatic water balance from 1958-2015. *Scientific Data*, 5(1):170191, 2018.

[2] S. A. Ackerman, K. I. Strabala, W. P. Menzel, R. A. Frey, C. C. Moeller, and L. E. Gumley. Discriminating clear sky from clouds with MODIS. *Journal of Geophysical Research Atmospheres*, 103(D24):32141–32157, 1998.

[3] R. F. Adler, G. J. Huffman, A. Chang, R. Ferraro, P. P. Xie, J. Janowiak, B. Rudolf, U. Schneider, S. Curtis, D. Bolvin, A. Gruber, J. Susskind, P. Arkin, and E. Nelkin. The version-2 global precipitation climatology project (GPCP) monthly precipitation analysis (1979-present). *Journal of Hydrometeorology*, 4(6):1147–1167, 2003.

[4] A. Agoumi and R. Balaghi. Ressources en eau et bassins versants du Maroc : 50 ans de développement (1955-2005). Technical report, 2006.

[5] M. Ait Kadi. Irrigation Water Pricing Policy in Morocco's Large-Scale Irrigation Projects. *Hommes, Terre & Eaux*, 32(124):25–33, 2002.

[6] O. A. Alduchov and R. E. Eskridge. Improved Magnus form approximation of saturation vapor pressure. *Journal of Applied Meteorology*, 35(4):601–609, 1996.

[7] R. Allan and T. Ansell. A new globally complete monthly historical gridded mean sea level pressure dataset (HadSLP2): 1850-2004. *Journal of Climate*, 19(22):5816–5842, 2006.

[8] E. Alonso-González, J. I. López-Moreno, S. Gascoin, M. García-Valdecasas Ojeda, A. Sanmiguel-Vallelado, F. Navarro-Serrano, J. Revuelto, A. Ceballos, M. J. Esteban-Parra, and R. Essery. Daily gridded datasets of snow depth and snow water equivalent for the Iberian Peninsula from 1980 to 2014. *Earth System Science Data*, 10(1):303–315, 2018.

[9] E A Anderson. A Point of Energy and Mass Balance Model of Snow Cover. Technical report, U.S. National Oceanic and Atmospheric Administration NOAA Technical Report NWS 19, Silver Springs, MD, 1976.

[10] E. A. Anderson. Snow Accumulation and Ablation Model – SNOW-17. Technical report, U.S. National Weather Service, Silver Springs, MD, 2006.

[11] H. Ashouri, K. L. Hsu, S. Sorooshian, D. K. Braithwaite, K. R. Knapp, L. D. Cecil, B. R. Nelson, and O. P. Prat. PERSIANN-CDR: Daily precipitation climate data record from multisatellite observations for hydrological and climate studies. *Bulletin of the American Meteorological Society*, 96(1):69–83, 2015.

[12] S. Asseng, I. Foster, and N. C. Turner. The impact of temperature variability on wheat yields. *Global Change Biology*, 17(2):997–1012, 2011.

[13] M. W. Baba, S. Gascoin, C. Kinnard, A. Marchane, and L. Hanich. Effect of Digital Elevation Model Resolution on the Simulation of the Snow Cover Evolution in the High Atlas. *Water Resources Research*, 55(7):5360–5378, 2019.

[14] R. Balaghi, M. Jlibene, B. Tychon, and H. Heerens. Agrometeorological forecasting of cereal crop yields in Morocco. Technical report, National Institute for Agronomic Research (INRA), Morocco, 2012.

[15] M. P. Baldwin and T. J. Dunkerton. Propagation of the Arctic Oscillation from the stratosphere to the troposphere. *Journal of Geophysical Research: Atmospheres*, 104(D24):30937–30946, 1999.

[16] M. J. Barcikowska, S. B. Kapnick, and F. Feser. Impact of large-scale circulation changes in the North Atlantic sector on the current and future Mediterranean winter hydroclimate. *Climate Dynamics*, 50(5-6):2039–2059, 2018.

[17] A. G. Barnston and R. E. Livezey. Classification, seasonality and persistence of low-frequency atmospheric circulation patterns. *Monthly Weather Review*, 115(6):1083–1126, 1987.

[18] A. G. Barnston and T. M. Smith. Specification and Prediction of Global Surface Temperature and Precipitation from Global SST Using CCA. *Journal of Climate*, 9(11):2660–2697, 1996.

[19] W. R. Berghuijs, R. A. Woods, and M. Hrachowitz. A precipitation shift from snow towards rain leads to a decrease in streamflow. *Nature Climate Change*, 4(7):583–586, 2014.

[20] J. Bjerknes. Atlantic Air-Sea Interaction. *Advances in Geophysics*, 10(C):1–82, 1964.

[21] M. L. Blackmon, R. A. Madden, J. M. Wallace, and D. S. Gutzler. Geographical variations in the vertical structure of geopotential height fluctuations. *Journal of the Atmospheric Sciences*, 36(12):2450–2466, 1979.

[22] I. Bladé, D. Fortuny, G. J. Van Oldenborgh, and B. Liebmann. The summer North Atlantic Oscillation in CMIP3 models and related uncertainties in projected summer drying in Europe. *Journal of Geophysical Research Atmospheres*, 117(16):D16104, 2012.

[23] F. Boberg and J. H. Christensen. Overestimation of Mediterranean summer temperature projections due to model deficiencies. *Nature Climate Change*, 2(6):433–436, 2012.

[24] R. Bojariu and L. Gimeno. Predictability and numerical modelling of the North Atlantic Oscillation. *Earth-Science Reviews*, 63(1-2):145–168, 2003.

[25] R. Bojariu and L. Gimeno. The role of snow cover fluctuations in multiannual NAO persistence. *Geophysical Research Letters*, 30(4):1156, 2003.

[26] H.-J. Bolle. *Climate, Climate Variability, and Impacts in the Mediterranean Area: An Overview*, pages 5–86. Springer, 2003.

[27] K. Born, A. H. Fink, and H. Paeth. Dry and wet periods in the northwestern Maghreb for present day and future climate conditions. *Meteorologische Zeitschrift*, 17(5):533–551, 2008.

[28] H. Bouamri, A. Boudhar, S. Gascoin, and C. Kinnard. Performance of temperature and radiation index models for point-scale snow water equivalent (SWE) simulations in the Moroccan High Atlas Mountains. *Hydrological Sciences Journal*, 63(12):1844–1862, 2018.

[29] A. Boudhar, G. Boulet, L. Hanich, J. E. Sicart, and A. Chehbouni. Energy fluxes and melt rate of a seasonal snow cover in the Moroccan High Atlas. *Hydrological Sciences Journal*, 61(5):931–943, 2016.

[30] A. Boudhar, B. Duchemin, L. Hanich, G. Boulet, and A. Chehbouni. Spatial distribution of the air temperature in mountainous areas using satellite thermal infra-red data. *Comptes Rendus - Geoscience*, 343(1):32–42, 2011.

[31] A. Boudhar, B. Duchemin, L. Hanich, L. Jarlan, A. Chaponnière, P. Maisongrande, G. Boulet, and A. Chehbouni. Long-term analysis of snow-covered area in the Moroccan High-Atlas through remote sensing. *International Journal of Applied Earth Observation and Geoinformation*, 12(SUPPL. 1), 2010.

[32] A. Boudhar, L. Hanich, G. Boulet, B. Duchemin, B. Berjamy, and A. Chehbouni. Evaluation of the Snowmelt Runoff model in the Moroccan High Atlas Mountains using two snow-cover estimates. *Hydrological Sciences Journal*, 54(6):1094–1113, 2009.

[33] S. Brands, R. Manzanas, J. M. Gutiérrez, and J. Cohen. Seasonal Predictability of Wintertime Precipitation in Europe Using the Snow Advance Index. *Journal of Climate*, 25(12):4023–4028, 2012.

[34] B. W. Brock, I. C. Willis, and M. J. Sharp. Measurement and parameterization of albedo variations at haut glacier d'arolla, Switzerland. *Journal of Glaciology*, 46(155):675–688, 2000.

[35] R. Brogli, N. Kröner, S. L. Sørland, D. Lüthi, and C. Schär. The role of hadley circulation and lapse-rate changes for the future European summer climate. *Journal of Climate*, 32(2):385–404, 2019.

[36] R. Brogli, S. L. Sørland, N. Kröner, and C. Schär. Causes of future Mediterranean precipitation decline depend on the season. *Environmental Research Letters*, 14(11):114017, 2019.

[37] W. Brutsaert. *Evaporation into the Atmosphere*. Dordrecht: Kluwer Academic, 1982.

[38] M. P. Byrne and P. A. O'Gorman. Understanding decreases in land relative humidity with global warming: Conceptual model and GCM simulations. *Journal of Climate*, 29(24):9045–9061, 2016.

[39] M. P. Byrne and P. A. O'Gorman. Trends in continental temperature and humidity directly linked to ocean warming. *Proceedings of the National Academy of Sciences of the United States of America*, 115(19):4863–4868, 2018.

[40] T. Carroll, D. Cline, C. Olheiser, A. Rost, A. Nilsson, G. Fall, C. Bovitz, and L. Li. NOAA's National Snow Analyses. In Nils Svartholm, editor, *Proceedings of the 74th Annual Meeting of the Western Snow Conference*, pages 1–14, 2006.

[41] A. Chehbouni, R. Escadafal, B. Duchemin, G. Boulet, V. Simonneaux, G. Dedieu, B. Mougenot, S. Khabba, H. Kharrou, P. Maisongrande, O. Merlin, A. Chaponnière, J. Ezzahar, S. Er-Raki, J. Hoedjes, R. Hadria, A. Abourida, A. Cheggour, F. Raibi, A. Boudhar, I. Benhadj, L. Hanich, A. Benkaddour, N. Guemouria, A. H. Chehbouni, A. Lahrouni, A. Olioso, F. Jacob, D. G. Williams, and J. A. Sobrino. An integrated modelling and remote sensing approach for hydrological study in arid and semi-arid regions: The SUDMED programme. *International Journal of Remote Sensing*, 29(17-18):5161–5181, 2008.

[42] V. W. Chu, L. C. Smith, A. K. Rennermalm, R. R. Forster, and J. E. Box. Hydrologic controls on coastal suspended sediment plumes around the Greenland Ice Sheet. *Cryosphere*, 6(1):1–19, 2012.

[43] M. P. Clark, J. Hendrikx, A. G. Slater, D. Kavetski, B. Anderson, N. J. Cullen, T. Kerr, E. Örn Hreinsson, and R. A. Woods. Representing spatial variability of snow water equivalent in hydrologic and land-surface models: A review. *Water Resources Research*, 47(7), 2011.

[44] J. Cohen, M. Barlow, P. J. Kushner, and K. Saito. Stratosphere–Troposphere Coupling and Links with Eurasian Land Surface Variability. *Journal of Climate*, 20(21):5335–5343, nov 2007.

[45] J. Cohen and D. Entekhabi. Eurasian snow cover variability and Northern Hemisphere climate predictability. *Geophysical Research Letters*, 26(3):345–348, 1999.

[46] J. Cohen and J. Jones. A new index for more accurate winter predictions. *Geophysical Research Letters*, 38(21), 2011.

[47] S. Coles. *An Introduction to Statistical Modeling of Extreme Values*. Springer Series in Statistics. Springer London, London, 2001.

[48] G. P. Compo, J. S. Whitaker, P. D. Sardeshmukh, N. Matsui, R. J. Allan, X. Yin, B. E. Gleason, R. S. Vose, G. Rutledge, P. Bessemoulin, S. BroNnimann, M. Brunet, R. I. Crouthamel, A. N. Grant, P. Y. Groisman, P. D. Jones, M. C. Kruk, A. C. Kruger, G. J. Marshall, M. Maugeri, H. Y. Mok, O. Nordli, T. F. Ross, R. M. Trigo, X. L. Wang,

S. D. Woodruff, and S. J. Worley. The Twentieth Century Reanalysis Project. *Quarterly Journal of the Royal Meteorological Society*, 137(654):1–28, 2011.

[49] A. Czaja and C. Frankignoul. Observed impact of Atlantic SST anomalies on the North Atlantic oscillation. *Journal of Climate*, 15(6):606–623, 2002.

[50] A. Czaja, A. W. Robertson, and T. Huck. *The role of atlantic ocean-atmosphere coupling in affecting North Atlantic oscillation variability*, volume 134, pages 147–172. American Geophysical Union, 2003.

[51] Y Daki, R Lachgar, and G Zahour. Étude Hydroclimatique du bassin du haut Oum-Er-Rbia. *International Journal of Innovation and Applied Studies*, 12(3):644–658, 2015.

[52] F. V. Davenport, J. E. Herrera-Estrada, M. Burke, and N. S. Diffenbaugh. Flood Size Increases Nonlinearly Across the Western United States in Response to Lower Snow-Precipitation Ratios. *Water Resources Research*, 56(1), 2020.

[53] P. Davini and C. Cagnazzo. On the misinterpretation of the North Atlantic Oscillation in CMIP5 models. *Climate Dynamics*, 43(5-6):1497–1511, 2014.

[54] A. C. Davison, S. A. Padoan, and M. Ribatet. Statistical Modeling of Spatial Extremes. *Statistical Science*, 27(2):161–186, may 2012.

[55] D. P. Dee, S. M. Uppala, A. J. Simmons, P. Berrisford, P. Poli, S. Kobayashi, U. Andrae, M. A. Balmaseda, G. Balsamo, P. Bauer, P. Bechtold, A. C.M. Beljaars, L. van de Berg, J. Bidlot, N. Bormann, C. Delsol, R. Dragani, M. Fuentes, A. J. Geer, L. Haimberger, S. B. Healy, H. Hersbach, E. V. Hólm, L. Isaksen, P. Kållberg, M. Köhler, M. Matricardi, A. P. Mcnally, B. M. Monge-Sanz, J. J. Morcrette, B. K. Park, C. Peubey, P. de Rosnay, C. Tavolato, J. N. Thépaut, and F. Vitart. The ERA-Interim reanalysis: Configuration and performance of the data assimilation system. *Quarterly Journal of the Royal Meteorological Society*, 137(656):553–597, 2011.

[56] Y. Derin, E. Anagnostou, A. Berne, M. Borga, B. Boudevillain, W. Buytaert, C. H. Chang, G. Delrieu, Y. Hong, Y. C. Hsu, W. Lavado-Casimiro, B. Manz, S. Moges, E. I. Nikolopoulos, D. Sahlu, F. Salerno, J. P. Rodríguez-Sánchez, H. J. Vergara, and K. K. Yilmaz. Multiregional satellite precipitation products evaluation over complex terrain. *Journal of Hydrometeorology*, 17(6):1817–1836, 2016.

[57] D. Deryng, D. Conway, N. Ramankutty, J. Price, and R. Warren. Global crop yield response to extreme heat stress under multiple climate change futures. *Environmental Research Letters*, 9(3):034011, 2014.

[58] C. Deser, L. Terray, and A. S. Phillips. Forced and internal components of winter air temperature trends over North America during the past 50 years: Mechanisms and implications. *Journal of Climate*, 29(6):2237–2258, 2016.

[59] N. S. Diffenbaugh and F. Giorgi. Climate change hotspots in the CMIP5 global climate model ensemble. *Climatic Change*, 114(3-4):813–822, 2012.

[60] F. J. Doblas-Reyes, M. Déqué, and J.-P. Piedelievre. Multi-model spread and probabilistic seasonal forecasts in PROVOST. *Quarterly Journal of the Royal Meteorological Society*, 126(567):2069–2087, 2010.

[61] A. J. Dobson. *An Introduction to Generalized Linear Models*. Chapman and Hall, London, 1990.

[62] C. W. Downer, F. L. Ogden, J. Neidzialek, and S. Liu. *Gridded surface/subsurface hydrologic analysis (GSSHA) model: A model for simulating diverse streamflow-producing processes*, pages 131–157. Taylor & Francis, CRC Press, Boca Raton, FL, 2005.

[63] M. Drévillon, L. Terray, P. Rogel, and C. Cassou. Mid latitude Atlantic SST influence on European winter climate variability in the NCEP Reanalysis. *Climate Dynamics*, 18(3-4):331–344, 2001.

[64] F. Driouech, M. Déqué, and E. Sánchez-Gómez. Weather regimes-Moroccan precipitation link in a regional climate change simulation. *Global and Planetary Change*, 72(1-2):1–10, 2010.

[65] M. Dubrovský, M. Hayes, P. Duce, M. Trnka, M. Svoboda, and P. Zara. Multi-GCM projections of future drought and climate variability indicators for the Mediterranean region. *Regional Environmental Change*, 14(5):1907–1919, 2014.

[66] J. A. Duffie and W. A. Beckman. *Solar Engineering of Thermal Processes: Fourth Edition*. Wiley, New York, 2013.

[67] J. L. Dufresne, M. A. Foujols, S. Denvil, A. Caubel, O. Marti, O. Aumont, Y. Balkanski, S. Bekki, H. Bellenger, R. Benshila, S. Bony, L. Bopp, P. Braconnot, P. Brockmann, P. Cadule, F. Cheruy, F. Codron, A. Cozic, D. Cugnet, N. de Noblet, J. P. Duvel, C. Ethé, L. Fairhead, T. Fichefet, S. Flavoni, P. Friedlingstein, J. Y. Grandpeix, L. Guez, E. Guilyardi, D. Hauglustaine, F. Hourdin, A. Idelkadi, J. Ghattas, S. Joussaume, M. Kageyama, G. Krinner, S. Labetoulle, A. Lahellec, M. P. Lefebvre, F. Lefevre, C. Levy, Z. X. Li, J. Lloyd, F. Lott, G. Madec, M. Mancip, M. Marchand, S. Masson, Y. Meurdesoif, J. Mignot, I. Musat, S. Parouty, J. Polcher, C. Rio, M. Schulz, D. Swingedouw, S. Szopa, C. Talandier, P. Terray, N. Viovy, and N. Vuichard. Climate change projections using the IPSL-CM5 Earth System Model: From CMIP3 to CMIP5. *Climate Dynamics*, 40(9-10):2123–2165, 2013.

[68] J. P. Dunne, J. G. John, A. J. Adcroft, S. M. Griffies, R. W. Hallberg, E. Shevliakova, R. J. Stouffer, W. Cooke, K. A. Dunne, M. J. Harrison, J. P. Krasting, S. L. Malyshev, P. C. D. Milly, P. J. Phillipps, L. T. Sentman, B. L. Samuels, M. J. Spelman, M. Winton, A.T. Wittenberg, and N. Zadeh. GFDL's ESM2 global coupled climate-carbon earth system models. Part I: Physical formulation and baseline simulation characteristics. *Journal of Climate*, 25(19):6646–6665, 2012.

[69] N. Dunstone, D. Smith, A. Scaife, L. Hermanson, R. Eade, N. Robinson, M. Andrews, and J. Knight. Skilful predictions of the winter North Atlantic Oscillation one year ahead. *Nature Geoscience*, 9(11):809–814, 2016.

[70] J. M. Eden, G. J. van Oldenborgh, E. Hawkins, and E. B. Suckling. A global empirical system for probabilistic seasonal climate prediction. *Geoscientific Model Development*, 8(12):3947–3973, 2015.

[71] U. Ehret, E. Zehe, V. Wulfmeyer, K. Warrach-Sagi, and J. Liebert. Should we apply bias correction to global and regional climate model data? *Hydrology and Earth System Sciences*, 16(9):3391–3404, 2012.

[72] E. M. El Khalki, Y. Tramblay, M. El Mehdi Saidi, C. Bouvier, L. Hanich, M. Benrhanem, and M. Alaouri. Comparison of modeling approaches for flood forecasting in the High Atlas Mountains of Morocco. *Arabian Journal of Geosciences*, 11(15):410, 2018.

[73] N. El Moçayd, S. Kang, and E. A. B. Eltahir. Climate change impacts on the Water Highway project in Morocco. *Hydrology and Earth System Sciences*, 24(3):1467–1483, 2020.

[74] M. El Mourid and M. Karrout. Agriculture in arid and semi-arid regions of Morocco : Challenges and Prospects. *Revue Al Awamia*, 92:83–91, 1996.

[75] S. R. Fassnacht, J. I. López-Moreno, C. Ma, A. N. Weber, A. K.D. Pfohl, S. K. Kampf, and M. Kappas. Spatio-temporal snowmelt variability across the headwaters of the Southern Rocky Mountains. *Frontiers of Earth Science*, 11(3):505–514, 2017.

[76] B. Fatna and H. Abderrahim. *La sécheresse agricole au Maroc*, pages 31–41. IAHS Publication no. 240, 1997.

[77] A. Fayad, S. Gascoin, G. Faour, J. I. López-Moreno, L. Drapeau, M. Le Page, and R. Escadafal. Snow hydrology in Mediterranean mountain regions: A review. *Journal of Hydrology*, 551:374–396, 2017.

[78] S. B. Feldstein. The timescale, power spectra, and climate noise properties of teleconnection patterns. *Journal of Climate*, 13(24):4430–4440, 2000.

[79] S. Fernández-González, S. C. Pereira, A. Castro, A. Rocha, and R. Fraile. Connection between autumn Sea Surface Temperature and winter precipitation in the Iberian Peninsula. *Global and Planetary Change*, 121:9–18, 2014.

[80] S. Filahi, Y. Tramblay, L. Mouhir, and E. P. Diaconescu. Projected changes in temperature and precipitation indices in Morocco from high-resolution regional climate models. *International Journal of Climatology*, 37(14):4846–4863, 2017.

[81] C. G Fletcher. *Investigations into seasonal predictability of North Atlantic winter climate*. Doctoral thesis, University of London, 2005.

[82] C. G. Fletcher, S. C. Hardiman, P. J. Kushner, and J. Cohen. The Dynamical Response to Snow Cover Perturbations in a Large Ensemble of Atmospheric GCM Integrations. *Journal of Climate*, 22(5):1208–1222, 2009.

[83] M. L. Follum, C. W. Downer, J. D. Niemann, S. M. Roylance, and C. M. Vuyovich. A radiation-derived temperature-index snow routine for the GSSHA hydrologic model. *Journal of Hydrology*, 529(P3):723–736, 2015.

[84] M. L. Follum, J. D. Niemann, and S. R. Fassnacht. A comparison of snowmelt-derived streamflow from temperature-index and modified-temperature-index snow models. *Hydrological Processes*, 33(23):3030–3045, 2019.

[85] K. J. Franz, P. Butcher, and N. K. Ajami. Addressing snow model uncertainty for hydrologic prediction. *Advances in Water Resources*, 33(8):820–832, 2010.

[86] J. Friedman, T. Hastie, and R. Tibshirani. Regularization Paths for Generalized Linear Models via Coordinate Descent. *Journal of Statistical Software*, 33(1):1–22, 2010.

[87] C. Funk and Climate Hazards Group. CHIRPS. 2015.

[88] C. Funk, P. Peterson, M. Landsfeld, D. Pedreros, J. Verdin, S. Shukla, G. Husak, J. Rowland, L. Harrison, A. Hoell, and J. Michaelsen. The climate hazards infrared precipitation with stations—a new environmental record for monitoring extremes. *Scientific Data*, 2(1):150066, 2015.

[89] J. C. Furtado, J. L. Cohen, and E. Tziperman. The combined influences of autumnal snow and sea ice on Northern Hemisphere winters. *Geophysical Research Letters*, 43(7):3478–3485, 2016.

[90] X. Gao, J. S. Pal, and F. Giorgi. Projected changes in mean and extreme precipitation over the Mediterranean region from a high resolution double nested RCM simulation. *Geophysical Research Letters*, 33(3), 2006.

[91] F. Gascon, C. Bouzinac, O. Thépaut, M. Jung, B. Francesconi, J. Louis, V. Lonjou, B. Lafrance, S. Massera, A. Gaudel-Vacaresse, F. Languille, B. Alhammoud, F. Viallefont, B. Pflug, J. Bieniarz, S. Clerc, L. Pessiot, T. Trémas, E. Cadau, R. De Bonis, C. Isola, P. Martimort, and V. Fernandez. Copernicus Sentinel-2A Calibration and Products Validation Status. *Remote Sensing*, 9(6):584, jun 2017.

[92] G. Gastineau and C. Frankignoul. Influence of the North Atlantic SST Variability on the Atmospheric Circulation during the Twentieth Century. *Journal of Climate*, 28(4):1396–1416, 2015.

[93] G. Gastineau, B. L'Hévéder, F. Codron, and C. Frankignoul. Mechanisms determining the winter atmospheric response to the Atlantic overturning circulation. *Journal of Climate*, 29(10):3767–3785, 2016.

[94] W. L. Gates, J. S. Boyle, C. Covey, C. G. Dease, C. M. Doutriaux, R. S. Drach, M. Fiorino, P. J. Gleckler, J. J. Hnilo, S. M. Marlais, T. J. Phillips, G. L. Potter, B. D. Santer, K. R. Sperber, K. E. Taylor, and D. N. Williams. An Overview of the Results of the Atmospheric Model Intercomparison Project (AMIP I). *Bulletin of the American Meteorological Society*, 80(1):29–55, 1999.

[95] M. Gervais, J. Shaman, and Y. Kushnir. Impacts of the North Atlantic warming hole in future climate projections: Mean atmospheric circulation and the North Atlantic jet. *Journal of Climate*, 32(10):2673–2689, 2019.

[96] R. L. Gianotti and E. A. B. Eltahir. Regional climate modeling over the maritime continent. Part I: New parameterization for convective cloud fraction. *Journal of Climate*, 27(4):1488–1503, 2014.

[97] R. L. Gianotti and E. A. B. Eltahir. Regional climate modeling over the maritime continent. Part II: New parameterization for autoconversion of convective rainfall. *Journal of Climate*, 27(4):1504–1523, 2014.

[98] R. L. Gianotti, D. Zhang, and E. A. B. Eltahir. Assessment of the regional climate model version 3 over the maritime continent using different cumulus parameterization and land surface schemes. *Journal of Climate*, 25(2):638–656, 2012.

[99] F. Giorgi. Climate change hot-spots. *Geophysical Research Letters*, 33(8):L08707, 2006.

[100] F. Giorgi and X. Bi. Updated regional precipitation and temperature changes for the 21st century from ensembles of recenet AOGCM simulations. *Geophysical Research Letters*, 32(21):1–4, 2005.

[101] F. Giorgi and P. Lionello. Climate change projections for the Mediterranean region. *Global and Planetary Change*, 63(2-3):90–104, 2008.

[102] R. Grotjahn. Weather extremes that impact various agricultural commodities. In *AGU Books*. AGU, 2017.

[103] B. Guan, N. P. Molotch, D. E. Waliser, S. M. Jepsen, T. H. Painter, and J. Dozier. Snow water equivalent in the Sierra Nevada: Blending snow sensor observations with snowmelt model simulations. *Water Resources Research*, 49(8):5029–5046, 2013.

[104] D. K. Hall, J. E. Box, K. A. Casey, S. J. Hook, C. A. Shuman, and K. Steffen. Comparison of satellite-derived and in-situ observations of ice and snow surface temperatures over Greenland. *Remote Sensing of Environment*, 112(10):3739–3749, 2008.

[105] D. K. Hall and G. A. Riggs. MODIS/Terra Snow Cover Daily L3 Global 500m SIN Grid, Version 6 [subset 9W-4W/30N-34N, from 2000-02-22 to 2018-07-27], 2016.

[106] N. M. J. Hall, H. Lin, and J. Derome. The extratropical signal generated by a midlatitude SST anomaly. Part II: Influence on seasonal forecasts. *Journal of Climate*, 14(12):2696–2709, 2001.

[107] N. Harnik, E. Galanti, O. Martius, and O. Adam. The anomalous merging of the African and North Atlantic jet streams during the northern hemisphere Winter of 2010. *Journal of Climate*, 27(19):7319–7334, 2014.

[108] I. Harris, P. D. Jones, T. J. Osborn, and D. H. Lister. Updated high-resolution grids of monthly climatic observations - the CRU TS3.10 Dataset. *International Journal of Climatology*, 34(3):623–642, 2014.

[109] H. Hashemi, M. Nordin, V. Lakshmi, G. J. Huffman, and R. Knight. Bias correction of long-term satellite monthly precipitation product (TRMM 3B43) over the conterminous United States. *Journal of Hydrometeorology*, 18(9):2491–2509, 2017.

[110] M. He, T. S. Hogue, K. J. Franz, S. A. Margulis, and J. A. Vrugt. Characterizing parameter sensitivity and uncertainty for a snow model across hydroclimatic regimes. *Advances in Water Resources*, 34(1):114–127, 2011.

[111] N. R. Hedstrom and J. W. Pomeroy. Measurements and modelling of snow interception in the boreal forest. *Hydrological Processes*, 12(10-11):1611–1625, 1998.

[112] I. M. Held, P. L. Panetta, and R. T. Pierrehumbert. Stationary external Rossby waves in vertical shear. *Journal of the Atmospheric Sciences*, 42(9):865–883, 1985.

[113] I. M. Held, M. Ting, and H. Wang. Northern winter stationary waves: Theory and modeling. *Journal of Climate*, 15(16):2125–2144, 2002.

[114] P. Hellegers, W. Immerzeel, and P. Droogers. Economic concepts to address future water supply–demand imbalances in Iran, Morocco and Saudi Arabia. *Journal of Hydrology*, 502:62–67, oct 2013.

[115] J. Herrero and M. J. Polo. Evaposublimation from the snow in the Mediterranean mountains of Sierra Nevada (Spain). *Cryosphere*, 10(6):2981–2998, 2016.

[116] E. Hertig and Y. Tramblay. Regional downscaling of Mediterranean droughts under past and future climatic conditions. *Global and Planetary Change*, 151:36–48, 2017.

[117] R. Hock. A distributed temperature-index ice- and snowmelt model including potential direct solar radiation. *Journal of Glaciology*, 45(149):101–111, 1999.

[118] M. Hoerling, J. Eischeid, J. Perlwitz, X. Quan, T. Zhang, and P. Pegion. On the increased frequency of mediterranean drought. *Journal of Climate*, 25(6):2146–2161, 2012.

[119] M. P. Hoerling, J. W. Hurrell, and T. Xu. Tropical origins for recent North Atlantic climate change. *Science*, 292(5514):90–92, 2001.

[120] A. A. M. Holtslag, E. I. F. De Bruijn, and H. L. Pan. A high resolution air mass transformation model for short-range weather forecasting. *Monthly Weather Review*, 118(8):1561–1575, 1990.

[121] B. J. Hoskins and T. Ambrizzi. Rossby wave propagation on a realistic longitudinally varying flow. *Journal of the Atmospheric Sciences*, 50(12):1661–1671, 1993.

[122] B. J. Hoskins and D. J. Karoly. The steady linear response of a spherical atmosphere to thermal and orographic forcing. *Journal of the Atmospheric Sciences*, 38(6):1179–1196, 1981.

[123] M. Hssaisoune, L. Bouchaou, A. Sifeddine, I. Bouimetarhan, and A. Chehbouni. Moroccan Groundwater Resources and Evolution with Global Climate Changes. *Geosciences*, 10(2):81, feb 2020.

[124] B. Huang, P. W. Thorne, V. F. Banzon, T. Boyer, G. Chepurin, J. H. Lawrimore, M. J. Menne, T. M. Smith, R. S. Vose, and H. M. Zhang. Extended reconstructed Sea surface temperature, Version 5 (ERSSTv5): Upgrades, validations, and intercomparisons. *Journal of Climate*, 30(20):8179–8205, 2017.

[125] G. Huffman, D. Bolvin, D. Braithwaite, K. Hsu, R. Joyce, and P. Xie. Integrated Multi-satellitE Retrievals for GPM (IMERG), version 4.4., 2014.

[126] G. J. Huffman, R. F. Adler, D. T. Bolvin, G. Gu, E. J. Nelkin, K. P. Bowman, Y. Hong, E. F. Stocker, and D. B. Wolff. The TRMM Multisatellite Precipitation Analysis (TMPA): Quasi-global, multiyear, combined-sensor precipitation estimates at fine scales. *Journal of Hydrometeorology*, 8(1):38–55, 2007.

[127] J. V. Hurley and J. Galewsky. A last-saturation diagnosis of subtropical water vapor response to global warming. *Geophysical Research Letters*, 37(6):n/a–n/a, mar 2010.

[128] J. W. Hurrell. Decadal trends in the North Atlantic oscillation: Regional temperatures and precipitation. *Science*, 269(5224):676–679, 1995.

[129] J.W. Hurrell, Y. Kushnir, G. Ottersen, and M. Visbeck. *An overview of the north atlantic oscillation*, volume 134, pages 1–35. American Geophysical Union, 2003.

[130] E. S. Im and E. A. B. Eltahir. Simulation of the diurnal variation of rainfall over the western Maritime Continent using a regional climate model. *Climate Dynamics*, 51(1-2):73–88, 2018.

[131] E. S. Im and E. A. B. Eltahir. Simulations of the observed 'jump' in the West African monsoon and its underlying dynamics using the MIT regional climate model. *International Journal of Climatology*, 38(2):841–852, 2018.

[132] E. S. Im, R. L. Gianotti, and E. A. B. Eltahir. Improving the simulation of the West African monsoon using the MIT regional climate model. *Journal of Climate*, 27(6):2209–2229, 2014.

[133] IPCC. Climate Change 2013: The Physical Science Basis. Contribution of Working Group I to the Fifth Assessment Report of the Intergovernmental Panel on Climate Change [Stocker, T.F., D. Qin, G.-K. Plattner, M. Tignor, S.K. Allen, J. Boschung, A. Nauels, Y. Xia,. Technical report, IPCC, Cambridge University Press, Cambridge, United Kingdom and New York, NY, USA, 2013.

[134] L. Jarlan, J. Abaoui, B. Duchemin, A. Ouldbba, Y. M. Tourre, S. Khabba, M. Le Page, R. Balaghi, A. Mokssit, and G. Chehbouni. Linkages between common wheat yields and climate in Morocco (1982-2008). *International journal of biometeorology*, 58(7):1489–1502, 2014.

[135] A. Jarvis, H. I. Reuter, A. Nelson, and E. Guevara. Hole-filled SRTM for the globe Version 4, available from the CGIAR-CSI SRTM 90m Database, 2008.

[136] Å. Johansson, A. Barnston, S. Saha, and H. Van Den Dool. On the level and origin of seasonal forecast skill in Northern Europe. *Journal of the Atmospheric Sciences*, 55(1):103–127, 1998.

[137] M. M. Junge and D. B. Stephenson. Mediated and direct effects of the North Atlantic Ocean on winter temperatures in Northwest Europe. *International Journal of Climatology*, 23(3):245–261, 2003.

[138] E. Kalnay, M. Kanamitsu, R. Kistler, W. Collins, D. Deaven, L. Gandin, M. Iredell, S. Saha, G. White, J. Woollen, Y. Zhu, M. Chelliah, W. Ebisuzaki, W. Higgins, J. Janowiak, K. C. Mo, C. Ropelewski, J. Wang, A. Leetmaa, R. Reynolds, Roy Jenne, and Dennis Joseph. The NCEP/NCAR 40-year reanalysis project. *Bulletin of the American Meteorological Society*, 77(3):437–471, 1996.

[139] S. Kang, A. Tuel, and E. A. B. Eltahir. High-Resolution Projections of Intensifying Drought over the Eastern Mediterranean. *Climate Dynamics*, 2020.

[140] G. Kaser, D. R. Hardy, T. Mölg, R. S. Bradley, and T. M. Hyera. Modern glacier retreat on Kilimanjaro as evidence of climate change: observations and facts. *International Journal of Climatology*, 24(3):329–339, mar 2004.

[141] C. Kelley, M. Ting, R. Seager, and Y. Kushnir. The relative contributions of radiative forcing and internal climate variability to the late 20th Century winter drying of the Mediterranean region. *Climate Dynamics*, 38(9-10):2001–2015, 2012.

[142] C. P. Kelley. *Recent and future drying of the Mediterranean region: anthropogenic forcing, natural variability and social impacts*. Doctoral thesis, Columbia University, 2014.

[143] C. P. Kelley, S. Mohtadi, M. A. Cane, R. Seager, and Y. Kushnir. Climate change in the Fertile Crescent and implications of the recent Syrian drought. *Proceedings of the National Academy of Sciences of the United States of America*, 112(11):3241–3246, 2015.

[144] J. J. Kennedy. A review of uncertainty in in situ measurements and data sets of sea surface temperature. *Reviews of Geophysics*, 52(1):1–32, 2014.

[145] V. V. Kharin and F. W. Zwiers. On the ROC score of probability forecasts. *Journal of Climate*, 16(24):4145–4150, 2003.

[146] J. T. Kiehl, J. J. Hack, G. B. Bonan, B. A. Boville, B. P. Briegleb, D. L. Williamson, and P. J. Rasch. Description of the NCAR Community Climate Model (CCM3) (No. NCAR/TN-420+STR). Technical report, University Corporation for Atmospheric Research, 1996.

[147] P. Knippertz, M. Christoph, and P. Speth. Long-term precipitation variability in Morocco and the link to the large-scale circulation in recent and future climates. *Meteorology and Atmospheric Physics*, 83(1-2):67–88, 2003.

[148] V. Kotroni and K. Lagouvardos. Lightning in the Mediterranean and its relation with sea-surface temperature. *Environmental Research Letters*, 11(3):034006, mar 2016.

[149] Y. Kushnir. Interdecadal Variations in North Atlantic Sea Surface Temperature and Associated Atmospheric Conditions. *Journal of Climate*, 7(1):141–157, 1994.

[150] P. J. Lamb and R. A. Peppler. North Atlantic oscillation: concept and an application. *Bull. Am. Meteorol. Soc.*, 68(10 , Oct. 1987):1218–1225, 1987.

[151] D. W. Lawlor and R. A. C. Mitchell. Crop ecosystem responses to climatic change: wheat. In *Climate change and global crop productivity.*, pages 57–80. CABI, Wallingford, 2000.

[152] H. Li, J. Sheffield, and E. F. Wood. Bias correction of monthly precipitation and temperature fields from Intergovernmental Panel on Climate Change AR4 models using equidistant quantile matching. *Journal of Geophysical Research Atmospheres*, 115(10), 2010.

[153] X. Z. Liang, K. E. Kunkel, G. A. Meehl, R. G. Jones, and J. X. L. Wang. Regional climate models downscaling analysis of general circulation models present climate biases propagation into future change projections. *Geophysical Research Letters*, 35(8), 2008.

[154] H. Lievens, M. Demuzere, H.-P. Marshall, R. H. Reichle, L. Brucker, I. Brangers, P. de Rosnay, M. Dumont, M. Girotto, W. W. Immerzeel, T. Jonas, E. J. Kim, I. Koch, C. Marty, T. Saloranta, J. Schöber, and G. J. M. De Lannoy. Snow depth variability in the Northern Hemisphere mountains observed from space. *Nature Communications*, 10(1):4629, dec 2019.

[155] G. E. Liston and K. Elder. A distributed snow-evolution modeling system (snowmodel). *Journal of Hydrometeorology*, 7(6):1259–1276, 2006.

[156] B. Lloyd-Hughes and M. A. Saunders. Seasonal prediction of European spring precipitation from El Niño-Southern Oscillation and Local sea-surface temperatures. *International Journal of Climatology*, 22(1):1–14, 2002.

[157] J. I. López-Moreno, S. Gascoin, J. Herrero, E. A. Sproles, M. Pons, E. Alonso-González, L. Hanich, A. Boudhar, K. N. Musselman, N. P. Molotch, J. Sickman, and J. Pomeroy. Different sensitivities of snowpacks to warming in Mediterranean climate mountain areas. *Environmental Research Letters*, 12(7), 2017.

[158] M. N. Lorenzo, I. Iglesias, J. J. Taboada, and M. Gómez-Gesteira. Relationship between monthly rainfall in northwest Iberian Peninsula and North Atlantic sea surface temperature. *International Journal of Climatology*, pages n/a–n/a, 2009.

[159] M. N. Lorenzo, J. J. Taboada, I. Iglesias, and M. Gómez-Gesteira. Predictability of the spring rainfall in Northwestern Iberian Peninsula from sea surfaces temperature of ENSO areas. *Climatic Change*, 107(3-4):329–341, 2011.

[160] J. Lu, G. A. Vecchi, and T. Reichler. Expansion of the Hadley cell under global warming. *Geophysical Research Letters*, 34(6):L06805, 2007.

[161] T. Luo, R. Reig., and P. Young. Aqueduct Projected Water Stress Country Rankings. Technical Note. Technical report, World Resources Institute, Washington, D.C., 2015.

[162] M. P. Marcella and E. A. B. Eltahir. Modeling the summertime climate of Southwest Asia: The role of land surface processes in shaping the climate of semiarid regions. *Journal of Climate*, 25(2):704–719, 2012.

[163] M. P. Marcella and E. A. B. Eltahir. Introducing an irrigation scheme to a regional climate model: A case study over West Africa. *Journal of Climate*, 27(15):5708–5723, 2014.

[164] A. Marchane, L. Jarlan, A. Boudhar, Y. Tramblay, and L. Hanich. Linkages between snow cover, temperature and rainfall and the North Atlantic Oscillation over Morocco. *Climate Research*, 69(3):229–238, 2016.

[165] A. Marchane, L. Jarlan, L. Hanich, A. Boudhar, S. Gascoin, A. Tavernier, N. Filali, M. Le Page, O. Hagolle, and B. Berjamy. Assessment of daily MODIS snow cover products to monitor snow cover dynamics over the Moroccan Atlas mountain range. *Remote Sensing of Environment*, 160:72–86, 2015.

[166] A. Marchane, Y. Tramblay, L. Hanich, D. Ruelland, and L. Jarlan. Climate change impacts on surface water resources in the Rheraya catchment (High Atlas, Morocco). *Hydrological Sciences Journal*, 62(6):979–995, 2017.

[167] A. Mariotti, N. Zeng, and K. M. Lau. Euro-Mediterranean rainfall and ENSO-a seasonally varying relationship. *Geophysical Research Letters*, 29(12):59–1–59–4, 2002.

[168] A. Mariotti, N. Zeng, J. H. Yoon, V. Artale, A. Navarra, P. Alpert, and L. Z. X. Li. Mediterranean water cycle changes: Transition to drier 21st century conditions in observations and CMIP3 simulations. *Environmental Research Letters*, 3(4):44001, 2008.

[169] D. Marks, J. Domingo, D. Susong, T. Link, and D. Garen. A spatially distributed energy balance snowmelt model for application in mountain basins. *Hydrological Processes*, 13(12-13):1935–1959, 1999.

[170] C. F. McSweeney, R. G. Jones, R. W. Lee, and D. P. Rowell. Selecting CMIP5 GCMs for downscaling over multiple regions. *Climate Dynamics*, 44(11-12):3237–3260, 2015.

[171] MEMEE. Stratégie Nationale de l'Eau. Technical report, Ministère de l'Énergie, des Mines, de l'Eau et de l'Environnement., Rabat, Morocco, 2009.

[172] M. J. Menne, I. Durre, R. S. Vose, B. E. Gleason, and T. G. Houston. An Overview of the Global Historical Climatology Network-Daily Database. *Journal of Atmospheric and Oceanic Technology*, 29(7):897–910, 2012.

[173] J. Michaelsen. Cross-Validation in Statistical Climate Forecast Models. *Journal of Climate and Applied Meteorology*, 26(11):1589–1600, 1987.

[174] P.-A. Michelangeli, M. Vrac, and H. Loukos. Probabilistic downscaling approaches: Application to wind cumulative distribution functions. *Geophysical Research Letters*, 36(11):L11708, 2009.

[175] D. J. Mildrexler, M. Zhao, and S. W. Running. A global comparison between station air temperatures and MODIS land surface temperatures reveals the cooling role of forests. *Journal of Geophysical Research: Biogeosciences*, 116(3), 2011.

[176] A. Milewski, R. Elkadiri, and M. Durham. Assessment and comparison of TMPA satellite precipitation products in varying climatic and topographic regimes in Morocco. *Remote Sensing*, 7(5):5697–5717, 2015.

[177] N. Mishra, C. Prodhomme, and V. Guemas. Multi-model skill assessment of seasonal temperature and precipitation forecasts over Europe. *Climate Dynamics*, 52(7-8):4207–4225, 2019.

[178] T. Mölg. Ablation and associated energy balance of a horizontal glacier surface on Kilimanjaro. *Journal of Geophysical Research*, 109(D16):D16104, 2004.

[179] N. P. Molotch. Reconstructing snow water equivalent in the Rio Grande headwaters using remotely sensed snow cover data and a spatially distributed snowmelt model. *Hydrological Processes*, 23(7):1076–1089, 2009.

[180] N. P. Molotch and S. A. Margulis. Estimating the distribution of snow water equivalent using remotely sensed snow cover data and a spatially distributed snowmelt model: A multi-resolution, multi-sensor comparison. *Advances in Water Resources*, 31(11):1503–1514, 2008.

[181] E. Muñoz, J. L. Arumí, D. Rivera, A. Montecinos, M. Billib, and C. Álvarez. Gridded data for a hydrological model in a scarce-data basin. *Proceedings of the Institution of Civil Engineers - Water Management*, 167(5):249–258, 2014.

[182] J. E. Nash and J. V. Sutcliffe. River flow forecasting through conceptual models part I - A discussion of principles. *Journal of Hydrology*, 10(3):282–290, 1970.

[183] Observatory of Economic Complexity. Observatory of Economic Complexity.

[184] Y. J. Orsolini, I. T. Kindem, and N. G. Kvamstø. On the potential impact of the stratosphere upon seasonal dynamical hindcasts of the North Atlantic Oscillation: a pilot study. *Climate Dynamics*, 36(3-4):579–588, 2011.

[185] H. Ouatiki, A. Boudhar, Y. Tramblay, L. Jarlan, T. Benabdelouhab, L. Hanich, M. R. El Meslouhi, and A. Chehbouni. Evaluation of TRMM 3B42 V7 rainfall product over the Oum Er Rbia watershed in Morocco. *Climate*, 5(1), 2017.

[186] J. S. Pal and E. A. B. Eltahir. Future temperature in southwest Asia projected to exceed a threshold for human adaptability. *Nature Climate Change*, 6(2):197–200, 2016.

[187] J. S. Pal, F. Giorgi, X. Bi, N. Elguindi, F. Solmon, X. Gao, S. A. Rauscher, R. Francisco, A. Zakey, J. Winter, M. Ashfaq, F. S. Syed, J. L. Bell, N. S. Differbaugh, J. Karmacharya, A. Konari, D. Martinez, R. P. Da Rocha, L. C. Sloan, and A. L. Steiner. Regional climate modeling for the developing world: The ICTP RegCM3 and RegCNET. *Bulletin of the American Meteorological Society*, 88(9):1395–1409, 2007.

[188] J. S. Pal, E. E. Small, and E. A. B. Eltahir. Simulation of regional-scale water and energy budgets: Representation of subgrid cloud and precipitation processes within RegCM. *Journal of Geophysical Research Atmospheres*, 105(D24):29579–29594, 2000.

[189] S. Park and C. B. Leovy. Marine Low-Cloud Anomalies Associated with ENSO. *Journal of Climate*, 17(17):3448–3469, 2004.

[190] Y. Peings, D. Saint-Martin, and H. Douville. A Numerical Sensitivity Study of the Influence of Siberian Snow on the Northern Annular Mode. *Journal of Climate*, 25(2):592–607, 2012.

[191] S. Peng, W. A. Robinson, and S. Li. Mechanisms for the NAO responses to the North Atlantic SST tripole. *Journal of Climate*, 16(12):1987–2004, 2003.

[192] N. Pepin, R. S. Bradley, H. F. Diaz, M. Baraer, E. B. Caceres, N. Forsythe, H. Fowler, G. Greenwood, M. Z. Hashmi, X. D. Liu, J. R. Miller, L. Ning, A. Ohmura, E. Palazzi, I. Rangwala, W. Schöner, I. Severskiy, M. Shahgedanova, M. B. Wang, S. N. Williamson, and D. Q. Yang. Elevation-dependent warming in mountain regions of the world. *Nature Climate Change*, 5(5):424–430, 2015.

[193] J. Perlwitz and H.-F. Graf. The Statistical Connection between Tropospheric and Stratospheric Circulation of the Northern Hemisphere in Winter. *Journal of Climate*, 8(10):2281–2295, 1995.

[194] C. A. Pires and R. A. P. Perdigão. Non-Gaussianity and asymmetry of the winter monthly precipitation estimation from the NAO. *Monthly Weather Review*, 135(2):430–448, 2007.

[195] S. Planton, P. Lionello, V. Artale, R. Aznar, A. Carrillo, J. Colin, L. Congedi, C. Dubois, A. Elizalde, S. Gualdi, E. Hertig, J. Jacobeit, G. Jordà, L. Li, A. Mariotti, C. Piani, P. Ruti, E. Sanchez-Gomez, G. Sannino, F. Sevault, S. Somot, and M. Tsimplis. *The climate of the Mediterranean region in future climate projections*, pages 449–502. Elsevier, 2012.

[196] S. Platnick, S. A. Ackerman, M. D. King, K. Meyer, W. P. Menzel, R. E. Holz, B. A. Baum, and P. Yang. MODIS atmosphere L2 cloud product (06_L2), 2015.

[197] P. Poli, H. Hersbach, D. P. Dee, P. Berrisford, A. J. Simmons, F. Vitart, P. Laloyaux, D. G. H. Tan, C. Peubey, J. N. Thépaut, Y. Trémolet, E. V. Hólm, M. Bonavita, L. Isaksen, and M. Fisher. ERA-20C: An atmospheric reanalysis of the twentieth century. *Journal of Climate*, 29(11):4083–4097, 2016.

[198] D. Pozo-Vázquez, S. R. Gámiz-Fortis, J. Tovar-Pescador, M. J. Esteban-Parra, and Y. Castro-Díez. El Niño-southern oscillation events and associated European winter precipitation anomalies. *International Journal of Climatology*, 25(1):17–31, 2005.

[199] P. V. V. Prasad and M. Djanaguiraman. Response of floret fertility and individual grain weight of wheat to high temperature stress: sensitive stages and thresholds for temperature and duration. *Functional Plant Biology*, 41(12):1261, 2014.

[200] B. Qian and M. A. Saunders. Seasonal predictability of wintertime storminess over the North Atlantic. *Geophysical Research Letters*, 30(13):1698, 2003.

[201] M. S. Raleigh and J. D. Lundquist. Comparing and combining SWE estimates from the SNOW-17 model using PRISM and SWE reconstruction. *Water Resources Research*, 48(1), 2012.

[202] M. S. Raleigh and J. D. Lundquist. Comparing and combining SWE estimates from the SNOW-17 model using PRISM and SWE reconstruction. *Water Resources Research*, 48(1), jan 2012.

[203] I. Rangwala and J. R. Miller. Climate change in mountains: A review of elevation-dependent warming and its possible causes. *Climatic Change*, 114(3-4):527–547, 2012.

[204] R. A. S. Ratcliffe and R. Murray. New lag associations between North Atlantic sea temperature and European pressure applied to long-range weather forecasting. *Quarterly Journal of the Royal Meteorological Society*, 96(408):226–246, apr 1970.

[205] N. A. Rayner, D. E. Parker, E. B. Horton, C. K. Folland, L. V. Alexander, D. P. Rowell, E. C. Kent, and A. Kaplan. Global analyses of sea surface temperature, sea ice, and night marine air temperature since the late nineteenth century. *Journal of Geophysical Research D: Atmospheres*, 108(14):4407, 2003.

[206] R. W. Reynolds, T. M. Smith, C. Liu, D. B. Chelton, K. S. Casey, and M. G. Schlax. Daily high-resolution-blended analyses for sea surface temperature. *Journal of Climate*, 20(22):5473–5496, 2007.

[207] M. Ribatet. SpatialExtremes: Modelling Spatial Extremes., 2015.

[208] D. Rind. The consequences of not knowing low- and high-latitude Climate sensitivity. *Bulletin of the American Meteorological Society*, 89(6):855–864, 2008.

[209] A. W. Robertson, C. R. Mechoso, and Y.-J. Kim. The Influence of Atlantic Sea Surface Temperature Anomalies on the North Atlantic Oscillation. *Journal of Climate*, 13(1):122–138, 2000.

[210] B. Rodriguez-Fonseca and M. de Castro. On the connection between winter anomalous precipitation in the Iberian Peninsula and North West Africa and the summer subtropical Atlantic sea surface temperature. *Geophysical Research Letters*, 29(18):10–1–10–4, 2002.

[211] B. Rodríguez-Fonseca, I. Polo, E. Serrano, and M. Castro. Evaluation of the North Atlantic SST forcing on the European and Northern African winter climate. *International Journal of Climatology*, 26(2):179–191, 2006.

[212] M. J. Rodwell and C. K. Folland. Atlantic air–sea interaction and seasonal predictability. *Quarterly Journal of the Royal Meteorological Society*, 128(583):1413–1443, 2002.

[213] M. J. Rodwell and B. J. Hoskins. Monsoons and the dynamics of deserts. *Quarterly Journal of the Royal Meteorological Society*, 122(534):1385–1404, 1996.

[214] M. J. Rodwell, D. P. Rowell, and C. K. Folland. Oceanic forcing of the wintertime North Atlantic Oscillation and European climate. *Nature*, 398(6725):320–323, 1999.

[215] M. Rojas, L. Z. Li, M. Kanakidou, N. Hatzianastassiou, G. Seze, and H. Le Treut. Winter weather regimes over the Mediterranean region: Their role for the regional climate and projected changes in the twenty-first century. *Climate Dynamics*, 41(3-4):551–571, 2013.

[216] R. Romera, E. Sánchez, M. Domínguez, M. Á. Gaertner, and C. Gallardo. Evaluation of present-climate precipitation in 25 km resolution regional climate model simulations over Northwest Africa. *Climate Research*, 66(2):125–139, 2015.

[217] G. Sannino, A. Bargagli, and V. Artale. Numerical modeling of the mean exchange through the Strait of Gibraltar. *Journal of Geophysical Research C: Oceans*, 107(8):9–1, 2002.

[218] K. Saunders, A. G. Stephenson, P. G. Taylor, and D. Karoly. The spatial distribution of rainfall extremes and the influence of El Niño Southern Oscillation. *Weather and Climate Extremes*, 18:17–28, 2017.

[219] M. A. Saunders and B. Qian. Seasonal predictability of the winter NAO from north Atlantic sea surface temperatures. *Geophysical Research Letters*, 29(22):6–1–6–4, 2002.

[220] M. A. Saunders, B. Qian, and B. Lloyd-Hughes. Summer snow extent heralding of the winter North Atlantic Oscillation. *Geophysical Research Letters*, 30(7), 2003.

[221] A. A. Scaife, A. Arribas, E. Blockley, A. Brookshaw, R. T. Clark, N. Dunstone, R. Eade, D. Fereday, C. K. Folland, M. Gordon, L. Hermanson, J. R. Knight, D. J. Lea, C. MacLachlan, A. Maidens, M. Martin, A. K. Peterson, D. Smith, M. Vellinga, E. Wallace, J. Waters, and A. Williams. Skillful long-range prediction of European and North American winters. *Geophysical Research Letters*, 41(7):2514–2519, 2014.

[222] J. Scheff and D. Frierson. Twenty-First-Century multimodel subtropical precipitation declines are mostly midlatitude shifts. *Journal of Climate*, 25(12):4330–4347, 2012.

[223] J. Schilling, K. P. Freier, E. Hertig, and J. Scheffran. Climate change, vulnerability and adaptation in North Africa with focus on Morocco. *Agriculture, Ecosystems and Environment*, 156:12–26, 2012.

[224] O. Schulz and C. de Jong. Snowmelt and sublimation: field experiments and modelling in the High Atlas Mountains of Morocco. *Hydrology and Earth System Sciences*, 8(6):1076–1089, 2004.

[225] R. Seager, H. Liu, N. Henderson, I. R. Simpson, C. Kelley, T. Shaw, Y. Kushnir, and M. Ting. Causes of increasing aridification of the Mediterranean region in response to rising greenhouse gases. *Journal of Climate*, 27(12):4655–4676, 2014.

[226] R. Seager, T. J. Osborn, Y. Kushnir, I. R. Simpson, J. Nakamura, and H. Liu. Climate variability and change of Mediterranean-type climates. *Journal of Climate*, 32(10):2887–2915, 2019.

[227] M. Seif-Ennasr, R. Zaaboul, A. Hirich, G. N. Caroletti, L. Bouchaou, Z. E. A. El Morjani, E. H. Beraaouz, R. A. McDonnell, and R. Choukr-Allah. Climate change and adaptive water management measures in Chtouka Aït Baha region (Morocco). *Science of the Total Environment*, 573:862–875, 2016.

[228] J. Shaman and E. Tziperman. An atmospheric teleconnection linking ENSO and Southwestern European precipitation. *Journal of Climate*, 24(1):124–139, 2011.

[229] E. Shamir and K. P. Georgakakos. Estimating snow depletion curves for American River basins using distributed snow modeling. *Journal of Hydrology*, 334(1-2):162–173, 2007.

[230] E. Shamir and K. P. Georgakakos. MODIS Land Surface Temperature as an index of surface air temperature for operational snowpack estimation. *Remote Sensing of Environment*, 152:83–98, 2014.

[231] I. R. Simpson, R. Seager, M. Ting, and T. A. Shaw. Causes of change in Northern Hemisphere winter meridional winds and regional hydroclimate. *Nature Climate Change*, 6(1):65–70, 2016.

[232] I. R. Simpson, S. G. Yeager, K. A. McKinnon, and C. Deser. Decadal predictability of late winter precipitation in western Europe through an ocean–jet stream connection. *Nature Geoscience*, 12(8):613–619, 2019.

[233] D. M. Smith, A. A. Scaife, R. Eade, and J. R. Knight. Seasonal to decadal prediction of the winter North Atlantic Oscillation: Emerging capability and future prospects. *Quarterly Journal of the Royal Meteorological Society*, 142(695):611–617, 2016.

[234] S. A. Solman, M. N. Nuñez, and M. F. Cabré. Regional climate change experiments over southern South America. I: Present climate. *Climate Dynamics*, 30(5):533–552, 2008.

[235] S. Steinschneider, Y.-C. E. Yang, and C. Brown. Panel regression techniques for identifying impacts of anthropogenic landscape change on hydrologic response. *Water Resources Research*, 49(12):7874–7886, 2013.

[236] D. B. Stephenson, V. Pavan, and R. Bojariu. Is the North Atlantic Oscillation a random walk? *International Journal of Climatology*, 20(1):1–18, 2000.

[237] L. Stour and A. Agoumi. Sécheresse climatique au Maroc durant les dernières décennies. *Hydroécologie Appliquée*, 16:215–232, 2008.

[238] U. Strasser, M. Bernhardt, M. Weber, G. E. Liston, and W. Mauser. Is snow sublimation important in the alpine water balance? *Cryosphere*, 2(1):53–66, 2008.

[239] R. T. Sutton, B. Dong, and J. M. Gregory. Land/sea warming ratio in response to climate change: IPCC AR4 model results and comparison with observations. *Geophysical Research Letters*, 34(2):L02701, 2007.

[240] R. T. Sutton and D. L. R. Hodson. Influence of the ocean on North Atlantic climate variability 1871-1999. *Journal of Climate*, 16(20):3296–3313, 2003.

[241] K. E. Taylor, R. J. Stouffer, and G. A. Meehl. An overview of CMIP5 and the experiment design. *Bulletin of the American Meteorological Society*, 93(4):485–498, 2012.

[242] C. Tebaldi, R. L. Smith, D. Nychka, and L. O. Mearns. Quantifying uncertainty in projections of regional climate change: A Bayesian approach to the analysis of multimodel ensembles. *Journal of Climate*, 18(10):1524–1540, 2005.

[243] E. Thibaud, R. Mutzner, and A. C. Davison. Threshold modeling of extreme spatial rainfall. *Water Resources Research*, 49(8):4633–4644, aug 2013.

[244] D. W. J. Thompson, S. Lee, and M. P. Baldwin. *Atmospheric processes governing the northern hemisphere annular mode/north atlantic oscillation*, volume 134, pages 81–112. American Geophysical Union, 2003.

[245] S. Totz, E. Tziperman, D. Coumou, K. Pfeiffer, and J. Cohen. Winter Precipitation Forecast in the European and Mediterranean Regions Using Cluster Analysis. *Geophysical Research Letters*, 44(24):12,418–12,426, 2017.

[246] Y. Tramblay, L. Jarlan, L. Hanich, and S. Somot. Future Scenarios of Surface Water Resources Availability in North African Dams. *Water Resources Management*, 32(4):1291–1306, 2018.

[247] Y. Tramblay, D. Ruelland, S. Somot, R. Bouaicha, and E. Servat. High-resolution Med-CORDEX regional climate model simulations for hydrological impact studies: A first evaluation of the ALADIN-Climate model in Morocco. *Hydrology and Earth System Sciences*, 17(10):3721–3739, 2013.

[248] K. E. Trenberth and J. T. Fasullo. An apparent hiatus in global warming? *Earth's Future*, 1(1):19–32, 2013.

[249] A. Tuel, A. Chehbouni, and E. A. B. Eltahir. Dynamics of seasonal snowpack over the High Atlas. *in review for Journal of Hydrology*, 1(1):1–1, 2020.

[250] A. Tuel and E. A. B. Eltahir. Large-scale circulation and precipitation decline in the Mediterranean. *AGU Fall Meeting Abstracts*, 2018.

[251] A. Tuel and E. A. B. Eltahir. Seasonal Precipitation Forecast Over Morocco. *Water Resources Research*, 54(11):9118–9130, 2018.

[252] A. Tuel and E. A. B. Eltahir. Why Is the Mediterranean a Climate Change Hot Spot? *Journal of Climate*, 33(14):5829–5843, 2020.

[253] A. Tuel, S. Kang, and E. A. B. Eltahir. High-resolution climate change projections over the Western Mediterranean. *Climate Dynamics*, 1:1, 2020.

[254] A. Tuel, P. A. O'Gorman, and E. A. B. Eltahir. Elements of the dynamical response to climate change over the Mediterranean. *in review for Journal of Climate*, 1(1):1, 2020.

[255] S. J. E. Van Dijck, A. Laouina, A. V. Carvalho, S. Loos, A. M. Schipper, H. Van der Kwast, R. Nafaa, M. Antari, A. Rocha, C. Borrego, and C. J. Ritsema. Desertification in Northern Morocco due to Effects of Climate Change on Groundwater Recharge. In *Desertification in the Mediterranean Region. A Security Issue*, pages 549–577. Kluwer Academic Publishers, Dordrecht, 2006.

[256] D. P. van Vuuren, J. Edmonds, M. Kainuma, K. Riahi, A. Thomson, K. Hibbard, G. C. Hurtt, T. Kram, V. Krey, J. F. Lamarque, T. Masui, M. Meinshausen, N. Nakicenovic, S. J. Smith, and S. K. Rose. The representative concentration pathways: An overview. *Climatic Change*, 109(1):5–31, 2011.

[257] S. M. Vicente-Serrano, S. Beguería, J. I. López-Moreno, A. M. El Kenawy, and M. Angulo-Martínez. Daily atmospheric circulation events and extreme precipitation risk in northeast Spain: Role of the North Atlantic Oscillation, the Western Mediterranean Oscillation, and the Mediterranean Oscillation. *Journal of Geophysical Research Atmospheres*, 114(8), 2009.

[258] R. S. Vose, D. Arndt, V. F. Banzon, D. R. Easterling, B. Gleason, B. Huang, E. Kearns, J. H. Lawrimore, M. J. Menne, T. C. Peterson, R. W. Reynolds, T. M. Smith, C. N. Williams, and D. B. Wuertz. NOAA's merged land-ocean surface temperature analysis. *Bulletin of the American Meteorological Society*, 93(11):1677–1685, 2012.

[259] D. B. Walton, A. Hall, N. Berg, M. Schwartz, and F. Sun. Incorporating Snow Albedo Feedback into Downscaled Temperature and Snow Cover Projections for California's Sierra Nevada. *Journal of Climate*, 30(4):1417–1438, 2017.

[260] Z. Wan. New refinements and validation of the MODIS Land-Surface Temperature/Emissivity products. *Remote Sensing of Environment*, 112(1):59–74, 2008.

[261] Z. Wan, S. Hook, and G. Hulley. MOD11A1 MODIS/Terra Land Surface Temperature/Emissivity Daily L3 Global 1km SIN Grid V006 [subset 9W-4W/30N-34N, from 2000-02-22 to 2018-07-27], 2015.

[262] D. Wang, C. Wang, X. Yang, and J. Lu. Winter Northern Hemisphere surface air temperature variability associated with the Arctic Oscillation and North Atlantic Oscillation. *Geophysical Research Letters*, 32(16):1–4, 2005.

[263] L. Wang, M. Ting, and P. J. Kushner. A robust empirical seasonal prediction of winter NAO and surface climate. *Scientific Reports*, 7(1), 2017.

[264] X. Wang, J. Li, C. Sun, and T. Liu. NAO and its relationship with the Northern Hemisphere mean surface temperature in CMIP5 simulations. *Journal of Geophysical Research*, 122(8):4202–4227, 2017.

[265] Y. Wang, M. Wang, and J. Zhao. A Comparison of MODIS LST Retrievals with in Situ Observations from AWS over the Lambert Glacier Basin, East Antarctica. *International Journal of Geosciences*, 04(03):611–617, 2013.

[266] A. Weisheimer and T. N. Palmer. On the reliability of seasonal climate forecasts. *Journal of The Royal Society Interface*, 11(96):20131162, jul 2014.

[267] D. S. Wilks. *Statistical Methods in the Atmospheric Sciences (2nd Ed.)*. Academic Press, 2 edition, 2005.

[268] S. N. Williamson, D. S. Hik, J. A. Gamon, J. L. Kavanaugh, and G. E. Flowers. Estimating temperature fields from MODIS land surface temperature and air temperature observations in a sub-arctic alpine environment. *Remote Sensing*, 6(2):946–963, 2014.

[269] R. C.J. Wills, R. H. White, and X. J. Levine. Northern Hemisphere Stationary Waves in a Changing Climate. *Current Climate Change Reports*, 5(4):372–389, 2019.

[270] J. M. Winter, J. S. Pal, and E. A. B. Eltahir. Coupling of integrated biosphere simulator to regional climate model version 3. *Journal of Climate*, 22(10):2743–2757, 2009.

[271] T. Woollings, J. M. Gregory, J. G. Pinto, M. Reyers, and D. J. Brayshaw. Response of the North Atlantic storm track to climate change shaped by ocean-atmosphere coupling. *Nature Geoscience*, 5(5):313–317, 2012.

[272] World Bank. World Development Indicators, The World Bank Group, 2020.

[273] M. L. Wrzesien, M. T. Durand, T. M. Pavelsky, I. M. Howat, S. A. Margulis, and L. S. Huning. Comparison of Methods to Estimate Snow Water Equivalent at the Mountain Range Scale: A Case Study of the California Sierra Nevada. *Journal of Hydrometeorology*, 18(4):1101–1119, 2017.

[274] Y. Xu. Evaluation of mineral dust aerosol optical depth and related components from the CHIMERE-DUST model using satellite remote sensing and ground-based observations. *Atmospheric Environment*, 191:395–413, 2018.

[275] J. H. Yin. A consistent poleward shift of the storm tracks in simulations of 21st century climate. *Geophysical Research Letters*, 32(18):1–4, 2005.

[276] D. Zanchettin, A. Rubino, D. Matei, O. Bothe, and J. H. Jungclaus. Multidecadal-to-centennial SST variability in the MPI-ESM simulation ensemble for the last millennium. *Climate Dynamics*, 40(5-6):1301–1318, 2013.

[277] G. Zappa, M. K. Hawcroft, L. Shaffrey, E. Black, and D. J. Brayshaw. Extratropical cyclones and the projected decline of winter Mediterranean precipitation in the CMIP5 models. *Climate Dynamics*, 45(7-8):1727–1738, 2015.

[278] G. Zappa, B. J. Hoskins, and T. G. Shepherd. The dependence of wintertime Mediterranean precipitation on the atmospheric circulation response to climate change. *Environmental Research Letters*, 10(10):104012, 2015.

[279] G. Zappa and T. G. Shepherd. Storylines of atmospheric circulation change for European regional climate impact assessment. *Journal of Climate*, 30(16):6561–6577, 2017.

[280] X. Zeng, M. Zhao, and R. E. Dickinson. Intercomparison of bulk aerodynamic algorithms for the computation of sea surface fluxes using TOGA COARE and TAO data. *Journal of Climate*, 11(10):2628–2644, oct 1998.

[281] Y. Zhang, T. Li, B. Wang, G. Wu, U. Schneider, B. Andreas, Finger Peter, M.-C. Anja, R. Bruno, Z. Markus, N. Sen Roy, S. Kaur, J. He, C. Sun, Y. Liu, J. Matsumoto, W. Li, A. Yatagai, K. Kamiguchi, O. Arakawa, A. Hamada, N. Yasutomi, A. Kitoh, K. Ashok, S. K. Behera, S. A. Rao, H. Weng, T. Yamagata, S. Kobayashi, Y. Ota, Y. Harada, A. Ebita, M. Moriya, H. Onoda, K. Onogi, H. Kamahori, C. Kobayashi, H. Endo, K. Miyaoka, K. Takahashi, B. Wang, H. Lin, Z. M. M. Sein, B. A. Ogwang, V. Ongoma, F. K. Ogou, K. Batebana, G. J. Huffman, R. F. Adler, P. Arkin, A. Chang, R. Ferraro, A. Gruber, J. Janowiak, A. McNab, B. Rudolf, and U. Schneider. GPCC Full Data Monthly Product Version 7.0 at 0.5 degree: Monthly Land-Surface Precipitation from Rain-Gauges built on GTS-based and Historic Data. *Bulletin of the American Meteorological Society*, 15(1):5–20, 2015.

[282] W. Zkhiri, Y. Tramblay, L. Hanich, L. Jarlan, and D. Ruelland. Spatiotemporal characterization of current and future droughts in the High Atlas basins (Morocco). *Theoretical and Applied Climatology*, 135(1-2):593–605, 2019.

[283] E. Zorita, V. Kharin, and H. von Storch. The Atmospheric Circulation and Sea Surface Temperature in the North Atlantic Area in Winter: Their Interaction and Relevance for Iberian Precipitation. *Journal of Climate*, 5(10):1097–1108, 1992.